



THE UNIVERSITY OF QUEENSLAND  
AUSTRALIA

# Infragravity Wave Forcing in the Surf and Swash Zone

Theo Garcia Rolim de Moura

MSc.

*A thesis submitted for the degree of Doctor of Philosophy at*

*The University of Queensland in 2016*

School of Civil Engineering

Coastal Engineering Research Group

## Abstract

Infragravity waves, also known as surf beat, are important morphodynamic drivers in shallow water, especially inside the surf and swash zone where the short wave energy is dissipated due to breaking. In the past decades, great progress has been acquired in the understanding of surf beat and its implication in the coastal environments. However, many key features are still not fully understood, especially for complex natural systems. This thesis investigates infragravity wave dynamics in the surf and swash zone through a re-analysis of laboratory data, new numerical modelling and novel field measurements.

The generation of infragravity waves in the surf zone is commonly associated with two individual mechanisms: release of second-order group-forced long waves and long waves generated by group-induced surf zone breakpoint oscillations. Both mechanisms are forced by radiation stress gradients, but due to their individual nature, different relationships between short and infragravity waves are expected. Determining these relationships, their effectiveness, and the governing hydrodynamic and morphodynamic conditions for each mechanism is complex. In the field, observations are still, to some extent, limited and generally restrained to small wave conditions.

The first part of the thesis presents a comprehensive study of different infragravity wave generation mechanisms that includes a critical literature review, a re-analysis of previous laboratory data and an extensive numerical modelling investigation. This work provided new information about the implication of the different processes associated to bound wave shoaling, release and dissipation. In addition, key aspects related to the propagation patterns of infragravity waves have been identified. From the numerical investigation and the large amount of laboratory data re-analysed, clear and distinct relationships between the breakpoint and shoreline excursion have been established for each generation mechanism. The second part of the thesis presents a novel method to determine the dominant infragravity mechanism in the inner surf and swash zone in the field. In the field, the breakpoint oscillations and the shoreline motion are measured remotely via video and



their relationship identified via cross-correlation. The identification of the dominant forcing mode, either bound wave or breakpoint, is interpreted based on the specific relationships previously determined.

The results of thirteen field data sets collected from three different beaches indicate that, inside the surf zone, the dominance of bound wave or breakpoint forcing is strongly dependent on the surf zone width and the type of short wave breaking. Infragravity generation by bound wave release was stronger for conditions with relatively narrow surf zones and plunging waves; breakpoint forcing was dominant for wider surf zones and spilling breaker conditions, suggesting also that the bound waves remained forced inside the surf zone, being dissipated during short wave breaking. The numerical and laboratory results have also suggested a similar interpretation.

This thesis has shown that the breakpoint and shoreline oscillations are relevant features to interpret the surf beat mechanics. The adopted methodology is based on commonly used techniques that can be easily implemented in remote sensing systems used for regular coastal monitoring, enabling easier data collection in more extreme wave conditions.

## **Declaration by author**

This thesis is composed of my original work, and contains no material previously published or written by another person except where due reference has been made in the text. I have clearly stated the contribution by others to jointly-authored works that I have included in my thesis.

I have clearly stated the contribution of others to my thesis as a whole, including statistical assistance, survey design, data analysis, significant technical procedures, professional editorial advice, and any other original research work used or reported in my thesis. The content of my thesis is the result of work I have carried out since the commencement of my research higher degree candidature and does not include a substantial part of work that has been submitted to qualify for the award of any other degree or diploma in any university or other tertiary institution. I have clearly stated which parts of my thesis, if any, have been submitted to qualify for another award.

I acknowledge that an electronic copy of my thesis must be lodged with the University Library and, subject to the policy and procedures of The University of Queensland, the thesis be made available for research and study in accordance with the Copyright Act 1968 unless a period of embargo has been approved by the Dean of the Graduate School.

I acknowledge that copyright of all material contained in my thesis resides with the copyright holder(s) of that material. Where appropriate I have obtained copyright permission from the copyright holder to reproduce material in this thesis.

### **Publications during candidature**

**Moura, T.**, Olfateh, M., Callaghan, D.P., Nielsen, P., You, Y.G. and Baldock, T.E., 2013. *Tidal amplitude and wave setup in trained and untrained river entrances*. Coasts and Ports, Sydney.

### **Publications included on this thesis**

No publications included.

### **Contributions by others to the thesis**

No contributions by others.

### **Statement of parts of the thesis submitted to qualify for the award of another degree**

None.

## Acknowledgements

First, and most importantly, I would like to thank my principal supervisor Tom Baldock for his enormous support, guidance and patience throughout my candidature. Thank you also to my co-supervisors Peter Nielsen and David Callaghan for the interesting and inspiring discussions. Thank you to all my colleagues in the Coastal Engineering Group for sharing your knowledge with me every Friday. Thanks also to The National Council for Scientific and Technological Development (CNPq-Brazil) for financial support.

I would like to thank my wife Joana for always being there for me. I have no doubt that without your help this thesis would not have been completed. Finally, a special thank you to my beloved parents. Sadly you are no longer with us, but I hope you are proud of me up there.

**keywords**

infragravity waves, surf beat generation mechanisms, surf zone dynamics, numerical modelling.

**Australian and New Zealand Standard Research Classifications (ANZSRC)**

040503 Physical Oceanography 50%

090599 Civil Engineering not elsewhere classified 50%

**Fields of Research(FoR) Classification**

code: 0405, Oceanography, 50%

code: 0905, Civil Engineering, 50%

# Contents

<b>Abstract</b>	<b>i</b>
<b>Declaration by author</b>	<b>iii</b>
<b>Acknowledgements</b>	<b>v</b>
<b>Contents</b>	<b>vii</b>
<b>List of Figures</b>	<b>x</b>
<b>List of Tables</b>	<b>xxi</b>
<b>Abbreviations</b>	<b>xxii</b>
<b>Symbols</b>	<b>xxiii</b>
<b>1 Introduction</b>	<b>1</b>
<b>2 The Generation Mechanisms of Infragravity Waves</b>	<b>4</b>
2.1 Bound Waves - Steady and Transient Concepts . . . . .	4
2.2 Breakpoint Forcing . . . . .	10
2.3 The Key Questions . . . . .	14
<b>3 The Main Aspects of Surf Beat</b>	<b>17</b>
3.1 Propagation Patterns - Identifying Generation Mechanisms . . . . .	18
3.2 Infragravity Wave Data Analysis . . . . .	19
3.2.1 Standing Wave Pattern . . . . .	22
3.2.2 A Note on the Separation of Incident and Reflected Waves. . . . .	24
3.3 Bound Wave Shoaling . . . . .	28
3.4 The Positive Part of the Bound Wave . . . . .	34
3.5 Infragravity Wave Dissipation and Bound Wave Release . . . . .	42
3.6 Infragravity Wave Dependence on Short Wave Amplitude . . . . .	47
3.7 Radiated Breakpoint Forced Long Wave . . . . .	51
3.8 Frequency Down-shift . . . . .	58

---

3.9	Conclusion . . . . .	60
<b>4</b>	<b>FUNWAVE: Description, Testing and Numerical Simplifications</b>	<b>62</b>
4.1	FUNWAVE Description . . . . .	62
4.2	Numerical Model Validation Tests . . . . .	64
4.2.1	Bichromatic Wave Groups . . . . .	64
4.2.2	Random Waves . . . . .	66
4.2.3	Transient Wave Group . . . . .	66
4.2.4	Results . . . . .	67
4.3	Numerical Simplification of Infragravity Wave Dynamics . . . . .	76
4.4	Long Waves Generated by Radiation Stress Forcing . . . . .	77
4.4.1	Analytical Benchmark - Horizontal Bottom Tests . . . . .	78
4.4.1.1	Non Resonant / Resonant Condition Flat Bottom . . . . .	78
4.4.2	Propagation Over Sloping Bottoms . . . . .	81
4.4.3	Transient Wave Group . . . . .	83
4.5	Breakpoint Forcing in FUNWAVE . . . . .	84
4.6	Conclusion . . . . .	92
<b>5</b>	<b>Infragravity Waves: A Numerical Investigation</b>	<b>94</b>
5.1	Bound Wave Shoaling . . . . .	94
5.2	Bound Wave: Forced and Free Waves . . . . .	98
5.3	Identifying Breakpoint Forced Waves by Controlling Short Wave Breaking . . . . .	102
5.4	Infragravity Wave Dissipation and Bound Wave Release. . . . .	104
5.5	Relationship Between Wave Groups, Breakpoint, Shoreline Excur- sion and Infragravity Waves . . . . .	111
5.5.1	Cross-correlation Between Breakpoint and Shoreline Excur- sion: Determining Surf Zone Infragravity Wave Forcing, Ran- dom Wave Cases. . . . .	119
5.6	Conclusion . . . . .	122
<b>6</b>	<b>Infragravity Dynamics on Natural Beaches</b>	<b>124</b>
6.1	Introduction . . . . .	124
6.2	Data Collection and Analysis . . . . .	126
6.2.1	Conto Beach . . . . .	131
6.2.2	Palm Beach . . . . .	133
6.2.2.1	Tallow Beach . . . . .	136
6.3	Results and Discussion . . . . .	138
6.3.1	Power Relationship Between Short and Infragravity Wave Height . . . . .	138
6.3.2	Incident and Outgoing Infragravity Waves . . . . .	142
6.3.3	Breakpoint Forced Wave and the Positive Part of Bound Wave	145
6.3.4	Relationship Between Wave Groups, Breakpoint, Shoreline Excursion and Infragravity waves . . . . .	146
6.3.5	Determining Surf Zone Infragravity Wave Forcing . . . . .	147

---

6.4	Conclusions . . . . .	154
<b>7</b>	<b>Thesis Summary and Future Research</b>	<b>156</b>
7.1	Summary of Conclusions . . . . .	156
7.2	Suggestions for Future Research . . . . .	159
	 <b>Bibliography</b>	 <b>160</b>



# List of Figures

1.1	Nearshore fluid dynamics, induced by offshore generated wind waves, divided by frequency and cross-shore location, Blue dashed line broad spectrum of the research (bound wave forcing, shoaling, propagation patterns of infragravity waves), red line is the main focus of the Thesis (infragravity wave dissipation and dominant forcing in the surf zone). After Holman et al. (2015).	3
2.1	Spatial representation of bound wave and forcing (full line). Dashed line, steady solution (equation 2.12). Dotted line, resonant condition (equation 2.14).	6
2.2	Schematic representation of waves generated by an abrupt onset of a moving radiation stress forcing (dashed line), surface elevation (black line).	8
2.3	The graphical interpretation of the bound wave by Longuet-Higgins and Stewart (1962) with positive and negative part (left) and Mei et al. (2005) purely negative (right). <i>Env</i> is the short wave envelope.	9
2.4	Space-time evolution of the forcing function for a sinusoidal breakpoint excursion (thick gray line). The thin gray lines are the cross-shore step functions at distinct instants in time. The black lines are the time evolution of the forcing at the cross-shore locations $x_a$ and $x_b$ . Adapted from Symonds et al. (1982).	11
2.5	Schematic representation of the forcing function for a sinusoidal varying breakpoint. Grey line - mean setup ( $n = 0$ ), black line - first harmonic (group frequency, $n = 1$ ), dashed line - second harmonic ( $n = 2$ ) and dot-dashed line third harmonic ( $n = 3$ ). Adapted from Symonds et al. (1982).	13
3.1	Components of the cross-shore infragravity signal. BLW- bound long wave, RBLW- released bound long wave, IBFLW- incident break point forced long wave, OBFLW- outgoing breaking point forced long wave and BP- breakpoint position. After Contardo and Symonds (2013).	19
3.2	Components of the cross-shore infragravity signal. Incident and reflected waves, full line - position A, dashed line - position B in Figure 3.1.	21
3.3	Cross-correlation result between two signals measured at different locations, see Figure 3.1.	22

3.4	Cross-correlation between surface elevation at different locations with respect to $x = 500\text{m}$ for a standing wave with $T = 126.7\text{s}$ . . . . .	23
3.5	Cross-correlation between surface elevation at different location with respect to $x = 500\text{m}$ for a sum of standing waves. Incident waves (top left), reflected waves (top right), total signal (bottom). . . . .	24
3.6	Comparison between separation methods, outside the surf zone. (a)-(b) Total Surface elevation at two different locations. (c) Incident, (d) reflected and (e) total infragravity band only at the first location. Random wave case J6033A (table 4.2), methods I (black) and II (grey). The second location (b) is only used in method I. . . . .	26
3.7	Comparison between separation methods. (a)-(b) Total Surface elevation at two different locations. (c) Incident, (d) reflected and (e) total infragravity band only at the first location. Transient case G08A (table 4.3), methods I (black) and II (grey). The second location (b) is only used in method I. . . . .	27
3.8	Schematic representation of the surface elevation at a fixed position for the conceptual model. Dot-dashed line - bound wave propagating with group velocity $c_g$ . Dashed line - free wave generated during the shoaling process propagating with $\sqrt{gh}$ . Full line - total signal. $A$ represents the amplitude of each wave. . . . .	32
3.9	Total infragravity wave amplitude at a fixed position on the virtual slope for wave groups with the same $c_g$ but different $f_g$ . Conceptual model of bound and free wave interference. . . . .	33
3.10	Left: Total infragravity wave shoaling for different frequencies, gray dashed line $\sim h^{-5/2}$ , gray dash-dotted line $\sim h^{-1/4}$ . Right: Theoretical rates of energy transfer calculated based on the observed lags using equation 3.12. . . . .	34
3.11	a) Space-time evolution of wave envelope amplitude , (b) total infragravity surface elevation, including mean setup $f < 0.4\text{Hz}$ . (c) band-pass filtered surface elevation $0.13 < f \leq 0.4\text{Hz}$ , without mean setup, (d) low-pass filtered surface elevation $f \leq 0.13\text{Hz}$ , without mean setup, (e) mean setup. Random wave case J6033A (see table 4.2) on a plane beach. Lines A and B are locations along which data is extracted for Figure 3.13. . . . .	37
3.12	(a) Space-time evolution of wave envelope amplitude , (b) total infragravity surface elevation, including mean setup $f < 0.4\text{Hz}$ . (c) band-pass filtered surface elevation $0.13 < f \leq 0.4\text{Hz}$ , without mean setup, (d) low-pass filtered surface elevation $f \leq 0.13\text{Hz}$ , without mean setup, (e) mean setup. Random wave case J6033A on a barred beach. Bar crest is located at $x = -2.1\text{m}$ . Lines A and B are locations along which data is extracted for Figure 3.14. . . . .	38

- 3.13 (Left) Spatial visualization at  $t = 41.3\text{s}$  (B in Figure 3.11) of short wave envelope (dashed black line), total long wave surface elevation (gray dashed), long wave and no setup (full black line) and mean setup (full grey line). (Right) Time evolution of short wave envelope (dashed line) and total long wave (full line) at  $x = -3.75\text{m}$  (A in Figure 3.11). Random wave case J6033A. . . . . 39
- 3.14 (Right) Spatial visualization at  $t = 41\text{s}$  (B in Figure 3.11) of short wave envelope (dashed black line), total long wave surface elevation (gray dashed), long wave and no setup (full black line) and mean setup (full grey line). (Left) Time evolution of short wave envelope (dashed line) and total long wave (full line) at position  $x = -4.45\text{m}$  (A in Figure 3.11). Random wave case J6033A on a barred beach. . . . . 39
- 3.15 Cross-correlation between short wave envelope and long wave at  $x = -3.15\text{m}$ , dashed line is the travel time of the bound wave to the shoreline plus the travel time of the free wave reflected at the shoreline. Random wave case J6010A.  $BW_N/BW_P$  are the peaks related to the negative/positive part of the bound wave, and  $Ref$  are the peaks related to the reflected signal. . . . . 40
- 3.16 Cross-correlation between short wave envelope at  $x = -3.15\text{m}$  (dash-dotted line) and long wave at different position along the wave flume. Dashed line is the mean breakpoint position. Random wave case J6010A. . . . . 41
- 3.17 Schematic representation of forcing decay and surface elevation response. (top) Abrupt removal, (bottom) slow decay. . . . . 43
- 3.18 Infragravity surface elevation, Transient case G08A (table 4.3). Adapted from Baldock (2006). Colormap in meters. . . . . 44
- 3.19 Run-up amplitude for bichromatic wave groups. Left: Vertical run-up amplitude at the group frequency,  $\Delta$ – series A,  $\nabla$ – series B, + series C and  $\bigcirc$ – series D. Black line is the run-up saturation limit according to (Baldock and Holmes, 1999). Right: Run-up versus wave group length normalized by short wave length, series A. Colorbar is the relative groupiness. Data from Baldock et al. (2000). . . . . 46
- 3.20 Run-up amplitude for bichromatic wave groups, series A. Data from Baldock et al. (2000). . . . . 47
- 3.21 Short wave envelope amplitude. Random wave cases J6033A (full line), J6033B (dashed line) and J6033C (dashed-dotted line). . . . . 48
- 3.22 Power relationship, at discrete frequencies ( $\Delta f = 0.018\text{Hz}$ ), between infragravity wave and the target incident short wave height. Random wave cases J6033A ( $H_{m0} = 0.141\text{m}$ ), J6033B ( $H_{m0} = 0.106\text{m}$ ) and J6033C ( $H_{m0} = 0.071\text{m}$ ), Colormap is the power  $p$ . . . . . 49
- 3.23 Power relation, at discrete frequencies ( $\Delta f = .018\text{Hz}$ ), between infragravity wave and the target incident short wave height. Incident (left) and outgoing infragravity wave (right). Random wave cases J6033A ( $H_{m0} = 0.141\text{m}$ ), J6033B ( $H_{m0} = 0.106\text{m}$ ) and J6033C ( $H_{m0} = 0.071\text{m}$ ). Colormap is the power  $p$ . . . . . 50

3.24	Short wave envelope spectrum normalized by the target wave height ( $H_{sh}^2$ ). Random wave cases J6033A (left), J6033B (center) and J6033C (right). . . . .	51
3.25	Surface elevation for bichromatic wave groups, case B1025A (table 4.1). $f_R$ is the repeat frequency. . . . .	53
3.26	Vertical run-up oscillations for different bichromatic wave groups. Each time series is normalized by its maximum amplitude, time is scaled according to each repeat frequency $T_R = 1/f_R$ . . . . .	53
3.27	(a) space and time evolution of wave envelope amplitude, (b) total infragravity surface elevation (including mean setup), (c) surface elevation at the group frequency (without mean setup), (d) low-pass filtered surface elevation at and below $f_R$ (without mean setup) and (e) mean setup. Black line is the low-pass filtered breakpoint position numerically calculated (Chapter 4). Bichromatic wave case B1060A. Colormap in $p$ . . . . .	55
3.28	Cross-correlation between incident and outgoing long wave at $x = -2\text{m}$ , dotted line is the travel time from the breakpoint to measurement position. Dashed line is travel time for the shoreline reflected wave. Random wave case J6033A. . . . .	57
3.29	Cross-correlation between incident long wave at $x = -4\text{m}$ and outgoing long wave at: $x = -4\text{m}$ (black), $x = -2.8\text{m}$ (red) and $x = 1.8\text{m}$ (green). Dotted line travel time related to the breakpoint radiated outgoing wave. Dashed line, travel time related to the shoreline reflected wave. Random wave case J6033A. . . . .	57
3.30	Random wave case J6033C, top panel- wave envelope spectrum, mid panel - infragravity spectrum, bottom panel - bottom slope. Left-plane beach, right- barred beach. Colormap in $m^2/Hz$ . . . . .	59
4.1	Wave flume and instrumentation. From Baldock and Huntley (2002). . . . .	65
4.2	Time series of surface elevation at different cross-shore locations, case B1025A. Top to bottom, cross-shore distance from the shoreline: -11 m, -6 m, -2.75 m, -0.85 m, at the still water line (SWL) and vertical shoreline excursion. Black line: predicted, grey line: data. . . . .	67
4.3	Time series of surface elevation at different cross-shore locations, case J6010A. Top to bottom, cross-shore distance from the shoreline: -11 m, -6 m, -2.75 m, -0.85 m, at the SWL and vertical shoreline excursion. Black: predicted, gray: data. . . . .	68
4.4	Predicted $Hm0_{error}$ . $\Delta$ — bichromatic cases; $\bigcirc$ — random cases. . . . .	69
4.5	Run-up height $Rm0$ , measured versus predicted. +: Total ; $\bigcirc$ : Primary frequencies; $\diamond$ : Infragravity frequencies; black: bichromatic wave group cases; grey: random wave cases. Dashed line represents $\pm 20\%$ error and solid line is perfect agreement. . . . .	71

4.6	$Hm0_{IG}$ and $Rm0_{IG}$ for the random cases. (a) J1010C, (b) J1033C, (c) J6010A, (d) J6010B, (e) J6010C, (f) J6033A, (g) J6033B and (h) J6033C. Measured (grey) and simulated (black). The most shoreward data point is the shoreline oscillation. . . . .	72
4.7	Space-time evolution of infragravity surface elevation (top) and mean setup (bottom). Laboratory data (a) and (b), numerical results (c) and (d). Bichromatic wave case B1020A. Black line is the simulated breakpoint excursion. Colormap in meters. . . . .	73
4.8	Numerical results of (a) space-time evolution of wave envelope amplitude, (b) total infragravity surface elevation (including mean setup), (c) surface elevation at the group frequency (without mean setup), (d) low-pass filtered surface elevation at and below $f_R$ (without mean setup) and (e) mean setup. Black line is the low-pass filtered breakpoint position. Bichromatic wave case B1060A. . . . .	74
4.9	Total and low-pass filtered surface elevation at different locations. Grey- measured, black - simulated. Transient case G08A. . . . .	75
4.10	Spatial evolution of wave group envelope (dashed) and long wave (solid) at different instants (from $a$ to $d$ ). Grey - measured, black - simulated. . . . .	76
4.11	Surface elevation normalized by initial forced wave amplitude, non-resonant condition. Dashed line - $F_{S_{xx}}$ normalized by its maximum amplitude, Black line - non-linear terms only, grey line - dispersive terms included. . . . .	78
4.12	Surface elevation normalized by initial forced wave amplitude, resonant condition. Dashed line - $F_{S_{xx}}$ normalized by its maximum amplitude, black line - non-linear terms only, gray line - dispersive terms included. . . . .	79
4.13	Spatial evolution of wave amplitude and lags for a forcing switched to resonant condition at $x/Lg = 0.1$ . The cross-shore distance is normalized by the length of the forcing. Full line - long wave amplitude normalized by the initial forced wave amplitude. Dashed line, lag normalized by the expected full resonant lag. . . . .	80
4.14	Schematic representation of the performed simulations. $IBW$ is the incident bound wave, $IFW_0$ is the forward free wave generated to balance the initial condition, and it propagates away from the IBW over the horizontal bottom. $IBW/IFW$ is the positive part of the bound wave generated during the shoaling process. Dotted-dashed line is the representation of the forcing. $A_{for}$ is the amplitude of the forced wave on the horizontal bottom and $A$ is the total bound wave amplitude in the shoaling zone. . . . .	82
4.15	Long wave amplitude (solid lines) propagating over a slope ( $\beta = 0.05$ ). The forcing speed is defined by equation 4.6, $T = 6s$ (gray) and $T = 15s$ (black). Dashed line ( $\sim h^{-5/2}$ ), Dashed-dotted line ( $\sim h^{-1/4}$ ). . . . .	83

4.16	Long wave amplitude (solid lines) propagating over a slope ( $\beta = 0.01$ ). The forcing speed is defined by equation 4.6, $T = 6s$ (gray) and $T = 15s$ (black). Dashed line ( $\sim h^{-5/2}$ ), Dashed-dotted line ( $\sim h^{-1/4}$ ). . . . .	83
4.17	Low-frequency surface elevation at different time instants. Dashed line - full simulation, black line - radiation stress forcing only. . . . .	84
4.18	Surface elevation at different time instants, constructive interference. Dashed line - mean breakpoint position, $\Delta a = 0.26$ and $\chi = 1.1$ . . . . .	85
4.19	Surface elevation at different time instants, destructive interference. Dashed line - mean breakpoint position, $\Delta a = 0.21$ and $\chi = 3.65$ . . . . .	85
4.20	Wave amplitude outside the surf zone ( $X = -200m$ ) normalized by the wave amplitude close to the shoreline ( $X = -15m$ ). Grey line is the analytical solution for $\Delta a = 0.2$ (Symonds et al., 1982). Mean breakpoint at $X = -100m$ . . . . .	86
4.21	Left: Space-time evolution of the surface elevation generated by breakpoint forcing at a single frequency, white line is the breakpoint excursion. Right: Cross-correlation between time evolution of the breakpoint excursion and surface elevation. Mean breakpoint $X = -100m$ (dashed white line), breakpoint modulation amplitude $\Delta a = 0.14$ , $\chi = 1.45$ , $f = 0.01Hz$ . . . . .	87
4.22	Left: Space-time evolution of the surface elevation generated by breakpoint forcing, white line is the breakpoint excursion. Right: Cross-correlation between time evolution of the breakpoint excursion and surface elevation. Summation of three individual single frequency cases with mean breakpoint $X = -100m$ (dashed white line) and respective breakpoint modulation amplitude ( $\Delta a = 0.11$ , $0.13$ and $0.10$ ), normalized surf zone width ( $\chi = 2.6236$ , $1.45$ and $6.57$ ) and frequencies ( $f = 0.014$ , $0.0095$ and $0.02Hz$ ). . . . .	88
4.23	Space-time surface elevation at $f_R$ for the bichromatic case B1060A. Left - measured, center - full simulation and right - breakpoint forcing only ( $\chi \approx 0.3$ ). The surface elevation is normalized by its maximum in each plot. White line is the breakpoint excursion . . . . .	89
4.24	Spectra of surface elevation at the shoaling zone $X = -3m$ (a-b), short wave envelope at $X = -3m$ (c-d), run-up (e-f) and breakpoint excursion (g-h). Vertical lines, group frequency (dot-dashed) and repeat frequency (dashed). Bichromatic cases B1045A (left) and B1060A (right). The highlighted triad frequencies are indicated by arrows. Black line numerical results, grey line measured data. . . . .	91
4.25	Space-time evolution of surface elevation at discrete frequencies, $f_g$ (left) and $2f_2 - f_1$ (right), bichromatic case B1045A. Colormap in centimeters. . . . .	92
5.1	Surface elevation in the shoaling zone, waves generated by different forcing length but same propagation speed. FUNWAVE results. Each line represents a different group length, from shortest 200m (blue line), to the longest 345m (dark red). . . . .	95

5.2	Surface elevation on the horizontal bottom, after the shoaling zone. The waves are generated by different forcing length but with the same propagation speed. Leading positive free waves and negative forced waves. FUNWAVE results. . . . .	97
5.3	Surface elevation on the horizontal bottom, after the shoaling zone. The waves are generated by different forcing length but with the same propagation speed. Leading positive free waves and negative forced waves. Conceptual model results (Section 3.3). . . . .	97
5.4	Short (black) and infragravity (grey) surface elevation time series at $x = 10\text{m}$ (a, b and c), $x = 26\text{m}$ (d, e f) and $x = 448\text{m}$ (g, h and i). There is no wave breaking for the case in left panels. The center and right panels are cases with different wave breaking/dissipation intensity. The infragravity waves are multiplied by a factor of ten. . . . .	101
5.5	Relationship between short ( $A_s$ ) and infragravity wave ( $A_{IG}$ ) amplitude. The numerical subscripts indicate spatial location. Black line (+), $A_s$ at $x = 10\text{m}$ and $A_{IG}$ at $x = 448\text{m}$ , $m = 1.89$ , without short wave dissipation. Grey line ( $\odot$ ), $\Delta A_s$ ( $x = 10$ and $x = 26\text{m}$ ) and $A_{IG}$ , $m = 1.03$ , with short wave dissipation (the free waves generated with the bound waves are subtracted, see section 5.3). . . . .	102
5.6	Infragravity surface elevation at $x = 10\text{m}$ , total signal (grey line), incident signal (dashed line) and outgoing signal (full black line). Top panel (no dissipation/breaking), center panel (mild dissipation) and bottom panel (strong dissipation). The total infragravity signal for each case is also respectively shown in panels a, b and c in Figure 5.4. . . . .	104
5.7	Space-time surface elevation generated by two different simulations. Left: abrupt forcing removal (blue line in Figure 5.8). Right: slowest forcing decay (magenta line in Figure 5.8). The horizontal dot-dashed lines are the time limits of the forcing decay. The black line indicates the instant plotted for each simulation in Figure 5.8, with the spatial limits defined by the thick black line. $IFW_0$ and $OFW_0$ are, respectively, the incident and the outgoing free waves generated to compensate the initial condition. $IBW$ is the incident bound wave, traveling with speed $< \sqrt{gh}$ . $RIFW$ and $ROFW$ are, respectively, the released incident and outgoing free waves. . . . .	106
5.8	Free waves generated by the forcing offset. The blue line represent an abrupt damping, the longer the depression the longer the $F_{S_{xx}}$ decay region. Each color represents a $0.2Lg$ increment of the decaying zone. . . . .	107
5.9	Spatial surface elevation (black line) at different instants generated by $F_{S_{xx}}$ propagating over a sloping bottom. The vertical grey dots indicate the region where the forcing (dashed line) is damped. Shortest (left) and longest (right) forcing cases. . . . .	108
5.10	Short (grey line) and infragravity wave amplitude (thick black line) and depth ( $h/20$ ) (thin black line). $x_1$ and $x_2$ are the defined breaking zone. . . . .	110

- 5.11 Infragravity wave dissipation during short wave breaking for different simulated bichromatic cases over two different slopes  $\beta = 0.01$  (left) and  $0.04$  (right). The colorbar is the normalized groupiness at  $x_2$ . . . . . 111
- 5.12 Correlation between wave envelope (in the shoaling zone) and breakpoint excursion (black), and between shoreline excursion and infragravity surface elevation in the inner surf zone (grey), for the random cases (table 4.2) reproduced for different slopes,  $\circ$  for  $\beta = 0.1$ ,  $\triangle$  for  $\beta = 0.04$ ,  $\nabla$  for  $\beta = 0.02$ . . . . . 112
- 5.13 Schematic representation of surf beat generated by bound wave release and breakpoint forcing. (a) Cross-shore evolution of the wave group, bound and breakpoint forced long wave. The vertical colored lines indicate the breakpoint position. Gray line is the released bound wave. The red line is the incident breakpoint forced long wave. (b) Breakpoint excursion (black line) and shoreline response to long waves generated by the breakpoint forcing (red line) and released bound wave (grey line). (c) Cross-correlation between breakpoint and shoreline excursion, bound wave release (grey line) and breakpoint forced long wave (red line).  $\tau$  is the travel time for a shallow water wave to travel from the breakpoint to the shoreline. 114
- 5.14 Schematic representation of surf beat generated by the bound mechanism. (a) Cross-shore evolution of the short wave group and the bound with a leading surge. Vertical lines are the inner (red line) and outer (green line) breakpoint limits. Gray line is the released bound wave. (b) Breakpoint excursion and shoreline oscillation. (c) Cross-correlation between breakpoint and shoreline excursion.  $\tau$  is the travel time for a shallow water wave to travel from the breakpoint to the shoreline. . . . . 115
- 5.15 Schematic representation of surf beat generated by the resonant bound wave. (a) Cross-shore evolution of the short wave group and the resonant bound wave. (b) Breakpoint excursion and shoreline response. (c) Cross-correlation between breakpoint and shoreline excursion.  $\tau$  is the travel for a shallow water wave to travel from the breakpoint to the shoreline. . . . . 116
- 5.16 Cross-correlation between breakpoint and shoreline excursion, for the summation of the 50 different single frequency cases. Dashed line is  $T_{mb,swl}$ . . . . . 117
- 5.17 Space-time surface elevation evolution for the random breakpoint forcing. Left: Total signal, right: excluding mean set-up. Note the different colorbar limits (in meters) for each panel. Black line represents the breakpoint excursion. . . . . 118
- 5.18 Wave amplitude outside the surf zone ( $x = -200\text{m}$ ) normalized by the wave amplitude close to the shoreline ( $x = -15\text{m}$ ).  $\circ$  - individual single frequency cases,  $\triangle$  - multi frequency breakpoint oscillation. Grey line is the analytical solution for  $\Delta a = 0.2$  (Symonds et al., 1982). . . . . 118



5.19	Cross-correlation between breakpoint and shoreline excursion, for the random case. Dashed line is $T_{mb,swl}$ . . . . .	119
5.20	Cross-correlation between breakpoint and shoreline excursion for the eight random cases (Table 4.2), simulated for three different slopes. (a,d and g) J1010C (black) and J1033C (light gray), (b, e and h) J6010A (black), J6010B (dark gray) and J6010C (light gray). (c, f and i) J6033A (black), J6033B (dark gray) and J6033C (light gray). Top panels $\beta = 0.1$ , mid panels $\beta = 0.05$ and bottom panels $\beta = 0.02$ . Dashed lines are $T_{mb,swl}$ with the respective colors. For J1010C and J1033C $T_{mb,swl}$ is nearly the same. . . . .	121
5.21	Cross-correlation between breakpoint and shoreline excursion. Right panel: case J1010C, center panel: case J6010A, left panel: case J6033A. Black line: full simulation, green line: breakpoint forcing, red line: bound wave forcing, bottom slope $\beta = 0.1$ . Dashed lines are $T_{mb,swl}$ . . . . .	122
6.1	(a) Original image with the cross-shore transect. (b) Timestack of the swash and surf zone, Palm Beach QLD. Breakpoint (black line) and shoreline (grey line) excursion. (c) and (d) Short (black) and infragravity waves (red) at $PT_{off}$ and $PT_{in}$ , respectively. . . . .	129
6.2	Geographic location of the field sites. (a) Conto Beach, WA, (b) Palm Beach, QLD and (c) Tallow Beach, NSW. The red line and the triangle indicate, respectively, the cross-shore location of the timestack and camera position for each beach. Adapted from Google Earth. . . . .	131
6.3	Wave conditions at the Cape Naturaliste wave buoy (grey line) and at $PT_{off}$ (black line). Top panel: $H_{sig}$ solid line and $H_{max}$ dashed line. . . . .	132
6.4	Sequence (a-i) of average pixel intensity images for Conto Beach. Total time of 18 minutes, each image is average over 2 minutes. Black line is the Cross-shore location of the timestacks. . . . .	133
6.5	Palm Beach profile, measured at 30/04/10. Data from Haines (2013). . . . .	134
6.6	Wave conditions at the Gold Coast wave buoy (gray line) and at $PT_{off}$ (black line). Top panel: $H_{sig}$ solid line and $H_{max}$ dashed line. Top panel: $H_{sig}$ solid line and $H_{max}$ dashed line. . . . .	135
6.7	Image of pixel intensity average over 5 minutes, Palm Beach. . . . .	135
6.8	Wave conditions at the Gold Coast wave buoy for the second field-work experiment in Palm Beach. Top panel: $H_{sig}$ solid line and $H_{max}$ dashed line. . . . .	136
6.9	Wave conditions at the Gold Coast wave buoy (gray line) and at $PT_{off}$ (black line). Top panel: $H_{sig}$ solid line and $H_{max}$ dashed line. . . . .	137
6.10	Image of pixel intensity averaged over 5 minutes, Tallow Beach. . . . .	137
6.11	Wave conditions at the Byron Bay wave buoy. Top panel: $H_{sig}$ solid line and $H_{max}$ dashed line. . . . .	138
6.12	Power relation between $Hm0$ and $Hm0_{IG}$ . $\Delta$ — $Hm0$ and $Hm0_{IG}$ at $PT_{off}$ . $\circ$ — $Hm0$ at $PT_{off}$ and $Hm0_{IG}$ at $PT_{in}$ . . . . .	139

- 6.13 Surface elevation spectrum. Left:  $PT_{off}$  and right:  $PT_{in}$ . Top, center and bottom panels are, respectively, Conto, Palm and Tallow Beach. Different days of data collection are represented by different colors indicated in Table 6.1. . . . . 140
- 6.14 Power relation between  $Hm0$  and  $Hm0_{IGi}$ .  $\Delta$ –  $Hm0$  and  $Hm0_{IGi}$  at  $PT_{off}$ .  $\circ$ –  $Hm0$  at  $PT_{off}$  and  $Hm0_{IGi}$  at  $PT_{in}$ . Left:  $0.0025 < f_{IG3} \leq 0.01\text{Hz}$ , center:  $0.01 < f_{IG2} \leq 0.02\text{Hz}$  and right:  $0.02 < f_{IG1} \leq 0.04\text{Hz}$ . Full gray circles  $R < 1$ . . . . . 141
- 6.15 Cross-correlation between infragravity surface elevation at  $PT_{off}$  and  $PT_{in}$ . Left: Conto Beach, center: Palm Beach and right: Tallow Beach.  $I, I$  and  $R, R$  are the correlation peaks related to incident-incident signal and reflected-reflected signal respectively. . . . . 143
- 6.16 Cross-correlation between wave envelope and infragravity surface elevation at  $PT_{off}$  Left: Conto Beach, center: Palm Beach and right: Tallow Beach.  $BW_N/BW_P$  are the peaks related to the cross-correlation between short wave envelope ( $Env$ ) and the negative/positive part of the bound wave.  $Env, R$  is the cross-correlation between the short wave envelope and the reflected signal. . . . . 144
- 6.17 Cross-correlation between low-frequency motion at  $PT_{off}$  and the breakpoint excursion. Left: Conto Beach, center: Palm Beach and right: Tallow Beach.  $(I, Bre/R, Bre)$  are the correlation peaks related to the incident/reflected infragravity wave signal and the breakpoint oscillation. . . . . 145
- 6.18 Cross-correlation between infragravity surface elevation at  $PT_{in}$  and Shoreline excursion. Left: Conto Beach, center: Palm Beach and right: Tallow Beach. . . . . 146
- 6.19 Cross-correlation between wave envelope at  $PT_{off}$  and breakpoint excursion. Left: Conto Beach, center: Palm Beach and right: Tallow Beach. . . . . 147
- 6.20 Cross-correlation between breakpoint and run-up excursion. Left: Conto Beach, center: Palm Beach and right: Tallow Beach. Dashed lines are the mean propagation time of the bore from the breakpoint to the shoreline. . . . . 148
- 6.21 Cross-correlation between wave envelope at  $PT_{off}$  and run-up excursion. Left: Conto Beach, center: Palm Beach and right: Tallow Beach. . . . . 148
- 6.22 Timestack and cross-correlation between breakpoint and run-up excursion for *Palm01* (left) and *Palm04* (right). Dashed lines are the mean propagation time of the bores from the initial breakpoint to the maximum run-up. . . . . 149
- 6.23 Top panels: original image; Mid panels: timestacks; Bottom panels: cross-correlation between breakpoint and run-up excursion for *Palm04, 05, 06*. Dashed lines are the mean propagation time of the bores from the initial breakpoint to the maximum run-up. . . . . 152

- 6.24 Normalized power spectrum of surface elevation (full line) and short wave envelope (dot-dashed line) at  $PT_{off}$  (a-b-c), run-up (d-e-f) and breakpoint excursion (g-h-i). Vertical dashed lines indicate the frequency peaks that are on the surface elevation, run-up and breakpoint excursion spectra, but are not in the short wave envelope spectrum. Panels: *Palm03* (left), *Conto03* (center) and *Conto04* (right). . . . . 153

# List of Tables

4.1	Bichromatic wave groups, initial conditions. Primary wave amplitudes $a_1 = a_2 = 2.5\text{cm}$ . . . . .	64
4.2	Random wave cases, initial wave characteristics. . . . .	66
4.3	Transient wave group, initial wave characteristics. . . . .	66
5.1	Details of the bichromatic wave group simulations. . . . .	110
6.1	Field experiments and conditions. Location, date, peak period ( $T_p$ ) and significant wave height ( $H_s$ ) at the nearest wave buoy, $H_s$ , $T_{low}$ (peak period at the infragravity frequency) and depth ( $h$ ) at $PT_{off}$ . Normalized bed slope $\beta_n$ and surf beat similarity $\xi_{sb}$ . The color lines are use for differentiation in the following figures. . . . .	130
6.2	Target frequency ( $f$ ), mean surf zone width ( $X_{mean}$ ), normalized surf zone width ( $\chi$ ) and expected outgoing wave amplitude interference. . . . .	153

# Abbreviations

<b>BLW</b>	<b>B</b> ound <b>L</b> ong <b>W</b> ave
<b>RBLW</b>	<b>R</b> eleased <b>B</b> ound <b>L</b> ong <b>W</b> ave
<b>IBFLW</b>	<b>I</b> ncident <b>B</b> reak <b>F</b> orced <b>L</b> ong <b>W</b> ave
<b>OBFLW</b>	<b>O</b> utgoing <b>B</b> reak <b>F</b> orced <b>L</b> ong <b>W</b> ave
<b>BP</b>	<b>B</b> reak <b>P</b> oint
<b>SWL</b>	<b>S</b> till <b>W</b> ater <b>L</b> ine
<b>IBW</b>	<b>I</b> ncident <b>B</b> ound <b>W</b> ave
<b>IFW</b>	<b>I</b> ncident <b>F</b> ree <b>W</b> ave
<b>OFW</b>	<b>O</b> utgoing <b>F</b> ree <b>W</b> ave
<b>RIFW</b>	<b>R</b> eleased <b>I</b> ncident <b>F</b> ree <b>W</b> ave
<b>ROFW</b>	<b>R</b> eleased <b>O</b> utgoing <b>F</b> ree <b>W</b> ave

# Symbols

Symbol	Name	Unit
$\eta$	Surface elevation.	$L$
$\bar{\eta}$	Mean surface elevation.	$L$
$u$	Horizontal velocity in the direction of the wave propagation.	$LT^{-1}$
$\bar{u}$	Mean horizontal velocity.	$LT^{-1}$
$a_{m,n}$	Primary wave amplitude.	$L$
$a$	Normalized wave amplitude.	—
$k$	Wave number.	$L^{-1}$
$k_s$	Short wave number.	$L^{-1}$
$k_b$	Wave group number.	$L^{-1}$
$k_f$	Free wave number.	$L^{-1}$
$\psi$	Initial primary wave phase.	—
$T$	Wave period.	$T$
$T_p$	Peak wave period.	$T$
$f$	Frequency.	$T^{-1}$
$f_g$	Wave group frequency.	$T^{-1}$
$f_R$	Repeat frequency.	$T^{-1}$
$f_c$	Central frequency.	$T^{-1}$
$\sigma$	Radian frequency. ( $2\pi f$ )	$T^{-1}$
$S_{xx}$	Shore normal wave radiation stress.	$MT^{-2}$
$g$	Acceleration due to gravity.	$MT^{-2}$
$\rho$	Density.	$ML^{-3}$
$h$	Water depth.	$L$

---

$X$	Normalized mean breakpoint position.	—
$A$	Amplitude.	$L$
$A_{forced}$	Forced wave amplitude.	$L$
$A_{free}$	Free wave amplitude.	$L$
$H$	Wave height.	$L$
$H_{sh}$	Short wave height.	$L$
$H_{IG}$	Infragravity wave height.	$L$
$\beta$	Bottom slope.	—
$\beta_n$	Normalized bottom slope.	—
$\chi$	Normalized surf zone width.	—
$\xi_{sb}$	Surf beat similarity parameter.	—
$\beta_H$	Adapted normalized beach slope.	—
$R$	Reflection coefficient.	—
$\gamma$	Peak enhancement factor.	—
$U_s$	Mass transport velocity due to waves.	$LT^{-1}$
$U_c$	Free stream velocity.	$LT^{-1}$
$E$	Energy density.	$MT^{-2}$
$W$	Energy flux.	$MLT^{-3}$
$L_{scale}$	Horizontal length scale.	—
$x_{mb}$	Mean cross-shore location of the breakpoint.	$L$
$x_{swl}$	Cross-shore location of the shoreline at SWL.	$L$
$T_{mb,swl}$	Travel time for a shallow water wave from the $x_{mb}$ to $x_{swl}$ .	$T$

# Chapter 1

## Introduction

The coastal zone is a very dynamic region, driven by the interaction between sea and terrestrial processes, having great ecological, economical and social importance. Thus, there have been longstanding efforts to better understand and live with the natural variability and hazards associated with the coastal zone.

Some of the most important processes in coastal zones are related to short waves (periods between 1-20s) or wave-driven hydrodynamics. In the nearshore region, the momentum budget provided by short waves generated in deep water spreads to a wide range of processes (Figure 1.1), from very high (turbulence) to very low frequencies (far infragravity waves and mean flow). Lying between 0.04Hz and 0.003Hz are the infragravity waves. These long waves are forced by short wave modulation and are considered one of the main morphodynamic drivers in shallow waters, becoming increasingly more important towards the shoreline due to their unsaturated nature (Raubenheimer and Guza, 1996, Ruessink et al., 1998).

From the different nearshore regions the swash zone is of special interest for coastal researchers and planners as it plays an important role on the design of coastal structures (Kobayashi, 1999), on the sediment transport and on the subaerial sediment budget, determining erosion and accretion processes (Butt and Russell, 2000), forcing groundwater flows (Nielsen, 1999) and influencing intertidal ecology (McArdle and McLachlan, 1992). However, too little is known about the swash



zone morphodynamics, and it is an area of great challenge for present and future research (Nielsen, 2009). One of the crucial steps is understanding the behavior of infragravity waves at the boundary (inner surf zone) and in the swash zone.

In the surf zone, infragravity waves can be generated by different mechanisms, principally by incident bound waves (Longuet-Higgins and Stewart, 1960) and by surf zone width modulation, normally called breakpoint forcing (Symonds et al., 1982). In the field, reflected trapped or edge wave are also possible (Gallagher, 1971).

The infragravity wave forcing mechanisms are associated with radiation stress gradients due to short wave groupiness. However, the relationship between short waves and the respectively generated infragravity waves is distinct for different forcing mechanisms. Therefore the contribution of infragravity waves to the nearshore dynamics is likely to depend on the efficiency of the different forcing mechanisms. While it is likely that they occur simultaneously, determining the relative importance of each, under natural conditions, is still an important question yet to be fully answered. In order to attempt resolving this issue it is necessary to have a clear understanding of the processes associated to infragravity waves, starting from their formation, propagation and dissipation. Comprehending their relationship with other variables such as the short wave envelope, and the shoreline and breakpoint excursion is also important.

For that reason in this thesis a comprehensive study of infragravity waves is presented. The work is divided in two main parts: the first part contains 4 chapters. In Chapter 2, the theory of the infragravity wave generation mechanisms are introduced and followed by detailed description of the main questions investigated here. These questions are explored in Chapter 3 based on a critical literature review and a re-analysis of previously published laboratory data. In Chapter 4, FUNWAVE, a Boussinesq-type numerical model, is introduced and tested against laboratory data. Also, the two main infragravity wave forcing mechanisms are implemented and validated. The numerical model is then used for an extensive investigation of infragravity waves (Chapter 5). The findings from the first part

of the Thesis are used in the second part (Chapter 6), where a novel method to determine the dominant infragravity mechanism in the inner surf and swash zone in the field is proposed and applied to different field experiments. The method uses the relationship between breakpoint and shoreline oscillations (investigated in the first part) to determine the dominant forcing mechanism. To the author's knowledge, the relationship between breakpoint excursion and infragravity waves has not been directly investigated, experimentally or numerically. Lastly, in Chapter 7, the summary of conclusions and suggestions for future research are presented.

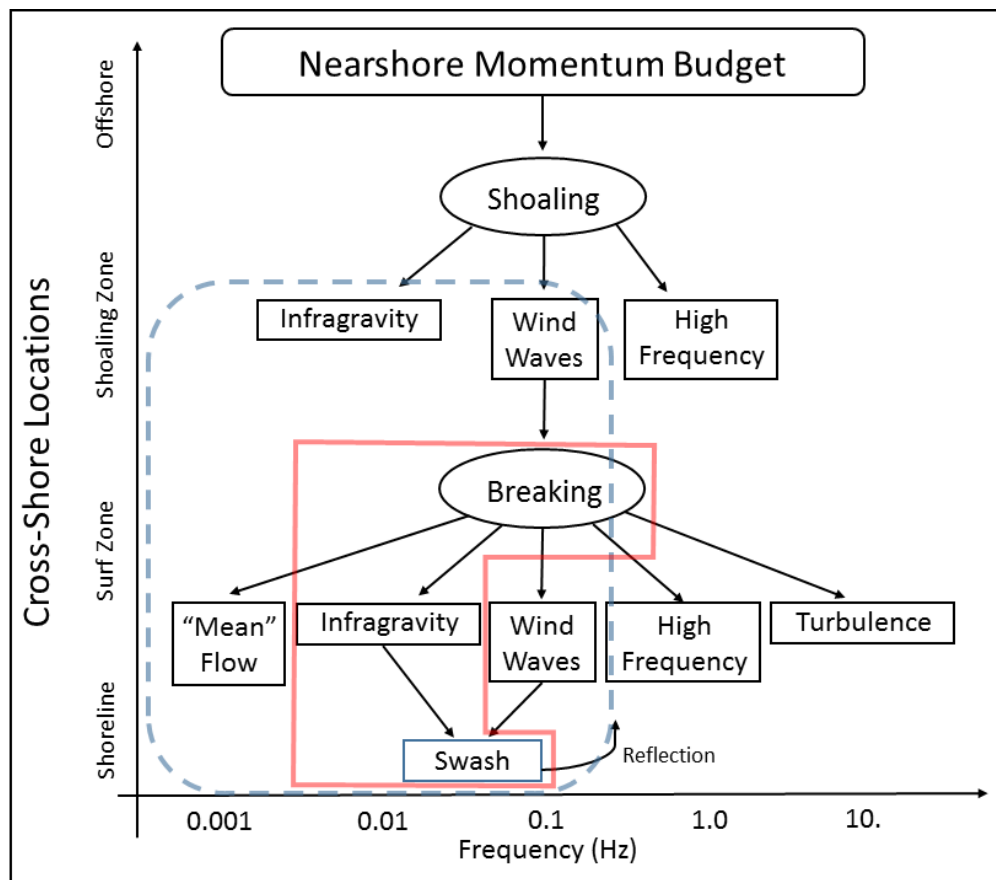


FIGURE 1.1: Nearshore fluid dynamics, induced by offshore generated wind waves, divided by frequency and cross-shore location, Blue dashed line broad spectrum of the research (bound wave forcing, shoaling, propagation patterns of infragravity waves), red line is the main focus of the Thesis (infragravity wave dissipation and dominant forcing in the surf zone). After Holman et al. (2015).

# Chapter 2

## The Generation Mechanisms of Infragravity Waves

In this Chapter the two main theories of surf beat generation are presented followed by the introduction of the main aspects of the investigation.

### 2.1 Bound Waves - Steady and Transient Concepts

The concept of radiation stress ( $S_{ij}$ ), defined as the excess of momentum flux in the  $i$  direction across the  $j$  plane, due to the presence of waves was first introduced by Longuet-Higgins and Stewart (1960) and explored further in Longuet-Higgins and Stewart (1962) and Longuet-Higgins and Stewart (1964). In a wave group the extra force originating from the gradient of the radiation stress results in a set-down wave under the higher waves in the group as in figure (2.1). Three different mathematical approaches were presented by Longuet-Higgins and Stewart (1962): the first followed the Stokes method and the bound wave is expressed as the second order subharmonic wave-wave interaction between two primary waves, the solution for velocity,  $u$ , and surface elevation,  $\eta$ , is given as

$$u^{(2)} = -K \sum_{m,n} \frac{a_m a_n c_g^2}{gh\theta - c_g^2} \frac{\cosh \Delta k(z+h)}{\cosh \Delta kh} \cos(\Delta kx - \Delta \sigma t + \Delta \psi), \quad (2.1)$$

$$\begin{aligned} g\zeta^{(2)} = & -K \sum_{m,n} \frac{a_m a_n c_g^2}{gh\theta - c_g^2} \cos(\Delta kx - \Delta \sigma t + \Delta \psi), \\ & - \sum_{m,n} \frac{a_m a_n \sigma^2}{4 \sinh^2 kh} \cos(\Delta kx - \Delta \sigma t + \Delta \psi), \end{aligned} \quad (2.2)$$

$$\theta = \frac{\tanh \Delta kh}{\Delta kh}, \quad (2.3)$$

$$K = \frac{\sigma^2}{4 \sinh^2 kh} \frac{\sinh 4kh + 3 \sinh 2kh + 2kh}{\sinh 2kh + 2kh}, \quad (2.4)$$

$$\Delta k = k_n - k_m, \quad \Delta \sigma = \sigma_n - \sigma_m \quad \text{and} \quad \Delta \psi = \psi_n - \psi_m, \quad (2.5)$$

where  $(^{(2)})$  are the second order terms,  $a_{(m,n)}$ ,  $k$ ,  $\sigma$  and  $\psi$  are the primary wave amplitude, wave number, frequency and initial phase, respectively. Subscripts  $n$  and  $m$  are the summation index for the short waves and  $c_g$  is the group velocity.

In the second method the forced wave was treated as the surface response to a “virtual pressure”. The solution derived from the third method is perhaps the most widely used and was obtained by using the conservation of mass and momentum. This method is only valid for long bound waves. Assuming constant depth and steady wave group conditions the mean surface elevation and horizontal velocity is

$$\rho\bar{\eta} = -\frac{S_{xx}}{gh - c_g^2} + \text{const}, \quad (2.6)$$

$$\bar{u} = -\frac{c_g}{h(gh - c_g^2)}S_x - \frac{E}{\rho hc} + \text{const}, \quad (2.7)$$

$$S_{xx} = \frac{3}{16}\rho g H^2. \quad (2.8)$$

Beneath higher waves the radiation stress ( $S_{xx} \propto H^2$ ) is large, resulting in a more negative  $\bar{\eta}$  than beneath lower waves (Figure 2.1).

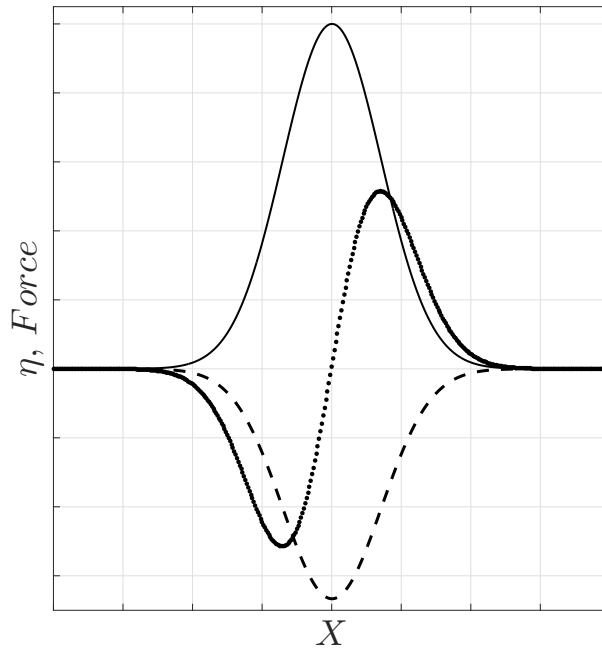


FIGURE 2.1: Spatial representation of bound wave and forcing (full line). Dashed line, steady solution (equation 2.12). Dotted line, resonant condition (equation 2.14).

Bed slope effects were briefly discussed in Longuet-Higgins and Stewart (1964, 1962). It was shown that the horizontal gradient of the surface elevation, forced by the horizontal gradient of the radiation stress, is inversely proportional to the depth,

$$\frac{d\bar{\eta}}{dx} = -\frac{1}{\rho gh} \frac{dS_{xx}}{dx}. \quad (2.9)$$

The mathematical derivation presented above is based on a steady state scenario where the solutions are time-independent. However, natural waves are transient and by treating the equations as such, interesting aspects emerge from the solutions. Dynamical theories of water motions induced by moving pressure are well documented and dates back to Proudman (1929). Whitham (1962) first addressed this issue to the bound wave problem, later Molin (1982) and Mei and Benmoussa (1984) extended the investigation to sloping bottoms.

Recently Nielsen et al. (2008) presented a comprehensive study of transient geophysical processes that were interpreted by analytical solutions for 1-D linear long waves. Using a similar approach Nielsen and Baldock (2010) provided a transient analytical solution to the linear shallow water equation with the radiation stress term (equation 2.10). In this equation, the bound wave is the non-homogeneous part of the solution, propagating with the forcing speed (in this case  $c_g$ ). By taking the constant in equation 2.6 as zero, the bound wave becomes purely negative. Therefore, to conserve mass, any change in the non-homogeneous part is balanced by the homogeneous part, which propagates with  $\pm\sqrt{gh}$ , i.e. free waves are generated.

$$\frac{\partial^2 \eta}{\partial t^2} - gh \frac{\partial^2 \eta}{\partial x^2} = \frac{1}{\rho} \frac{\partial^2 S_{xx}}{\partial x^2}. \quad (2.10)$$

The analytical solutions for a 1-D scenario with horizontal bottom are given as

$$\eta_{free\pm} = \left( -\frac{A_{forced}}{2} \left[ 1 \pm \frac{c_g}{\sqrt{gh}} \right] \right) f(x \mp \sqrt{gh}t) \quad (2.11)$$

$$\eta_{forced} = A_{forced} f(x - c_g t) = \frac{-S_0}{\rho(gh - c_g^2)} f(x - c_g t), \quad (2.12)$$

where  $\eta_{free+}$  and  $\eta_{free-}$  are the free waves that propagate in opposite directions and  $\eta_{forced}$  is identical to equation 2.6 with zero constant. The behavior of the above equation are exemplified by a hypothetical scenario where an abrupt onset of a non-resonant ( $c_g \neq \sqrt{gh}$ ) force with constant speed is applied over the water column, disturbing the initial condition of zero velocity and zero surface elevation. The resultant surface elevation is then a combination of a free wave propagating in one direction and a forced wave plus a second free wave propagating in the opposite direction, as in Figure 2.2. Due to the abrupt onset of the steady forcing, the shape of the free waves are the same as the forced one, with their amplitudes depending on the ratio of the forcing speed and the shallow water speed.

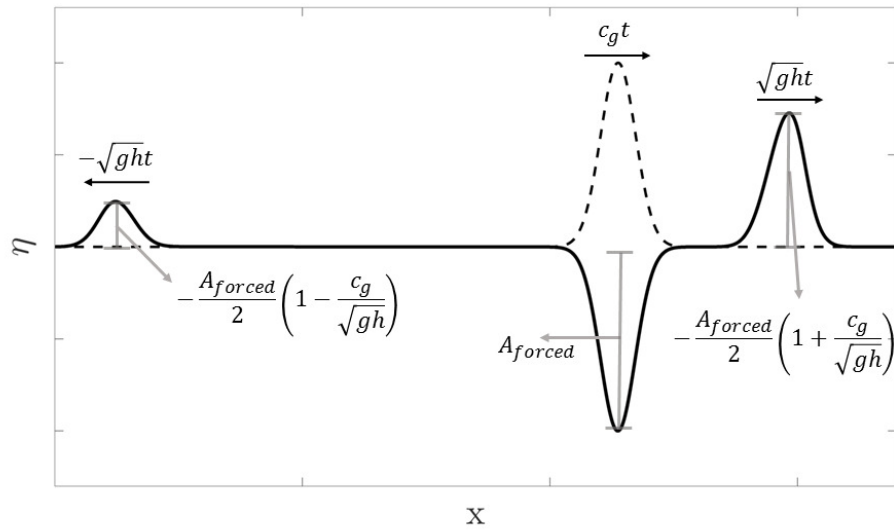


FIGURE 2.2: Schematic representation of waves generated by an abrupt onset of a moving radiation stress forcing (dashed line), surface elevation (black line)..

To the author's understanding there is no clear consensus whether the bound waves are purely depression waves or not, and the theory proposed by Longuet-Higgins and Stewart, which is the main reference for bound wave studies, allows different interpretations. That is exemplified in Figure 2.3 which shows the graphical representation of the bound wave presented by Longuet-Higgins and Stewart (1962) and Mei et al. (2005). Probably the only difference between the two interpretation is the constant of integration, which for a steady condition is arbitrarily chosen. However, when Longuet-Higgins and Stewart (1962) (pages 494-495) discussed bound waves advancing into still water line the conclusion was that the bound waves were purely negative. For this case, the constant is set to zero to satisfy the still water condition. Furthermore, it is suggested that equation 2.12 is valid only for a mild transition from the undisturbed to the disturbed zone, while abrupt changes would lead to more complex solutions. This seems to corroborate Nielsen et al. (2008), who showed that the gradual perturbation in the forced solution stretches and reduces the amplitude of the free waves. In other words, in the perturbation limit, the free long waves vanish (further discussion on the gradual changes in the forcing is in Section 3.5, Figure 3.17).

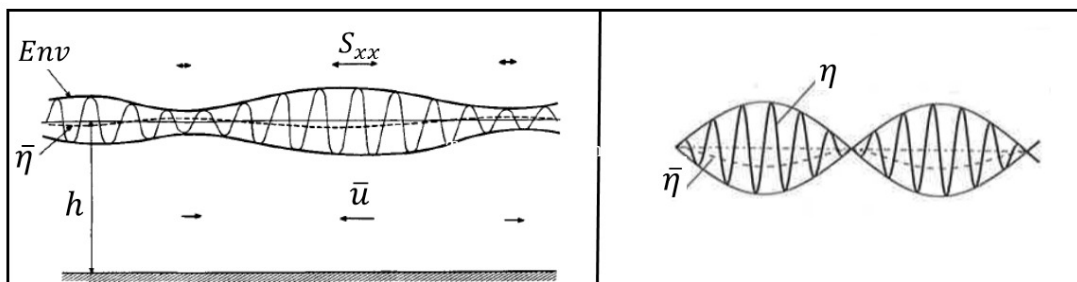


FIGURE 2.3: The graphical interpretation of the bound wave by Longuet-Higgins and Stewart (1962) with positive and negative part (left) and Mei et al. (2005) purely negative (right).  $Env$  is the short wave envelope.

When the forcing is resonant (the short waves are in shallow water,  $c_g = \sqrt{gh}$ ) equation 2.6 breaks down. Longuet-Higgins and Stewart (1962) derive an alternative solution assuming that the resonant condition was fully developed in time,



$$\bar{\eta} \sim -\frac{S_{xx}}{\rho\sigma^2h^2}. \quad (2.13)$$

Nielsen and Baldock (2010) suggested that for a resonant condition no asymptotic solution exists and the forcing is constantly transferring energy to the forced wave which, due to the same propagation speeds, remains attached to the forward free wave, both experiencing a linear growth as

$$\eta_{resonant} = \frac{-S_0}{2\rho\sqrt{gh}}tf'(x - \sqrt{gh}). \quad (2.14)$$

In contrast to Longuet-Higgins and Stewart (1962), the solution is a time growing bound wave evolving with the shape of the horizontal derivative of the forcing ( $\partial f/\partial x$ ). Taking a Gaussian-type force as an example, the surface elevation is a time-growing  $\mathcal{N}$ -shaped wave as in Figure 2.1.

Even though all the derivations presented above are made assuming constant depth, apart from equation 2.9, qualitative insights of bound waves propagating over sloping bottoms can be obtained from those solutions, further discussion is presented in the following chapters.

## 2.2 Breakpoint Forcing

Another possible source of infragravity waves is the breakpoint oscillation due to amplitude-modulated waves. This mechanism was first addressed by Symonds et al. (1982) who provided an analytical solution for free long waves generated at the breaking region by considering a saturated surf zone. Linear shallow water equations with the spatial gradient of  $S_{xx}$  as forcing were used to interpret the problem. The following non-dimensional form is obtained by scaling the variables with the mean breakpoint position ( $X$ ), and group frequency  $\sigma$ .

$$\chi \frac{\partial U}{\partial t} + \frac{\partial \zeta}{\partial x} = -\frac{1}{2x} \frac{\partial(a^2)}{\partial x}, \quad (2.15)$$

$$\frac{\partial \zeta}{\partial t} + \frac{\partial(xU)}{\partial x} = 0, \quad (2.16)$$

$$\chi = (\sigma^2 X/g \tan \beta), \quad (2.17)$$

where  $U$  is the depth integrated velocity in  $x$  direction,  $\chi$  is the non-dimensional surf zone width and  $a$  is the non-dimensional wave amplitude. The right side of equation 2.15 is the scaled forcing and is 1 shoreward and 0 seaward of the breakpoint, in other words, if the wave is breaking  $\frac{1}{2x} \frac{\partial a^2}{\partial x} = 1$ , otherwise  $\frac{1}{2x} \frac{\partial a^2}{\partial x} = 0$ . Figure (2.4) shows a schematic representation of the forcing function for a sinusoidal breakpoint excursion. At each instant in time the cross-shore representation of the forcing is a step function (thin gray lines). Alternatively, a time series of the function at a fixed position ( $x_a$ ,  $x_b$ ) within the breaking zone (black lines) is represented by a repeating rectangle function where the forcing duration increases at locations closer to the shoreline.

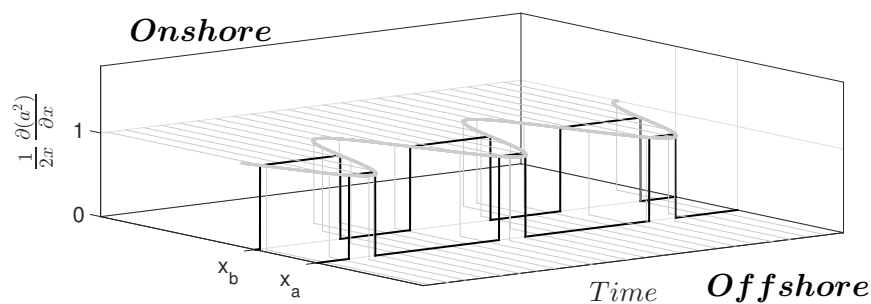


FIGURE 2.4: Space-time evolution of the forcing function for a sinusoidal breakpoint excursion (thick gray line). The thin gray lines are the cross-shore step functions at distinct instants in time. The black lines are the time evolution of the forcing at the cross-shore locations  $x_a$  and  $x_b$ . Adapted from Symonds et al. (1982).

At each location, in the cross-shore, the time evolution of the forcing is then expressed in a Fourier series and the constants are obtained using the limits of the breakpoint excursion ( $x_2$  and  $x_1$ ).

$$\frac{1}{2x} \frac{d(a^2)}{dx} = a_0(x) + 2 \sum_{n=0}^{\infty} (a_n(x) \cos nt + b_n(x) \sin nt). \quad (2.18)$$

By assuming negligible travel time between  $x_2$  and  $x_1$  (small amplitude modulation  $\delta a$ ) the amplitudes are

$$a_0(x) = \frac{\tau}{\pi}, \quad (2.19)$$

$$a_n(x) = \frac{\sin n\tau}{n\tau}, \quad (2.20)$$

$$\tau = \cos^{-1} \left( \frac{x-1}{\delta a} \right), \quad (2.21)$$

where  $b_n$  are zero for all  $n$  and  $x$  is the breakpoint position relative to the mean ( $X$ ). The mean amplitude ( $a_0$ ), or the setup, and the first three harmonics are shown in Figure (2.5).

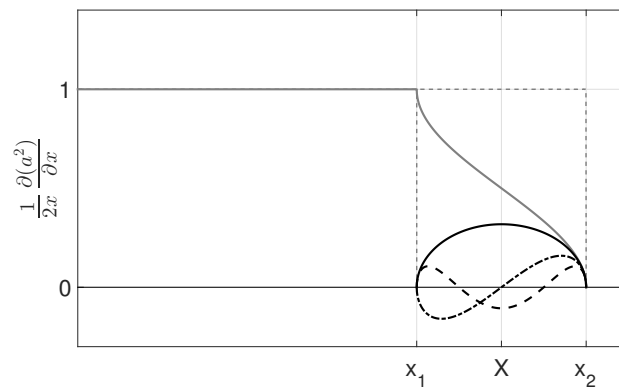


FIGURE 2.5: Schematic representation of the forcing function for a sinusoidal varying breakpoint. Grey line - mean setup ( $n = 0$ ), black line - first harmonic (group frequency,  $n = 1$ ), dashed line - second harmonic ( $n = 2$ ) and dot-dashed line third harmonic ( $n = 3$ ). Adapted from Symonds et al. (1982).

Based on this representation, the breakpoint region is treated as a wave-maker, where identical waves with  $\pi$  phase difference are radiated seaward and shoreward. The latter wave then reflects at the shoreline and propagates seaward. Therefore inside the surf zone a standing wave pattern is observed with a progressive outgoing wave outside the surf zone. The outgoing wave is the summation of the two seaward propagating waves and therefore the total outgoing wave amplitude is strongly dependent on their relative phase. At the group frequency maximum response is obtained for  $\chi = 1.2$  and minimum for  $\chi = 3.6$ . Baldock et al. (2000) and Baldock and Huntley (2002) found good agreement between experiments and this model for bichromatic and random waves. The theory was later extended to a barred beach profile (Symonds and Bowen, 1984).

Note that no assumption are made about short wave shoaling and set-down, and the forcing originates from the time varying saturated surf zone only, with the incident bound wave excluded.

## 2.3 The Key Questions

As presented in the previous chapter, the final goal of the Thesis is to determine surf beat characteristics in the inner surf and swash zone, based on the relationship of the breakpoint and shoreline excursion. However, before interpreting the results obtained from the cross-correlation between these two features, a full understanding of all the hydrodynamic aspects related to the forcing mechanisms and the waves generated by them is needed. The vast literature over the infragravity wave theme has provided an extensive amount of information, but conflicting results and interpretations have raised some important questions that are further investigated in this work. These questions are described below:

- Do changes in the forcing (wave groups) and bound wave generate free waves?
- Is bound wave purely negative?
- How do free waves affect the bound wave shoaling properties?
- Is the positive part of the bound wave, observed during the shoaling process, free or forced?

It is mathematically clear that, in the steady state scenario, no free waves are needed as the mean water level (the constant in the dynamic boundary) is arbitrarily chosen. In the transient scenario, this is not the case and by assuming the constant as zero the bound wave becomes then a pure depression, and changes in shape are constantly balanced by free waves. Even though the generation of free waves have been discussed in different studies (Mei and Benmoussa, 1984, Nagase and Mizuguchi, 2001, Nielsen and Baldock, 2010), it is not clearly addressed in others and the interpretation of the results relies on the steady solution (Baldock, 2006, Battjes et al., 2004, Janssen et al., 2003, Masselink, 1995). Whether the generation of free waves happens for real waves it is not clear and perhaps difficult to confirm. However, it is important to comprehend its possible effects in the interpretation of infragravity waves.

- Is the bound wave released and/or dissipated?

During short wave breaking the assumption of bound wave release is commonly adopted (Battjes et al., 2004, Dong et al., 2009, Janssen et al., 2003). However, strong infragravity wave dissipation is also commonly observed, suggesting that bound waves are not released during the breaking process, but remain locked in the surf zone decaying with the forcing (short waves) (Baldock, 2012). Dissipation in the surf zone may also occur due to other factors that are independent of the nature of the infragravity wave (forced or free). However, the dissipation due to decaying of the forcing should affect only the forced wave. Linking to the paragraph above, assuming that bound waves remain locked and decays in the surf zone, its positive part also should decay if it is forced or remain unchanged if it is free.

- Is the breakpoint a proxy for the wave envelope outside the surf zone?
- Is the run-up a proxy for the infragravity waves in the inner surf and swash zone?

From the above theories it is clear that the breakpoint should behave in accordance with the modulation of the short waves, and the run-up should contain the infragravity signal present in the inner surf and swash zone. For this reason, in the field, it is proposed to use the relationship between breakpoint and the shoreline motion to extract information about the surf beat. However, before applying this methodology it is important to confirm that these assumptions hold for more complex cases.

- What is the expected relationship between breakpoint and shoreline excursion for each surf beat mechanisms?

The short wave modulation is responsible for the generation of bound waves and breakpoint forced waves, as both theories depend on the radiation stress gradients. However, due to their distinct nature a different relationship with the short

wave envelope/breakpoint and infragravity wave is expected for each mechanism. Therefore, in order to use the breakpoint and shoreline oscillations to investigate the forcing mechanisms these relationships need to be well understood. A detailed analysis is given in the next chapter.

# Chapter 3

## The Main Aspects of Surf Beat

Infragravity wave generation, propagation and dissipation have been widely investigated in the past decades. However, due to their complexity, some processes are still not fully understood. Here, a critical literature review, combined with a re-analysis of previously published laboratory data, is presented to explain the main aspects of the infragravity waves, as well as the key open questions investigated in the thesis.

The laboratory experiments revisited here were carried out in a wave flume 18 m long, 0.9 m wide, with working water depth,  $h$ , of 0.8 m. Most of the cases were collected on a plane sloping beach ( $\beta = 0.1$ ), with some random cases performed on a barred beach. Data were collected using surface-piercing resistance-type wave gauges and a run-up wire within the swash zone. The cases include bichromatic (Baldock et al., 2000), random (Baldock and Huntley, 2002, Baldock et al., 2004) and transient wave groups (Baldock, 2006). Further details of both wave flume and instrumentation is found in the papers cited above. The wave conditions of selected cases are shown in tables 4.1, 4.2 and 4.3; these cases are also used to test the numerical model (Chapter 4). The random-wave cases reanalyzed here are considered to be deterministic rather than a single realization of random data (Baldock and Huntley, 2002), and therefore the statistical parameters do not require the confidence limits associated with stochastic processes.



### 3.1 Propagation Patterns - Identifying Generation Mechanisms

The total infragravity signal is composed of incident and outgoing waves (assuming only cross-shore propagation). Following the schematic representation in Figure 3.1, waves propagating in the shoreward direction outside the surf zone are forced waves, evolving phase locked with the wave envelope, termed the bound long wave (BLW). As discussed before, free incident waves are also possible, but generally assumed negligible on the shelf (Herbers et al., 1994). Inside the surf zone, the bound wave is commonly assumed to be released as a free long wave during short wave breaking. Also at the breakpoint free waves are generated in both directions, therefore the components propagating towards the shore are a summation of the released bound long wave (RBLW) and the incident break point forced long wave (IBFLW), both reflecting at the shoreline, then propagating seaward. Directly from the breakpoint an out-going breaking point forced long wave (OBFLW) is generated. The final outgoing wave is a combination of the waves reflected at the shoreline plus the waves generated at the breakpoint, leading to possible constructive or destructive interactions (Baldock et al., 2000, Symonds et al., 1982). As shown in Figure 3.1 between two locations a different travel time occurs for each wave. These lags can be determined in the data using cross-correlation analysis, which is further discussed in the next section.

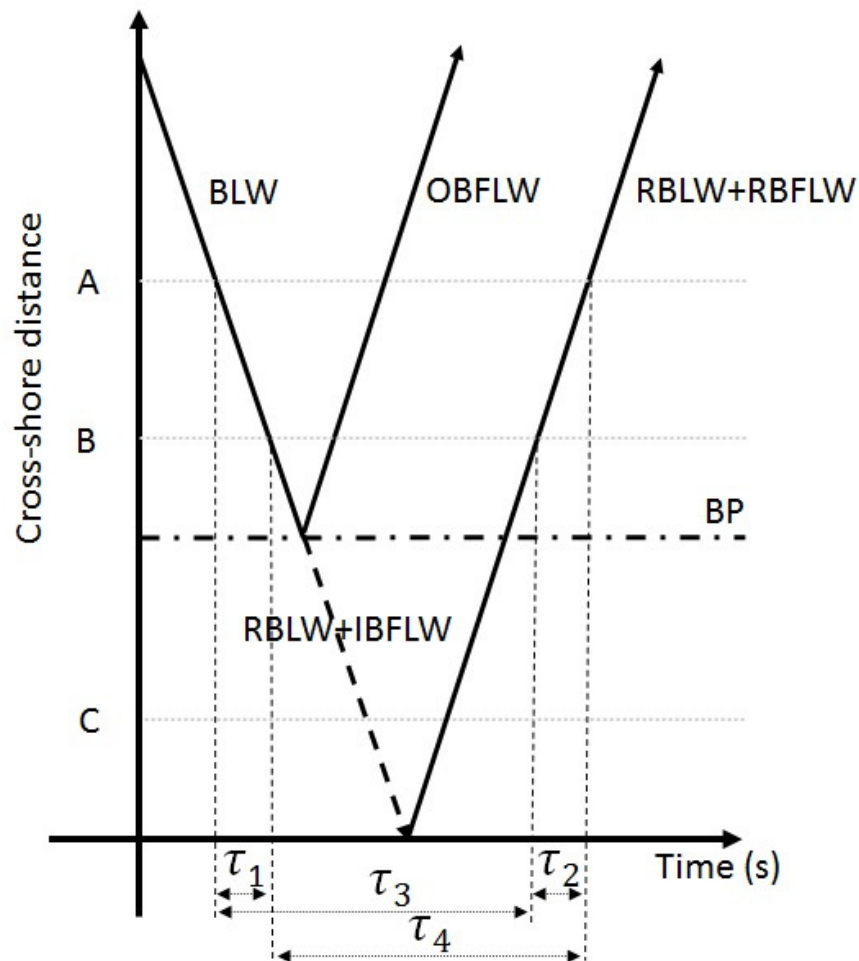


FIGURE 3.1: Components of the cross-shore infragravity signal. BLW- bound long wave, RBLW- released bound long wave, IBFLW- incident break point forced long wave, OBFLW- outgoing breaking point forced long wave and BP- breakpoint position. After Contardo and Symonds (2013).

## 3.2 Infragravity Wave Data Analysis

Different methods are used to investigate infragravity waves, for instance the power relationship between short and infragravity wave heights provides information about forcing mechanisms (Figure 3.23). Spectral analysis is commonly used for data interpretation and as tool to produce other information such as rates of energy transfer (Henderson et al., 2006, Sheremet et al., 2002, Thomson et al., 2006). Propagation patterns, at discrete frequencies, are obtained via cross-spectral coherence and phase calculation (Contardo and Symonds, 2013). More

complex analysis in the frequency domains such as bi-spectra are used to investigate forced infragravity waves in terms of triad wave-wave interactions (Elgar and Guza, 1985, Guedes et al., 2013, Herbers et al., 1994).

One of the most simple but powerful tools is the cross-correlation analysis which has been commonly applied on parameters such as the wave envelope, and low-pass filtered surface elevation and velocities to determine propagation patterns, lags and generation mechanism. Even though it is a very common method, interpretation of the results can become complicated, specially for complex signals. Therefore typical results obtained from the application of cross-correlation analysis to infragravity waves are worth highlighting prior to considering data or model results.

The cross-correlation in its normalized form is expressed by

$$R_{xy}(\tau) = \frac{\langle x(t)y(t + \tau) \rangle}{\sigma_x \sigma_y}, \quad (3.1)$$

where  $\sigma_x$  and  $\sigma_y$  are the standard deviation for the two time series  $x$  and  $y$ .  $\langle \rangle$  denotes ensemble average and  $\tau$  is the time lag. For this study a 95% confidence interval is used and the limits are estimated as

$$cf^{\pm} = \pm \sqrt{\frac{1.96}{N}}, \quad (3.2)$$

where  $cf^{\pm}$  are the upper and lower limits and  $N$  is the number of points in the time series (Box et al., 1994, Contardo and Symonds, 2013).

Figure 3.3 shows a typical cross-correlation result for two time series of infragravity waves, measured at two different positions ( $A$  and  $B$ ) both containing incident and reflected waves (assuming only cross-shore motion), as illustrated in Figures 3.1 and 3.2. Due to the varying travel time, incident waves occur first at  $A(Inc_A)$ , then at  $B(Inc_B)$ , and the reflected waves appear first at  $B(Ref_B)$  and then at  $A(Ref_A)$ , as in Figure 3.2. The expected result is four different correlation peaks,

with lags representing different travel times. The peak arising from the incident waves is at  $\tau_1$ , which is the travel time for the incident wave to travel from  $A$  to  $B$ . The correlation peak for the reflected waves is at  $\tau_2$ , and as the reflected signal occurs first at  $B$  the lag or travel time is negative in the cross-correlation plot. Those peaks have been observed in laboratory and numerical experiments (Janssen et al., 2003, Lara et al., 2010). In the field, this picture is not always clear, but according to the results obtained in the present study they are still significant for some conditions. For example, clear correlation peaks between incident and reflected waves were observed in the field data measured at Palm Beach using pressure sensors (Figure 6.15B, Chapter 6).

The two other expected peaks are the correlations between the incident and reflected waves. The lags  $\tau_3/\tau_4$  are the incident wave travel time from the position  $A/B$  to the shoreline plus the travel time of the reflected wave from the shoreline to the position  $B/A$  (Figure 3.1). Both laboratory and field data analyzed here showed that often those correlation are smaller compared to the first two (the incident and reflected waves are generally better self correlated). However, the signal is still visible, even in the field (Figure 6.16, Chapter 6). The spatial and temporal visualization of this typical result is a double V-shaped cross-correlation plot as in Janssen et al. (2003) (their Figure 5) and is also demonstrated in the next section.

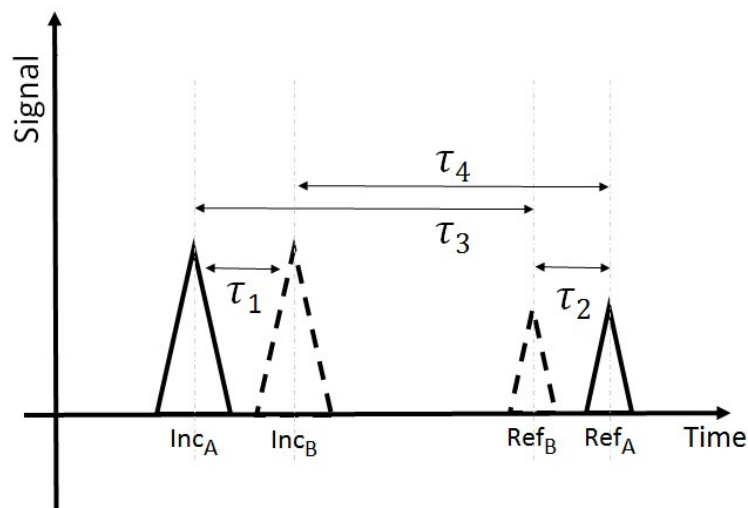


FIGURE 3.2: Components of the cross-shore infragravity signal. Incident and reflected waves, full line - position A, dashed line - position B in Figure 3.1.

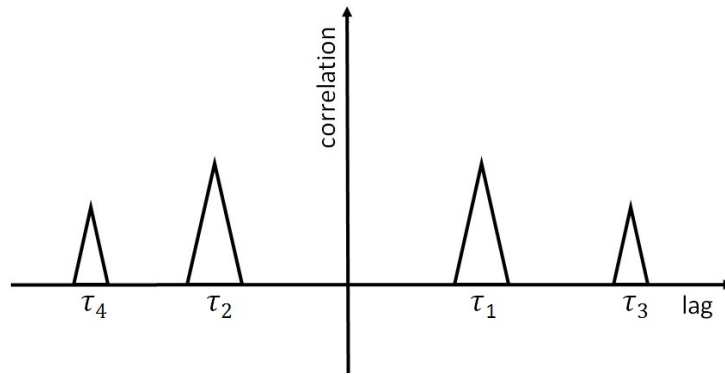


FIGURE 3.3: Cross-correlation result between two signals measured at different locations, see Figure 3.1.

### 3.2.1 Standing Wave Pattern

The discussion presented above introduced the interpretation of the cross-correlation analysis considering only the progressive propagation pattern of the incident and reflected waves. However, standing waves are common features of infragravity waves in the nearshore region, with the cross-shore standing wave a consequence of the superposition of incident and out-going waves. It is important to distinguish propagation patterns from standing wave structures in the cross-correlation analysis as they lead to different interpretations.

Both mechanisms under investigation here are capable of generating this pattern, but with some distinctions. The breakpoint mechanism, by itself, can only generate standing waves inside the surf zone. In this region, both incident and reflected free long waves shoal and deshoal at same rate, hence generating a full standing pattern (assuming full reflection and no dissipation). On the other hand, standing waves generated by the bound wave mechanism only are more likely to produce partially standing waves due to the different shoaling properties of the incident forced and the reflected free waves.

Here the cross-correlation pattern for linear standing waves are demonstrated for a single frequency and a frequency spectrum case. The standing waves are calculated using equation 3.3, and the cross-correlation analysis is applied to the surface elevation at different locations with respect to  $x = 500\text{m}$ .

$$\eta = 2a \cos(kx) \cos(\sigma t) \quad (3.3)$$

The expected results for the single frequency case is obtained, as shown in Figure 3.4. For the condition where the nodes and anti nodes are well defined the result is bands of positive (1) and negative (-1) correlation peaks, separated by the distance between nodes.

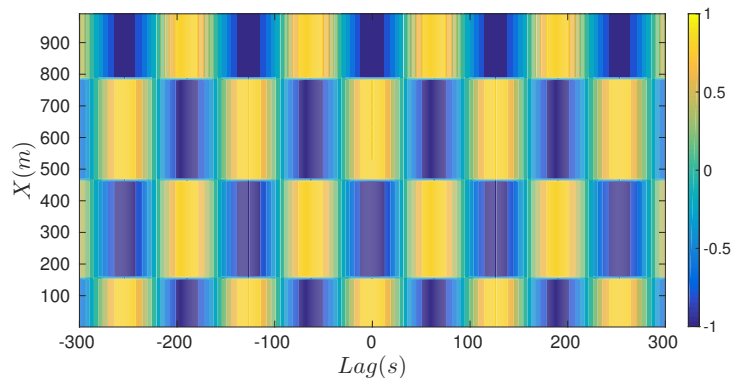


FIGURE 3.4: Cross-correlation between surface elevation at different locations with respect to  $x = 500\text{m}$  for a standing wave with  $T = 126.7\text{s}$ .

Interestingly, by applying the same analysis to a superposition of standing waves with different frequencies, the cross-correlation peaks are no longer related to standing patterns, but to the progressive features of the incident and reflected signal as shown in Figure 3.5 (bottom panel). The top panels are the results of the cross-correlation applied only to the incident (top left) and reflected (top right) signal. The two ridges in the top panels are part of the double V-shape in the bottom panel. The four ridges in the correlation signal represent the relations between incident and reflected waves at different locations. The lags are the time interval between each component, as described in the previous section. For this case, differently then the single frequency case, with the summation of standing waves of different frequencies and phases the nodal structures are smeared out.

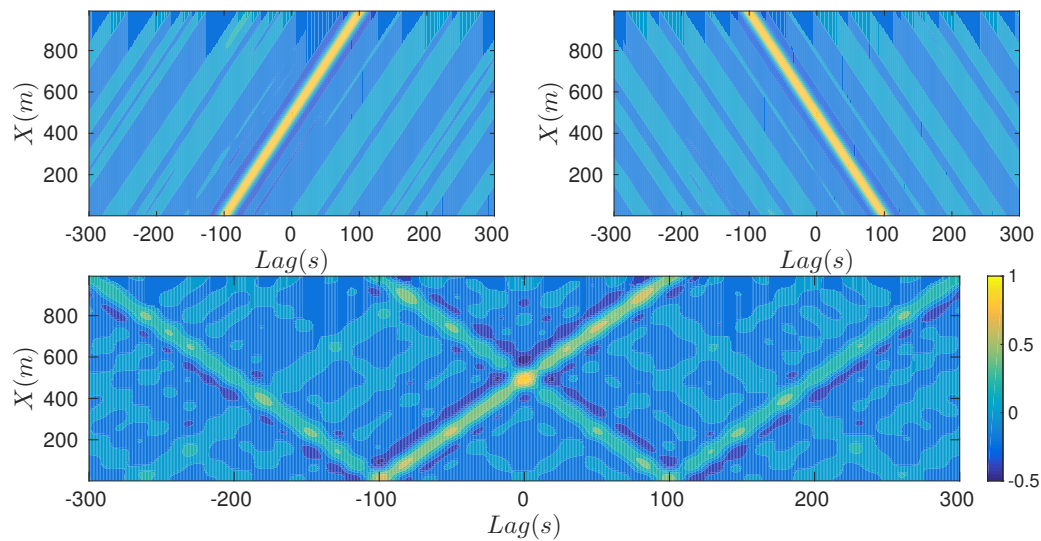


FIGURE 3.5: Cross-correlation between surface elevation at different location with respect to  $x = 500m$  for a sum of standing waves. Incident waves (top left), reflected waves (top right), total signal (bottom).

### 3.2.2 A Note on the Separation of Incident and Reflected Waves.

The total infragravity signal is composed of incident and outgoing waves (assuming only cross-shore propagation) that includes forced and free waves, where the latter may be generated by different mechanism. To help with interpretation, incident and reflected waves are commonly separated. However, as pointed out by van Dongeren et al. (2007), Baldock and Huntley (2002) and Baldock (2012) separation methods may introduce spurious waves which may lead to wrong interpretation of the processes.

Different methods can be used for free wave separation; here two commonly used techniques are tested. The first one uses surface elevation at different positions and through Fourier analysis and linear phase calculation the waves are separated (Frigaard and Brorsen, 1995, Kostense, 1984). Originally proposed for a horizontal bottom, slope effects were later introduced by Baldock and Simmonds (1999) (method I). The second method (equation 3.4) is based on the linear relationship between surface elevation and velocity of linear shallow water waves ( $c = \sqrt{gh}$ )

measured at the same location (Guza et al., 1984) (method II). The incident and reflected signal are separated as

$$\eta^{\pm} = \frac{1}{2} \left( \eta \pm u \sqrt{\frac{h}{g}} \right) \quad (3.4)$$

Here the two different methods are tested initially for simple superposition of synthetically generated linear waves, propagating in opposite direction and then for experimental data from a random wave case and a transient case, both performed on same sloping beach (details are presented in Chapter 4). The random case is based on surface elevation and velocity collected along the wave flume. Velocities were not measured for the transient case, therefore numerical results are used instead, comparison between model predictions and data are presented in Chapter 4.

As expected, for the synthetic linear waves, incident and reflected waves are correctly represented by both methods (not shown). For the experimental random case, outside the surf zone results are similar (Figure 3.6). However, for method I the mean water levels with opposite signs are observed in the incident and reflected signal. For instance, the mean water level from  $t = 20$  to  $t = 80$ s is constantly positive for the incident signal and negative for the reflected signal. The opposite occurs from  $t > 80$  to  $t = 100$ s. In the total signal the positive and negative levels cancel each other suggesting that they are likely to be spurious and generated by the separation procedure. The result for the transient case corroborates this observation, as again a larger incident wave is compensated by a larger reflected wave. The results also indicate the occurrence of reflected waves at  $T \approx 29$ s, but the real reflected wave only reaches the position 1 at  $t \approx 41$ s. A small phase change in the incident wave is also introduced by method I.



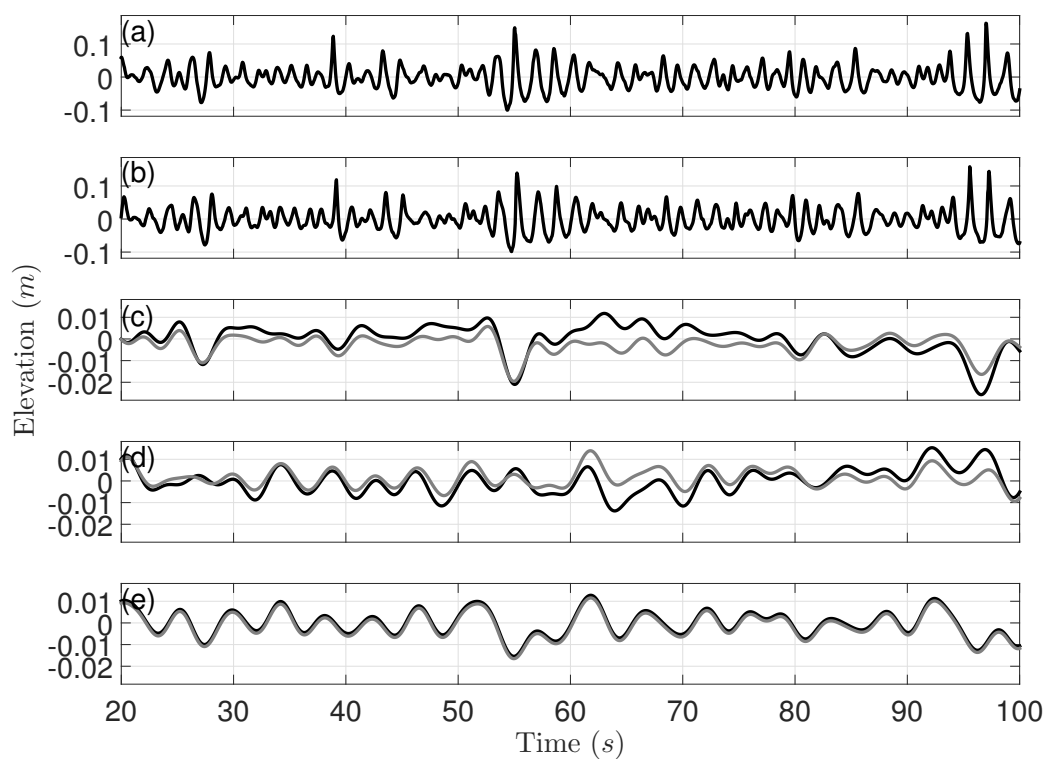


FIGURE 3.6: Comparison between separation methods, outside the surf zone. (a)-(b) Total Surface elevation at two different locations. (c) Incident, (d) reflected and (e) total infragravity band only at the first location. Random wave case J6033A (table 4.2), methods I (black) and II (grey). The second location (b) is only used in method I.

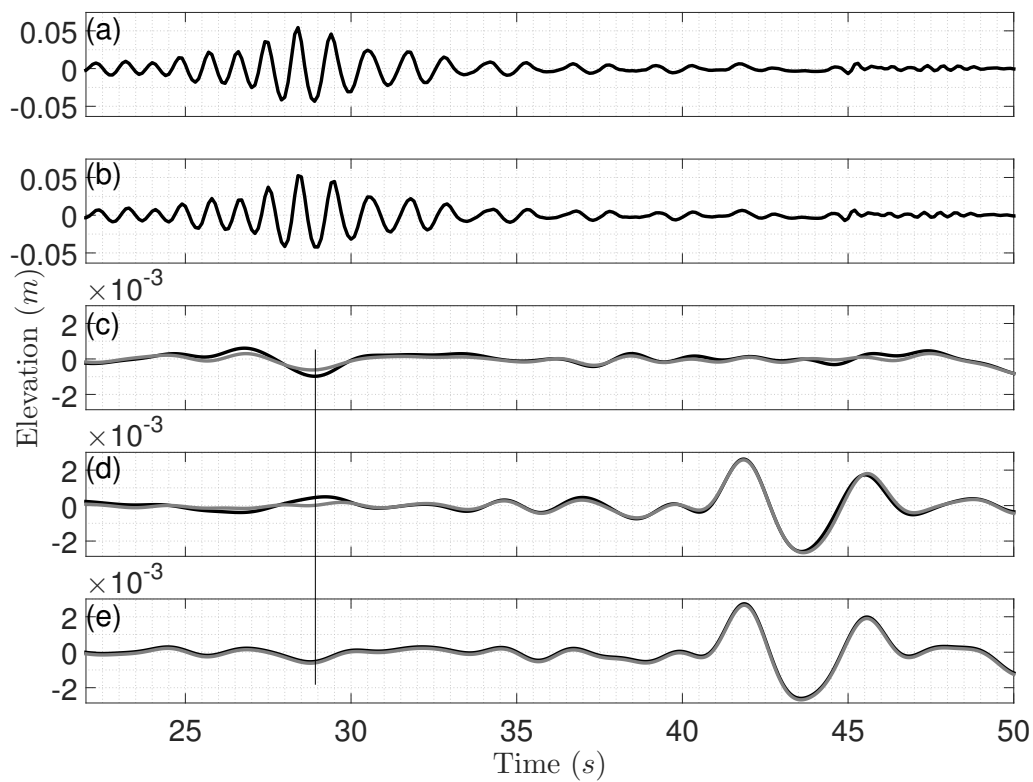


FIGURE 3.7: Comparison between separation methods. (a)-(b) Total Surface elevation at two different locations. (c) Incident, (d) reflected and (e) total infragravity band only at the first location. Transient case G08A (table 4.3), methods I (black) and II (grey). The second location (b) is only used in method I.

Method II produces more consistent results than method I, although the assumed linear relation between  $\eta$  and  $u$  and the assumption of incident waves traveling with shallow water speed might also introduce some discrepancy for conditions where the short waves within the group are not in shallow water. Also by assuming that incident waves are composed of forced and free waves changing  $\sqrt{gh}$  by  $c_g$  as in van Dongeren et al. (2007) may not be strictly correct. In this case, the separation is performed assuming that all incident waves are traveling with  $c_g$  which is not the correct assumption for the possible incident free waves. Quantifying those effects are beyond the scope of this research and relevant to later analysis.

### 3.3 Bound Wave Shoaling

The bound wave results from a reversible energy transfer from primary to coupled subharmonic waves Rapp and Melville (1990). There are two ways of expressing this: one is based on a wave-wave interaction approach, where higher-order components are generated from harmonic combinations, and the bound wave is the second order interaction between two primary harmonics as in Longuet-Higgins and Stewart (1960). Alternatively, an energy balance approach assuming a wave-current interaction can be used to describe the short wave forcing of long waves.

Waves interacting with free long waves were first introduced by Longuet-Higgins and Stewart (1960) and since that paper, slightly different equations and interpretations have been proposed mainly due to the treatment of the long wave as a slow varying current (Whitham, 1962). This issue was later explored by Schäffer (1993). Following Schäffer's description and assuming no dissipation, the total energy equation (short waves plus current) is written as

$$\frac{\partial E}{\partial t} + \frac{\partial W}{\partial x} = 0, \quad (3.5)$$

which can be divided into three parts or three energy equations, one for the short waves including the effect of the current; another for the slow-varying current including the effect of the short waves; and the last is the summation of the previous two. Total energy density ( $E$ ) and energy flux ( $W$ ) are then expressed as

$$E = E_c + E_s - \frac{1}{2}\rho(h + \bar{\eta})U_s^2 \quad (3.6)$$

$$W = W_c + W_s + U_c E_s - \frac{1}{2}\rho(h + \bar{\eta})UU_s^2 + U_c S_{xx} \quad (3.7)$$

$$U = U_c + U_s \quad (3.8)$$

where the subscripts ( $c$ ) and ( $s$ ) denotes respectively the slow-varying free current and (mean) fluxes due to short waves. The energy equation for the free slow varying current is obtained by subtracting the short wave energy equation

$$\begin{aligned} \frac{\partial}{\partial t} \left\{ E_s - \frac{1}{2} \rho (h + \bar{\eta}) U_s^2 \right\} + \frac{\partial}{\partial x} \left\{ U_c E_s + W_s - \frac{1}{2} \rho (h + \bar{\eta}) U U_s^2 \right\} \\ + S_{xx} \frac{\partial U_c}{\partial x} - U_s \frac{\partial S_{xx}}{\partial x} = 0, \end{aligned} \quad (3.9)$$

from the total energy equation so that

$$\frac{\partial E_c}{\partial t} + \frac{\partial W_c}{\partial x} + U \frac{\partial S_{xx}}{\partial x} = 0. \quad (3.10)$$

The last term in equation (3.10) is the work done on the total long wave or total velocity  $U$  by the radiation stress, therefore  $U$  also contains the short-wave contribution ( $U_s$ ) to the long wave, not only the free stream velocity  $U_c$ .

The energy balance approach when applied to energy transfer from the short waves to the bound wave commonly assumes no free stream current. The long wave signal is separated into incident and outgoing waves where the first part, outside the surf zone, is considered only as a forced wave. To the author's understanding by assuming  $U_c = 0$ , the only important term in the energy exchange is  $U_s \partial S_{xx} / \partial x$  (equation 3.9). According to Schäffer (1993) due to the linearized form of the governing equation short and long waves are independent with no mechanism of returning energy from forced to short waves, therefore following this approach the energy in the infragravity waves does not reverse back to the short waves.

Investigating energy transfer from short to forced infragravity waves (Henderson et al., 2006) who assumed no wave and mean current interaction, used a term similar to the second last term in equation (3.9 -  $S_{xx} \partial U_c / \partial x$ ) as the main driver. However, according to Schäffer (1993) the work is done by the free slow-varying current on the infragravity strain rate (see also Longuet-Higgins and Stewart (1960)).

The energy approach is also used to interpret bound wave shoaling. For instance, Madsen et al. (1997) have shown that bound wave amplitude in the shoaling zone depends on the group frequency, suggesting that the bound wave growth is limited by time (or distance). Battjes et al. (2004) showed that the shoaling rate of wave groups is determined by its length relative to bottom slope, varying from approximately  $h^{-1/4}$  for relatively lower frequencies to the equilibrium solution (equation 2.6,  $h^{-5/2}$ ) for relatively higher frequencies; this relation is mathematically expressed by the normalized bed slope

$$\beta_n = \frac{\beta}{2\pi f_g} \sqrt{\frac{g}{h}}, \quad (3.11)$$

where  $\beta$  is the beach slope  $f_g$  is the group frequency and  $h$  is usually taken as a representative depth of the shoaling zone.

On a slope the phase relationship between the short wave envelope and the bound wave differs from the equilibrium solution ( $\pi$ ), and the short wave envelope leads the bound wave. This extra lag has been associated with rates of energy transfer from the short waves ( $S_{xx}$ ) to the forced wave. Janssen et al. (2003), following the work of Bowers (1992) and Van Leeuwen (1992), presented analytical and more complex numerical solutions for the amplitude and phase shift induced by varying depth. Battjes et al. (2004), assuming quasi-steady waves, derived a phase-average rate of energy transfer based on the phase lag between the wave envelope and the forced wave ( $\Delta\phi$  - the deviation from the equilibrium solution,  $\pi$ ), the radiation stress ( $\hat{S}$ ) and the long wave velocity ( $\hat{U}$ ) amplitudes

$$R \approx U \frac{\partial S_{xx}}{\partial x} \cong \frac{1}{2} \kappa \hat{U}(f) \hat{S}(f) \sin(\Delta\phi), \quad (3.12)$$

where  $\kappa = 2\pi f/c_g$  is the forced wave number at individual frequencies  $f$  and  $(\hat{\quad})$  denotes real amplitudes. Good agreement between this model and laboratory data was found. However, this model also predicted energy exchange between incident short waves and outgoing free long waves. Baldock (2012) suggests this should

not occur since net energy transfers during free wave interactions are regarded as being very weak (Phillips, 1977).

Generally, the discussion regarding bound wave shoaling requires the assumption of steady wave condition, even though the possibility of free wave generation during the shoaling process is recognized in some studies. To the author's understanding both Janssen et al. (2003) and Battjes et al. (2004) did not consider free wave generation and its effects on  $\Delta\phi$  to estimate shoaling rate and energy transfer.

Nagase and Mizuguchi (2001) suggested that the observed smaller growth rate of the bound wave is a consequence of the superposition of forced and free waves. In this case, the free waves are generated due to the transient behavior of the bound (forced) wave on the slope (Mei and Benmoussa, 1984). As a bound wave (assumed purely negative) shoals free waves (surges) are generated to balance the changes in the forced solution (equation 2.12). A free wave travels faster ( $\sqrt{gh}$ ) than a forced wave which propagates at  $c_g$ , phase-locked with the short wave envelope. The summation of both waves results in a leading positive surge followed by a depression (Figure 3.8). Nagase and Mizuguchi also suggested that the combination of forced and free waves were responsible for the observed long wave phase deviation from the equilibrium solution. Based on this assumption, even if the shoaling of the forced wave is independent of  $f_g$  (following the equilibrium solution), due to the superposition of forced and free waves an apparent distinct rates of energy transfer (total wave amplitude) would exist for wave groups with different length and the same  $c_g$ . The lag of the negative pulse would also depend on  $f_g$ .

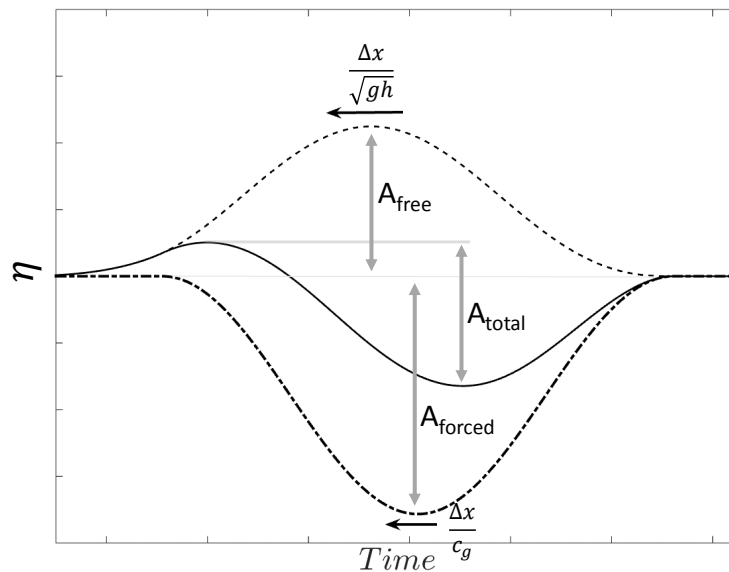


FIGURE 3.8: Schematic representation of the surface elevation at a fixed position for the conceptual model. Dot-dashed line - bound wave propagating with group velocity  $c_g$ . Dashed line - free wave generated during the shoaling process propagating with  $\sqrt{gh}$ . Full line - total signal.  $A$  represents the amplitude of each wave.

In order to test this hypotheses a simple conceptual model is proposed by assuming bound waves propagating over a horizontal bottom, with constant form and velocity, and with an increasing amplitude proportional to  $x\beta = h^{-5/2}$ , where  $x$  is the horizontal distance and  $\beta$  is a virtual slope. In other words, the bound wave is propagating with constant velocity over a horizontal bottom, with its amplitude increasing as it propagates with a shoaling rate equals to the equilibrium solution. At each time step the same gain in amplitude by the bound wave is added to the forward free wave (Figure 3.8). For groups with the same mean primary wave frequency and hence the same group velocity, the gain and phase of the total infragravity wave amplitude varies with the group frequency. Thus the bound wave shoaling is the same but an apparent frequency dependence occurs. This is demonstrated in Figure 3.9 that shows the total infragravity wave amplitude at a fixed position; the results are qualitatively similar to the numerical results in Madsen et al. (1997).

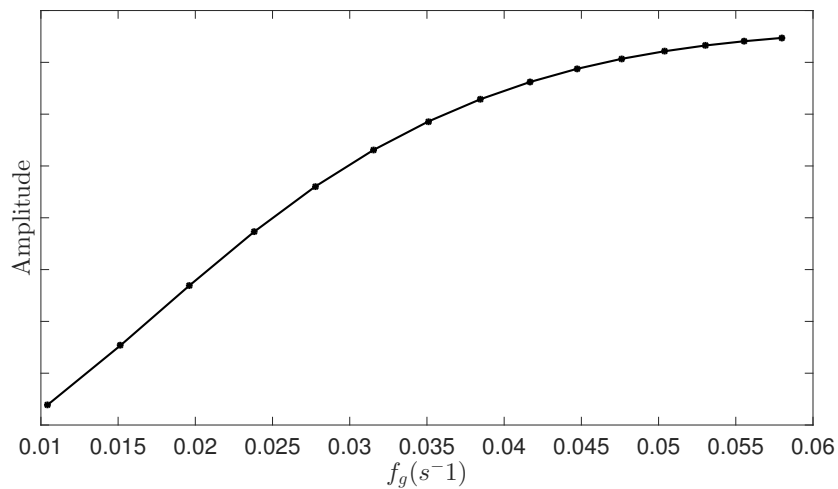


FIGURE 3.9: Total infragravity wave amplitude at a fixed position on the virtual slope for wave groups with the same  $c_g$  but different  $f_g$ . Conceptual model of bound and free wave interference.

In this simplistic approach, the only factor affecting the apparent changes in the shoaling rates is the behavior of the free wave relative to the wave group. Generally speaking, free waves generated by shorter wave groups will tend to get more separated from the bound wave than those generated by longer wave groups. In other words, in a longer group, the free wave needs to travel a longer distance to get away from the bound wave. Note that due to the difference between the free wave speed and  $c_g$ , a lag is expected for the total long wave. Hypothetical rates of energy transfer may also be obtained by inserting the calculated lags into equation 3.12. The rate of energy transfer also seems to increase with  $f_g$  (Figure 3.10). The shoaling rate for the long wave groups are closely proportional to  $\sim h^{1/4}$ , while the shoaling rate for the short groups are closely proportional to  $\sim h^{5/2}$ , qualitatively matching the behavior of the steep-slope and mild-slope regimes described by Battjes et al. (2004).



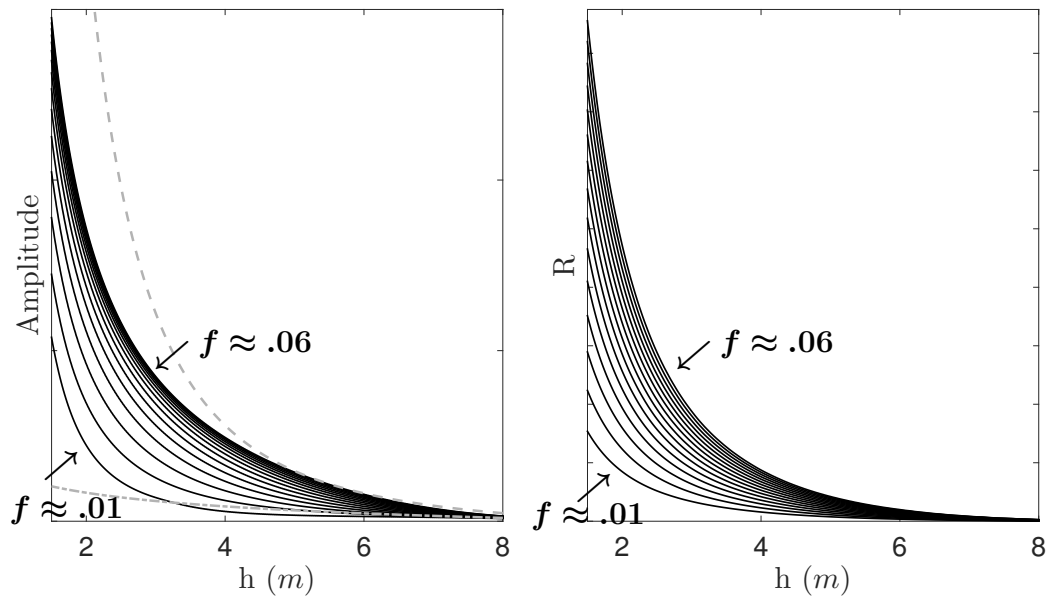


FIGURE 3.10: Left: Total infragravity wave shoaling for different frequencies, gray dashed line  $\sim h^{-5/2}$ , gray dash-dotted line  $\sim h^{-1/4}$ . Right: Theoretical rates of energy transfer calculated based on the observed lags using equation 3.12.

The results present for this conceptual model is perhaps too simplistic, but they indicate that adding free waves into the bound wave shoaling process may change the results and therefore its interpretation.

As shown in the next section, positive leading surges are common features observed during bound wave shoaling and becomes more relevant in shallower water close to the breakpoint. Therefore, it is important to distinguish its characteristics from the incident breakpoint forced long wave.

### 3.4 The Positive Part of the Bound Wave

The cross-correlation analysis present by List (1992) for both field data and numerical results showed that on a sloping bottom, and mainly inside the surf zone, the relation between the bound wave and wave envelope are quite different from the expected classical solution. Instead of a negative peak with zero lag, the correlation was divided into two peaks, one positive (leading) and other negative

(lagging) around the zero lag. This result indicates that the infragravity wave is composed of lagging depression and a leading surge similar to the  $\mathcal{N}$ -shaped wave presented in Figure 2.1. Furthermore, the linearized shallow water equation was used to evaluate conditions of bound wave forcing with and without the breakpoint forcing term. List observed that the results for these two conditions were almost unchanged, and while the negative part was partially interpreted using the bound wave theory, no clear explanation was provided for the lags and the positive peaks. Similar analysis and results were presented by Masselink (1995) however no clear answer was given for the cross-correlation results, specially for the positive peaks.

Pomeroy et al. (2012) investigating infragravity waves over a steep and shallow reef used a similar observation in their cross-correlation analysis to justify breakpoint forcing. In fact, the positive peaks over the shallow reef (after short wave breaking) were much stronger than the negative peaks, which could indicate a dynamic setup of breakpoint generated surf beat. However, a closer look on their Figures 5(a) and 10 shows that the strong positive correlation are present seaward of the breakpoint. Janssen et al. (2003) briefly acknowledged the positive correlation prior to the breakpoint, suggesting possible free wave generation during the shoaling process.

Baldock (2006) investigating transient wave groups propagating over a sloping bottom also observed a leading surge in the shoaling zone. Based on the lack of extra lag ( $\Delta\phi \approx \pi$ ) between the spatial wave envelope and the spatial long wave, and the matching of their respective gradients, Baldock suggested that the positive part of the bound wave was forced, and a consequence of the stronger response of the surface elevation to the radiation stress in shallower water, as in equation 2.9.

Due to the similarities of the measured bound wave with a  $\mathcal{N}$ -shaped wave, an analogy to the resonant mechanism (equation 2.13) was made by Nielsen and Baldock (2010). However, in the resonant solution there is a considerable lag between the spatial wave envelope and the bound wave (Figure 2.1), which is not observed in their data. The spatial evolution of the wave envelope and the infragravity waves for the transient case in Baldock (2006) is shown in Figure 4.10 Section 4.2.4, where this data set is used to test the numerical model.

---

Positive leading surges are also observed in the random data, re-analyzed here as shown in Figures 3.13 and 3.14 for a constant slope and a barred profile, respectively. Similar to the transient case (Baldock, 2006), spatially  $\Delta\phi \approx \pi$  with the respective horizontal gradients matching equation 2.9 (Figures 3.11 and 3.12).

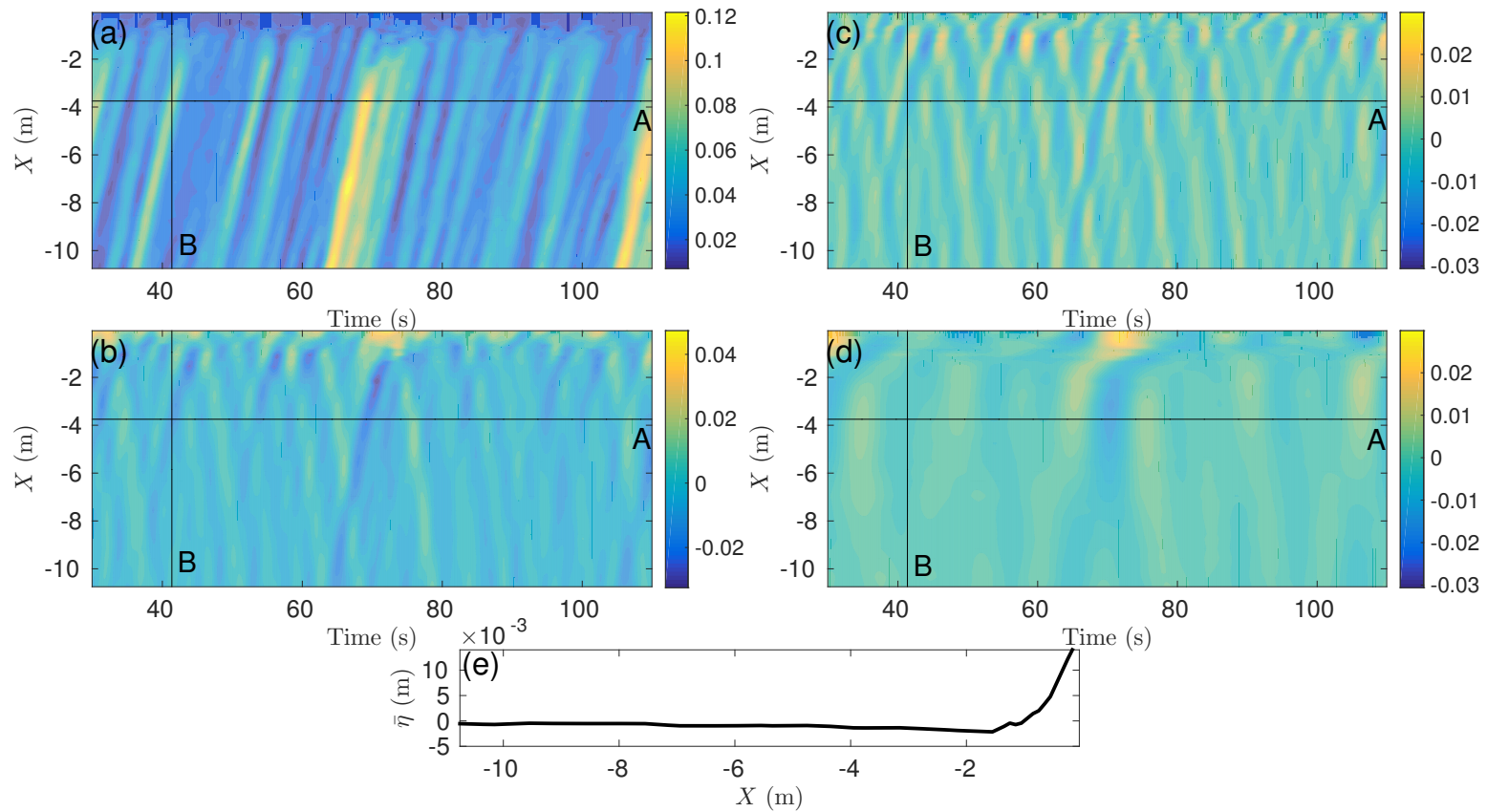


FIGURE 3.11: a) Space-time evolution of wave envelope amplitude, (b) total infragravity surface elevation, including mean setup  $f < 0.4\text{Hz}$ . (c) band-pass filtered surface elevation  $0.13 < f \leq 0.4\text{Hz}$ , without mean setup, (d) low-pass filtered surface elevation  $f \leq 0.13\text{Hz}$ , without mean setup, (e) mean setup. Random wave case J6033A (see table 4.2) on a plane beach. Lines A and B are locations along which data is extracted for Figure 3.13.

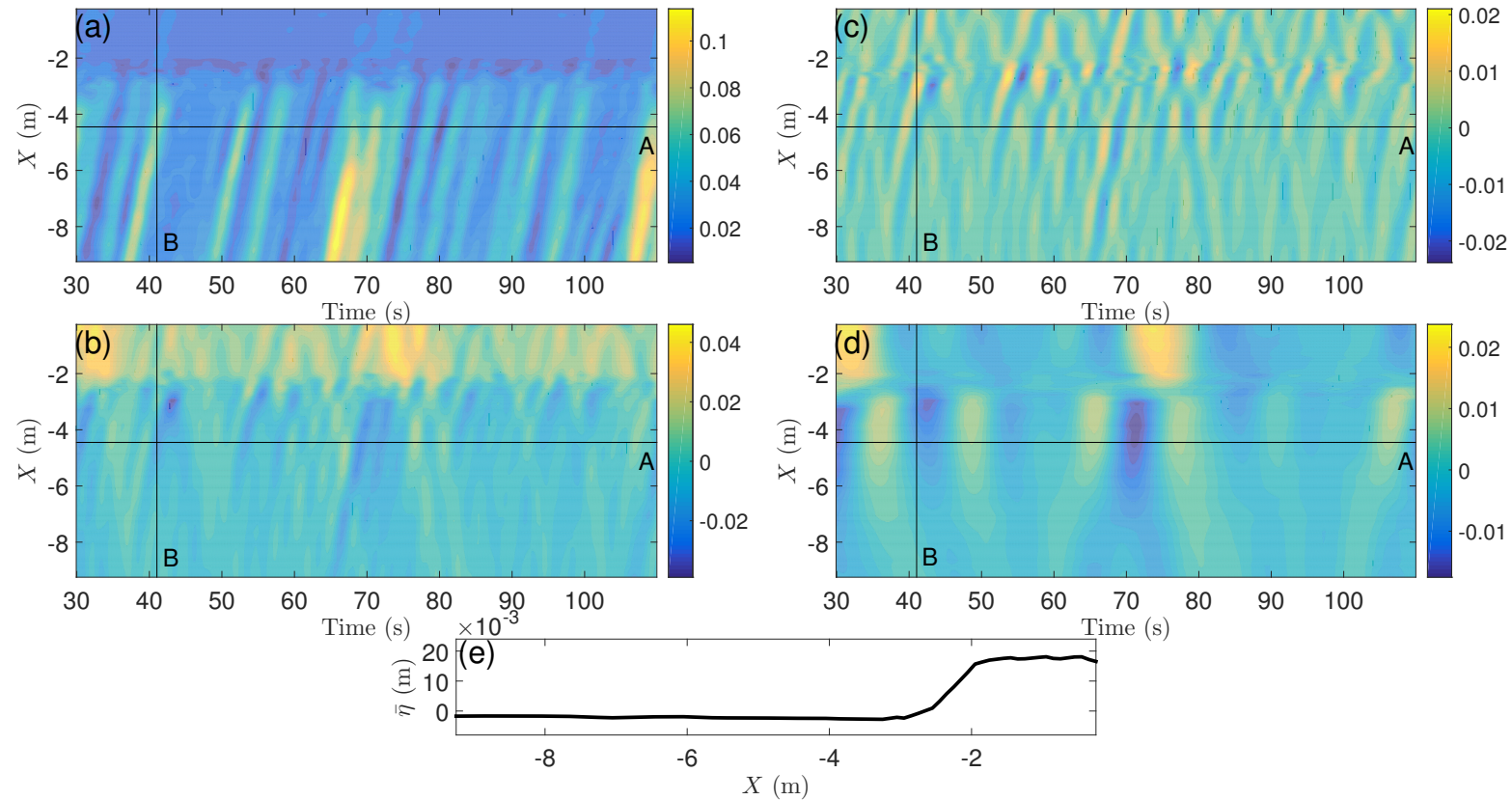


FIGURE 3.12: (a) Space-time evolution of wave envelope amplitude, (b) total infragravity surface elevation, including mean setup  $f < 0.4\text{Hz}$ . (c) band-pass filtered surface elevation  $0.13 < f \leq 0.4\text{Hz}$ , without mean setup, (d) low-pass filtered surface elevation  $f \leq 0.13\text{Hz}$ , without mean setup, (e) mean setup. Random wave case J6033A on a barred beach. Bar crest is located at  $x = -2.1\text{m}$ . Lines A and B are locations along which data is extracted for Figure 3.14.

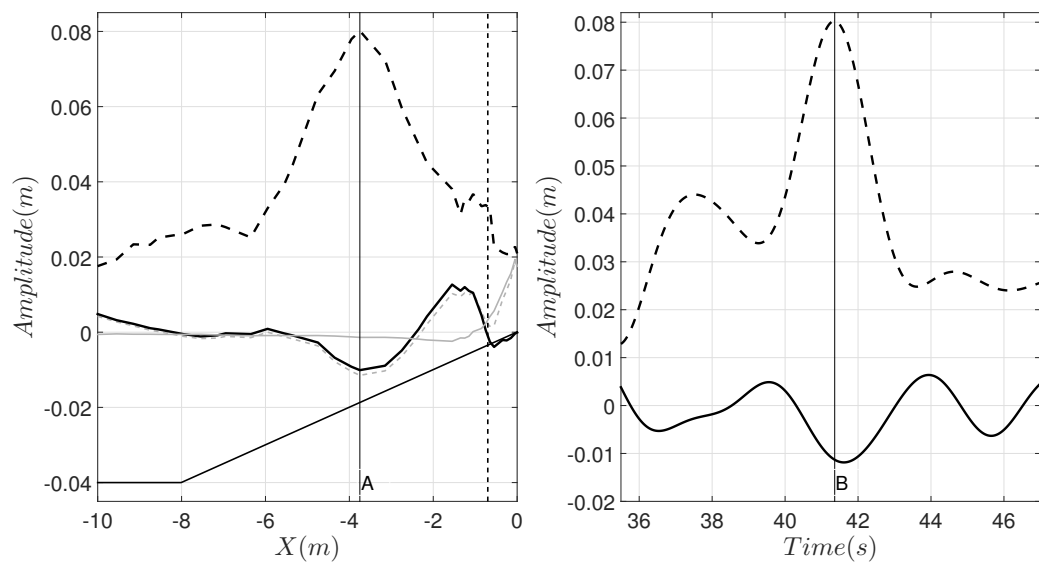


FIGURE 3.13: (Left) Spatial visualization at  $t = 41.3$ s (B in Figure 3.11) of short wave envelope (dashed black line), total long wave surface elevation (gray dashed), long wave and no setup (full black line) and mean setup (full grey line). (Right) Time evolution of short wave envelope (dashed line) and total long wave (full line) at  $x = -3.75$ m (A in Figure 3.11). Random wave case J6033A.

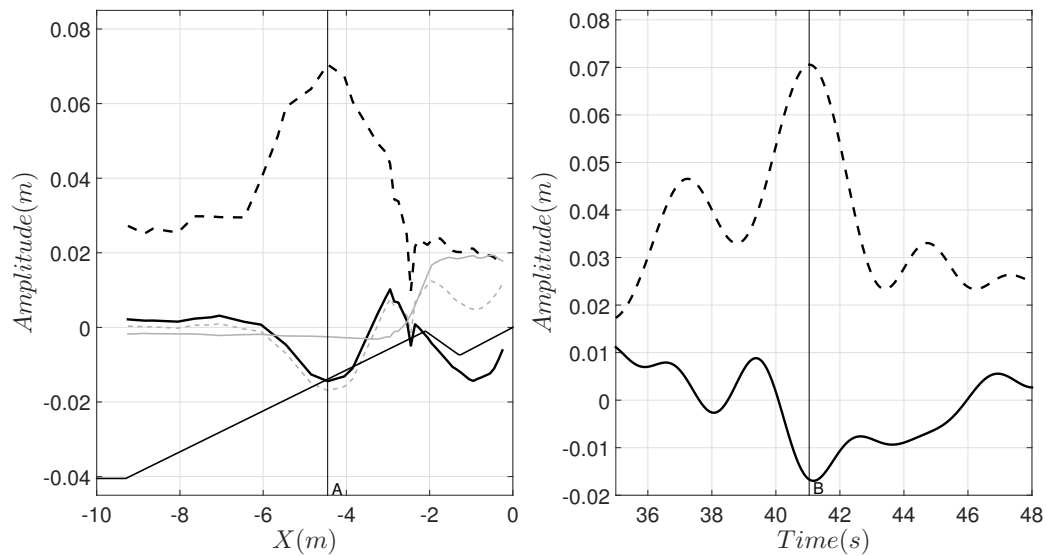


FIGURE 3.14: (Right) Spatial visualization at  $t = 41$ s (B in Figure 3.11) of short wave envelope (dashed black line), total long wave surface elevation (gray dashed), long wave and no setup (full black line) and mean setup (full grey line). (Left) Time evolution of short wave envelope (dashed line) and total long wave (full line) at position  $x = -4.45$ m (A in Figure 3.11). Random wave case J6033A on a barred beach.

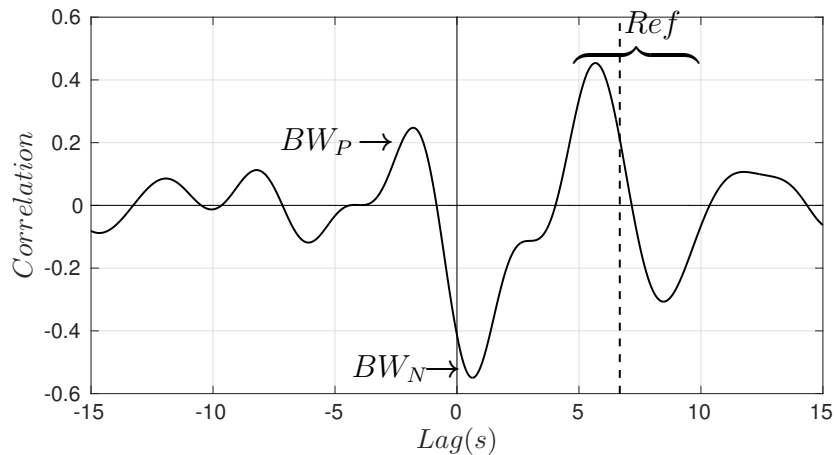


FIGURE 3.15: Cross-correlation between short wave envelope and long wave at  $x = -3.15\text{m}$ , dashed line is the travel time of the bound wave to the shoreline plus the travel time of the free wave reflected at the shoreline. Random wave case J6010A.  $BW_N/BW_P$  are the peaks related to the negative/positive part of the bound wave, and  $Ref$  are the peaks related to the reflected signal.

Due to the nature of the process, the leading surges are more easily identified in a spatial visualization than from a time series measured at a fixed location. Unfortunately, refined spatial information is only practical in laboratory and numerical experiments.

When applied to time series, the cross-correlation analysis is able to highlight the positive part of the bound wave, as shown in Figure 3.15 where the short wave envelope and the infragravity wave signal are cross-correlated at  $x = -3.15\text{m}$  (in the shoaling zone). The leading positive correlation peak at  $\tau \approx -2\text{s}$  and the strong negative peak at  $\tau \approx 1\text{s}$  represent a bound wave with a positive leading surge. The reflected wave has a similar shape, but with a better correlated positive leading surge.

Also, by cross-correlating the wave envelope, at fixed location, with the infragravity signal at different cross-shore locations it is possible to observe the relative evolution of the infragravity waves (Figure 3.16).

The interpretation of infragravity wave patterns found in the literature and the laboratory results analyzed here show that bound waves propagating over sloping bottom generate leading positive surges before the breakpoint. Those waves are strongly intensified inside the surf zone, suggesting a contribution of a dynamic

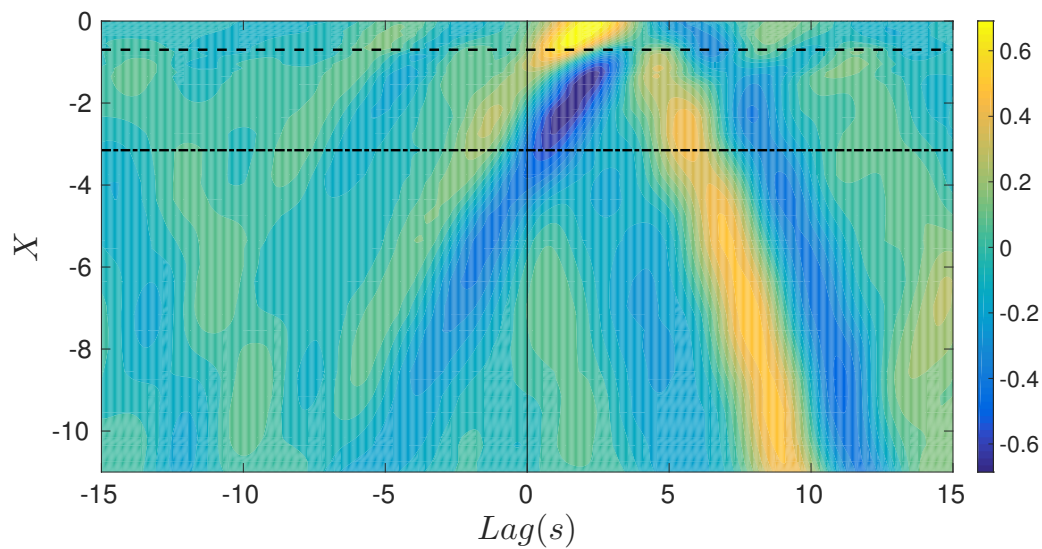


FIGURE 3.16: Cross-correlation between short wave envelope at  $x = -3.15\text{m}$  (dash-dotted line) and long wave at different position along the wave flume. Dashed line is the mean breakpoint position. Random wave case J6010A.

setup, or the forward breakpoint generated long wave (Baldock, 2006, Pomeroy et al., 2012). The positive signal also dominates the reflected waves, which is visible both in the space-time evolution of the infragravity surface elevation (Figures 3.11 and 3.12) and in cross-correlation results (Figures 3.15 and 3.16). These figures also indicate partial dissipation of the negative part of bound wave inside the surf zone. A possible explanation is that the bound wave is not released as a free wave during the breaking process, but remains locked and decays with the forcing (short wave breaking) inside the surf zone. Further aspects related to bound wave release and dissipation are discussed in the next section.

Although it is clear that bound wave shoaling generates a leading positive surge, whether this is forced, free or a combination of both is still not clear and further investigation is needed. An additional numerical investigation is presented in Chapter 5, sections 5.1 and 5.2.



### 3.5 Infragravity Wave Dissipation and Bound Wave Release

One important question yet to be fully answered is what happens to the bound wave after short wave dissipation (breaking)? The assumption of bound wave release is commonly used, where its justification is usually attributed to Longuet-Higgins and Stewart (1962). However, as pointed out by Baldock (2012) such statement was never made by those authors, on the contrary, they suggested possible partial reflection before the breaking region or/and bound wave decay inside the surf zone due to the dissipation of the short waves, indicating that the bound wave is still forced.

From the interpretation of the transient solution for linear long waves forced by the horizontal gradients of the radiation stress, Nielsen et al. (2008) suggested a mechanism for the conversion of forced wave into free wave (an analogy to bound wave release). The same approach may also suggest a mechanism for bound wave decay in the surf zone without any dissipation term.

Similar to the example given in Section 2.1 (see Figure 2.2), assuming an abrupt removal of the propagating forcing (which can be interpreted as a superposition of an opposite forcing with same shape and amplitude), in order to balance mass, two negative free waves are generated with their respective amplitude depending on  $c_g/\sqrt{gh}$  (equation 2.11). As shown, schematically, in Figure 3.17 (top graph) the abrupt change in the forcing ( $S_{xx} = 0$  at  $t = T$ ) radiates free waves with the same shape as the force wave. On the other hand, a gradual decaying of the forcing (lower graph) generates smaller and longer free waves. A very slow decaying rate results in the vanishing of both forced and free waves as demonstrated in Figure 3.17 (bottom graph).

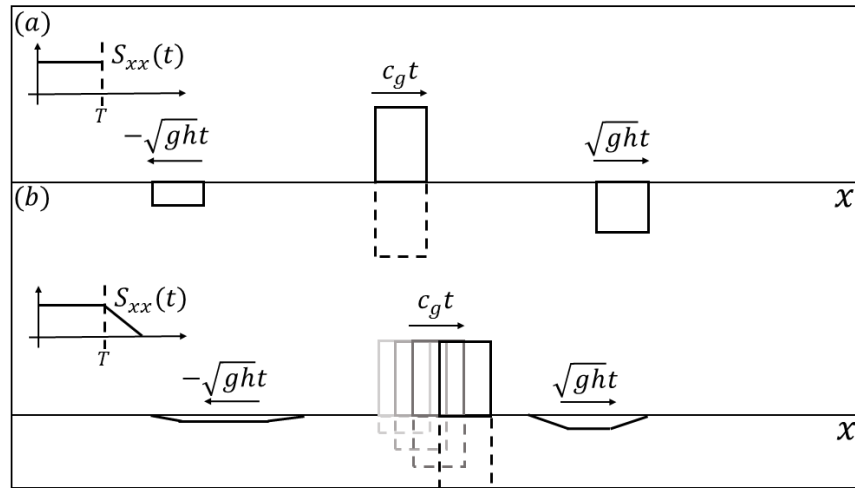


FIGURE 3.17: Schematic representation of forcing decay and surface elevation response. (top) Abrupt removal, (bottom) slow decay.

This approach also provides an alternative explanation for the outgoing waves radiated directly from the breaking zone, which are commonly attributed to the breakpoint forcing mechanism (Baldock, 2006, Contardo and Symonds, 2013, Lara et al., 2010). An example is given in Figure 3.18, which shows the infragravity surface elevation for one of the transient cases in Baldock (2006). The short wave dissipation occurs over a short space ( $-2 < x < -0.4\text{m}$ ), and from this region, at  $T \approx 36\text{s}$ , an outgoing negative pulse is radiated away. However, the amplitude of the wave is approximately twice that expected, according to equation 2.11.

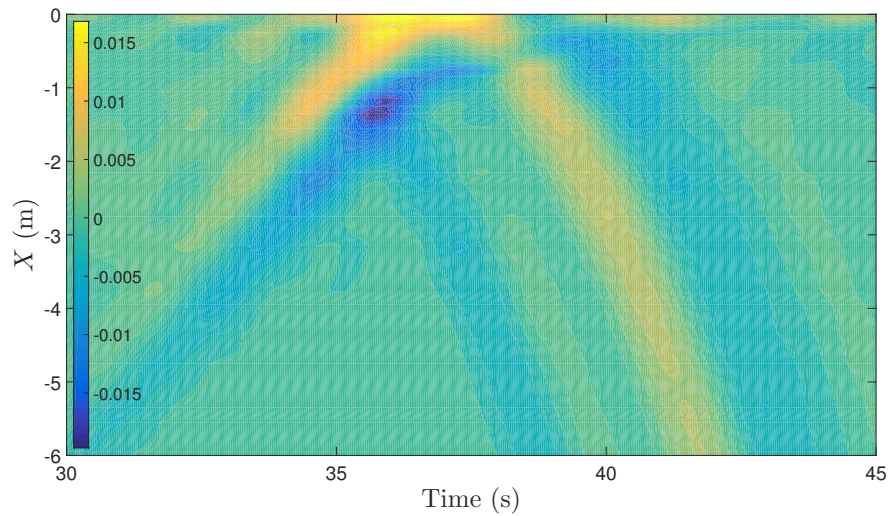


FIGURE 3.18: Infragravity surface elevation, Transient case G08A (table 4.3). Adapted from Baldock (2006). Colormap in meters.

Identifying whether the bound wave is released or/and dissipated is often difficult for many reasons: standing wave patterns generated by incident and reflected waves at the shoreline, difficulties in performing accurate incident and reflected wave separation inside the surf zone and also the presence of alternative sources of infragravity waves. In a comprehensive investigation Baldock (2012) demonstrated, using a series of previous published laboratory data and numerical results, that for some specific conditions the bound wave is strongly dissipated during the breaking of the short waves. It is further highlighted that the relationship between short and infragravity wave at the breakpoint is important to determine whether inside the surf zone bound wave is released or it remains forced, decaying with the dissipation of the short waves.

During the breaking process, three different conditions are possible. The least likely one is that both the short and forced waves are not in shallow water ( $c_g < \sqrt{gh}$  and  $L_G$  is not much longer than  $h$ ). A second, alternative condition, is when the bound wave is much longer than the depth  $h$  but the short waves are not, i.e., the group wave number  $k_b = \Delta\sigma/c_g$  is different to the wave number  $k_f$  of a free wave with frequency  $\Delta\sigma$ . The third possibility is  $k_b = k_f$  ( $k_b$  satisfies the linear

dispersion relation of a free wave), which only happens when both short and forced waves are in shallow water.

Bound wave release is considered to occur when  $k_b = k_f$ , being strictly valid only for the third condition. However, the second condition is also likely to occur under natural conditions. For instance, taking two wave groups with different mean periods of  $T_m = 8\text{s}$  and  $15\text{s}$ , the shallow water limits are  $h = 1.5$  and  $5.1\text{m}$ , respectively. Assuming breaking depths at  $h = 0.8H$  and waves with  $H = 2\text{m}$ , for the first case breaking occurs before the shallow water limit, in the other case this condition is well satisfied. This physical interpretation was used by Baldock et al. (2004) to explain the strong bound wave decay for conditions where short wave breaking occurs before the shallow water limit.

Battjes et al. (2004) suggested, based on different studies (Guza and Bowen, 1976, Madsen et al., 1997), that the dissipation inside the surf zone is related to the proximity of infragravity and short wave frequencies, where shorter infragravity waves would experience stronger decay due to short wave breaking, in other words, infragravity waves that are relatively short compared to the surf zone width are more easily dissipated than longer waves whose lengths are only a fraction of the surf zone.

Re-analysis results of the run-up data for the four different series of bichromatic wave groups measured by Baldock et al. (2000) corroborates partially Battjes et al. (2004). Run-up amplitude for the four different series follow a similar pattern (Figure 3.19), at lower frequencies ( $f < 0.3$ ,  $k_b$  is smaller than the short wave number  $k_s$ ) run-up amplitude increases with group frequency, and at higher frequencies ( $f > 0.3$ ,  $k_b \approx k_s$ ) strong amplitude decay is observed. Even though no wave separation was performed and breakpoint forcing may also be present, the results are qualitatively similar to the numerical results in Madsen et al. (1997) obtained considering only bound wave forcing and no reflection. Also the amplitudes are significantly below the saturation limit (Baldock and Holmes, 1999), suggesting that the dissipation is not due to infragravity wave breaking as observed by van Dongeren et al. (2007).

As shown in Figure 3.20, no clear relationship was observed between the run-up amplitude and  $k_b/k_f$ , estimated close to the breakpoint. In fact, for all cases in this data set the short wave breaking is likely to occur before the wave groups reach the shallow water limit. Also no relationship was observed between the remaining relative groupiness in the inner surf zone and the run-up amplitude (Figure 3.19). The relative groupiness is defined as the standard deviation of the short wave envelope close to the shoreline divided by the same parameter calculated at the toe of the slope. In case of the bound waves remaining forced in the surf zone a direct proportionality between the run-up amplitude and the relative groupiness would be expected.

The reduced amount of data (series A only) used in this analysis limits further conclusions about the dissipation of bound waves. For that reason, further numerical investigation is presented in Chapter 5.

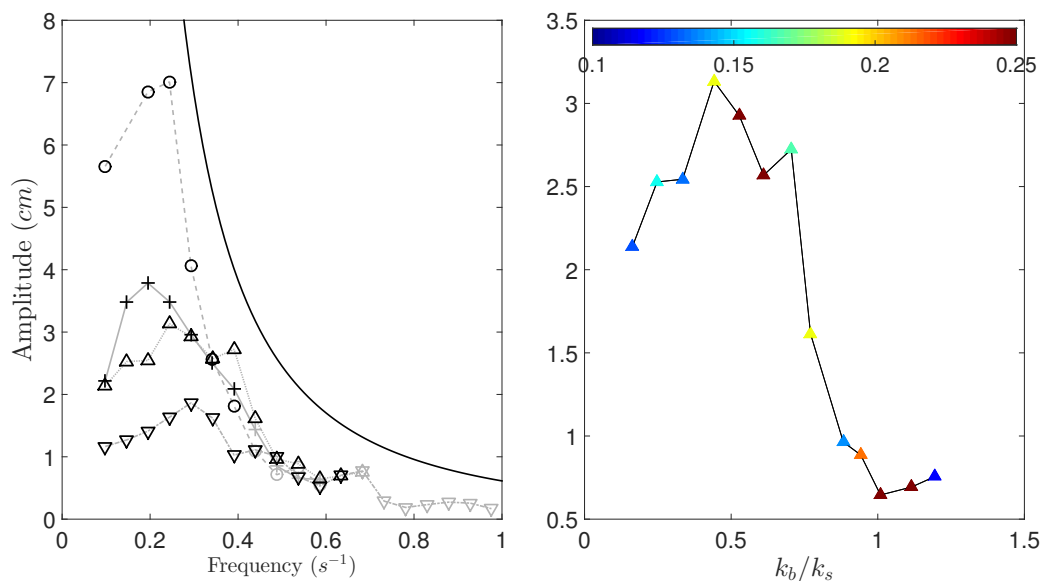


FIGURE 3.19: Run-up amplitude for bichromatic wave groups. Left: Vertical run-up amplitude at the group frequency,  $\triangle$ — series A,  $\nabla$ — series B, + series C and  $\circ$ — series D. Black line is the run-up saturation limit according to (Baldock and Holmes, 1999). Right: Run-up versus wave group length normalized by short wave length, series A. Colorbar is the relative groupiness. Data from Baldock et al. (2000).

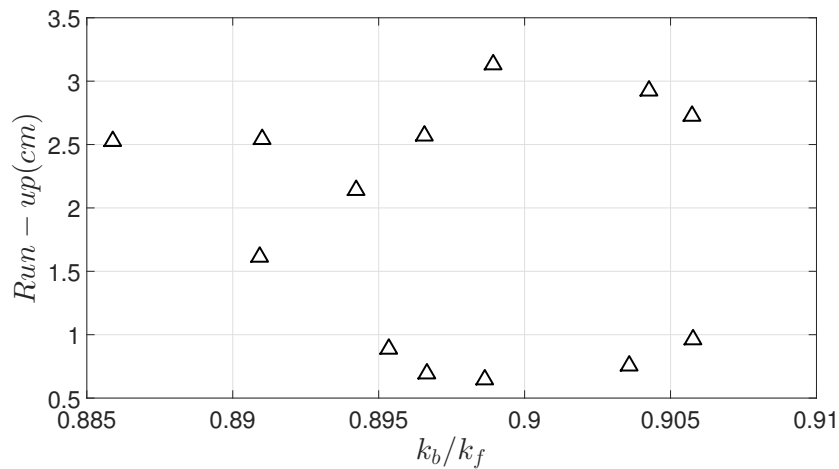


FIGURE 3.20: Run-up amplitude for bichromatic wave groups, series A. Data from Baldock et al. (2000).

### 3.6 Infragravity Wave Dependence on Short Wave Amplitude

The power relationship between short and infragravity wave height ( $H_{IG} \propto H_{sh}^p$ ) is a relevant source of information commonly used to characterize surf beat. For instance, bound waves are proportional to  $H_{sh}^2$ , and the breakpoint forcing goes as  $H_{sh}$  (Nagase and Mizuguchi, 2001). Battjes et al. (2004) and later Baldock (2012) have discussed the implication of these dependences on the relative importance of each mechanism for specific conditions. Basically, if the shoaling of the bound wave is strong, due to its quadratic dependence on  $H_{sh}$ , it dominates over the breakpoint forcing. On the contrary, for weak bound wave shoaling, the breakpoint mechanism becomes the main forcing. These conditions can be distinguished by the normalized bed slope equation 3.11.

Baldock and Huntley (2002) showed graphically that the relationship between short and infragravity wave amplitude is frequency dependent and also strongly influenced by the short wave breaking. Outside the surf zone,  $p$  reduces with increasing frequency, whereas inside the surf zone a linear dependence was observed for all the frequencies.

Here the same random wave cases as in Baldock and Huntley (2002) (J6033A, B and C, see details in table 4.2) are re-analyzed. The cases have the same spectrum shape, but distinct short wave amplitudes (Figure 3.21). For this reason, the power relationship between target  $H_{sh}$  (at the wave maker) and  $H_{IG}(f)$  (along the flume), at discrete frequencies, is calculated using least square and power law fitting. In other words, the slope ( $p$ ) of the best fitted straight line on a loglog graph of target  $H_{sh}$  and  $H_{IG}(f)$  is calculated (considering the three available point for each frequency).

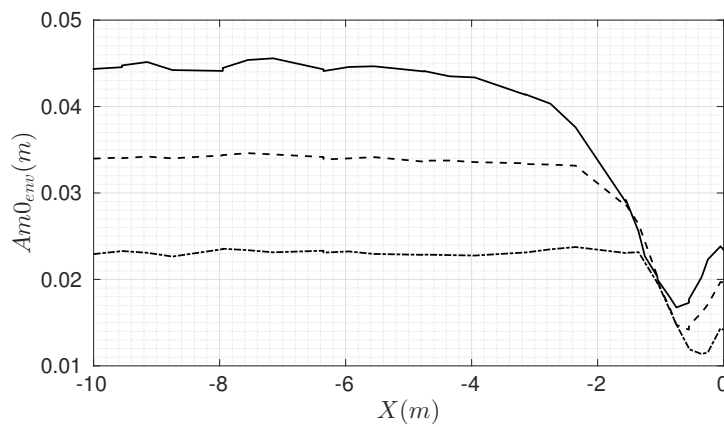


FIGURE 3.21: Short wave envelope amplitude. Random wave cases J6033A (full line), J6033B (dashed line) and J6033C (dashed-dotted line).

Figure 3.22 shows the calculated  $p$  for each frequency along the wave flume. Outside the surf zone, the same trend in Baldock and Huntley (2002) was obtained, however, no constant linear relationship was observed inside the surf zone. In fact, inside the surf zone  $p$  is also frequency dependent.

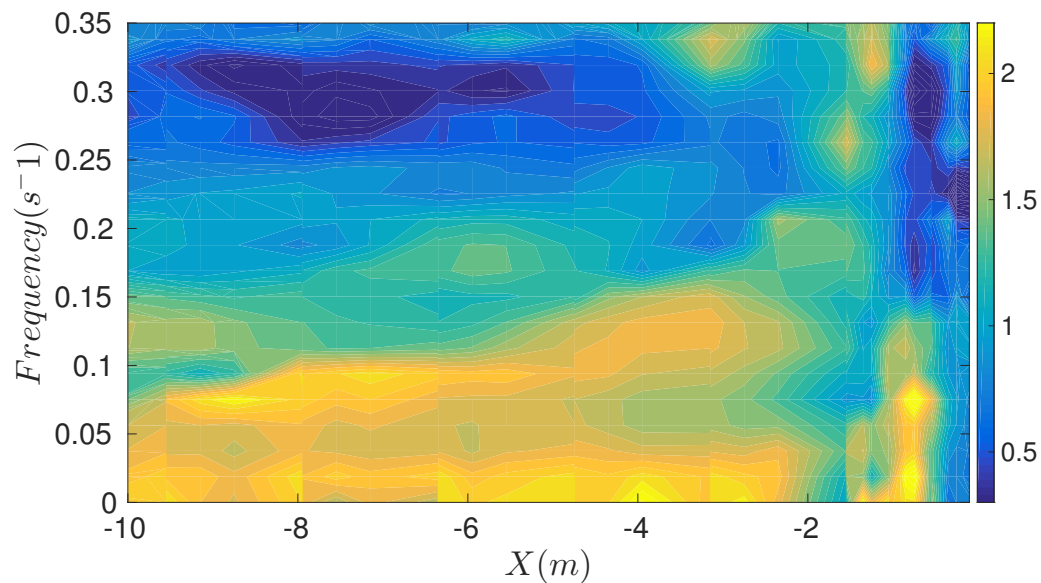


FIGURE 3.22: Power relationship, at discrete frequencies ( $\Delta f = 0.018\text{Hz}$ ), between infragravity wave and the target incident short wave height. Random wave cases J6033A ( $H_{m0} = 0.141\text{m}$ ), J6033B ( $H_{m0} = 0.106\text{m}$ ) and J6033C ( $H_{m0} = 0.071\text{m}$ ), Colormap is the power  $p$ .

Applying the same analysis, but considering  $H_{IG}(f)$  for incident and outgoing waves separately (using equation 3.4, Guza et al. (1984)), it becomes clear that the frequency dependence emerges from the bound wave dissipation in the surf zone. Figure 3.23 shows that for the incident wave  $p$  is relatively constant and close to 2 (quadratic) in the shoaling zone, an indication of bound wave forcing. In the surf zone  $p$  reduces, with stronger decay towards higher frequencies. For the lower frequencies  $p$  initially decays, but increases close to the shoreline. This is in accordance with the increasing groupiness, at these frequencies close to the shoreline (Figure 3.24). Note that for Figures 3.23 and 3.24 the frequency axis is horizontal and cross-shore axis is vertical.



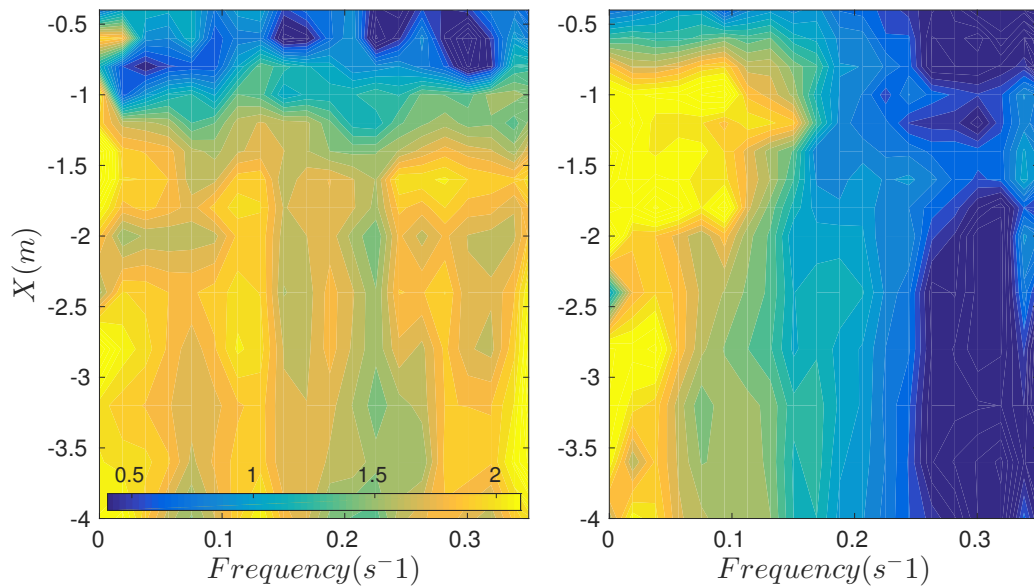


FIGURE 3.23: Power relation, at discrete frequencies ( $\Delta f = .018\text{Hz}$ ), between infragravity wave and the target incident short wave height. Incident (left) and outgoing infragravity wave (right). Random wave cases J6033A ( $H_{m0} = 0.141\text{m}$ ), J6033B ( $H_{m0} = 0.106\text{m}$ ) and J6033C ( $H_{m0} = 0.071\text{m}$ ). Colormap is the power  $p$ .

As expected, the length of the dissipation zone depends on the amplitude of the short waves (Figure 3.21), and as proposed by Battjes et al. (2004) stronger dissipation is observed for wider surf zones.

The normalized short wave envelope amplitude at discrete frequencies corroborates this hypotheses (Figure 3.24). Inside the surf zone, the forcing is relatively weaker for J6033A increasing towards J6033C, mainly for the higher frequencies. The forced infragravity waves (bound waves) will behave identically to the forcing, being relative larger for the smaller wave cases. Also, the reflected waves, at these frequencies, will be relatively stronger for the smaller wave cases, consistent with the  $p < 1$  for the outgoing waves (Figure 3.23).

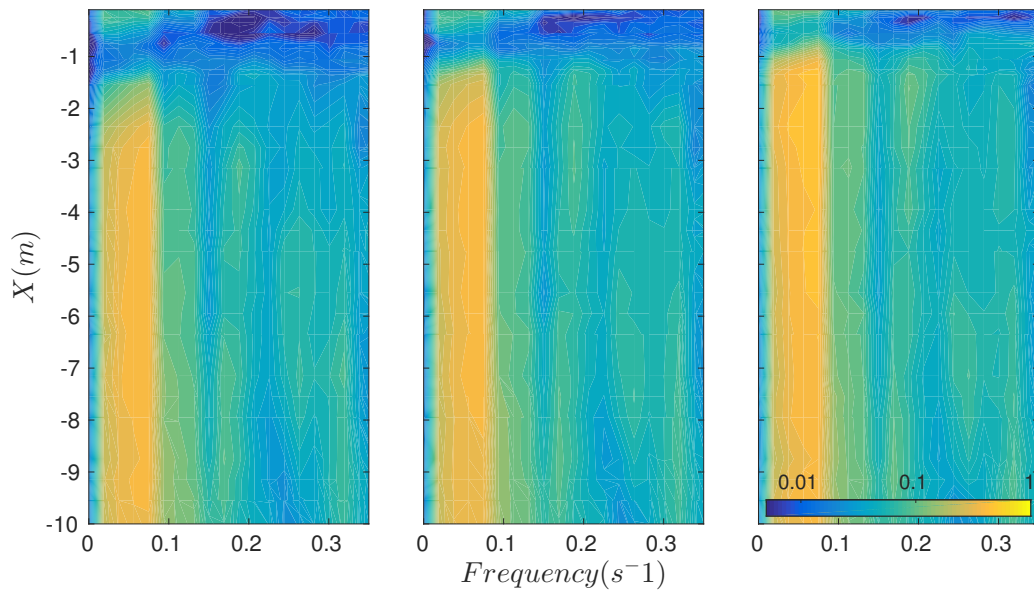


FIGURE 3.24: Short wave envelope spectrum normalized by the target wave height ( $H_{sh}^2$ ). Random wave cases J6033A (left), J6033B (center) and J6033C (right).

These results suggest that the different rates of dissipation of infragravity waves inside the surf zone for each case is the main cause of the frequency dependence of  $p$ . The small values of  $p < 1$  in the total signal, at high frequencies, indicates the dominance of outgoing waves. This is probably related to the relative reduced dissipation of the bound wave for the cases with smaller wave height.

### 3.7 Radiated Breakpoint Forced Long Wave

The effectiveness of the breakpoint mechanism is commonly evaluated in terms of the measured outgoing long wave, which has been demonstrated by different researchers to be qualitatively similar to the theoretical response proposed by Symonds et al. (1982). For instance, the double amplitude peak with a  $\chi$  (normalized surf zone width) dependency observed by Madsen et al. (1997) is only explained by the constructive/destructive interaction between shoreline reflected and outgoing breakpoint generated waves (Section 2.2).

Baldock et al. (2000) presented a wide discussion on surf beat generated by bi-chromatic wave groups, in total 65 different wave groups with distinct, wave amplitudes, modulation rates, primary and group frequencies were investigated. A similar outgoing wave amplitude (at  $f_g$ ) dependence on  $\chi$  was observed. Maximum constructive and destructive interference was obtained for  $\chi = 1.1$  and  $\chi > 4$ , respectively. However, different to Madsen et al. (1997) no second peak of the maximum response were observed.

Generally at the group frequency the outgoing wave contains breakpoint forced and reflected bound waves which complicates the distinction between the forcing mechanisms. Alternatively, Baldock et al. (2000) suggested the investigation of conditions where the frequency of the breakpoint oscillation and bound wave frequency differ. According to Longuet-Higgins and Stewart (1962) the bound wave has the same shape as the forcing, which is the short wave envelope. For that reason, the bound wave and forcing must have the same frequencies, and infragravity waves occurring at other frequencies are likely to be generated by an alternative mechanism.

In fact, for some of the cases in Baldock et al. (2000) matched this condition. After re-analyzing this data set, it was observed that the infragravity waves were not only restricted to frequencies associated to the short wave envelope. For instance, significant oscillations were measured at the repeat frequency ( $f_R$ ).  $f_R$  is the frequency at which the short wave phase within the group identically repeat (Baldock et al., 2000) as demonstrated in Figure 3.25.

It is later confirmed by the numerical simulations that the breakpoint oscillation has a strong component at  $f_R$  and other frequencies for those particular cases. Further investigation is presented in Chapter 4.

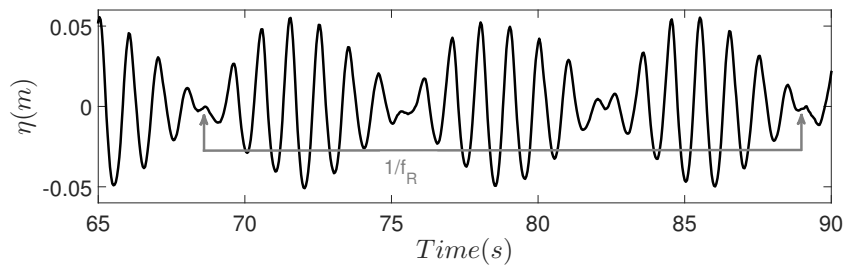


FIGURE 3.25: Surface elevation for bichromatic wave groups, case B1025A (table 4.1).  $f_R$  is the repeat frequency.

It was also clear that the oscillations at  $f_R$  were stronger for cases with shorter wave groups, where  $k_b \approx k_s$ , as in B1060A (table 4.1). For those conditions, inside the surf zone strong dissipation occurs at  $f_g$  and at the shoreline  $f_R$  becomes dominant (Figure 3.26).

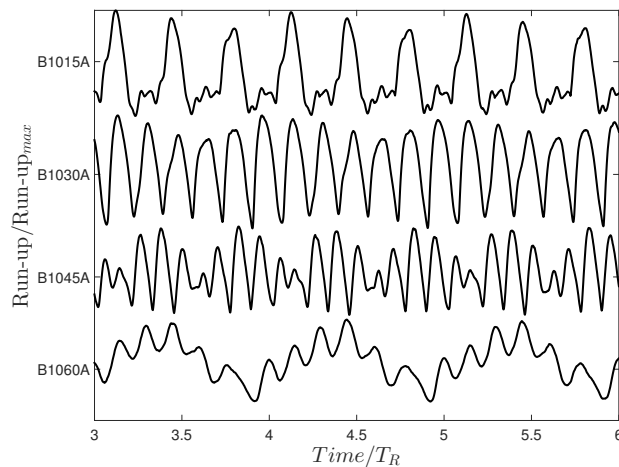


FIGURE 3.26: Vertical run-up oscillations for different bichromatic wave groups. Each time series is normalized by its maximum amplitude, time is scaled according to each repeat frequency  $T_R = 1/f_R$ .

The bichromatic case B1060A exemplifies this discussion. Figure (3.27) shows the measured space-time wave envelope amplitude, infragravity surface elevation and the simulated breakpoint excursion filtered at  $f_R$  (see Chapter 4). The correlation between the breakpoint and the changes in water levels inside the surf zone is clear (Figure 3.27d). This result indicates breakpoint forcing at this frequency (no

bound incident waves are present). Weak outgoing propagation patterns outside the surf zone can be explained by the very small  $\chi \approx 0.3$  at  $f_R$ .

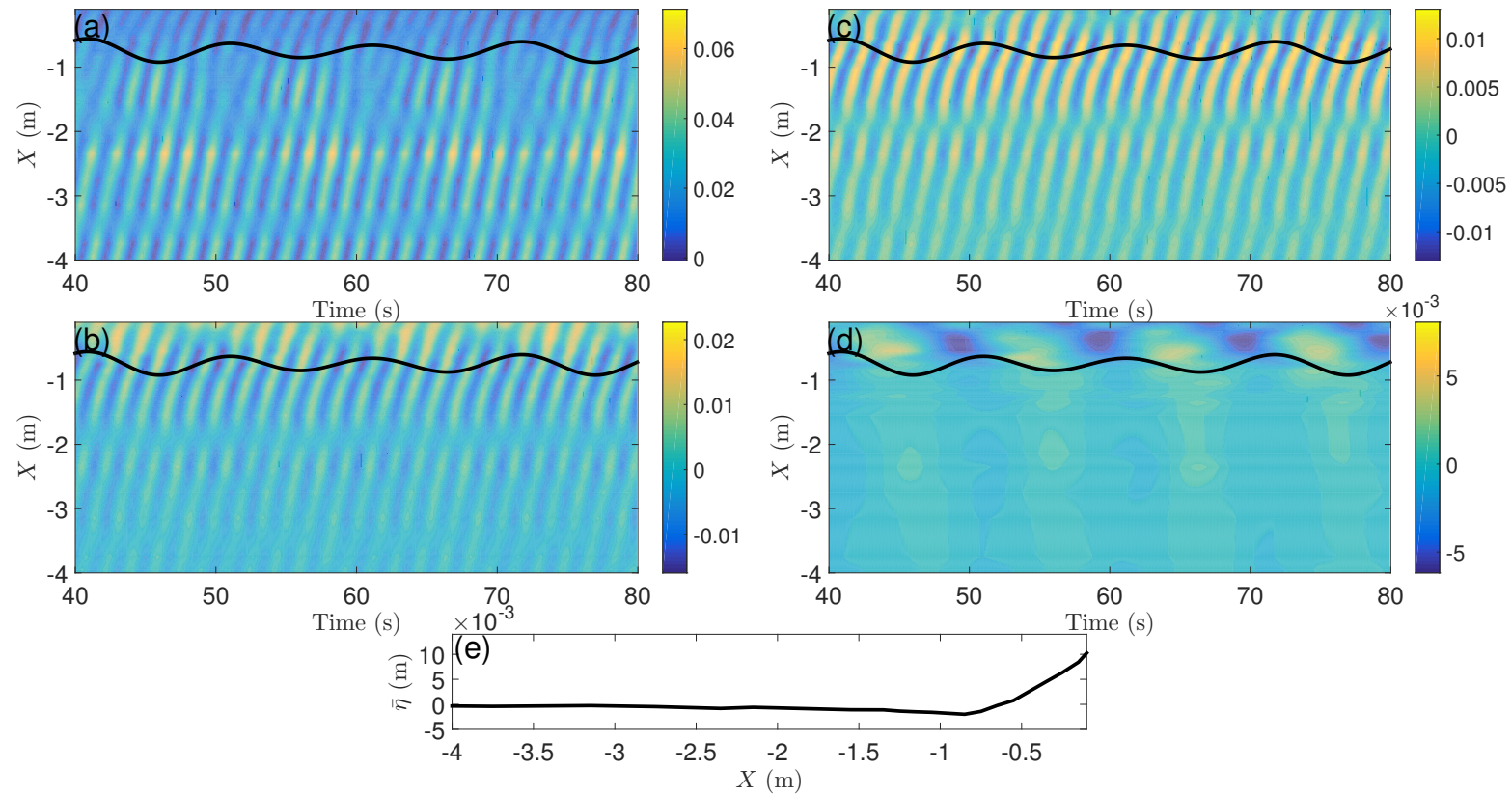


FIGURE 3.27: (a) space and time evolution of wave envelope amplitude, (b) total infragravity surface elevation (including mean setup), (c) surface elevation at the group frequency (without mean setup), (d) low-pass filtered surface elevation at and below  $f_R$  (without mean setup) and (e) mean setup. Black line is the low-pass filtered breakpoint position numerically calculated (Chapter 4). Bichromatic wave case B1060A. Colormap in  $p$ .

An alternative identification of the breakpoint mechanism is the outgoing wave radiated directly from the breakpoint. According to Symonds et al. (1982) the breakpoint behaves as a wave-maker where free incident and outgoing waves are equally generated with  $\pi$  phase difference. As mentioned before, directly radiated outgoing waves have been observed by Baldock (2006) and Lara et al. (2010) in transient wave groups; for random waves direct observation is difficult.

In the field, outgoing wave radiated directly from the breakpoint point was observed by Contardo and Symonds (2013). One of the methods use was the cross-correlation analysis between incident and reflected infragravity waves at different locations, two inside and one outside the surf zone. The cross-correlation results for the sensors inside the surf zone indicated waves reflected from the shoreline. For the sensor outside the surf zone, the cross-correlation showed a peak at a lag that would indicate outgoing waves propagating directly from the breakpoint, suggesting breakpoint forcing (Figure 7 in Contardo and Symonds (2013)). However, the lack of an expected correlation peak for the shoreline reflected wave was not pointed out by those authors, perhaps further investigation would be important to clarify the vanishing of the shoreline reflected wave.

Here the same analysis is applied to the eight random wave cases (table 4.2). Even though the experiments were performed on a steep slope, which would favor breakpoint forcing, no correlation peak for the outgoing wave radiated directly from the breakpoint was observed. Figure 3.28 shows the typical results obtained for a cross-correlation analysis between incident and outgoing waves measured at the same position outside the surf zone and close to the outer breakpoint. The peak correlations are related to the wave reflected at the shore line.

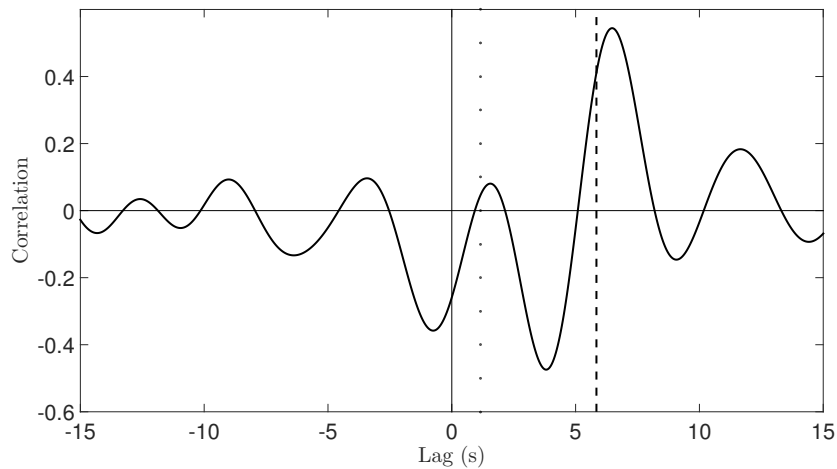


FIGURE 3.28: Cross-correlation between incident and outgoing long wave at  $x = -2\text{m}$ , dotted line is the travel time from the breakpoint to measurement position. Dashed line is travel time for the shoreline reflected wave. Random wave case J6033A.

The cross-correlation between the incident long wave at  $x = -4\text{m}$  and the outgoing long wave at different positions shows the progressive pattern of the reflected wave at the shoreline, with no signal of the outgoing waves radiated directly from the breakpoint (Figure 3.29).

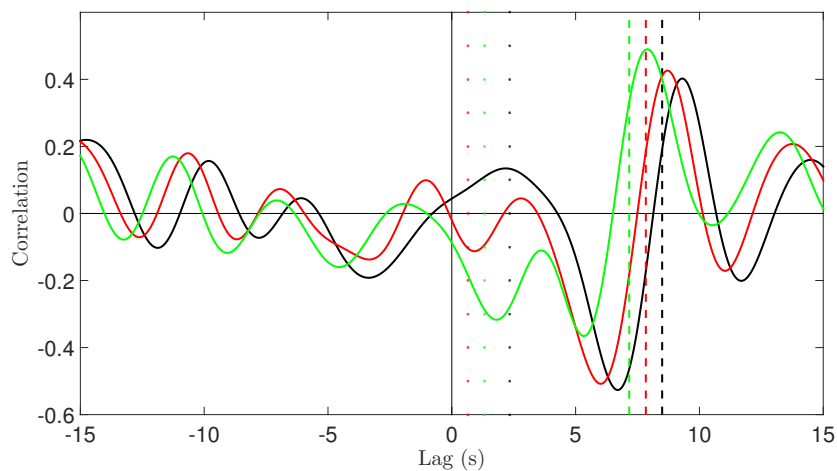


FIGURE 3.29: Cross-correlation between incident long wave at  $x = -4\text{m}$  and out-going long wave at:  $x = -4\text{m}$  (black),  $x = -2.8\text{m}$  (red) and  $x = 1.8\text{m}$  (green). Dotted line travel time related to the breakpoint radiated outgoing wave. Dashed line, travel time related to the shoreline reflected wave. Random wave case J6033A.



### 3.8 Frequency Down-shift

Baldock et al. (2004) performed the same experiments for the random cases discussed above for a barred profile, with the same slope ( $\beta = 0.1$ ) as the constant sloping beach. For that reason, outside the surf zone the short wave groups have same behavior (Figure 3.30). But even though the bound wave forcing is identical, clear changes in the infragravity wave patterns are observed and they are in good agreement with the breakpoint forcing mechanism.

As discussed by Baldock et al. (2004), in the barred beach case, the energy shift to lower frequencies inside the surf zone is in agreement with the resonant trapping of long waves (Symonds and Bowen, 1984), and the outgoing wave amplitude dependence on the normalized surf zone width ( $\chi$ ) is in agreement with Symonds et al. (1982). For the constant slope, constructive outgoing wave interference ( $0.5 \leq \chi \leq 2$ ) occurs for frequencies between 0.11 and 0.23Hz, while for the barred beach the same  $\chi$  values occur for frequencies between 0.07 and 0.14Hz.

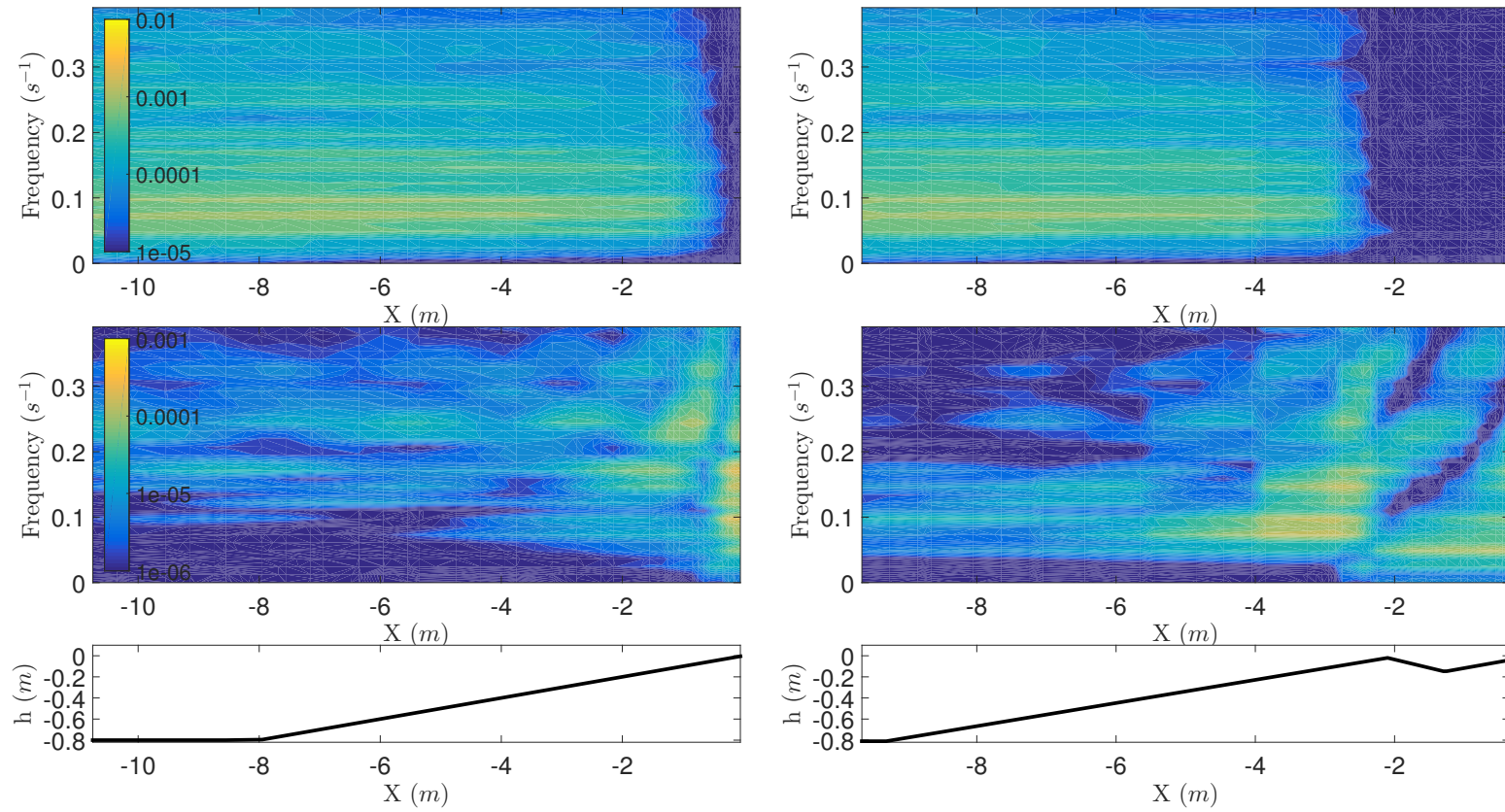


FIGURE 3.30: Random wave case J6033C, top panel- wave envelope spectrum, mid panel - infragravity spectrum, bottom panel - bottom slope. Left- plane beach, right- barred beach. Colormap in  $m^2/Hz$ .

### 3.9 Conclusion

The main aspects of surf beat have been discussed based on a critical literature review and re-analysis of laboratory data. The importance of the different infragravity waves generated by each forcing mechanism, as well as their propagation patterns and commonly used data analysis have been highlighted. The interpretation of cross-correlation results for signals containing incident and reflected waves was introduced. It was shown that the cross-correlation analysis provide distinct results when applied to a single or a spectrum of standing waves. For the first case, standing patterns are captured. For a spectrum the results show the progressive patterns of both the incident and reflected signal.

The bound wave shoaling is an important aspect for infragravity wave dynamics. Features that deviate from the equilibrium solution, such as bound wave lag, amplitude dependence on group frequency and changes in envelope and bound wave shape have been discussed. An alternative explanation for these processes was suggested based on the assumption of free wave generation due to changes in forcing and in the bound wave. A conceptual model of forced and free waves has shown that the superposition of these two waves leads to bound wave lag, and amplitude dependence on the group frequency, and hence different shoaling rates. The results matched qualitatively the findings of Madsen et al. (1997) and Battjes et al. (2004).

By cross-correlating the short wave envelope with the infragravity surface elevation, a positive correlation peak is observed before the group reaches the breakpoint. This is an indication of a surge leading the short wave envelope, explaining results presented by List (1992) and Masselink (1995). Due to particular similarities with the incident breakpoint forced long wave, the leading surge generated during the bound wave shoaling was further analyzed. The results show it as an important process that needs further investigation. The remaining question is whether the leading surge is forced or free.

The main aspects of infragravity wave dissipation inside the surf zone were presented, including the concepts of bound wave release and decay. The analysis of laboratory data corroborates the infragravity dissipation dependence on the ratio between  $k_b/k_s$  suggested by Battjes et al. (2004). Bound wave dissipation was also observed for random waves by analyzing the power relationship between the short wave and infragravity wave amplitude for the incident and outgoing wave signals. The frequency dependence of  $p$  for the total signal is related to the stronger dissipation of the incident bound wave at higher frequencies in the surf zone and the dominance of free outgoing waves at higher frequencies.

Using the same approach as Contardo and Symonds (2013) for the random wave cases, no directly radiated outgoing breakpoint forced long wave was detected. From the cross-correlation results only waves reflected from the shoreline were observed. Interestingly, even though the analysis presented here indicated weak or absent breakpoint forcing, other observations are well explained by the breakpoint forcing. For instance, the observed infragravity frequency down-shift with increasing surf zone width, matching outgoing wave dependence on  $\chi$  (Symonds et al., 1982) and the resonant response inside the surf zone (Symonds and Bowen, 1984). In the following chapters the topics presented here are further investigated numerically.

# Chapter 4

## **FUNWAVE: Description, Testing and Numerical Simplifications**

In this and the following chapter the infragravity waves are numerically investigated using FUNWAVE. Here the model is briefly described and validated against laboratory data. Also, the two main mechanisms of infragravity wave generation are implemented in the model. The implementation is tested against analytical solutions and laboratory data.

### **4.1 FUNWAVE Description**

FUNWAVE is an open source free surface wave model originally developed by Kirby et al. (1998) and later updated by Shi et al. (2012), which uses a hybrid finite volume - finite difference scheme to solve the weakly dispersive and fully nonlinear depth-integrated Boussinesq equations derived by Chen (2006). Shi et al. (2012) introduce a minor extension to Chen's momentum equation by using horizontal momentum flux ( $\mathbf{M}$ ) as a conserved variable, and then the depth-integrated volume conservation equation and the depth-average horizontal momentum equation are expressed respectively as

$$\eta_t + \nabla \cdot \mathbf{M} = 0, \quad (4.1)$$

$$\begin{aligned} \mathbf{V}_t + \nabla \cdot \left[ \frac{\mathbf{M}\mathbf{M}}{H} \right] + \nabla \cdot \left[ \frac{1}{2}g(\eta^2 + 2h\eta) \right] = \\ \eta_t(\mathbf{V}_1' - \bar{\mathbf{u}}_2) + H(\mathbf{u}_\alpha \cdot \bar{\mathbf{u}}_2 + \bar{\mathbf{u}}_2 \cdot \nabla \mathbf{u}_\alpha - \mathbf{V}_1'' - \mathbf{V}_2 - \mathbf{V}_3 - \mathbf{R}) + g\eta \nabla h, \end{aligned} \quad (4.2)$$

and

$$\mathbf{M} = H(\mathbf{u}_\alpha + \bar{\mathbf{u}}_2), \quad (4.3)$$

$$\mathbf{V} = H(\mathbf{u}_\alpha + \mathbf{V}_1'). \quad (4.4)$$

$H = \eta + h$  is the total local water depth, and  $\mathbf{V}_1 = \mathbf{V}_{1,t}' + \mathbf{V}_1''$  and  $\mathbf{V}_2$  are dispersive terms.  $\mathbf{V}_3$  is a second-order vertical vorticity term,  $\mathbf{u}_\alpha$  is the velocity at a reference level  $z = z_\alpha$  and  $\bar{\mathbf{u}}_2$  is the depth averaged  $O(kh)^2$  contribution to the horizontal velocity field.  $\mathbf{R}$  represents diffusive and dissipative terms. The full mathematical derivation, and the numerical schemes including wave breaking and shoreline motion are presented in Shi et al. (2012).

FUNWAVE has been extensively tested since its first version including wave transformation, nearshore circulation (Choi et al., 2015, Fengyan et al., 2013, Johnson and Pattiaratchi, 2006, Kirby et al., 1998, Shi et al., 2012), and extensive Tsunami benchmark testing (Fengyan et al., 2012, Tehranirad et al., 2011). In the next section, the model is further tested against a large set of laboratory experiments including bichromatic, random and transient wave cases. The main purpose of this verification is to evaluate the model's capability of simulating infragravity waves.

## 4.2 Numerical Model Validation Tests

The laboratory experiments were carried out in a wave flume 18 meters long, 0.9 meters wide, with working water depth,  $h$ , of 0.8 meters (Figure 4.1). The experiments were performed on plane sloping beach ( $\beta = 0.1$ ), surface elevation were collected using surface-piercing resistance-type wave gauges and shoreline motion was measured using a run-up wire. These data have been previously published and more information about the experiment set-ups are found in Baldock et al. (2000), Baldock and Huntley (2002) and Baldock (2006). The initial condition for each case is presented in tables 4.1, 4.2 and 4.3.

### 4.2.1 Bichromatic Wave Groups

Eight fully modulated bichromatic cases were selected. The details are presented in table 4.1, where  $f_1$  and  $f_2$  are the two primary frequencies,  $f_g$  is the group frequency and  $f_R$  is the repeat frequency (see Section 3.7).

TABLE 4.1: Bichromatic wave groups, initial conditions. Primary wave amplitudes  $a_1 = a_2 = 2.5\text{cm}$ .

case	$f_1(Hz)$	$f_2(Hz)$	$f_g(Hz)$	$f_R$
B1010A	1.025	0.928	0.098	0.049
B1015A	1.074	0.928	0.147	0.049
B1020A	1.074	0.879	0.195	0.098
B1025A	1.123	0.879	0.244	0.049
B1030A	1.123	0.830	0.293	0.049
B1045A	1.221	0.781	0.439	0.049
B1060A	1.269	0.683	0.586	0.098
B6020A	0.683	0.488	0.195	0.097

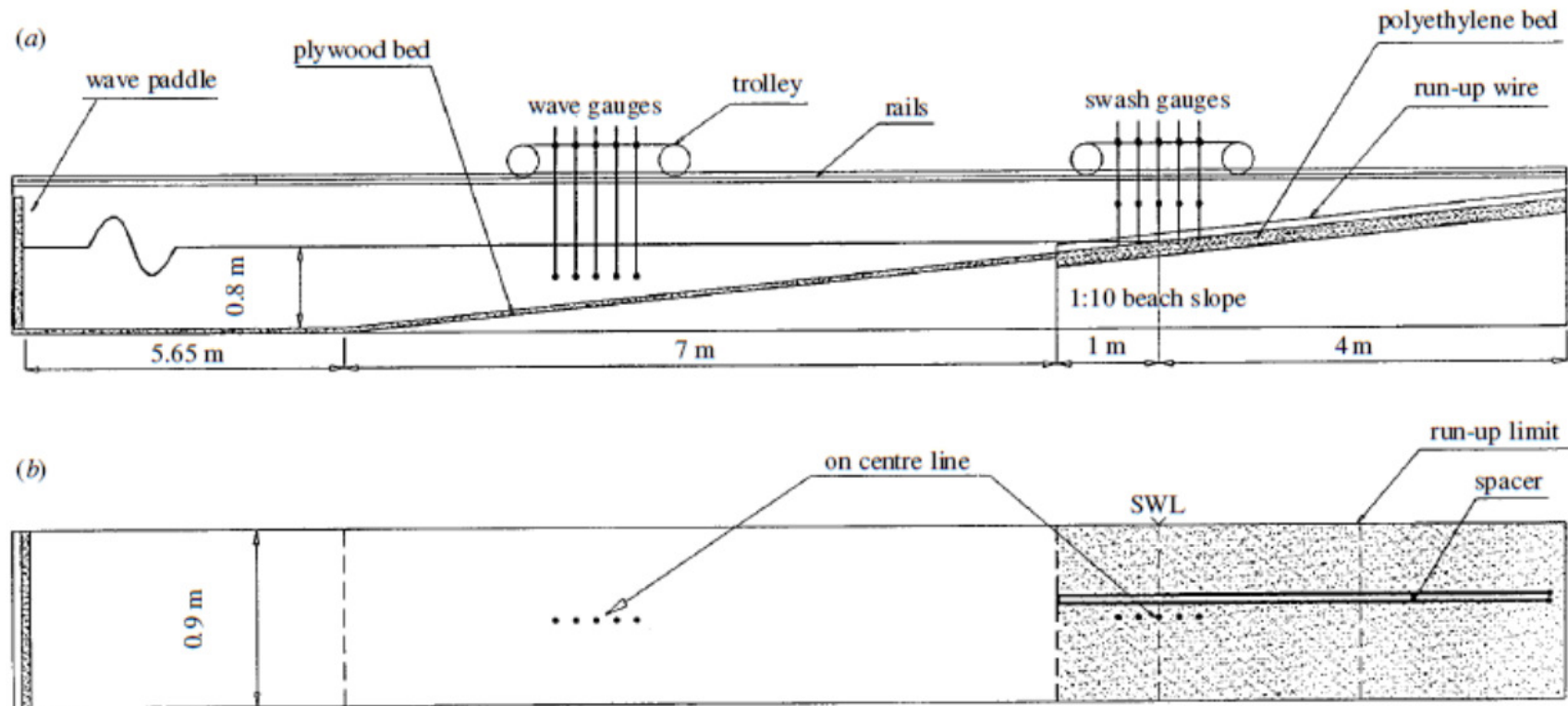


FIGURE 4.1: Wave flume and instrumentation. From Baldock and Huntley (2002).



### 4.2.2 Random Waves

The random waves were generated based on the JONSWAP spectrum (Hasselmann et al., 1973), with varying peak frequency  $f_p$ , offshore wave height  $H_{m0} = 4\sqrt{m_0}$  ( $m_0$  is the variance of  $\eta$ ) and peak enhancement factor,  $\gamma$ . The total of 8 cases are subdivided into three series according to their peak frequency and spectral shape. The lower and upper frequency limits ( $f_1$  and  $f_2$ ) for primary (linear) waves components are also given in table 4.2.

TABLE 4.2: Random wave cases, initial wave characteristics.

Case	$f_p(Hz)$	$f_1(Hz)$	$f_2(Hz)$	$\gamma$	$H_{m0}(cm)$
J1010C	1.0	0.65	1.74	1.0	7.1
J1033C	1.0	0.67	1.78	3.3	7.1
J6010A	0.6	0.41	1.48	1.0	14.1
J6010B	0.6	0.41	1.48	1.0	10.6
J6010C	0.6	0.41	1.48	1.0	7.1
J6033A	0.6	0.42	1.47	3.3	14.1
J6033B	0.6	0.42	1.47	3.3	10.6
J6033C	0.6	0.42	1.47	3.3	7.1

### 4.2.3 Transient Wave Group

The transient-focused wave group was generated from a 'top-hat' frequency spectra (Rapp and Melville, 1990). The initial characteristics are presented in table 4.3, where  $f_c$  is the central frequency,  $f_1$  and  $f_2$  upper and lower frequency limits of the primary waves.  $A$  is the total amplitude (sum of the amplitudes of the primary waves) and  $H_0/L_0$  is the offshore wave steepness.

TABLE 4.3: Transient wave group, initial wave characteristics.

Case	$f_c(Hz)$	$f_1(Hz)$	$f_2(Hz)$	$A(cm)$	$H_0/L_0$
G08A	1	1.2	0.8	6.0	0.088

#### 4.2.4 Results

The predicted and measured surface displacement at different positions along the wave flume are in good agreement for all cases. The wave generation mechanism in the model is capable of reproducing the target wave condition (Figures 4.2 and 4.3, top panel). Small changes during the propagation along the flume are observed. In general, wave crests are underestimated, suggesting some non-linearity is missed in the model.

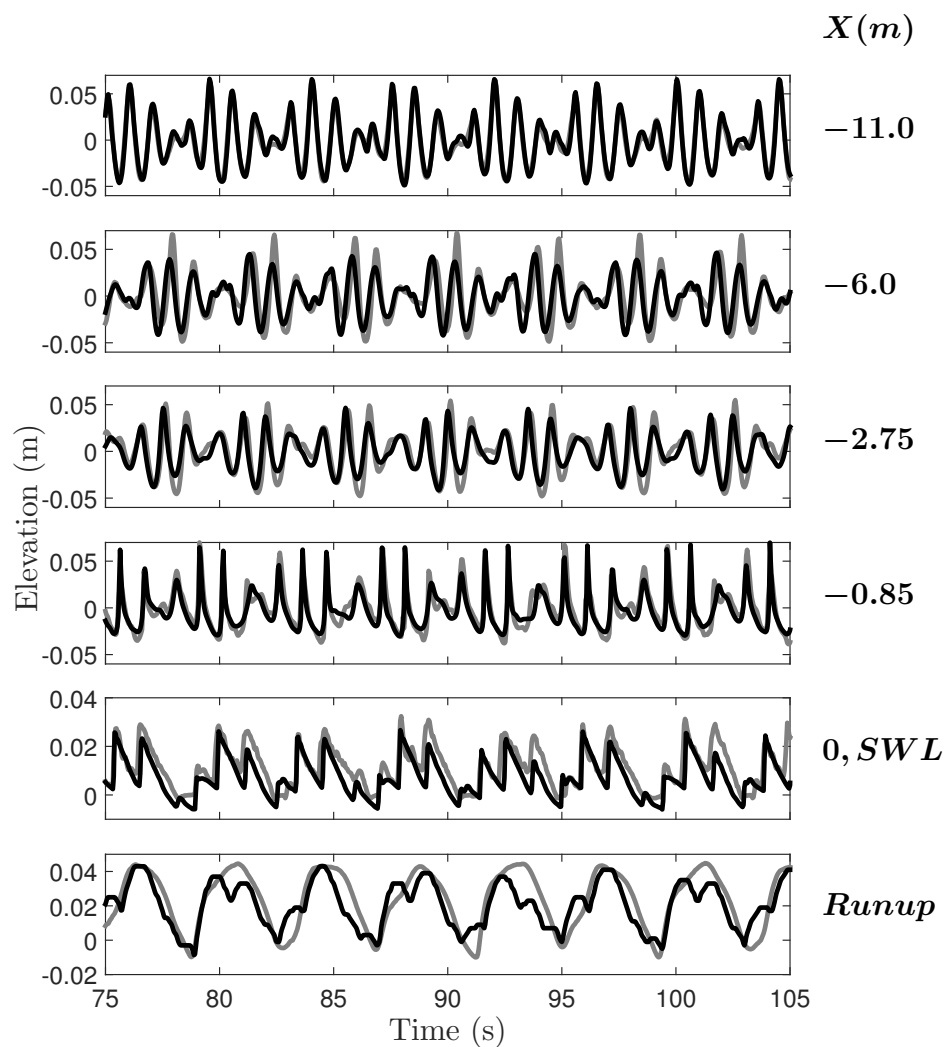


FIGURE 4.2: Time series of surface elevation at different cross-shore locations, case B1025A. Top to bottom, cross-shore distance from the shoreline: -11 m, -6 m, -2.75 m, -0.85 m, at the still water line (SWL) and vertical shoreline excursion. Black line: predicted, grey line: data.

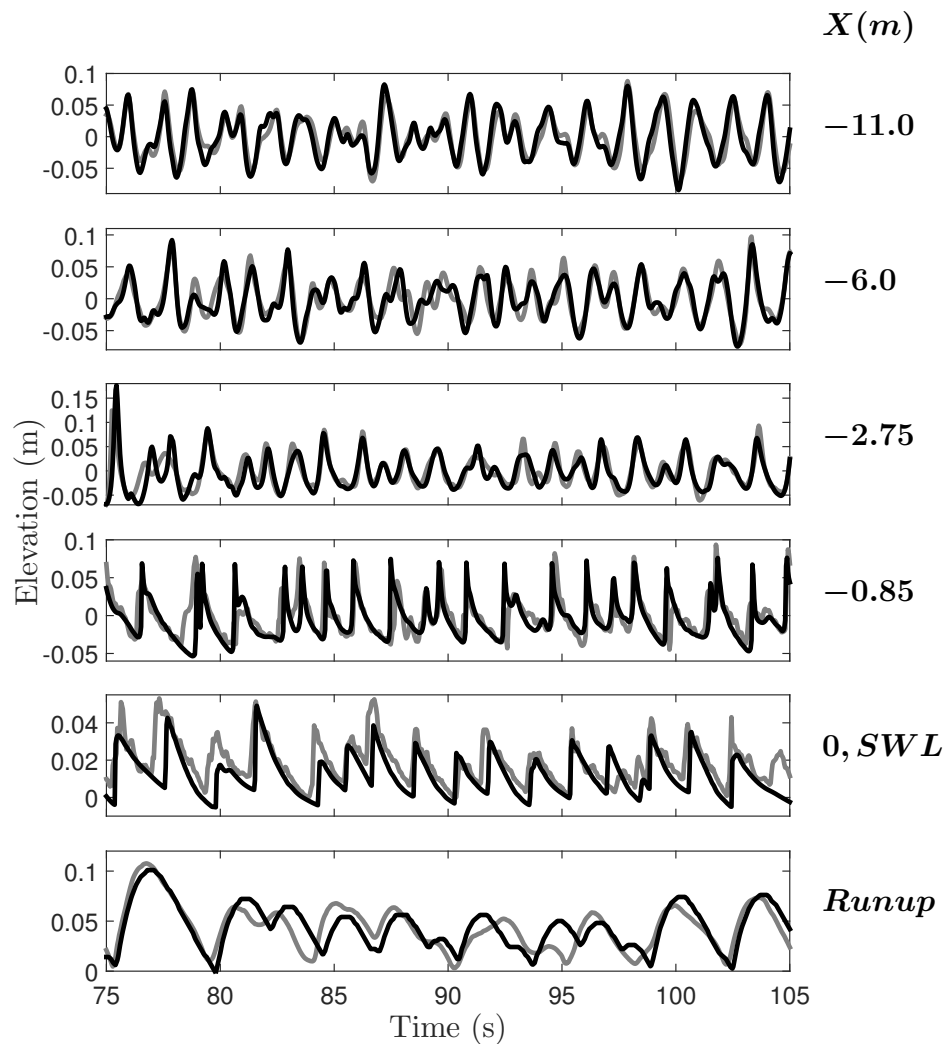


FIGURE 4.3: Time series of surface elevation at different cross-shore locations, case J6010A. Top to bottom, cross-shore distance from the shoreline: -11 m, -6 m, -2.75 m, -0.85 m, at the SWL and vertical shoreline excursion. Black: predicted, gray: data.

Figure 4.4 shows the comparison between measured and simulated wave heights ( $Hm0$ ) presented in terms of  $Hm0_{error}$ , defined as the difference between measured and simulated  $Hm0$  normalized by the measured  $Hm0$ . The results shows the model's capability of reproducing short wave propagation and dissipation due to breaking within a reasonable accuracy. On the flat bottom ( $h = 0.8\text{m}$ ) and on the deeper part of the slope ( $h > 0.6\text{m}$ ) the wave height difference is less than  $\pm 5\%$ . In the shoaling zone wave heights are usually underpredicted and the error is larger for cases with higher mean frequency. For instance, for the random cases

J1033C and J1033C the shoaling rates are strongly underpredicted ( $Hm0_{error}$  of approximately  $-13\%$  at  $h = 0.16\text{m}$ ). For cases with  $f_p = 0.6\text{Hz}$ ,  $Hm0_{error}$  is smaller than  $4\%$  through the entire shoaling region. FUNWAVE is only a weakly dispersive model, hence the more dispersive the waves, the less accurate is the model. In the inner surf zone wave heights are consistently overestimated, this overprediction reduces towards the swash zone, suggesting wave dissipation is not perfectly captured by the breaking scheme. As discussed below, the errors in the  $Hm0$  reflect on the infragravity waves (Figure 4.6) and in the mean water level (Figure 3.27), but the results are still in good agreement with the measured data.

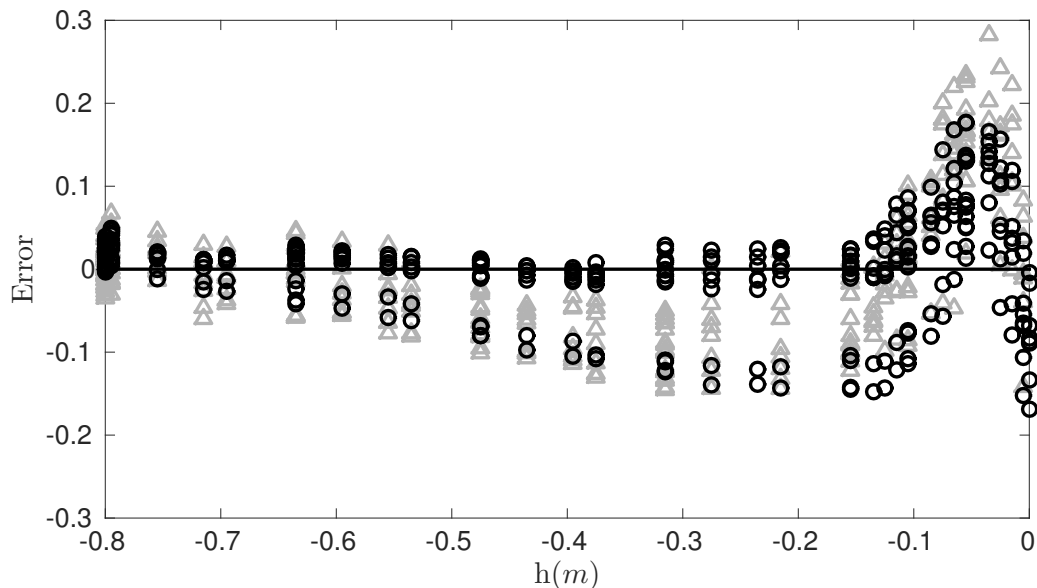


FIGURE 4.4: Predicted  $Hm0_{error}$ .  $\triangle$ — bichromatic cases;  $\circ$ — random cases.

Validation of run-up and shoreline motion in Boussinesq-type models is most widely assessed for solitary waves, for instance to represent inundation generated by tsunami or storm surge waves (Fuhrman and Madsen, 2009, Lynett et al., 2010, Madsen and Fuhrman, 2008, Tehranirad et al., 2011). The evaluation of the accuracy of the predicted moving boundary is not commonly assessed in wind-wave type of simulations. However, as part of this work includes the investigation of the

relationship between the breakpoint and shoreline excursions and the infragravity wave dynamics, it is important to verify the model's capability at the moving boundary at these frequencies, and for interacting swash events.

Results show that FUNWAVE reproduces, with reasonable accuracy, the time evolution of the run-up (Figures 4.2 and 4.3, bottom panels). Generally, for the bichromatic wave groups the phase of the infragravity oscillations are better simulated than for the random cases. However, the overall amplitude for the random cases are in better agreement with the data, for both short and infragravity waves (Figure 4.5). The comparison between measured and calculated  $Rm0 = 4\sqrt{m0}$  ( $m0$  is the variance of the run-up oscillation), shows that the short wave run-up is, for most cases, over predicted. Due to the weak dissipation of the short waves in the inner surf zone, larger short waves will reach the shore line contributing for the over predicted run-up at the primary frequencies. For some of the bichromatic cases,  $Rm0$  is overpredicted by more than 20%. Better agreement is found at the infragravity frequencies.

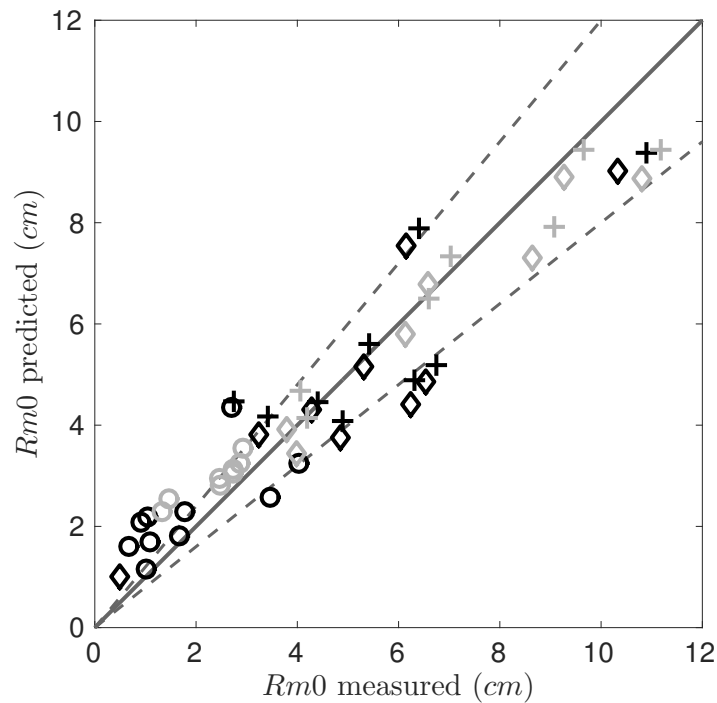


FIGURE 4.5: Run-up height  $Rm0$ , measured versus predicted. +: Total ;  $\circ$ : Primary frequencies;  $\diamond$ : Infragravity frequencies; black: bichromatic wave group cases; grey: random wave cases. Dashed line represents  $\pm 20\%$  error and solid line is perfect agreement.

The infragravity wave height ( $Hm0_{IG}$ ) along the flume is reasonably well predicted (Figure 4.6). For the high frequency cases  $J1033C$  and  $J1010C$ , in the shoaling zone, the infragravity waves are constantly underestimated, which is a consequence of the underpredicted short wave shoaling. But despite that, the spatial amplitude oscillations are well reproduced. For the low frequency cases, better agreement is found for the ones with smaller short waves. For instance, the nodal structures measured for cases  $J6010A$  and  $J6033A$  in shallow water are not reproduced well numerically, but are well captured in case  $J6010C$ . The errors in the predicted set-up (Figure 4.7) and run-up may affect significantly the superposition of incident and reflected infragravity waves. This analysis is left for future research.

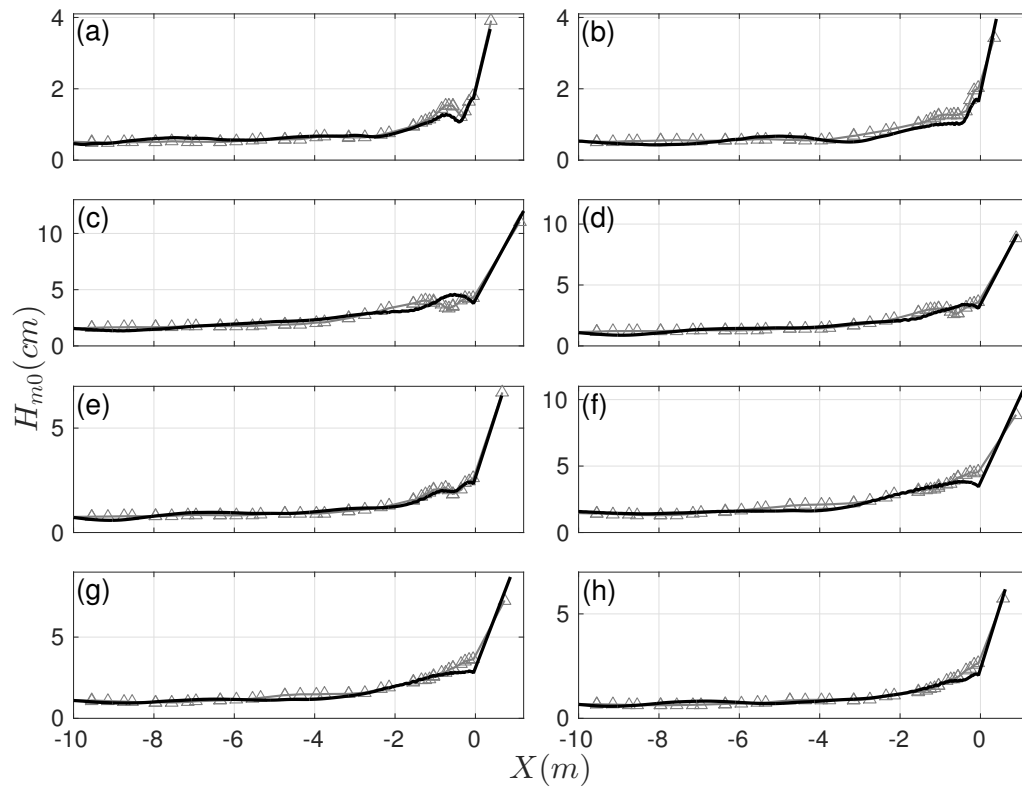


FIGURE 4.6:  $H_{m0_{IG}}$  and  $R_{m0_{IG}}$  for the random cases. (a) J1010C, (b) J1033C, (c) J6010A, (d) J6010B, (e) J6010C, (f) J6033A, (g) J6033B and (h) J6033C. Measured (grey) and simulated (black). The most shoreward data point is the shoreline oscillation.

Even though outside the surf zone the nodal structures differ slightly, in the region of main interest here (surf and swash zone), the infragravity wave propagation patterns are in excellent concordance (Figure 4.7). As mentioned above, the errors in the predicted mean set-up are likely to be generated by the weak dissipation during short wave breaking.

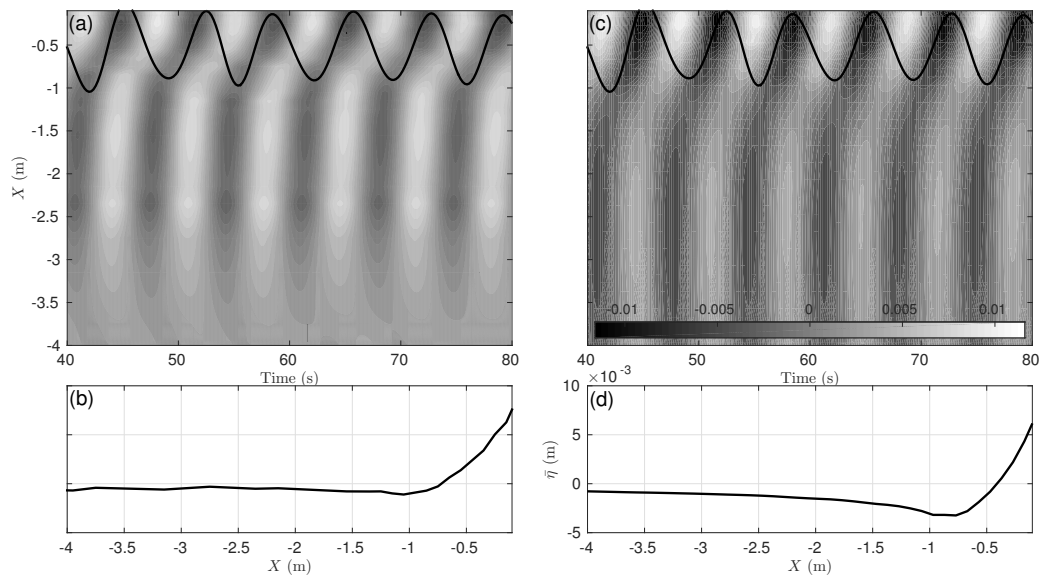


FIGURE 4.7: Space-time evolution of infragravity surface elevation (top) and mean setup (bottom). Laboratory data (a) and (b), numerical results (c) and (d). Bichromatic wave case B1020A. Black line is the simulated breakpoint excursion. Colormap in meters.

In Section 3.7 it was shown that some of the bichromatic cases have a considerable amount of energy at the repeat frequency ( $f_R$ ), which may become the dominant frequency in the inner swash zone (Figure 3.26). This signal is well marked in case B1060A (Figure 3.27). The data shows that, at  $f_R$ , the amplitudes are large inside the surf zone and weak outside the surf zone. Further analysis on the behavior of the surf zone oscillation showed a synchronization between both the breakpoint oscillation and infragravity waves. This, plus the lack of incident propagation patterns outside the surf zone, suggested that those waves were generated by breakpoint forcing. Numerically, similar patterns are observed at all frequencies, however there is more energy both inside and outside the surf zone at the repeat frequency (Figure 4.8). For comparison, both Figures 3.27 and 4.8 are plotted with the same colormap scale.

The similarities between these waves and those generated by the breakpoint forcing mechanism are further investigated below.



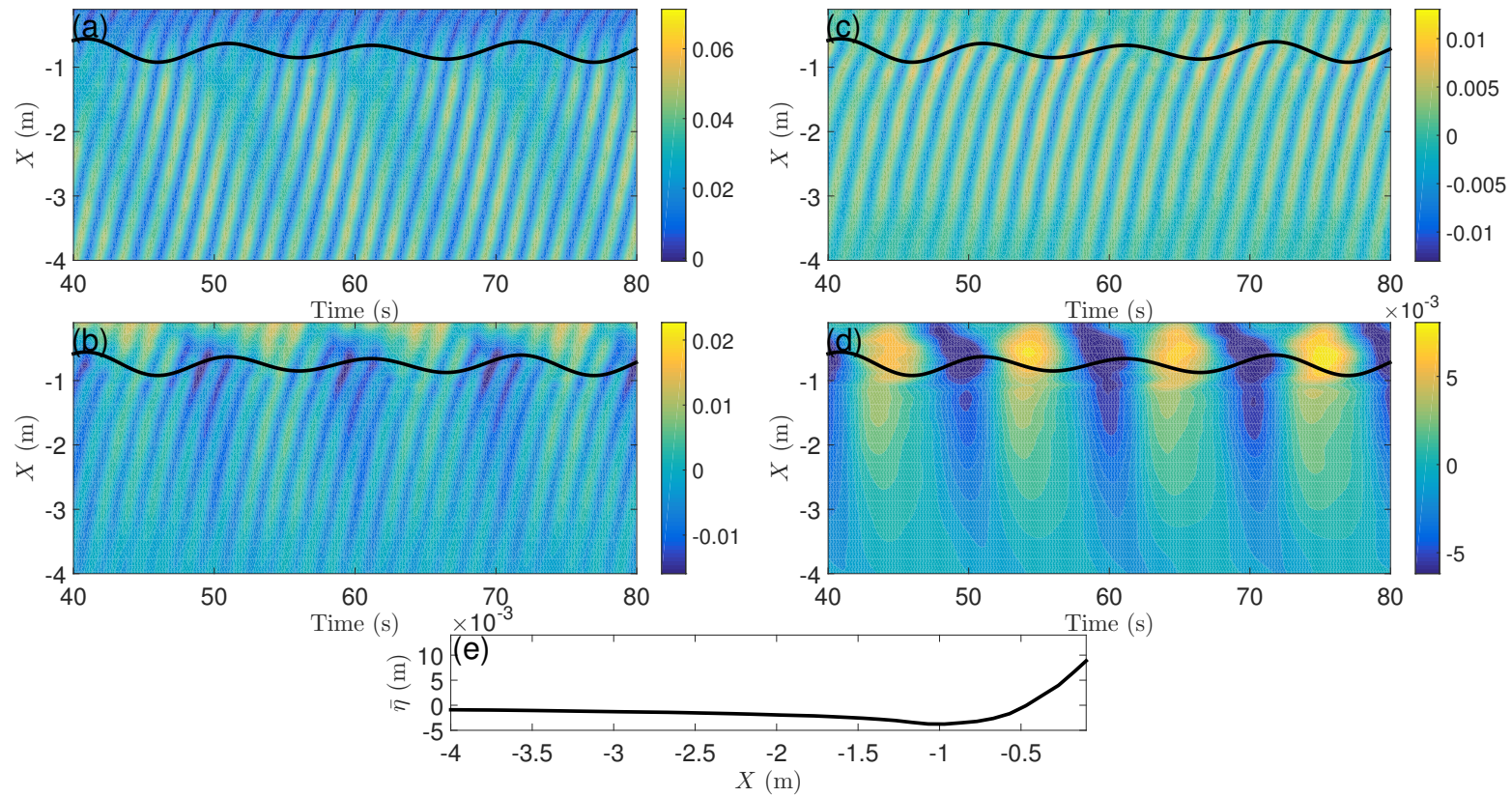


FIGURE 4.8: Numerical results of (a) space-time evolution of wave envelope amplitude, (b) total infragravity surface elevation (including mean setup), (c) surface elevation at the group frequency (without mean setup), (d) low-pass filtered surface elevation at and below  $f_R$  (without mean setup) and (e) mean setup. Black line is the low-pass filtered breakpoint position. Bichromatic wave case B1060A.

The transient case predictions are also in good overall agreement with data (Figure 4.9), however, similar to the previous cases, the long wave amplitude is underestimated. Minor phase discrepancy between the measured and simulated long wave is observed in very shallow water ( $h = 0.06\text{m}$ ).

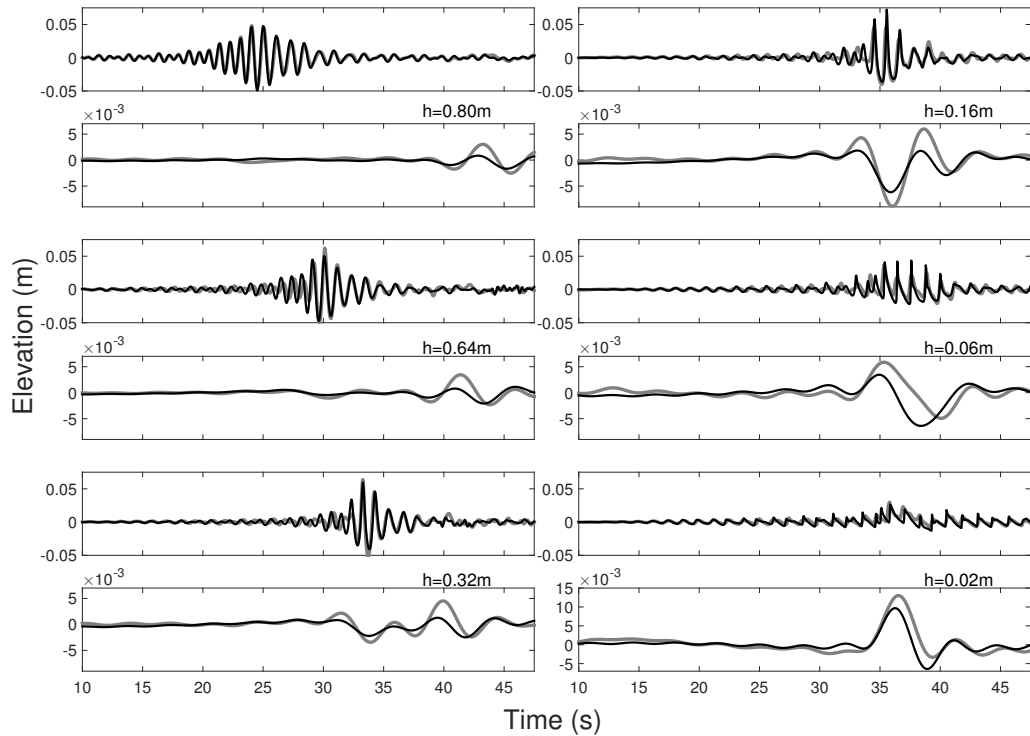


FIGURE 4.9: Total and low-pass filtered surface elevation at different locations. Grey- measured, black - simulated. Transient case G08A.

Even though the measured and simulated short wave envelope are in excellent agreement (Figure 4.10), the long wave is still underpredicted, indicating that the nonlinear energy transfer in the model is weaker than the observed. The spatial visualization of the wave envelope and the long wave in Figure 4.10, shows that for both model and data the negative part of the infragravity wave is constantly in anti-phase with the wave envelope, which may indicate that the total long wave signal is a forced wave, and the positive leading pulse is generated due to the stronger response of the surface elevation to the radiation stress forcing in shallower waters.

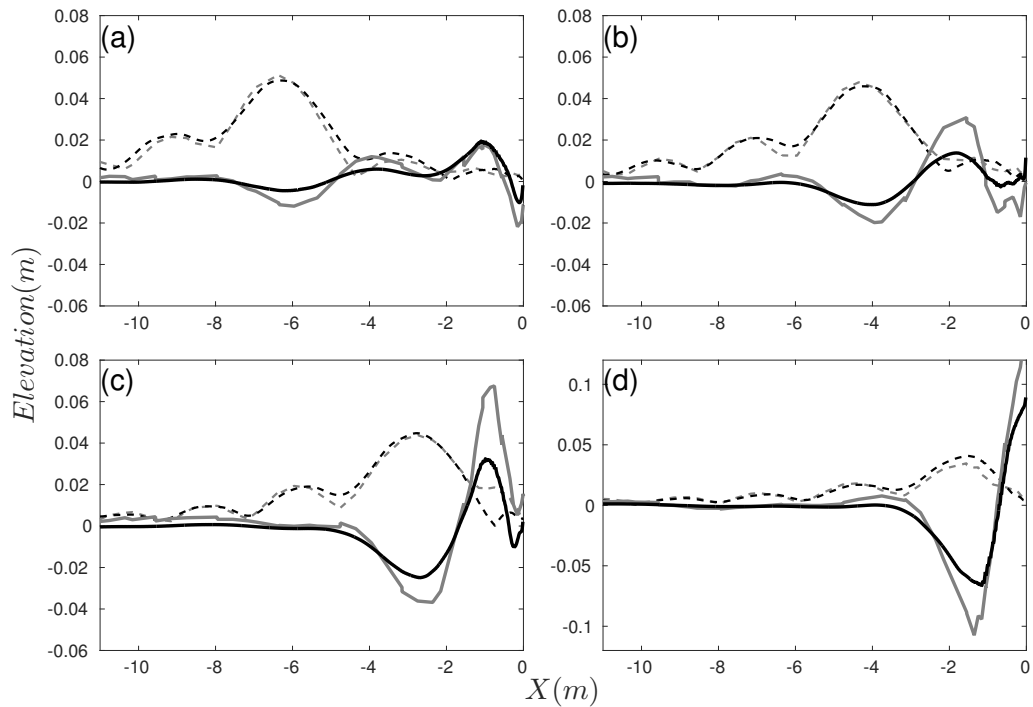


FIGURE 4.10: Spatial evolution of wave group envelope (dashed) and long wave (solid) at different instants (from *a* to *d*). Grey - measured, black - simulated.

### 4.3 Numerical Simplification of Infragravity Wave Dynamics

One of the main difficulties in understanding the infragravity wave dynamics is the complexity of the processes involved. The lack of analytical solutions for more complex situations makes the use of phase-resolved numerical models an important tool, allowing a more versatile approach to the problem. Different numerical models have been used to investigate the individual generation mechanisms of surf beat (List, 1992, Madsen et al., 1997, Pomeroy et al., 2012).

Here, the bound wave and breakpoint forcing mechanisms were implemented in FUNWAVE by adding the radiation stress forcing, respective to each mechanism, to the momentum equation 4.2. The bound waves are forced by the horizontal gradients of the radiation stress generated by the amplitude modulated short waves.

Similar approach is used in List (1992), Pomeroy et al. (2012) and Reniers et al. (2004). This method allows evaluation of the transient behavior of bound wave shoaling without simulating the short waves, so changes in the wave envelope during shoaling and short wave breaking are removed. For the breakpoint mechanism, initially, the first forcing harmonic of the breakpoint excursion (equations 2.18 and 2.2) was implemented in the model. Later, the step function proposed by Symonds et al. (1982) (see also Section 2.2) was also implemented to investigate random wave scenarios.

One of the main advantages of using these methods is the control over the forcing behavior, allowing a variety of specific conditions to be simulated. Initially, the results obtained from both methods were respectively compared to the analytical solution proposed by Nielsen and Baldock (2010) and Symonds et al. (1982).

## 4.4 Long Waves Generated by Radiation Stress Forcing

Following Nielsen and Baldock (2010) a Gaussian-shaped moving forcing was generated by the following expression:

$$F_{S_{xx}} = A \exp\left(\frac{x_i - x}{L_{scale}}\right)^2 \quad (4.5)$$

where  $A$  is the amplitude,  $x$  is the discretized spatial domain,  $L_{scale}$  sets the length scale, which can be associated with the wave group length ( $L_g$ ).  $x_i$  is the the central position of the forcing, updated every time step according to its propagation speed. To represent the evolution of short wave groups, the group velocity ( $c_g$ , equation 4.6) is used to control  $F_{S_{xx}}$  speed. Ultimately, the propagation pattern is defined by the short wave period  $T$  and local wave number  $k$ .

$$c_g = \frac{1}{2} \frac{gT}{2\pi} \tanh kh \left(1 + \frac{2kh}{\sinh 2kh}\right) \quad (4.6)$$

### 4.4.1 Analytical Benchmark - Horizontal Bottom Tests

By controlling the forcing speed over the horizontal bottom, the results for non-resonant and resonant conditions were tested against the Nielsen and Baldock (2010) solutions (equations 2.11, 2.12 and 2.14).

#### 4.4.1.1 Non Resonant / Resonant Condition Flat Bottom

The numerical results are in perfect agreement with the analytical solution, considering only the non-linear terms (no dispersion). For  $F_{S_{xx}}$  traveling at  $0.5\sqrt{gh}$ , the free wave amplitudes ( $A_{free-}, A_{free+}$ ) are respectively  $-0.25A_{forced}$  and  $-0.75A_{forced}$ , where  $A_{forced}$  is the amplitude of the forced wave, which in this case is steady. By including dispersive terms a similar result is obtained, but small changes to the shape of the free waves and the development of small tails was observed (Figure 4.11).

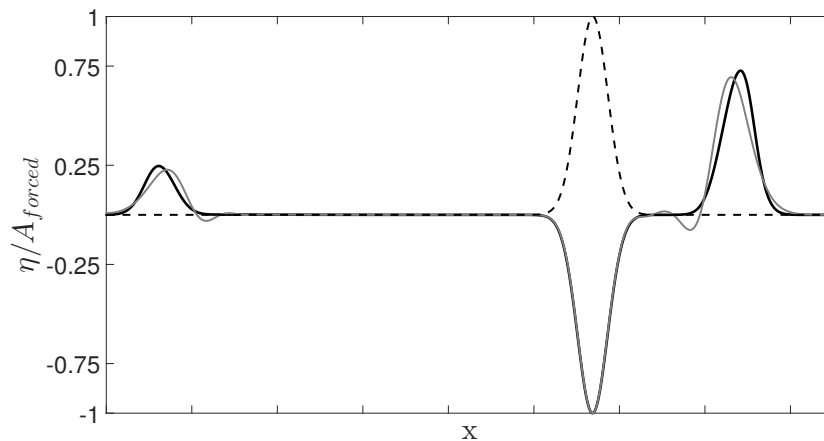


FIGURE 4.11: Surface elevation normalized by initial forced wave amplitude, non-resonant condition. Dashed line -  $F_{S_{xx}}$  normalized by its maximum amplitude, Black line - non-linear terms only, grey line - dispersive terms included.

For the resonant condition ( $c_g = \sqrt{gh}$ ) the result is a  $\mathcal{N}$ -shaped wave (Figure 4.12) emerging from the summation of the forced and the forward free wave, as demonstrated by Nielsen and Baldock (2010), with the amplitude increasing linearly in time (Figures 4.12 and 4.13). The resonant condition also induces a strong phase

change between the bound wave and the forcing. Note that, the phase difference between the short wave envelope and bound wave, according to the steady solution, is  $\Delta\phi = \pi$ . On the other hand, the lag generated by the resonant condition depends on the shape of the forcing, for instance, the lag expected for a sinusoidal wave group is  $\Delta\phi = -\pi/4$ . This very distinct relation between forcing and long wave can help to identify the generation mechanism. The resonant behavior can perhaps explain the large lags observed by Battjes et al. (2004) or the N-shaped cross-correlation observed by List (1992). However, as shown above, the transient wave group does not exhibit this behavior, with the forced wave in antiphase (lag of  $\pi$ ) with the forcing.

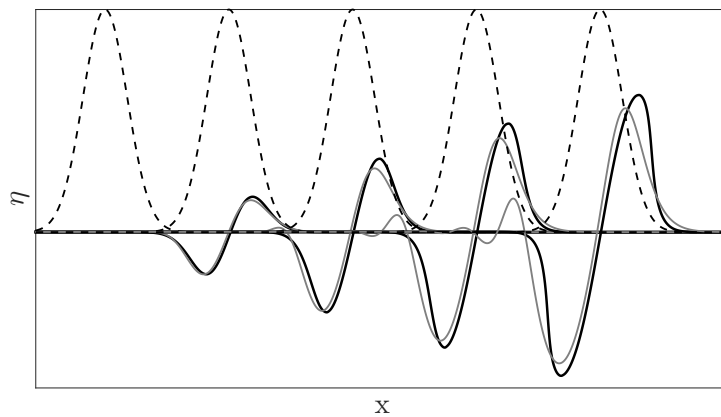


FIGURE 4.12: Surface elevation normalized by initial forced wave amplitude, resonant condition. Dashed line -  $F_{Sxx}$  normalized by its maximum amplitude, black line - non-linear terms only, gray line - dispersive terms included.

On natural beaches, waves propagate from deep (non-resonant region) to shallow water, and during the shoaling process, the resonant condition can be reached, for specific cases. As shown above, the non-resonant and resonant patterns are very distinct, hence they may assist the identification of infragravity wave processes. In order to do so, it is important to test how fast the infragravity wave shape adapts from a non-resonant to a resonant condition. This can be determined by calculating the lag between the bound wave and the forcing. For the purpose of comparing analytical and numerical results, the lags are calculated based on the spatial relationship between the forcing and the surface elevation, using the maximum amplitude of the Gaussian forcing as the reference position. Thus, the

lags are calculated at each time step and the values are plotted at the respective position  $x$  of the Gaussian peak.

The numerical tests were performed for a forcing propagating over a horizontal bottom with initial speed  $c < \sqrt{gh}$ . At a defined location ( $x/Lg = 0$  in Figure 4.13), where the initially generated free waves had propagated away from the forced wave (see schematic representation in Figure 4.14), the speed of the forcing starts to change asymptotically to  $\sqrt{gh}$ . The resonant condition is reached when the center of the Gaussian forcing is at  $x/Lg = 0.1$ . The results in Figure 4.13 show that as soon as  $c = \sqrt{gh}$  the amplitude starts to increase linearly in time, and the lag increases very quickly toward the expected resonant condition. Within a length of  $Lg$ , approximately 80% of the expected lag is reached. However, it takes much longer (forcing length  $7Lg$ ) to get the full resonant lag.

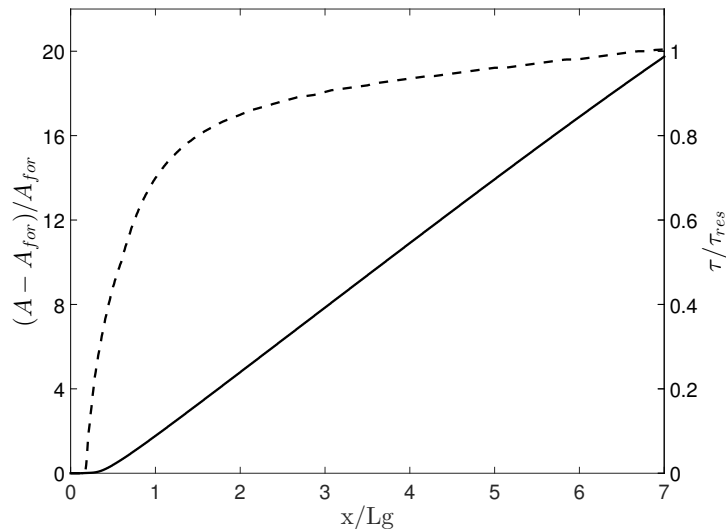


FIGURE 4.13: Spatial evolution of wave amplitude and lags for a forcing switched to resonant condition at  $x/Lg = 0.1$ . The cross-shore distance is normalized by the length of the forcing. Full line - long wave amplitude normalized by the initial forced wave amplitude. Dashed line, lag normalized by the expected full resonant lag.

From these result two observations, relevant to the infragravity wave topic, are highlighted: one is the fact that the linear growth starts before the shape of the bound wave has adjusted to its resonant shape. Secondly, the length/time it takes for the bound wave to reach the expected resonant shape is much longer

than the region/time of the shoaling process (on a natural beach) where resonance can occur. Even though the theory clearly shows that non-resonant and resonant behavior have distinct patterns, using this feature to distinguish the two different regimes may not be applicable under more realistic conditions. For that reason, it is suggested here that the large lags observed by Battjes et al. (2004) may not be justified by the resonant behavior. On the opposite, it may explain the large lags in the simulations performed by Lara et al. (2010), where the transient wave group propagates over a long and shallow horizontal bottom (see their Figure 13).

#### 4.4.2 Propagation Over Sloping Bottoms

To initially test the long wave shoaling over sloping bottoms, simulations were performed considering  $F_{S_{xx}}$  with the same  $L_g$  but different period  $T$  (traveling with different  $c_g$ ) and different bottom slopes. The analysis was focused on the evolution of forced waves, generated in the horizontal bottom, over sloping bottoms. Therefore, the horizontal bottom is set long enough for the initial free wave to propagate away from the forced wave as in Figure 4.14. Also, a shallower horizontal shelf after the shoaling zone is added, mainly to prevent reflection interference.



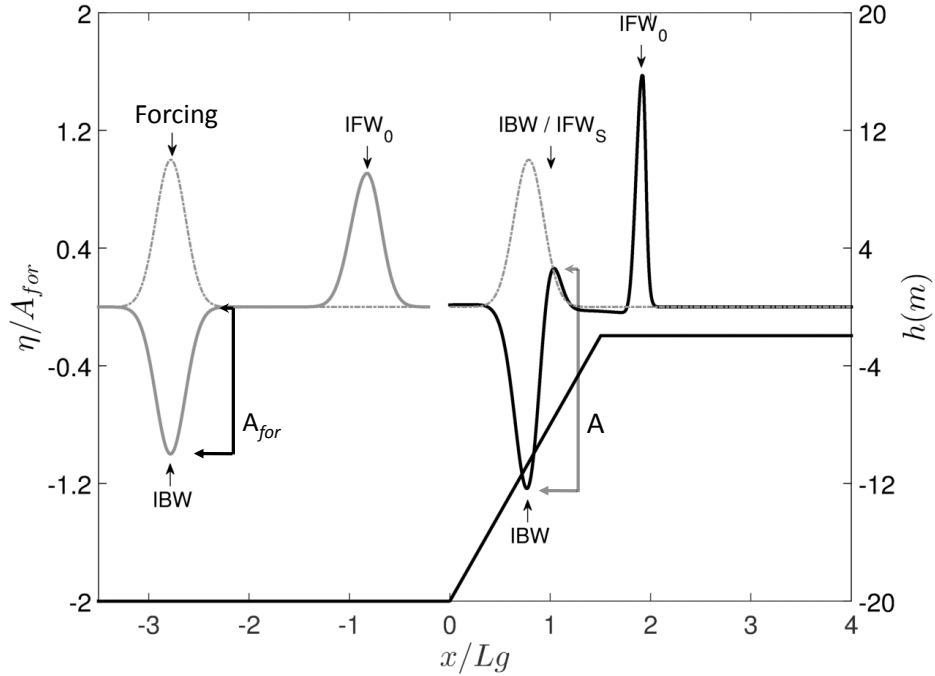


FIGURE 4.14: Schematic representation of the performed simulations. *IBW* is the incident bound wave, *IFW*<sub>0</sub> is the forward free wave generated to balance the initial condition, and it propagates away from the *IBW* over the horizontal bottom. *IBW/IFW* is the positive part of the bound wave generated during the shoaling process. Dotted-dashed line is the representation of the forcing.  $A_{for}$  is the amplitude of the forced wave on the horizontal bottom and  $A$  is the total bound wave amplitude in the shoaling zone.

The results presented in Figures 4.15 ( $\beta = 0.025$ ) and 4.16 ( $\beta = 0.01$ ) show the amplitude ( $A$ , defined according to Figure 4.14) of the long wave starting from the toe of the slope ( $x/L_g = 0$ ) for two different group velocities, one representing  $T = 15$ s (full black line) and another representing  $T = 6$ s (full gray line). As expected from the steady solution (equation 2.12) higher wave amplitudes are observed for cases with the forcing traveling with larger velocities ( $T = 15$ s). On each slope, the shoaling rates are very similar for each case, as the shoaling rate is governed by the slope and group frequency or the normalized beach slope (equation 3.11). For the steep slope, the shoaling is weak ( $\sim h^{-1/4}$ ), while, in the mild slope cases the shoaling is closer to the steady solution ( $\sim h^{-5/2}$ ), (Battjes et al., 2004, Schäffer, 1993).

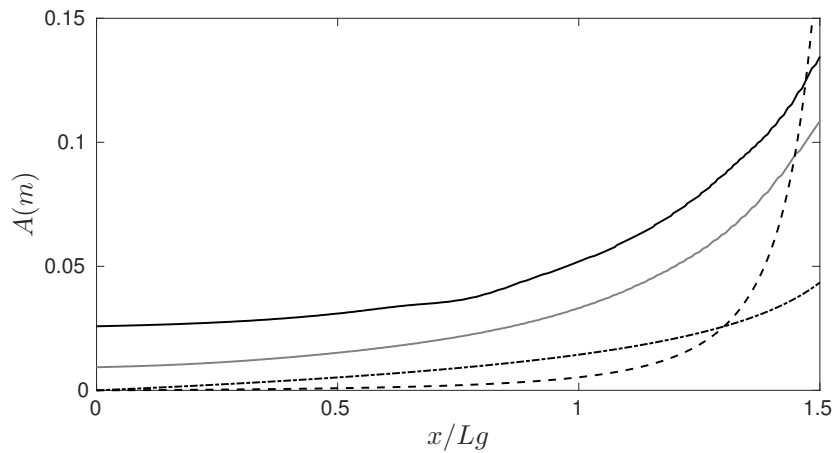


FIGURE 4.15: Long wave amplitude (solid lines) propagating over a slope ( $\beta = 0.05$ ). The forcing speed is defined by equation 4.6,  $T = 6$ s (gray) and  $T = 15$ s (black). Dashed line ( $\sim h^{-5/2}$ ), Dashed-dotted line ( $\sim h^{-1/4}$ ).

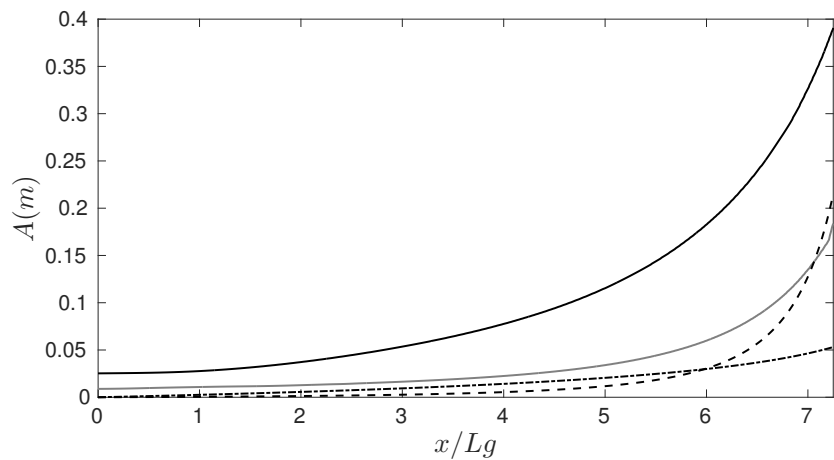


FIGURE 4.16: Long wave amplitude (solid lines) propagating over a slope ( $\beta = 0.01$ ). The forcing speed is defined by equation 4.6,  $T = 6$ s (gray) and  $T = 15$ s (black). Dashed line ( $\sim h^{-5/2}$ ), Dashed-dotted line ( $\sim h^{-1/4}$ ).

### 4.4.3 Transient Wave Group

Here the transient case (table 4.3) is used to test the radiation stress forcing approach. The spatial and time evolution of the simulated short wave envelope is extracted (Figure 4.10) and used as the boundary condition in the forcing-only simulation. Results for the surface elevation along the wave flume for different

instants are shown in Figure (4.17), both the infragravity shape and shoaling are reasonably well mimicked by the simplified approach.

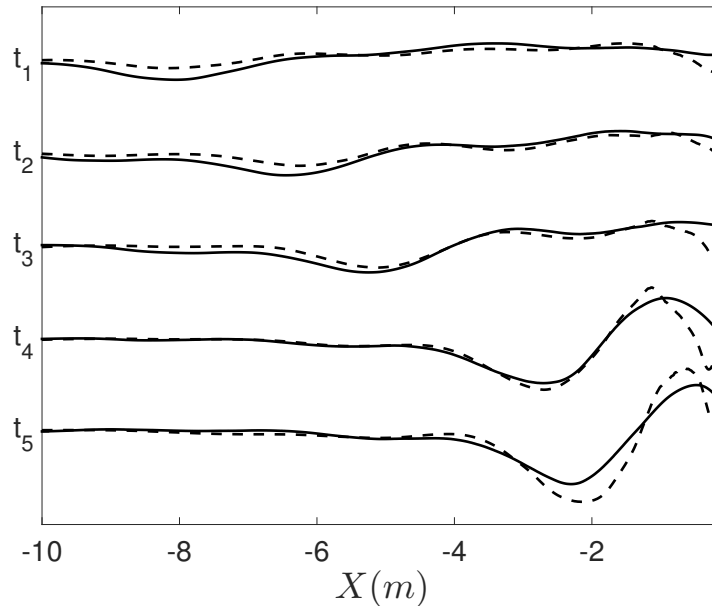


FIGURE 4.17: Low-frequency surface elevation at different time instants. Dashed line - full simulation, black line - radiation stress forcing only.

## 4.5 Breakpoint Forcing in FUNWAVE

The breakpoint forcing function proposed by Symonds et al. (1982) was implemented in FUNWAVE and was tested by checking the interference behavior between the waves radiated from the breaking zone (Section 2.2), which depends on the normalized surf zone width  $\chi = (\sigma^2 X / g \tan \beta)$ , where  $\sigma$  is the wave group frequency,  $X$  is the mean breakpoint position and  $\beta$  the bottom slope. According to Symonds et al. (1982) the amplitude of the outgoing wave outside the surf zone is maximum for  $\chi \approx 1.2$  and minimum for  $\chi \approx 3.6$ . Inside the surf zone the combination of incident and reflected breakpoint forced long waves generate a standing wave pattern, while outside the surf zone, only progressive outgoing waves are present.

The results confirm that the breakpoint mechanism was implemented correctly. Figures 4.18 and 4.19 show the surface elevation for conditions close to the two extremes discussed. While inside the surf zone, for both cases, the standing wave pattern is present, outside the surf zone, due to phase combination, the progressive outgoing wave is large for  $\chi = 1.1$  and almost negligible for  $\chi = 3.65$ .

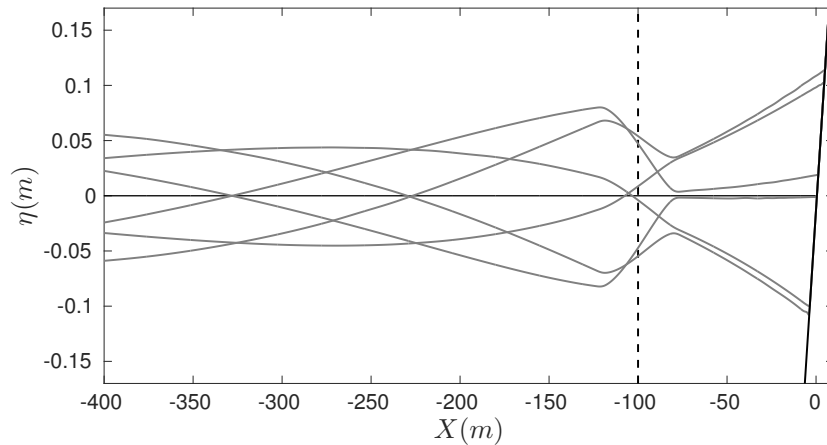


FIGURE 4.18: Surface elevation at different time instants, constructive interference. Dashed line - mean breakpoint position,  $\Delta a = 0.26$  and  $\chi = 1.1$ .

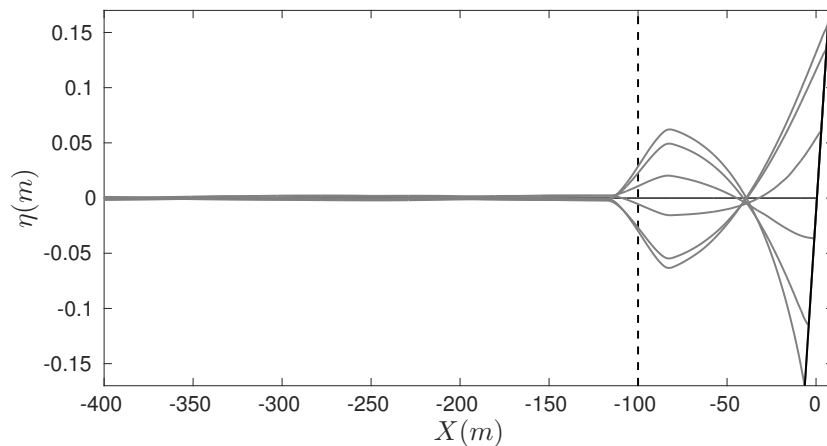


FIGURE 4.19: Surface elevation at different time instants, destructive interference. Dashed line - mean breakpoint position,  $\Delta a = 0.21$  and  $\chi = 3.65$ .

The outgoing wave dependence on  $\chi$  was further tested in the model. A series of 50 different simulations were carried out, using the mean breakpoint at fixed location ( $X = -100\text{m}$ ) and the following randomly selected variables: frequencies

within the infragravity band ( $0.04 < f < 0.004$ ); breakpoint modulation (in a range of  $0.1 < \Delta a < 0.3$ ) restricting the cases to weakly modulated conditions; initial phases ( $0$  to  $2\pi$ ). For each simulation, the wave amplitude measured at  $X = -200\text{m}$  was normalized by the wave amplitude close to the shoreline at  $X = -15\text{m}$  and plotted against  $\chi$  as in Figure (4.20). The interference pattern is in good agreement with Symonds et al. (1982).

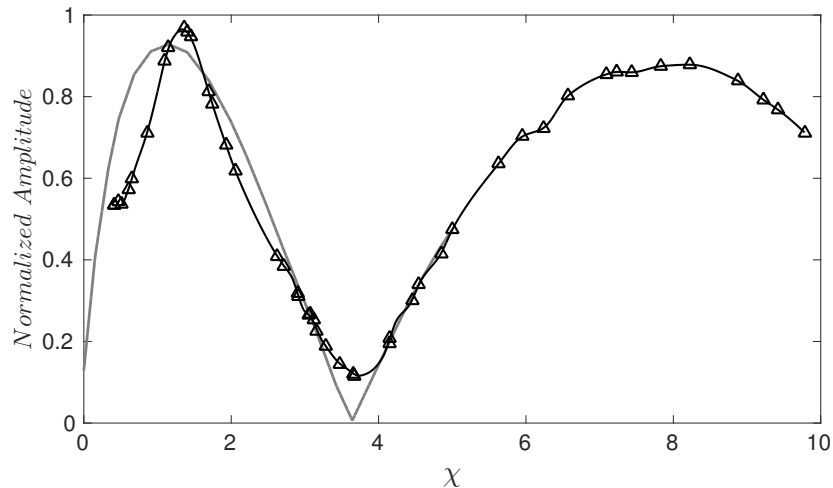


FIGURE 4.20: Wave amplitude outside the surf zone ( $X = -200\text{m}$ ) normalized by the wave amplitude close to the shoreline ( $X = -15\text{m}$ ). Grey line is the analytical solution for  $\Delta a = 0.2$  (Symonds et al., 1982). Mean breakpoint at  $X = -100\text{m}$

In order to use cross-correlation analysis to identify the main generation mechanism of infragravity waves in the surf zone it is important to establish whether the observed results are related to standing or progressive wave patterns.

In Section 3.2.1 the cross-correlation analysis of standing waves generated by incident and reflected linear waves were discussed. Considering only one frequency, the cross-correlation result displayed the expected standing wave pattern (Figure 3.4). However, for a summation of standing waves with different frequencies the cross-correlation analysis showed the propagation patterns of the incident and reflected waves (Figure 3.5).

Similarly, by applying the same analysis for the breakpoint forced simulations, standing waves (only inside the surf zone) are observed for a single frequency case.

This is demonstrated in Figure 4.21 that shows the space-time evolution of the surface elevation, the white line represents the breakpoint excursion. As expected, the result is a pure standing wave inside the surf zone, and an outgoing progressive wave outside the surf zone. By cross-correlating the breakpoint with the surface elevation at different locations, the same patterns are captured.

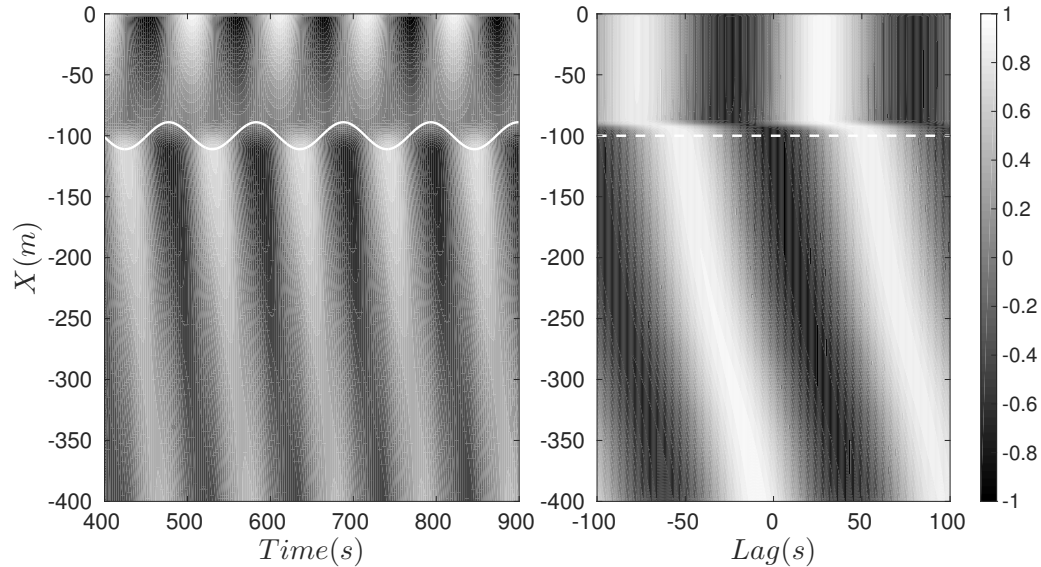


FIGURE 4.21: Left: Space-time evolution of the surface elevation generated by breakpoint forcing at a single frequency, white line is the breakpoint excursion. Right: Cross-correlation between time evolution of the breakpoint excursion and surface elevation. Mean breakpoint  $X = -100$ m (dashed white line), breakpoint modulation amplitude  $\Delta a = 0.14$ ,  $\chi = 1.45$ ,  $f = 0.01$ Hz.

By adding the results of three individual single frequency cases, inside the surf zone, the progressive features of the incident and reflected waves emerge (Figure 4.22). From the cross-correlation analysis between the breakpoint and surface elevation it is possible to identify the incident break point forced long wave, which is  $\pi$  out of phase with the breakpoint excursion, hence behaving as a dynamic set-up.

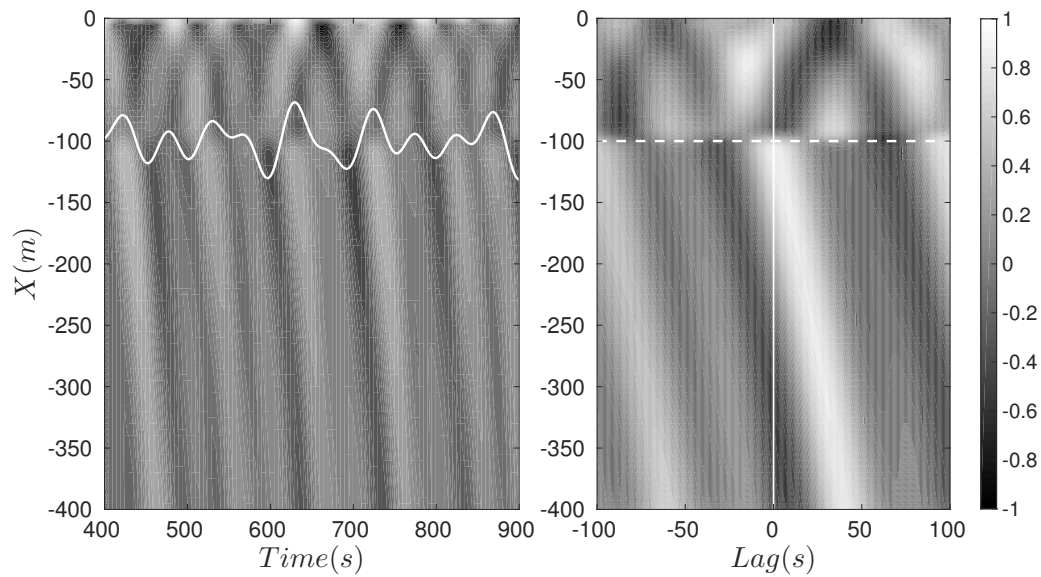


FIGURE 4.22: Left: Space-time evolution of the surface elevation generated by breakpoint forcing, white line is the breakpoint excursion. Right: Cross-correlation between time evolution of the breakpoint excursion and surface elevation. Summation of three individual single frequency cases with mean breakpoint  $X = -100\text{m}$  (dashed white line) and respective breakpoint modulation amplitude ( $\Delta a = 0.11, 0.13$  and  $0.10$ ), normalized surf zone width ( $\chi = 2.6236, 1.45$  and  $6.57$ ) and frequencies ( $f = 0.014, 0.0095$  and  $0.02\text{Hz}$ ).

The surface elevation pattern and its relationship with the surf zone oscillation, in Figure 4.21, resemble what is observed at the repeat frequency, for the bichromatic case B1060A. The similarities between data, full numerical and breakpoint forcing only simulations are highlighted in Figure 4.23. Based on that and in the previous discussion, it possible to infer that the energy measured at the repeat frequency, for this bichromatic case, is a result of the breakpoint forcing mechanism.

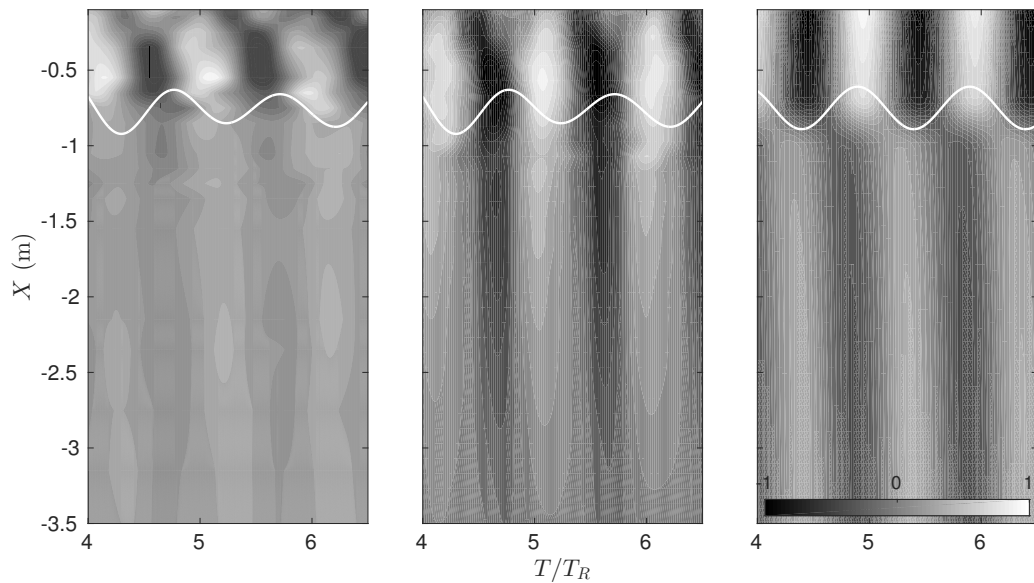


FIGURE 4.23: Space-time surface elevation at  $f_R$  for the bichromatic case B1060A. Left - measured, center - full simulation and right - breakpoint forcing only ( $\chi \approx 0.3$ ). The surface elevation is normalized by its maximum in each plot. White line is the breakpoint excursion

Determining the forcing mechanism based on the approach presented above is only viable for laboratory experiments and numerical simulations. In the field is very difficult to have a refined array of instruments to analyze, in detail, the space-time evolution of infragravity waves. In the next analysis it is shown that with a reduced amount of information (practical for field experiments) it is possible to distinguish forcing mechanism at some individual frequencies.

According to Longuet-Higgins and Stewart (1962) the bound wave has the same shape as the forcing, which is the short wave envelope. Therefore, the bound wave and forcing must have the same frequencies. By comparing the wave envelope and surface elevation spectra it is possible to detect possible frequency mismatches between the two signals. Note that, due to the possible formation of nodal structures, at a particular location, some of the frequencies in the wave group spectrum may not be present in the surface elevation spectrum. On the other hand frequencies that are in the surface elevation spectrum but not in the envelope spectrum, are likely to be generated by other mechanism, for instance,



breakpoint forcing. Furthermore, by adding to the analysis the infragravity information inside the surf zone, it is possible to identify waves at frequencies that have destructive interference outside the surf zone.

This analysis is exemplified for two bichromatic cases (B1045A and B1060A) in Figure 4.24. The results clearly shows that several frequencies in the surface elevation and run-up spectra are in the breakpoint spectrum, but not in the envelope spectrum. As demonstrated before, for case B1060A there is a strong infragravity wave signal at  $f_R$  that is not in the envelope spectrum. Even though the response at  $f_R$  is not significant for case B1045A it is significant at other frequencies, and they are likely to be forced by breakpoint oscillations. Baldock et al. (2000) also observed, in the surface elevation spectrum, harmonics of  $f_g$  and triad combinations. For the first one, it was suggested breakpoint forcing and the second one, near-resonant triad interaction (Freilich and Guza, 1993).

The results presented in Figure 4.24 might suggest an alternative interpretation. For the presented cases, the higher harmonics amplitudes of  $f_g$  are small, however they are present both in the envelope and breakpoint spectrum (the  $2f_g = 1.2\text{Hz}$  for case B1060A and higher harmonics  $3f_g$ , for both cases, are also present, but not shown). Hence, with this analysis is not possible to determine whether these waves are the result of the asymmetry of the wave envelope or forced by the breakpoint. Baldock et al. (2000) found, for these frequencies, a similar  $\chi$ -type interference pattern to the one expected for the breakpoint forcing.

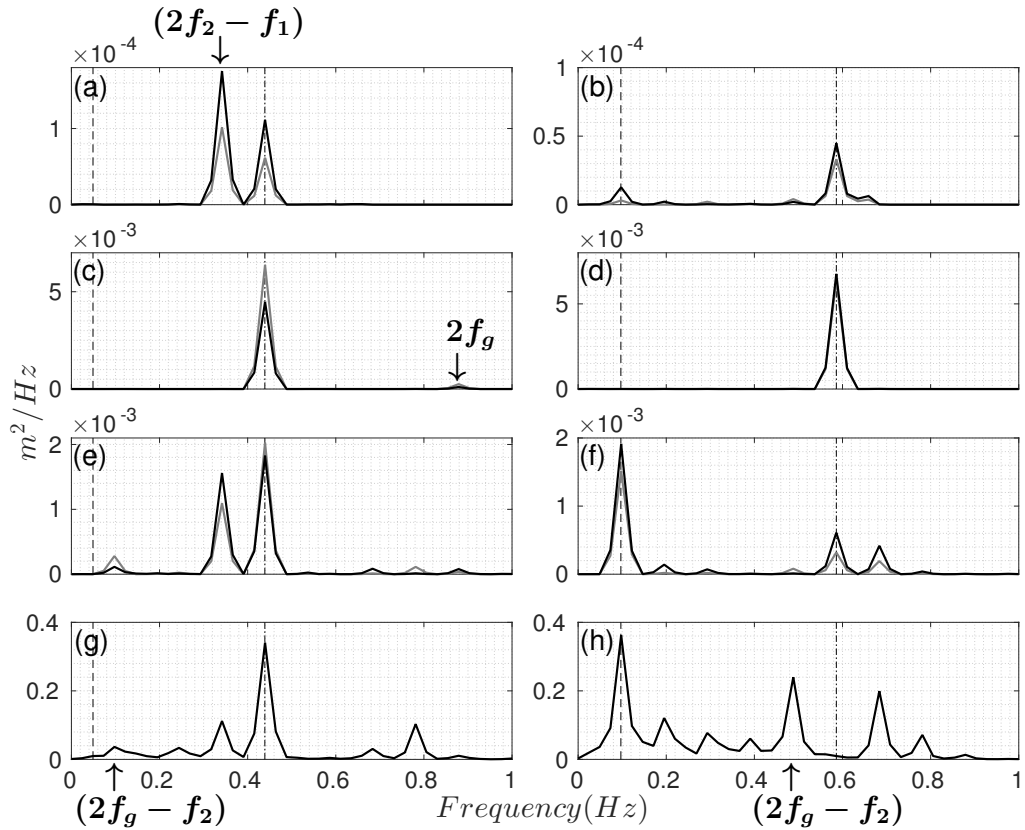


FIGURE 4.24: Spectra of surface elevation at the shoaling zone  $X = -3\text{m}$  (a-b), short wave envelope at  $X = -3\text{m}$  (c-d), run-up (e-f) and breakpoint excursion (g-h). Vertical lines, group frequency (dot-dashed) and repeat frequency (dashed). Bichromatic cases B1045A (left) and B1060A (right). The highlighted triad frequencies are indicated by arrows. Black line numerical results, grey line measured data.

Visible in the breakpoint oscillation spectrum are some of the frequencies that match triad combinations of primary frequencies and their harmonics. This may suggest that these waves that have been previously interpreted as triad interactions are actually forced by the breakpoint. This is probably the case for the frequency  $(2f_2 - f_1, \text{B1045A})$ , and is justified by examining its space-time evolution, shown in Figure 4.25 (laboratory data). Note that while at the group frequency the waves are mainly incident, at  $2f_2 - f_1$  the waves are purely outgoing waves (probably standing waves in the surf zone).

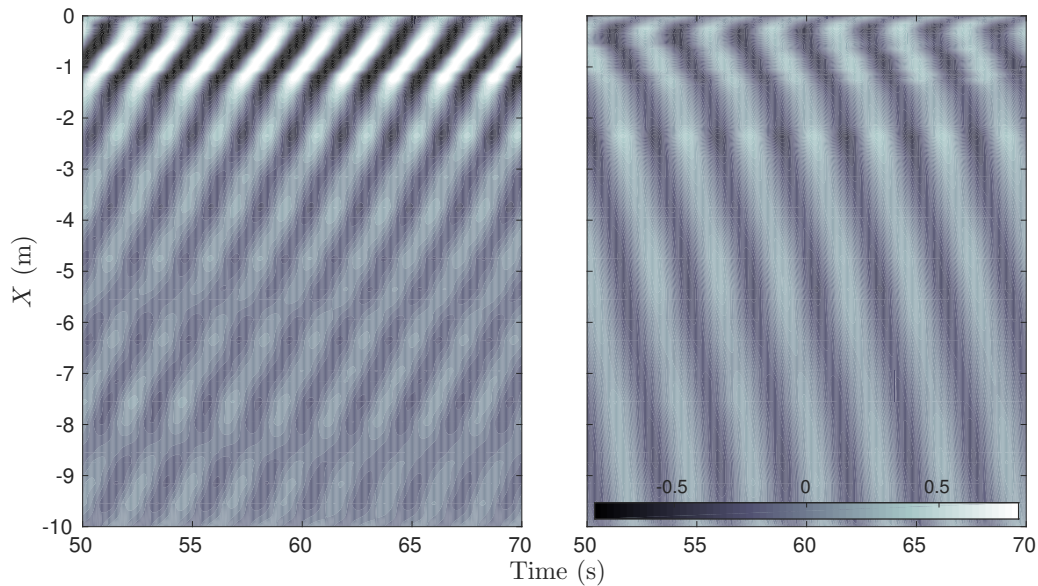


FIGURE 4.25: Space-time evolution of surface elevation at discrete frequencies,  $f_g$  (left) and  $2f_2 - f_1$  (right), bichromatic case B1045A. Colormap in centimeters.

## 4.6 Conclusion

FUNWAVE has been tested against a series of laboratory data including eight bichromatic cases, eight random cases and one transient case. The results show that the model can reasonably represent wave generation, propagation, dissipation and shoreline motion. For the primary waves the shoaling properties are better reproduced for cases with lower frequencies. Short wave run-up is generally overestimated, probably due to the weak dissipation of the short waves during the breaking process, which is likely to influence the mean setup levels. Infragravity waves are also well resolved by the model. Some of the observed discrepancies in the nodal structures may be affected by the errors in the run-up and mean setup. For the transient case the infragravity wave is consistently underestimated. However, the phase and the propagation patterns are in good agreement with the data.

Two numerical approaches were implemented in FUNWAVE to investigate, individually, bound wave and breakpoint forcing. The bound wave was represented

by a moving radiation stress forcing that was added to the momentum equation. The results were validated with analytical solutions for steady and transient conditions including non-resonant and resonant conditions. Further investigation showed that this approach can represent several aspects of the short wave envelope forcing, including reproducing with reasonable accuracy the transient wave group case.

In the second approach the breakpoint forcing function was implemented in FUNWAVE. The analysis of the propagation patterns and the outgoing wave amplitude dependence on the normalized beach slope, were used to validate the model. The results were in good agreement with Symonds et al. (1982). It was also demonstrated that the oscillations observed at particular frequencies, for the bichromatic cases B1060A and B1045A, are likely to be generated by the breakpoint mechanism.

Similarly to what was demonstrated in Section 3.2.1, inside the surf zone, the cross-correlation results for a summation of individual single-frequency breakpoint forced simulations displays the progressive patterns of both incident and outgoing waves. In the next chapter several properties of infragravity waves are further investigated numerically.

# Chapter 5

## Infragravity Waves: A Numerical Investigation

In this Chapter FUNWAVE and the implemented forcing mechanisms are used to investigate the particular aspects of infragravity waves discussed in Chapter 3 including bound wave shoaling and the properties of the positive leading surge, the breakpoint force wave generation and infragravity wave dissipation. The relationship between wave envelope and the breakpoint excursion and between the infragravity waves, in the inner surf zone, and shoreline excursion are established. Finally the main dominant mechanism in the surf zone is determined by analyzing the cross-correlation analysis between breakpoint and shoreline excursion.

### 5.1 Bound Wave Shoaling

Following the discussion presented in Section 3.3, the forced wave shoaling and the rate of energy transfer dependence on the group frequency are further investigated here using the radiation stress forcing approach that has been validated in Section 4.4. The analysis of the results are based on the same approach described in Section 4.4.2, where the shoaling of the bound wave is quantified starting from the steady solution. Hence, the initial forward free wave is not taken into account, only waves generated during the shoaling process, are considered, as demonstrated in Figure 4.14.

A total of seven cases are presented here, representing wave groups with the same primary mean wave period of  $T = 6$ s, but different group lengths, varying from 200m to 345m. The domain starts with a horizontal bottom ( $h = 20$ m) connected to a slope ( $\beta = .025$ ) followed by a long plateau ( $h = 5$ m). The setup of the numerical experiment is similar to the schematic representation in Figure 4.14. The length of the plateau is sufficient for the free waves, generated during the shoaling process, to propagate away from the forced waves. At  $h = 5$ m the group velocity is still smaller than  $\sqrt{gh}$ .

Figure 5.1 show the time evolution of the long wave surface elevation at a position on the slope for the different cases. The observed shoaling dependence on the group frequency is clear, as the shorter wave groups shoal more than the longer groups.

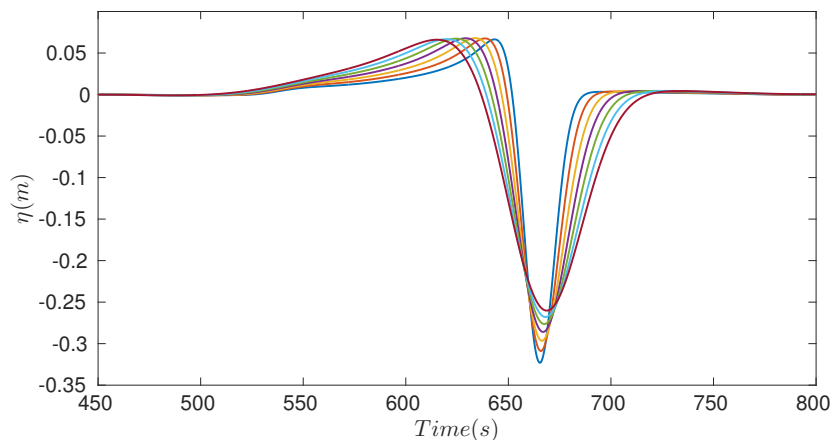


FIGURE 5.1: Surface elevation in the shoaling zone, waves generated by different forcing length but same propagation speed. FUNWAVE results. Each line represents a different group length, from shortest 200m (blue line), to the longest 345m (dark red).

A similar shoaling pattern was observed using the simplified conceptual model in Section 3.3, with the results matching qualitatively Madsen et al. (1997) and Battjes et al. (2004). In the conceptual model, the observed difference in shoaling rates is in fact only an interference between the forced and free wave generated during the shoaling process. In that model, all the bound waves were shoaling at the same rate ( $\sim h^{-5/2}$ ), and the apparent total shoaling dependence on group

frequency was a consequence of the relative travel distance of the generated free waves from the bound waves. Therefore, longer waves apparently shoal slower because the free waves need to propagate longer distance to get away from the forced waves (Figure 3.8).

On the horizontal bottom, after the shoaling zone, free and forced waves are separated as in Figure 5.2. As expected, all the forced waves reached the same amplitude. During the shoaling process, free waves are added to balance the forced solution, and at each instant, the amount of change in the bound wave is added to the free wave, which is propagating away from the forcing. For this reason, a shorter forcing generates a relative longer and smaller free wave than a longer forcing. This is observed in Figures 5.2 and 5.3, where both FUNWAVE and the conceptual model show similar results. The shorter the forcing the longer and smaller the free wave is relative to the forcing.

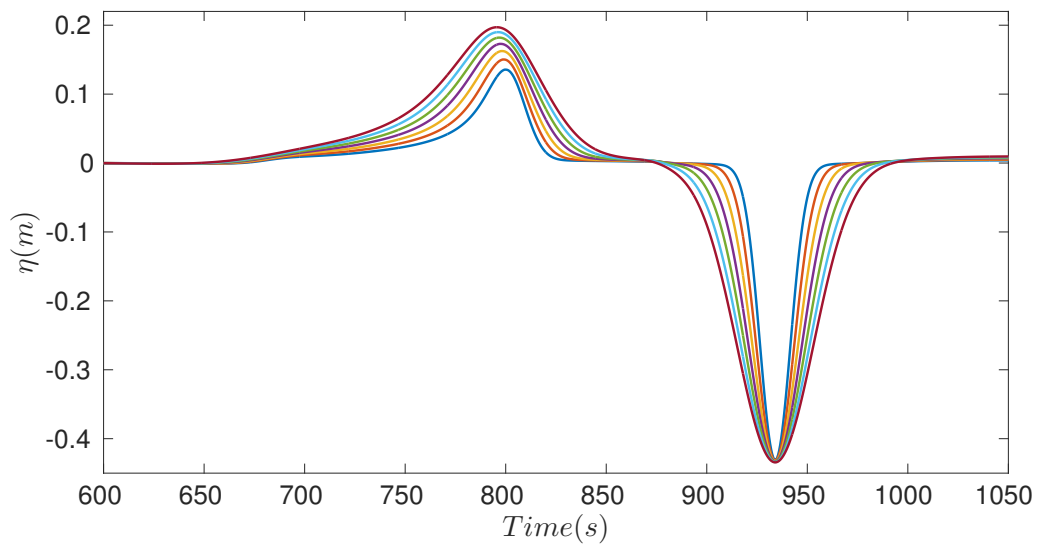


FIGURE 5.2: Surface elevation on the horizontal bottom, after the shoaling zone. The waves are generated by different forcing length but with the same propagation speed. Leading positive free waves and negative forced waves. FUNWAVE results.

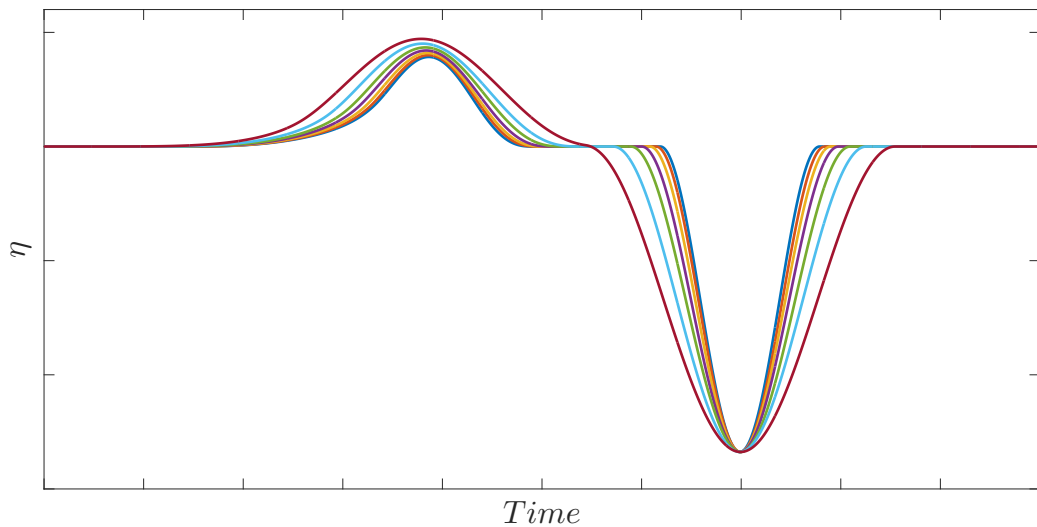


FIGURE 5.3: Surface elevation on the horizontal bottom, after the shoaling zone. The waves are generated by different forcing length but with the same propagation speed. Leading positive free waves and negative forced waves. Conceptual model results (Section 3.3).

The location of the free waves for each case in Figure 5.2 indicate that they have been generated at the same location and time, during the shoaling process, as proposed in the conceptual model. A frequency dependent shoaling rate would



lead to free waves being generated at different locations and time. For instance, consider a long bound wave that shoals less because the equilibrium solution is not reached on the slope, once this wave gets to the horizontal plateau, it will continue evolving to the equilibrium solution. Hence free waves are expected to be generated in this region as well. The similarities between the FUNWAVE and the conceptual model results supports this hypothesis that the bound wave shoaling is independent of the group frequency, and the observed dependence is due to the forced and free wave interference.

## 5.2 Bound Wave: Forced and Free Waves

The use of the radiation stress gradient in the momentum equation allows the individual treatment of infragravity waves. Once  $S_{xx}$  is known, the evolution of those waves can be resolved independently of the short waves, or decoupled from the short waves.

Taking the linear shallow water equation, for instance, and adding the radiation stress forcing (equation 2.10), the non-homogeneous solution is the forced wave traveling with the speed of the forcing ( $c_g$ ), and the homogeneous solution travels with  $\sqrt{gh}$ . Therefore, any change to the forced wave is balanced by the free waves. What is still not fully understood is if the generation of free waves only occurs due to the decoupled approach used and if, under real conditions (infragravity waves forced directly by the short waves), only the forced waves generated by the interaction of primary waves exist.

Under natural condition, or even in laboratory experiments, identifying if free waves are present is a complicated task due to the difficulties in separating forced and free incident infragravity waves. For this reason, here the generation of free waves, as a response to the bound wave changing, is investigated numerically. The aim is to determine if, similar to the decoupled approach, free waves are added to the bound wave when the model is forced by short wave groups.

In Boussinesq-type models, to avoid problems with wave relaxation at the boundaries, a source function, placed within the domain, is commonly used to generate waves (Wei et al., 1999). This source function can be added to the momentum equations, as a pressure disturbance, over a predefined region. Similar to a mechanical wave maker in wave flumes the forcing in the model is only capable of reproducing free waves. Hence, a common approach is to generate only the desired primary frequencies and the non-linear effects are resolved by the model or the natural hydrodynamics in the flume. For the latter, a second order correction is used to deal with the issue of the infragravity wave velocities and the no flow condition through the paddle (Hansen et al., 1980, Mizuguchi and Toita, 1996). This issue is restricted to wave flumes. In the numerical model the waves are generated through the pressure disturbance, and there is no wave blocking.

By numerically simulating bichromatic dispersive wave groups propagating over a long horizontal bottom it is possible to determine if, during the short wave generation, free waves are added to balance the bound wave. Since the short waves are dispersive the wave groups and the bound waves propagate slower than  $\sqrt{gh}$ . For this reason, at a certain position along the numerical flume, the possible free waves generated with the bound wave at the source region will be separated from the wave groups.

Figure 5.4 shows the surface displacement for a set of ten fully modulated wave groups with mean frequency of 0.8Hz and group frequency of 0.094Hz. The source function is placed at  $x = 5\text{m}$  of the numerical domain with a constant depth of 0.5m and length of 450m, excluding the sponge layers that are placed at each end of the flume. Nine experiments, varying only the wave group amplitude, are performed. Surface elevation are extracted at different locations.

Figure 5.4(g, h and i) shows the time series of  $\eta$  at  $x = 448\text{m}$ . The time history of the long waves, observed between  $t \approx 200$  and 300s, match the travel time ( $= 204\text{s}$ ) from the source region to  $x = 448\text{m}$  for a shallow water wave. Hence, similar to the decoupled approach, these free waves are generated together with the bound wave. The short wave group disintegration during the propagation, over the long

domain, does not affect the free waves previously generated (assuming no interaction between short and free long waves). Another indication that corroborates this conclusion is the fact that those free waves, measured at  $x = 448\text{m}$ , have a power relationship with the short wave height of  $m = 1.89$ , close to the theoretical  $H^2$  (Figure 5.5). This calculation is based on the infragravity wave variance at  $x = 448\text{m}$ , evaluated between  $t = 200$  and  $300\text{s}$ .

These results show clearly that by using the short wave evolution as the forcing term for the bound waves, free waves are also generated. Perhaps even more importantly, these findings suggests that free waves are also likely to occur during the shoaling process.

It is not clear to the author if, in the second order wave maker theory, these free waves, generated to compensate the bound wave are also removed. Hansen et al. (1980) included in the derivation an extra term which is related, according to them, “to a complicated 2nd order free-wave effect”, however it is not clear where the term originated from. Orszaghova et al. (2014) have implemented into a Boussinesq-type model the second-order correction proposed Schäffer (1996). According to their results, the correct bound wave at the wave maker, after suppressing all the free infragravity waves, is purely negative (see their Figure 6).

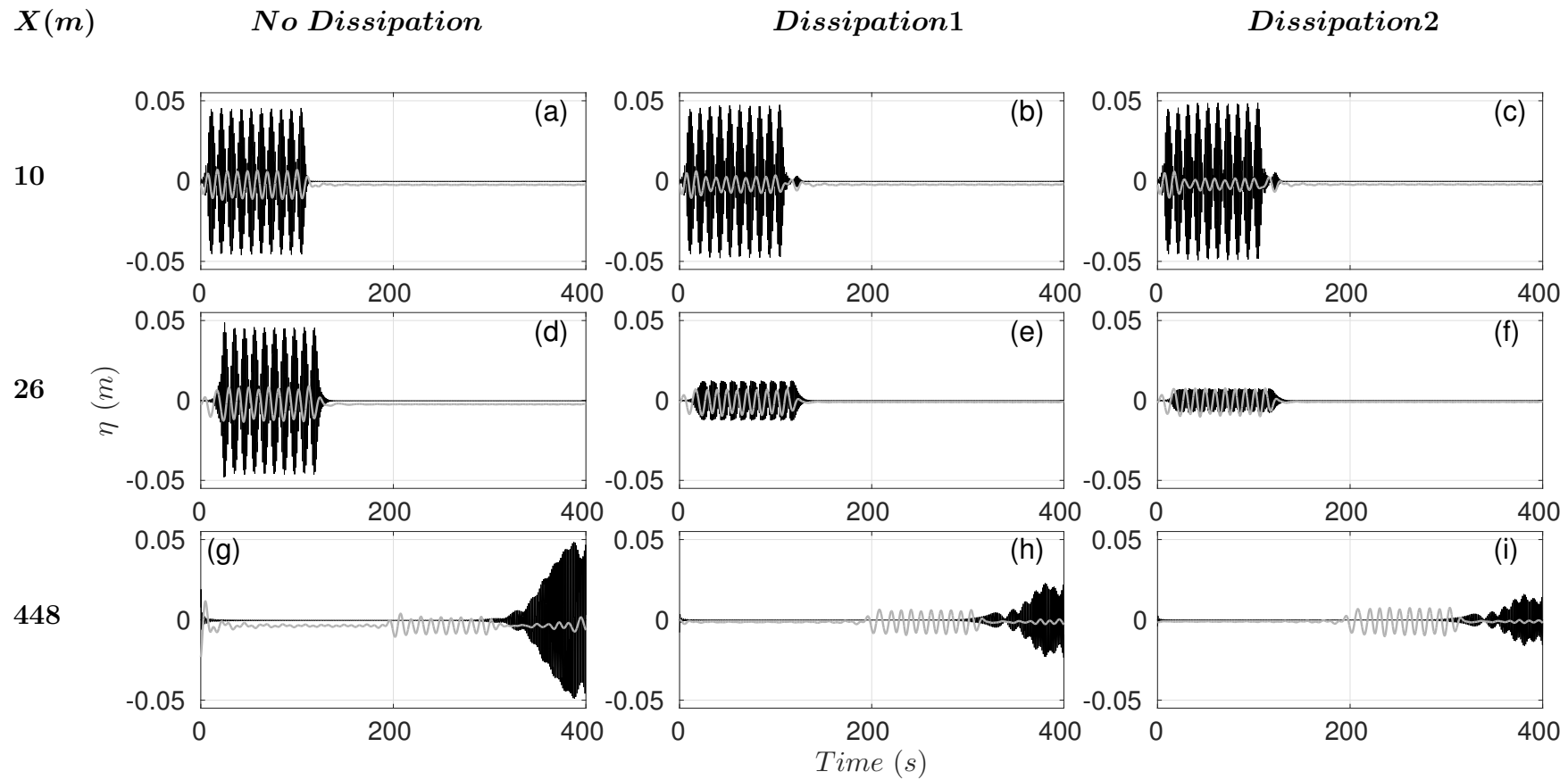


FIGURE 5.4: Short (black) and infragravity (grey) surface elevation time series at  $x = 10\text{m}$  (a, b and c),  $x = 26\text{m}$  (d, e f) and  $x = 448\text{m}$  (g, h and i). There is no wave breaking for the case in left panels. The center and right panels are cases with different wave breaking/dissipation intensity. The infragravity waves are multiplied by a factor of ten.

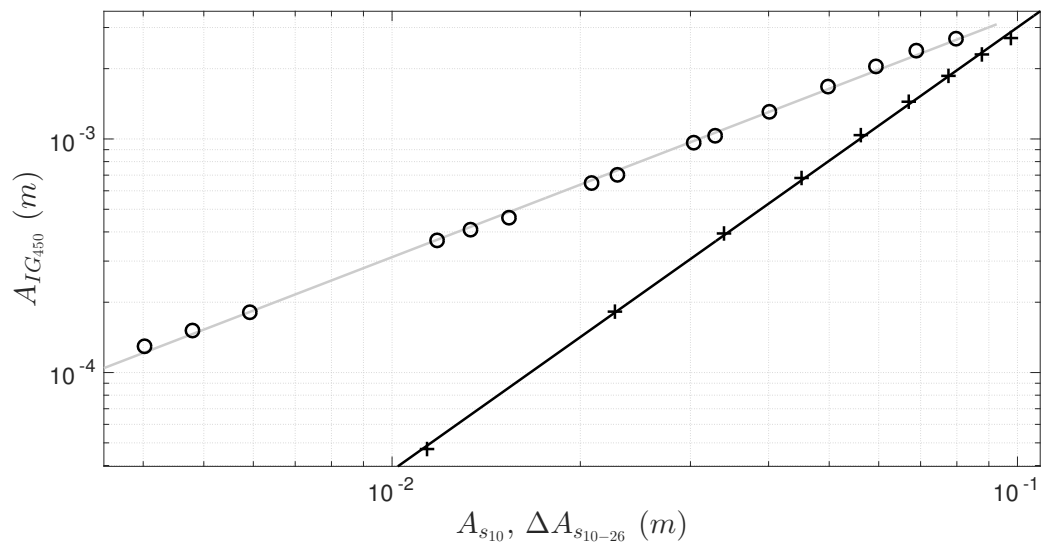


FIGURE 5.5: Relationship between short ( $A_s$ ) and infragravity wave ( $A_{IG}$ ) amplitude. The numerical subscripts indicate spatial location. Black line (+),  $A_s$  at  $x = 10\text{m}$  and  $A_{IG}$  at  $x = 448\text{m}$ ,  $m = 1.89$ , without short wave dissipation. Grey line (O),  $\Delta A_s$  ( $x = 10$  and  $x = 26\text{m}$ ) and  $A_{IG}$ ,  $m = 1.03$ , with short wave dissipation (the free waves generated with the bound waves are subtracted, see section 5.3).

### 5.3 Identifying Breakpoint Forced Waves by Controlling Short Wave Breaking

As introduced in Chapter 4.1, wave breaking in depth-average wave models is not physically represented accurately and the dissipation is treated numerically. There are different types of wave breaking schemes. For instance, FUNWAVE uses the intrinsic characteristic of the non-linear shallow water equations and the total variation diminishing method to dissipate wave energy (Tonelli and Petti, 2009). The advantage of using this method is that there is no need for a triggering mechanism to determine whether the wave is breaking or not. However, this breaking scheme is more complicated to control artificially. Wave breaking mechanisms such as the eddy viscosity model derived by Kennedy et al. (2000) use the time derivative of the surface elevation as the trigger, to start dissipation, and the thresholds are defined based on empirical observations and calibration data.

The identification of infragravity waves generated by the breakpoint forcing is commonly justified by comparing the common features between the simplified (infragravity wave only) breakpoint forcing model and the results obtained in the field, the laboratory or the full numerical simulations (including short waves). As demonstrated throughout the thesis, the direct identification of breakpoint generated infragravity waves is complicated due to the summation of bound waves and shoreline reflection.

Here a direct observation of breakpoint generated waves by short wave groups is attempted by using the eddy viscosity model to control the short wave breaking/dissipation. The same numerical set-up of the previous section is used. The wave breaking is restricted to a predefined region from  $x = 20$  to  $25\text{m}$ . Within this zone, the threshold of the triggering mechanism is reduced to force short wave dissipation. The amplitude of the free waves generated, during the breaking process, are evaluated at  $x = 448\text{m}$  (Figure 5.4). The free waves generated with the bound wave are removed by subtracting the time series of infragravity waves generated without short wave dissipation. Infragravity waves at  $x = 458\text{m}$  are evaluated between  $t = 200$  and  $300\text{s}$  (as before).

By comparing the results in Figure 5.4 it is clear that the dissipation of the short waves do change the infragravity waves. The superposition of bound waves and the infragravity waves generated during the dissipation of the short waves is visible both before and after the breaking zone. For instance, by separating incident and reflected signal (see Section 3.2.2) at  $x = 10\text{m}$  (before the breaking zone) outgoing waves are observed for the cases where short wave breaking occurs (Figure 5.6). This is in accordance with radiated outgoing breakpoint forced waves (Symonds et al., 1982) (Section 2.2). Furthermore, the power relationship between the amount of short wave dissipation  $A_{s10-26}$  (amplitude  $A$  at  $x = 10\text{m}$  subtracted from  $A$  at  $x = 26\text{m}$ ) and the infragravity waves (generated by the short wave dissipation) is calculated. In contrast to the nearly quadratic relationship observed for the free waves that were generated together with the short waves, the breakpoint forced waves have a linear relationship with short wave amplitude  $m = 1$  (Figure

5.5), suggesting that those waves were generated by a dynamic setup (Baldock and Huntley, 2002, Nagase and Mizuguchi, 2001).

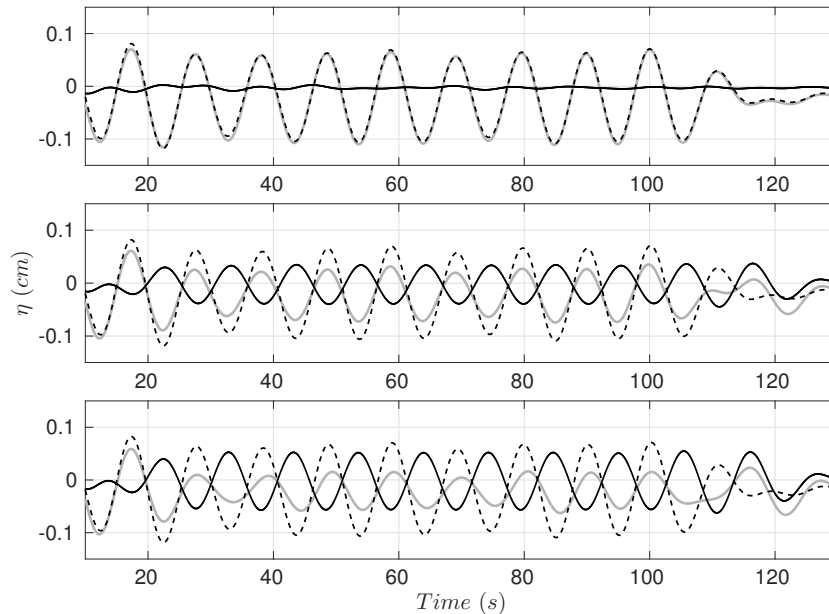


FIGURE 5.6: Infragravity surface elevation at  $x = 10\text{m}$ , total signal (grey line), incident signal (dashed line) and outgoing signal (full black line). Top panel (no dissipation/breaking), center panel (mild dissipation) and bottom panel (strong dissipation). The total infragravity signal for each case is also respectively shown in panels a, b and c in Figure 5.4.

## 5.4 Infragravity Wave Dissipation and Bound Wave Release.

Infragravity wave dissipation in the surf zone has been discussed previously (Section 3.5), based on the literature review and reanalysis of laboratory data. Three possible hypothesis for the observed infragravity wave decay, after short wave breaking, were analyzed.

Nielsen et al. (2008) proposed a mechanism for the conversion of a forced wave into free waves (an analogy to bound wave release). According to this approach, a reduction in the released wave amplitude is expected for a gradual forcing decay, as exemplified in Figure 3.17. In order to analyze the effects of the rate of forcing decay on the released wave amplitude, a group of simulations of Gaussian-shaped

forcing function (equation 4.5), propagating with constant speed ( $< \sqrt{gh}$ ) over a horizontal bottom, were performed. Similar to the previous cases, the simulations were designed to allow the initial free waves to propagate away from the forced waves, not interfering with the results. At a predefined location the forcing ( $F_{S_{xx}}$ ) is damped from its original value to zero. The only difference between each simulation is the linear damping rate of the forcing, in other words, for each simulation, the length of the linear transition between full forcing and zero forcing is different.

Figure 5.7 shows the space-time evolution of the surface elevation for two simulated cases. For all cases the forcing starts at  $T = 0\text{min}$  and  $x = 2000\text{m}$ , where forced ( $IBW$ ) and free waves ( $OFW_0$  and  $IFW_0$ ) are generated.  $F_{S_{xx}}$  propagates with constant amplitude from  $x = 2000$  to  $x = 2300\text{m}$ , from this location the forcing is removed either abruptly or at a linear rate as demonstrated, respectively, by left and right panels in Figure 5.7. The horizontal dot-dashed are the limits of the decaying region, and after that only free wave exist, note that for the abrupt case there is no decaying region, but only on instant and location where the forcing is turned off. The spatial shape of these waves are analyzed at the instant indicated by the horizontal black line. At this instant for all cases no forcing exists, therefore all the waves are free. The thick part of the line is the spatial region displayed in Figure 5.8.



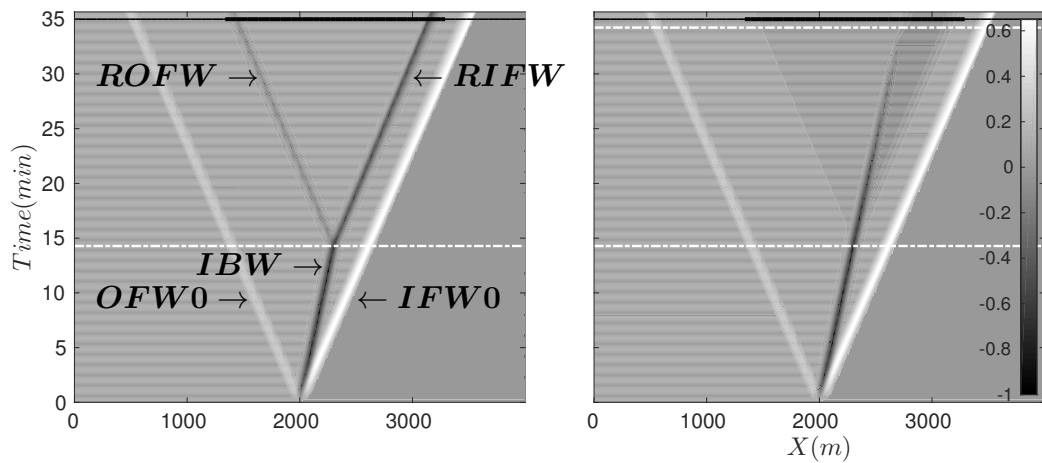


FIGURE 5.7: Space-time surface elevation generated by two different simulations. Left: abrupt forcing removal (blue line in Figure 5.8). Right: slowest forcing decay (magenta line in Figure 5.8). The horizontal dot-dashed lines are the time limits of the forcing decay. The black line indicates the instant plotted for each simulation in Figure 5.8, with the spatial limits defined by the thick black line.  $IFW_0$  and  $OFW_0$  are, respectively, the incident and the outgoing free waves generated to compensate the initial condition.  $IBW$  is the incident bound wave, traveling with speed  $< \sqrt{gh}$ .  $RIFW$  and  $ROFW$  are, respectively, the released incident and outgoing free waves.

As mentioned above, Figure 5.8 shows the spatial surface elevation taken at a instant where the forcing has ceased, therefore the only waves present are the two free waves, propagating in opposite directions. Each line shows a different decaying rate, the longer the waves the smaller is the rate of forcing decay. The blue line represents the abrupt forcing removal, and the bigger and the smaller waves are, respectively, the forward and backward propagating free waves. As expected, by reducing the decaying rate the free waves are stretched, reducing in amplitude. For instance, for a decaying zone of length  $Lg$  (green line in Figure 5.8) the forward free wave reduces its amplitude to approximately 42% of the amplitude of the forward wave in the abrupt case (blue line).

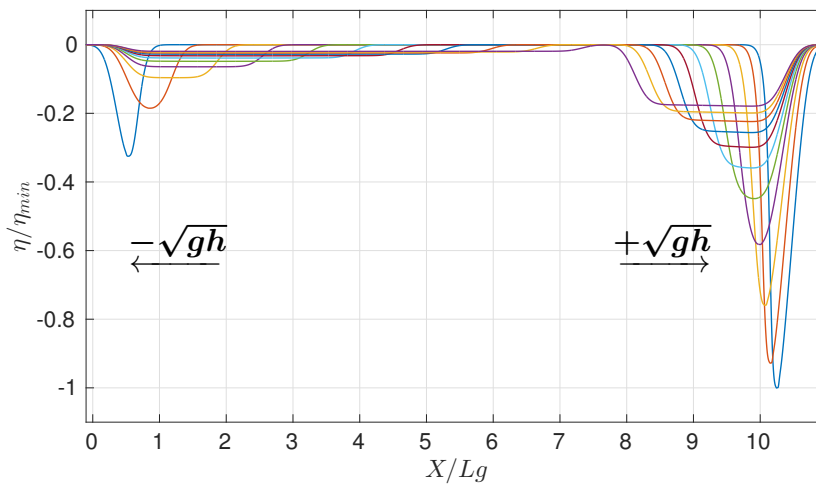


FIGURE 5.8: Free waves generated by the forcing offset. The blue line represent an abrupt damping, the longer the depression the longer the  $F_{S_{xx}}$  decay region. Each color represents a  $0.2Lg$  increment of the decaying zone.

The results show that, for a constant bottom, by increasing the dissipation zone the amplitude of the free waves reduces. Using the same approach on a sloping bottom the opposite results were found. Here instead of changing the length of the dissipation zone, the length of the Gaussian forcing function is changed in each simulation.

Following the previous findings, it was expected that stronger dissipation would occur for the shorter forcing. However, over the slope the longer the forcing the stronger is the decay of the free waves after  $F_{S_{xx}}$  is ceased as shown in Figure 5.9. Over the sloping bottom it is likely that the free wave generated during the shoaling process (positive) is interfering with the free waves generated by the decaying pressure (negative), partially canceling each other. This interference pattern is expected to be stronger for the waves generated by the longer forcing, and is similar to the bound wave amplitude dependence on the group frequency (when considering free wave generation) discussed in Sections 3.3 and 5.1.

Figure 5.9 corroborates this conclusion. For a longer forcing function (right panel), the positive free wave generated during the shoaling process is relatively bigger

than the free wave generated by a shorter forcing function (see Figure 5.2). However, the stronger interference between this positive free wave and the negative free wave (generated by the forcing decay) results in a reduction of the amplitude of both positive and negative part. While it is clear that this process occurs when the infragravity waves are forced by the radiation stress term, further investigation is needed to determine whether such behavior occurs under natural conditions.

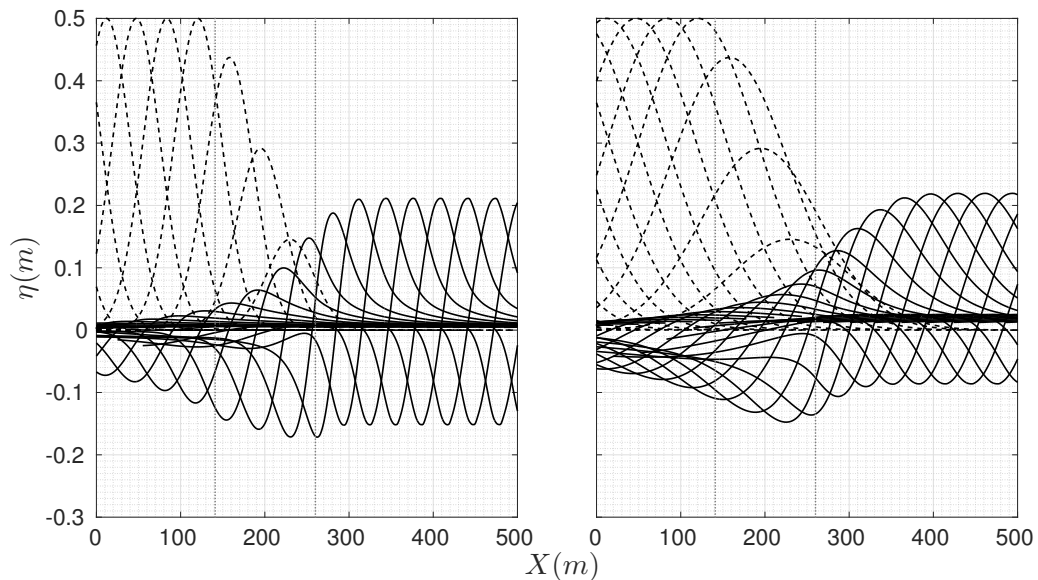


FIGURE 5.9: Spatial surface elevation (black line) at different instants generated by  $F_{S_{xx}}$  propagating over a sloping bottom. The vertical grey dots indicate the region where the forcing (dashed line) is damped. Shortest (left) and longest (right) forcing cases.

An alternative interpretation of bound wave dissipation was presented by Baldock (2012) and Baldock et al. (2004). According to them, if short wave breaking does not occur in shallow water, the bound wave is likely to remain forced, decaying with the forcing inside the surf zone.

Battjes et al. (2004) suggested a short and infragravity wave length dependence to justify the observed stronger decay of higher frequencies, within the infragravity band, in the surf and swash zone. For that reason, infragravity waves with frequency closer to the short waves are more affected by the short wave breaking. In other words, the breaking zone, where the dissipation occurs, is relatively wider

for shorter infragravity waves. Differently from the others, this hypothesis refers only to the energy dissipation of infragravity waves, independently of these being forced or free waves.

The reanalysis of the laboratory data (Figures 3.19) also indicated that infragravity waves with lengths closer to the short wave lengths are strongly dissipated. The groupiness decay in the surf zone was also calculated as an estimate of the amount of forcing remaining in the inner surf zone. Assuming that the bound waves are not released and remain forced in the surf zone, an infragravity wave amplitude dependence on the remaining groupiness is expected. However, this dependence was not clear from the 13 laboratory cases analyzed, probably due to the presence of breakpoint forcing specially for the longer wave groups.

In order to obtain a large number of conditions, a series of bichromatic wave group simulations were performed. The numerical wave flume was designed with an initial horizontal bottom ( $h = 0.80\text{m}$ ) connected to a constant slope up to a second horizontal part at  $h = 0.02\text{m}$  (Figure 5.10). This bottom shape was selected to reduce wave reflection. Sponge layers were also placed at both ends of the flume. A total of 200 simulations were carried out for different wave amplitudes, frequencies (primary and group) and two different slopes (table 5.1). For each case, short and infragravity wave (at the group frequency) amplitudes were calculated. The relative amount of infragravity wave dissipation, in the surf zone, was estimated from the difference in infragravity wave amplitude at the beginning ( $x_1$ ) and end ( $x_2$ ) of the short wave breaking. This result was normalized by the infragravity wave amplitude at  $x_1$ , as in Figure 5.10. The remaining relative groupiness at  $x_2$  is defined as the standard deviation of the short wave envelope at  $x_2$  divided by the same parameter calculated at the toe of the slope.

TABLE 5.1: Details of the bichromatic wave group simulations.

Amplitude ( $a_1 + a_2$ , m)	0.1
Modulations ( $a_1/a_2$ )	1 0.5 0.25
Primary Freq (Hz)	0.3:0.1:1.1
Group Freq (Hz)	0.05, 0.1:0.1:0.5
Slope ( $\beta$ )	0.025 0.01
N° Sim	200

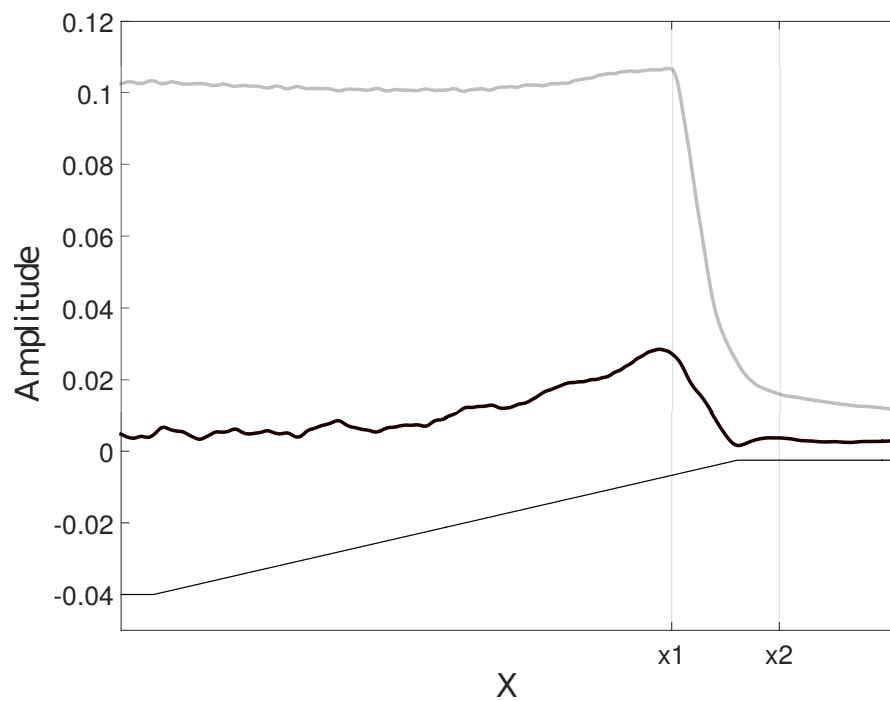


FIGURE 5.10: Short (grey line) and infragravity wave amplitude (thick black line) and depth ( $h/20$ ) (thin black line).  $x_1$  and  $x_2$  are the defined breaking zone.

Figure 5.11 shows, despite the large scatter, that the infragravity wave dissipation increases with  $k_b/k_s$  ( $k_b$  and  $k_s$  are, respectively, the bound wave number and the mean short wave number). The results also show that for some conditions the amount of infragravity wave dissipation is related to the remaining relative groupiness, partially explaining the data scatter. For instance, the cases performed for  $\beta = 0.04$  with  $k_b/k_s \approx 0.5$  show a large range of dissipation from 10% up to 90%, and the dissipation rate increases as the remaining groupiness reduces.

The infragravity wave dissipation dependence on  $k_b/k_s$  and the remaining groupiness suggests that both hypothesis are correct. The presence of breakpoint forcing is also important and will also increase the scatter.

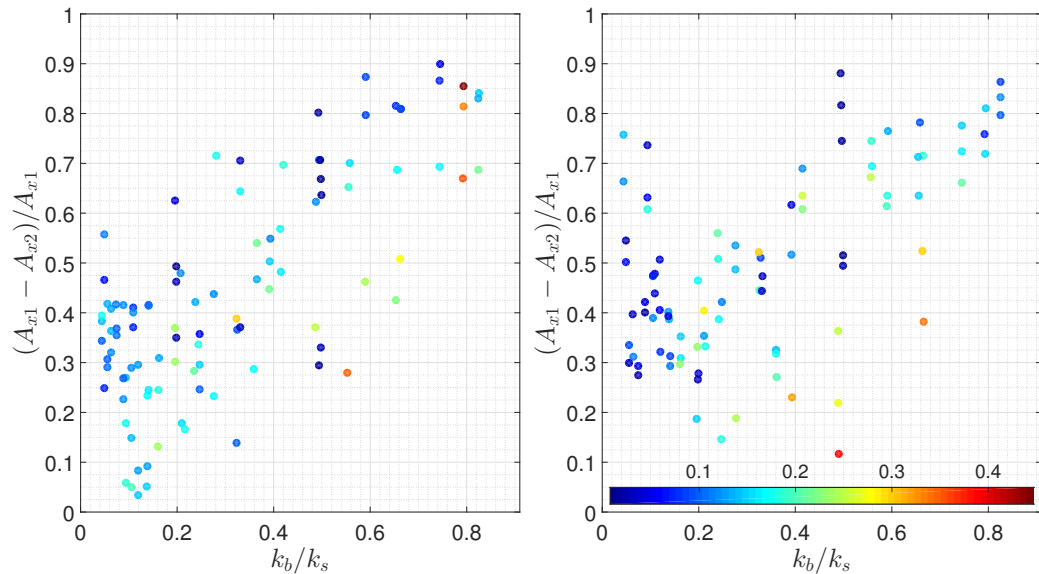


FIGURE 5.11: Infragravity wave dissipation during short wave breaking for different simulated bichromatic cases over two different slopes  $\beta = 0.01$  (left) and  $0.04$  (right). The colorbar is the normalized groupiness at  $x_2$ .

## 5.5 Relationship Between Wave Groups, Breakpoint, Shoreline Excursion and Infragravity Waves

In the surf zone, on natural beaches, infragravity waves are considered one of the main morphodynamic drivers. However, many of their features are not fully understood as pointed out above. Perhaps the main reason is the lack of data, as traditional instrumentation involves great effort and logistics. Furthermore, infragravity oscillations are more important during energetic events and placing instruments in the surf zone under such conditions is very difficult. Also, the spatial scale and the presence of nodal structures require a long and dense cross-shore array and the presence of edge waves can introduce further complications to the interpretation.

The presence of an antinode at the shoreline makes the measurements of its oscillations a good indicator of infragravity motions. One of the advantages of measuring the shoreline position is that it can be done remotely (Holland et al., 1997, Power et al., 2011, among others). The surf beat in the surf zone (generated by the breakpoint forcing and bound waves) are directly forced by wave groups at the breakpoint, therefore it is likely that the breakpoint oscillation is also a natural indicator of the forcing mechanism. To the author's knowledge, the relationship between breakpoint excursion and infragravity waves has not been directly investigated, experimentally or numerically.

The similarities between the short wave envelope and the breakpoint excursion, and between infragravity wave oscillation, in the inner surf zone, and at the shoreline, are demonstrated for the simulated random cases presented in table 4.2. Each case was reproduced for three different beach slopes ( $\beta = 0.1, 0.04$  and  $0.02$ ). The results presented in Figure 5.12 show that the shoreline and infragravity oscillations in the inner surf zone are consistently well correlated for all cases. The breakpoint excursion and the wave envelope are better correlated for the steeper beach and lower frequency cases.

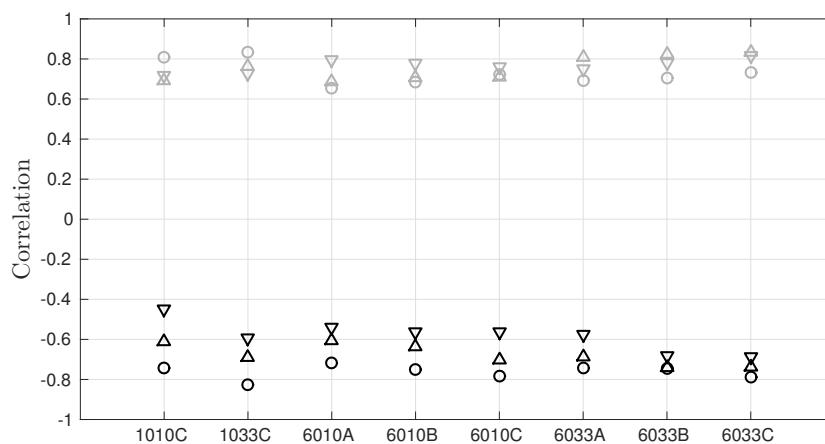


FIGURE 5.12: Correlation between wave envelope (in the shoaling zone) and breakpoint excursion (black), and between shoreline excursion and infragravity surface elevation in the inner surf zone (grey), for the random cases (table 4.2) reproduced for different slopes,  $\circ$  for  $\beta = 0.1$ ,  $\triangle$  for  $\beta = 0.04$ ,  $\nabla$  for  $\beta = 0.02$ .

Using the theoretical description for the mechanisms of surf beat generation (Chapter 2) it is possible to determine, for each condition, the expected relationship between the breakpoint and shoreline excursion. To simplify, an example is given for a single wave group, but the interpretation is applied to multiple frequency conditions, where the cross-correlation results display progressive patterns instead of the standing patterns commonly observed for single frequency cases. Further discussion is presented in Sections 3.2.1 and 4.5. Furthermore, only the incident waves (bound wave and incident breakpoint forced long wave) are considered in the following schematic representation.

Assume an idealized case with symmetrical wave groups propagating over a constant sloping bottom. According to the steady solution, the bound wave propagates phase-locked with the short wave group envelope, with  $\pi$  phase difference. When the wave group reaches the breaking zone, the smaller waves will break further shoreward, and as the group arrives, the higher waves will break, moving the breakpoint seaward. The maximum outer position of the breakpoint is at the breaking location of the biggest wave in the group. After the breaking of the largest wave the breakpoint starts to move back shoreward (Figure 5.13). By defining the horizontal axis positive shoreward and the vertical axis positive upwards, the breakpoint will then oscillate in antiphase with the wave envelope, and hence in phase with the bound wave.

For the same situation, consider only the breakpoint generation mechanism and a saturated surf zone. As the waves in the group start to break, the forcing region (Figure 2.4) moves out. Shoreward of the breakpoint the water level starts to rise, with a decrease seaward of the breaking zone. After the highest wave breaks, the breakpoint move shoreward again, the width of the forcing region decreases, reducing the water levels inside the surf zone and increasing the water levels outside the surf zone. The water level change, generated inside the surf zone, is the incident breakpoint forced long wave, that propagates shoreward as a free wave (Figure 5.13).



Figure 5.13b shows the cross-shore evolution of the expected breakpoint and shoreline excursion, for the two cases. As the released bound wave and the incident breakpoint forced wave propagate with same speed ( $\sqrt{gh}$ ) they reach the shoreline at the same time (after traveling through the surf zone), but with opposite phase. Therefore, when cross-correlating the breakpoint and shoreline excursion, an opposite correlation signal is expected for the two cases (Figure 5.13c). The lag of the correlation peak for both cases represents the propagation time from the breakpoint to the shoreline.

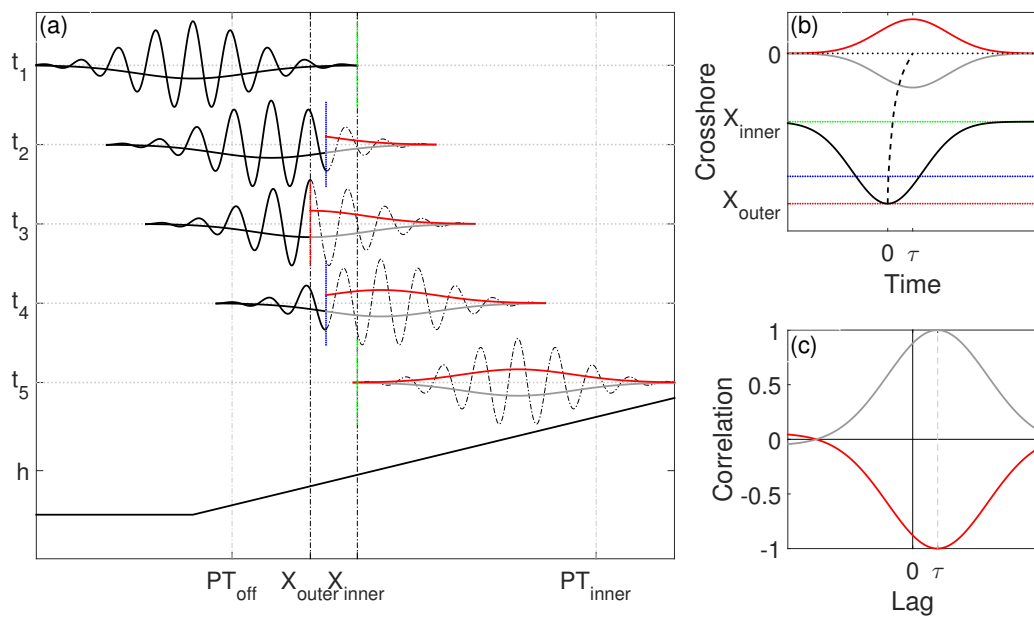


FIGURE 5.13: Schematic representation of surf beat generated by bound wave release and breakpoint forcing. (a) Cross-shore evolution of the wave group, bound and breakpoint forced long wave. The vertical colored lines indicate the breakpoint position. Gray line is the released bound wave. The red line is the incident breakpoint forced long wave. (b) Breakpoint excursion (black line) and shoreline response to long waves generated by the breakpoint forcing (red line) and released bound wave (grey line). (c) Cross-correlation between breakpoint and shoreline excursion, bound wave release (grey line) and breakpoint forced long wave (red line).  $\tau$  is the travel time for a shallow water wave to travel from the breakpoint to the shoreline.

If it is assumed that during the shoaling process the bound wave generates a positive leading part, the shoreline will then first move in the opposite direction of the breaking point. As the negative part of the bound wave gets to the shoreline,

both breakpoint and shoreline will move in the same direction. For this condition, the cross-correlation between breakpoint and shoreline has a leading negative peak (related to the positive surge) and a positive peak (related to the negative part of the bound wave), as in Figure 5.14.

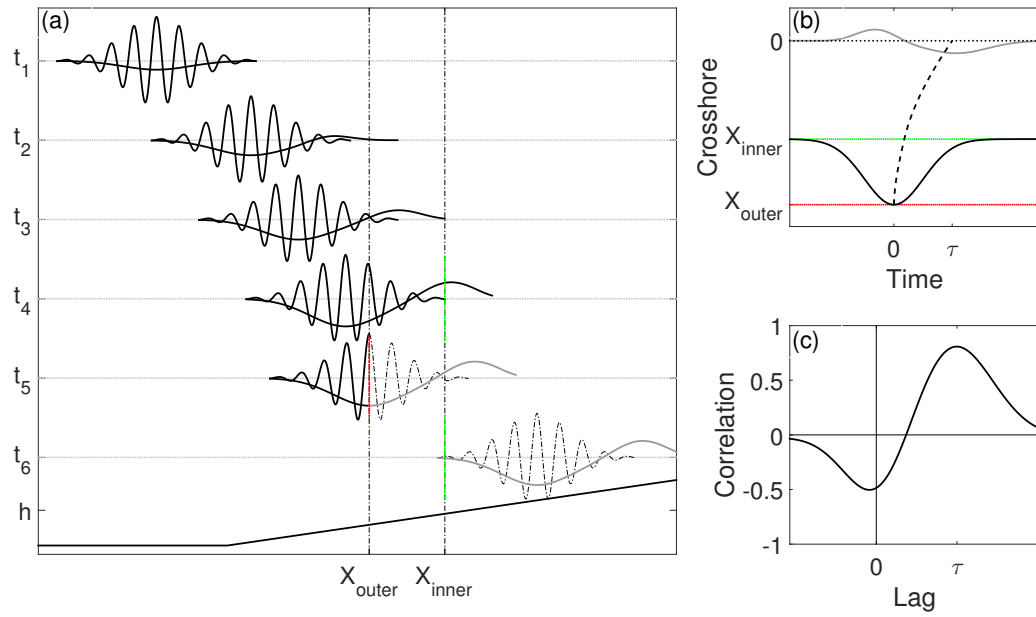


FIGURE 5.14: Schematic representation of surf beat generated by the bound mechanism. (a) Cross-shore evolution of the short wave group and the bound with a leading surge. Vertical lines are the inner (red line) and outer (green line) breakpoint limits. Gray line is the released bound wave. (b) Breakpoint excursion and shoreline oscillation. (c) Cross-correlation between breakpoint and shoreline excursion.  $\tau$  is the travel time for a shallow water wave to travel from the breakpoint to the shoreline.

In a case where the bound wave is lagging the group as it approaches the breakpoint, the lag of the positive peak in the cross-correlation is the travel time to the shore plus the amount of lag between bound wave and breakpoint/envelope. A similar association is possible for the resonant condition (Section 2.1), if this condition is satisfied before the breakpoint and the bound wave reaches the expected shape ( $\propto \frac{\partial S_{xx}}{\partial x}$ , equation 2.14), becoming symmetrically negative and positive within the wave envelope. In this case, the expected result of the cross-correlation between the breakpoint and the shoreline is two correlation peaks (negative and positive)

equally spaced around the travel time from the breakpoint to the shoreline (Figure 5.15).

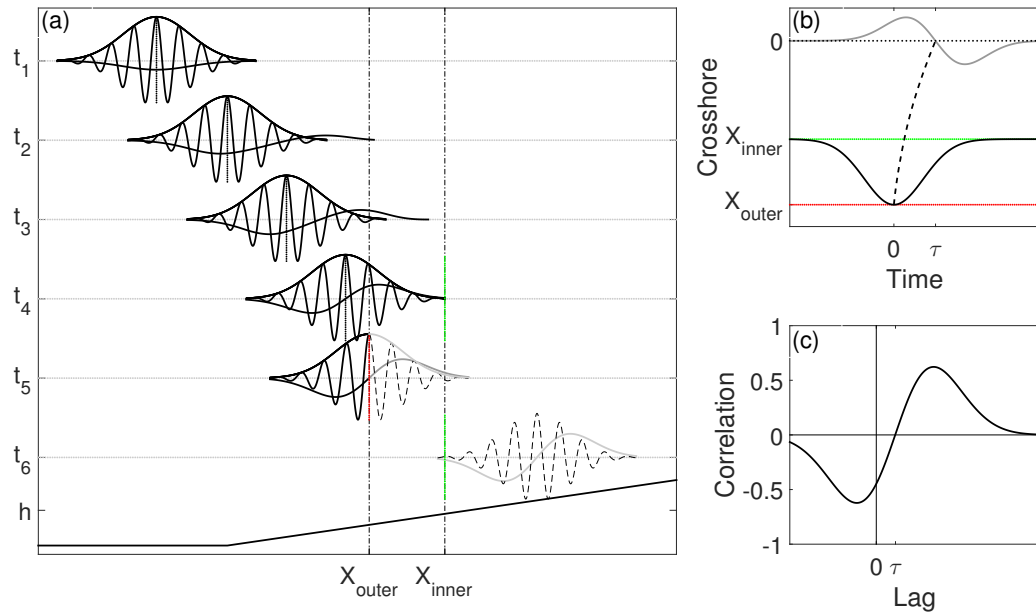


FIGURE 5.15: Schematic representation of surf beat generated by the resonant bound wave. (a) Cross-shore evolution of the short wave group and the resonant bound wave. (b) Breakpoint excursion and shoreline response. (c) Cross-correlation between breakpoint and shoreline excursion.  $\tau$  is the travel for a shallow water wave to travel from the breakpoint to the shoreline.

Base on the expected relationship, for each mechanism, the breakpoint and shoreline excursion can be used to identify the dominant forcing mechanism inside the surf zone. Here this analysis is demonstrated for a series of different conditions.

Initially, simulations are performed using breakpoint forcing only. First, breakpoint and shoreline excursion of the 50 different single long wave frequency cases, presented in Section 4.5, are superimposed and cross-correlated (Figure 5.16). The free wave travel time from the mean breakpoint to the shoreline position, at the still water, is displayed by the dashed black line and is calculated for a constant slope as

$$T_{mb,swl} = \int_{x_{swl}}^{x_{mb}} \frac{1}{\sqrt{gh}} dx = 2\sqrt{\frac{x_{mb}}{g\beta}}, \quad (5.1)$$

where  $x_{swl}$  and  $x_{mb}$  are respectively the cross-shore position of the shoreline at still water and the mean breakpoint position. The negative peak, in the cross-correlation, indicates the incident breakpoint forced long wave propagation.

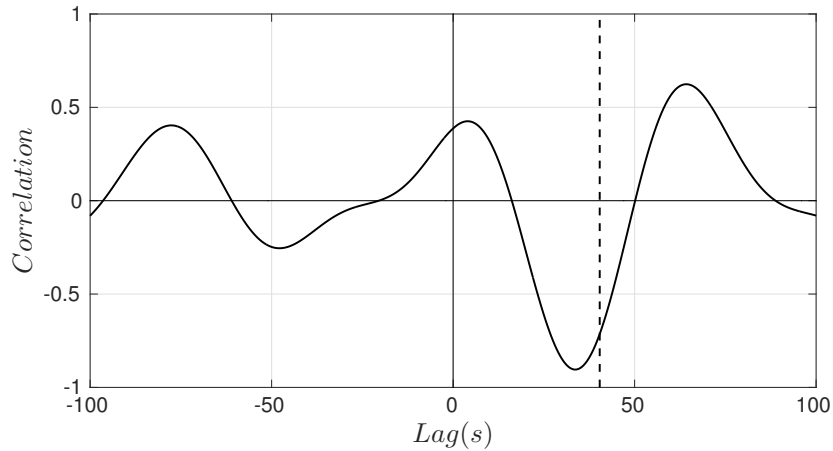


FIGURE 5.16: Cross-correlation between breakpoint and shoreline excursion, for the summation of the 50 different single frequency cases. Dashed line is  $T_{mb,swl}$ .

Instead of forcing the model with the term  $n = 1$  of the Fourier expansion (equations 2.18 and 2.2) that were derived for single frequency and a small modulation of the breakpoint, here the step function  $(\frac{1}{2x} \frac{d(a^2)}{dx})$ , 0 outside and 1 inside the surf zone) is implemented and tested. Following this approach, breakpoint oscillations generated by random waves are directly simulated.

Figure 5.17 shows the surface elevation for a simulation performed considering eleven different frequencies equally spaced ( $0.5 < \chi < 3.5$ ,  $\Delta\chi = 0.3$ ), with different initial phases and amplitude modulations. This case also includes the mean setup, whereas for the single frequency simulations only the the first harmonic was considered. The propagation patterns inside the surf zone are easily observed when the setup is removed.

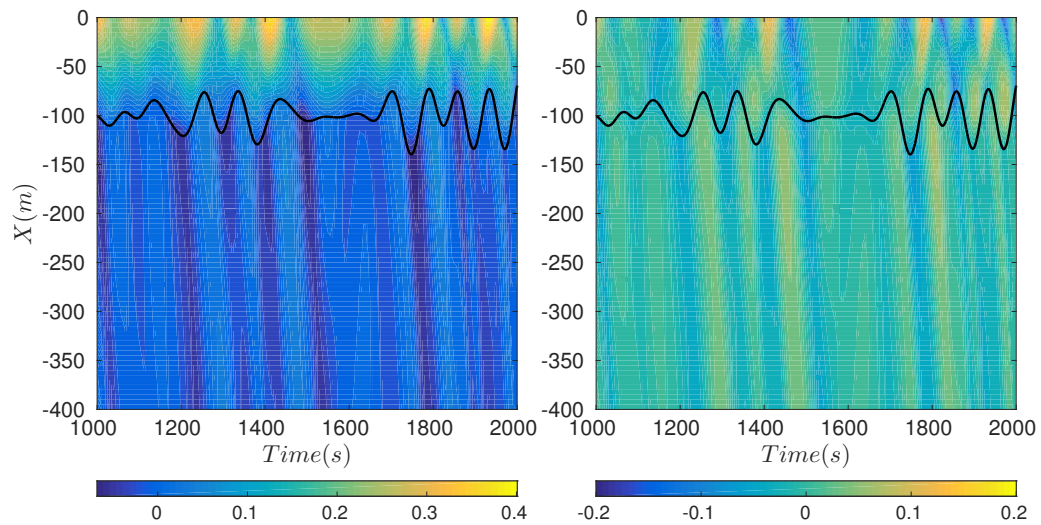


FIGURE 5.17: Space-time surface elevation evolution for the random breakpoint forcing. Left: Total signal, right: excluding mean set-up. Note the different colorbar limits (in meters) for each panel. Black line represents the breakpoint excursion.

The outgoing wave amplitude dependence on  $\chi$ , at discrete frequencies, is similar to the single frequency cases, and is in good agreement with Symonds et al. (1982) (Figure 5.18). For the random case, the range of the interference is smaller than both the analytical solution and the single frequency cases.

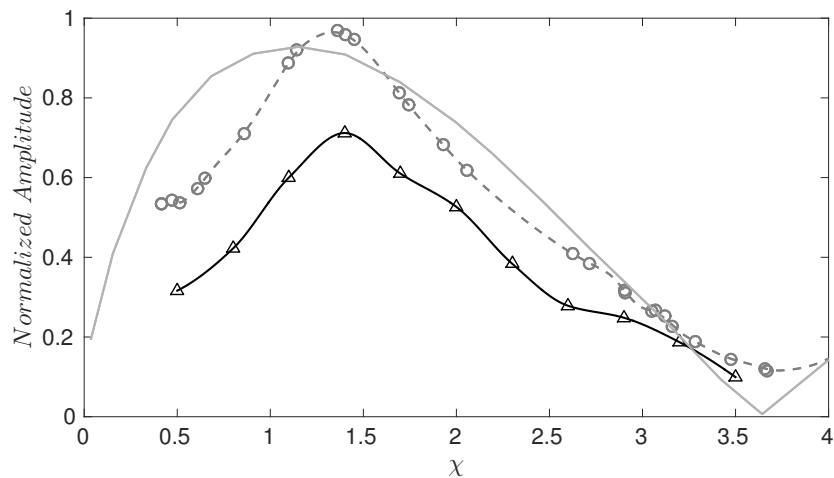


FIGURE 5.18: Wave amplitude outside the surf zone ( $x = -200\text{m}$ ) normalized by the wave amplitude close to the shoreline ( $x = -15\text{m}$ ).  $\circ$  - individual single frequency cases,  $\triangle$  - multi frequency breakpoint oscillation. Grey line is the analytical solution for  $\Delta a = 0.2$  (Symonds et al., 1982).

The cross-correlation analysis between the breakpoint and shoreline excursion show similar results to the previous simulations, where the negative peak indicates the shoreline response to the incident breakpoint forced long wave.

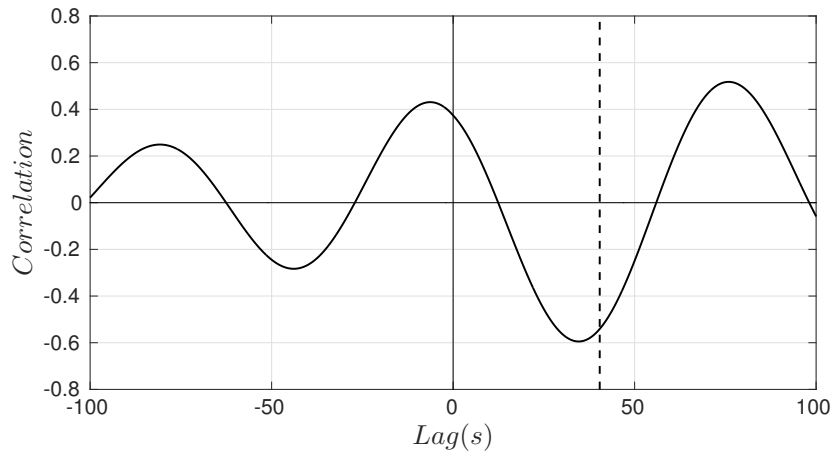


FIGURE 5.19: Cross-correlation between breakpoint and shoreline excursion, for the random case. Dashed line is  $T_{mb,swl}$ .

### 5.5.1 Cross-correlation Between Breakpoint and Shoreline Excursion: Determining Surf Zone Infragravity Wave Forcing, Random Wave Cases.

Determining the dominant mechanism forcing the infragravity waves has been part of different studies (Baldock and Huntley, 2002, Madsen et al., 1997, Schäffer, 1993, and many others), and in most of them the cross-correlation analysis is used to provide specific information about the propagation patterns (Contardo and Symonds, 2013, List, 1992, Masselink, 1995, Pomeroy et al., 2012). Here a similar approach has been used. However, instead of using measured wave information at different locations, the dominant forcing is determined by the relationship between the breakpoint and shoreline oscillations.

In the previous section, the expected relationship between the breakpoint and shoreline excursion and the expected cross-correlation pattern, for each mechanism, have been introduced. Here this approach is used to determine the main forcing mechanism, inside the surf zone, for the 8 random cases (table 4.2) that

were simulated for three different beach slopes. Figure 5.20 shows the cross-correlation between the breakpoint and shoreline excursion for each case. The peak and respective lags indicate that breakpoint forcing dominates inside the surf zone for all cases.

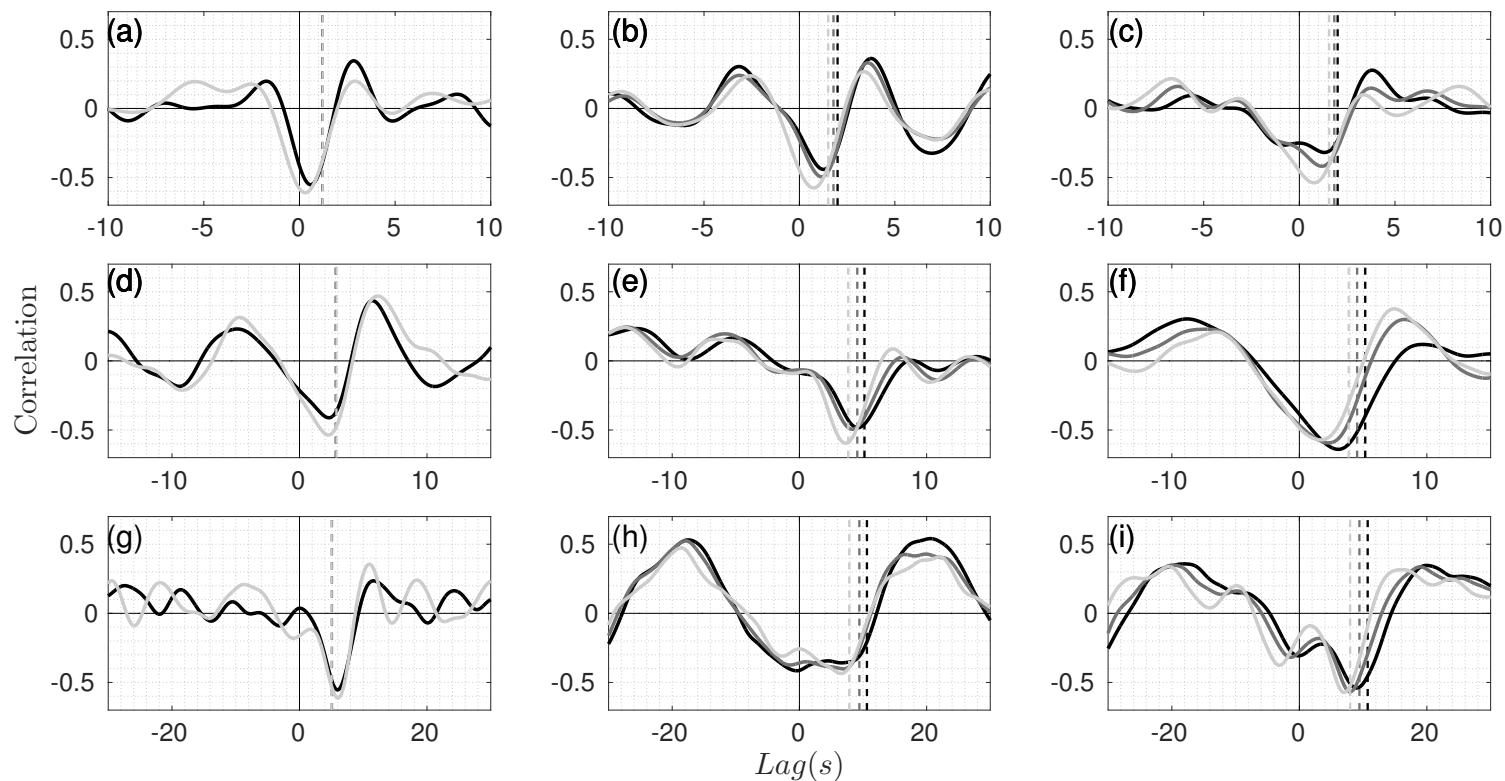


FIGURE 5.20: Cross-correlation between breakpoint and shoreline excursion for the eight random cases (Table 4.2), simulated for three different slopes. (a,d and g) J1010C (black) and J1033C (light gray), (b, e and h) J6010A (black), J6010B (dark gray) and J6010C (light gray). (c, f and i) J6033A (black), J6033B (dark gray) and J6033C (light gray). Top panels  $\beta = 0.1$ , mid panels  $\beta = 0.05$  and bottom panels  $\beta = 0.02$ . Dashed lines are  $T_{mb,swl}$  with the respective colors. For J1010C and J1033C  $T_{mb,swl}$  is nearly the same.



Simulating the same random cases, but using the bound wave forcing only (short wave envelope forcing) and the breakpoint forcing only (assuming saturated surf zone) it is also possible to show that the full simulation results have a closer match to the breakpoint forcing (Figure 5.21).

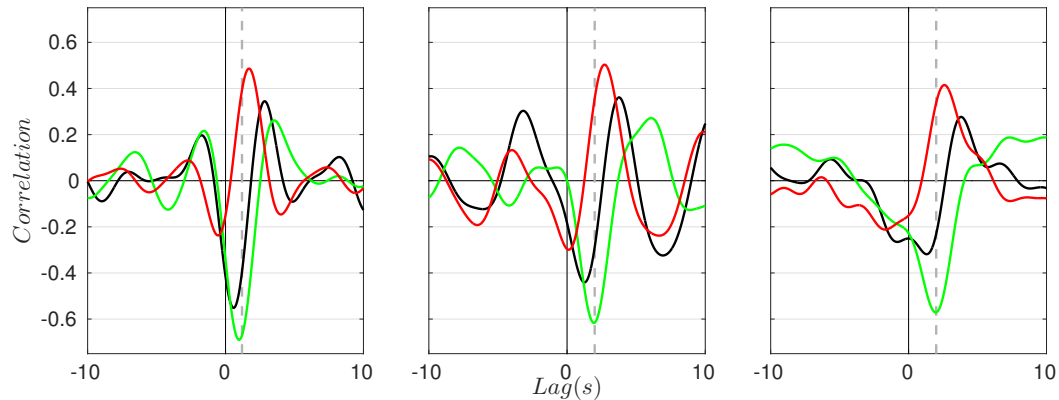


FIGURE 5.21: Cross-correlation between breakpoint and shoreline excursion. Right panel: case J1010C, center panel: case J6010A, left panel: case J6033A. Black line: full simulation, green line: breakpoint forcing, red line: bound wave forcing, bottom slope  $\beta = 0.1$ . Dashed lines are  $T_{mb,swl}$ .

## 5.6 Conclusion

In this Chapter several properties of infragravity waves have been investigated numerically using FUNWAVE. The bound wave shoaling investigation, using the radiation stress forcing approach, showed similar results to the conceptual model presented in Section 3.5. It was confirmed that the shoaling rate dependence on the group frequency and the relative phase change between surface elevation and forcing are caused by the free waves, generated to balance changes in the forced wave, during the shoaling process. Whether the shoaling of bound waves under natural conditions generates free waves is still no clear. However, to the author's understanding free wave generation is to be expected for any numerical model that treats infragravity waves separately from the short waves (forcing term only).

Treating the infragravity waves separately from the short waves is a commonly used approach where the results are often extended to real case scenario (including short

waves). For instance, such method is used to force morphological models, where short waves are resolved by phase-averaged methods and only the infragravity waves are phase-resolved (Reniers et al., 2004). Such methodology allows longer time steps, making practical the prediction of long term morphological evolution. Whether that is reasonable or not is beyond the scope of this work,

The simulated dispersive wave groups also suggested that free waves are needed to compensate the bound waves forced by the short waves. The result also indicates that during the bound wave shoaling free waves are likely to be generated.

Direct observation of breakpoint forced infragravity waves, generated by short wave groups, was possible by controlling the wave breaking and forcing short wave dissipation over a predefined region. The linear power relationship between infragravity waves, generated at the breaking region, and the short wave amplitude suggested that those waves were the dynamic set-up, or the incident breakpoint forced long wave.

It has been confirmed numerically that the breakpoint is a proxy for the wave envelope in the shoaling zone and the shoreline excursion a proxy for the infragravity waves in the inner surf zone. The expected relationship between breakpoint and shoreline excursion for the two different forcing mechanisms have been established.

Using the cross-correlation analysis of the breakpoint and shoreline excursion, for the random cases, it was possible to determine that, inside the surf zone, the main mechanism of surf beat generation is the breakpoint forcing in agreement with the findings in Baldock and Huntley (2002).

In the next chapter the findings and interpretation of the infragravity wave dynamics investigated in the present and previous chapters are extended to field application.

# Chapter 6

## Infragravity Dynamics on Natural Beaches

### 6.1 Introduction

Infragravity waves, also known as surf beats, are considered one of the main morphodynamic drivers in shallow waters. Due to short wave dissipation in the surf zone, the infragravity waves, which are generally unsaturated, become gradually more important towards the shoreline (Raubenheimer and Guza, 1996), controlling the swash dynamics on mild sloping beaches (Ruessink et al., 1998).

The swash zone is a region of special interest for coastal researchers and planners as it plays an important role on the design of coastal structures (Kobayashi, 1999), on the sediment transport and on the subaerial sediment budget, determining erosion and accretion processes (Butt and Russell, 2000), forcing groundwater flows (Nielsen, 1999) and influencing intertidal ecology (McArdle and McLachlan, 1992). However, too little is known about the swash zone morphodynamics, and it is an area of great challenge for present and future research (Nielsen, 2009). One of the crucial steps is understanding the behavior of infragravity waves at the boundary (inner surf zone) and in the swash zone.

As demonstrated in the previous chapters, the mechanics of infragravity waves by itself is complicated and not entirely understood, specially for natural systems. Fortunately, the recent evolution in instrumentation has led to a large number

of dedicated field experiments (Contardo and Symonds, 2013, Guedes et al., 2013, Pomeroy et al., 2012, Thomson et al., 2006, among others). However, in the surf zone, most of the data is restrained to a short period of acquisition (with a few exceptions) and small wave conditions as the deployment and maintenance of instruments in the surf zone during more energetic events becomes a very complicated task. This impose a major drawback, since the importance of infragravity waves increases with offshore short wave height (Raubenheimer and Guza, 1996). Therefore an alternative approach is required to provide infragravity wave information for long periods and for a wide range of wave conditions.

The fact that many nearshore processes have a visual manifestation makes remote sensing a great tool to investigate coastal processes (Holman et al., 1993). Also its versatility, reduced costs and logistics (when compared to traditional instrumentation), allows the monitoring of processes over wide spatial and temporal scales.

Video imagery has been extensively used to investigate beach processes including morphological evolution (Aarninkhof et al., 2005a, Holland et al., 1997, Lippmann et al., 1997, among others), short wave parameters (Lippmann and Holman, 1992) that have been extended to estimate bathymetry (Aarninkhof et al., 2005b, Stockdon and Holman, 2000) and swash processes, due to the relatively easy extraction of the run-up excursion from video images (Holland and Holman, 1993, Power et al., 2011), including infragravity swash dynamics (Guedes et al., 2011, Stockdon et al., 2006). Away from the swash zone, due to no direct visual manifestation, the application of remote sensing to infragravity waves has been limited.

In the surf zone, infragravity waves can be generated by different mechanisms, principally by incident bound waves (Longuet-Higgins and Stewart, 1960) and by breakpoint forcing (Symonds et al., 1982). In the field, reflected trapped or edge wave are also possible (Gallagher, 1971) however, this work is focused only on the cross-shore propagating waves (leaky waves). While it is clear that these, widely accepted, processes are likely to occur simultaneously, determining the relative importance of each, under natural conditions, is still an important question yet to

be fully answered. Interestingly, even though both mechanisms are forced by radiation stress gradients, the relationship between short waves and the respectively generated infragravity waves is distinct. Furthermore, it was demonstrated numerically, in Chapters 5.5 and 5.5.1, that the cross-correlation between the breakpoint excursion (proxy for the short wave envelope outside the surf zone) and the shoreline excursion can provide useful information about infragravity wave behavior in the inner and swash zone.

Using the visual manifestation of both breakpoint and shoreline motion, a novel method to determine the dominant infragravity mechanism in the inner surf and swash zone in the field is presented. The identification of the dominant forcing mode is made by interpreting the relationship between breakpoint oscillation and shoreline motion, which are measured remotely via video. The differentiation between bound wave and breakpoint forcing is based on the specific relationships previously determined in the Thesis.

The method is applied to three different beaches during distinct wave conditions. Pressure sensors and offshore wave information are also used in the analysis. The methodology, description of the field sites and particular characteristics of each fieldwork are described in the next section. The results and discussion are presented in section 6.3, followed by the final conclusions (section 6.4).

## **6.2 Data Collection and Analysis**

Thirteen field data sets were collected from three different beaches under different wave conditions (table 6.1). For each field site wave data and visual surf zone information were collected using pressure sensors and remote video sensing. Deep water wave conditions were obtained from the nearest wave buoy. During most of the data collection, two pressure sensors, one placed outside the surf zone and another close to the swash zone, were deployed. In total, 37 hours of pressure data were collected and converted to surface elevation using linear wave theory.

The video images (Figure 6.1a) were corrected for lens distortion and rectified, using collinearity equations and ground control points (Holland et al., 1997), converting image to ground coordinates. A cross-shore line of pixel intensity is extracted from each processed image, generating a detectable cross-shore time evolution of the surf and swash zone, also known as a timestack (Aagaard and Holm, 1989). From the timestacks, the time evolution of the breakpoint and run-up were extracted, as illustrated in Figure 6.1b. Due to the difficulties in fitting a single algorithm to suit all cases (especially to extract the run-up excursion) the breakpoint and shoreline excursion were selected manually. Difficulties related to automate shoreline detection have also been reported in different studies (Guedes et al., 2011, Power et al., 2011, Stockdon et al., 2006). Band-pass Fourier filtering, cross-correlation and spectral analysis were carried out to investigate infragravity wave dynamics. Both pressure and image data were collected at 4Hz, the cross-correlation (equation 3.1) is applied for time series of 2 hours duration (28800 data points), with bound limits of approximately  $\pm 0.01$  for a 95% confidence interval (Box et al., 1994).

Infragravity wave dependence on short wave amplitude was analyzed based on the data measured at  $PT_{off}$  and  $PT_{in}$ . The time series were divided into 30min bursts, where the total  $Hm0$  and infragravity  $Hm0_{IG}$  were calculated. Their power-law relationship is estimated using least square fitting; the same analysis is also applied to different infragravity frequency bands.

The relationship between infragravity waves, the wave envelope, the breakpoint and the run-up excursion are discussed, based on the cross-correlation analysis. The extracted breakpoint and run-up excursions are used to determine the dominant surf beat mechanism in the inner surf and swash zone, following their previously established relationship (Chapter 5.5.1). For each timestack, the bore propagation paths are averaged to produce an estimate of the travel time between the mean breakpoint position and the shoreline. Following the previous chapters, the cross-shore coordinate system orientation is defined as positive shoreward (horizontal) and upwards (vertical).

The normalized beach slope  $\beta_n$  (Battjes et al., 2004) (equation 3.11) and the surf beat similarity parameter,  $\xi_{sb} = \beta\sqrt{H/L}$  (Baldock, 2012) ( $H/L$  is the deep water wave steepness), were calculated (Table 6.1).

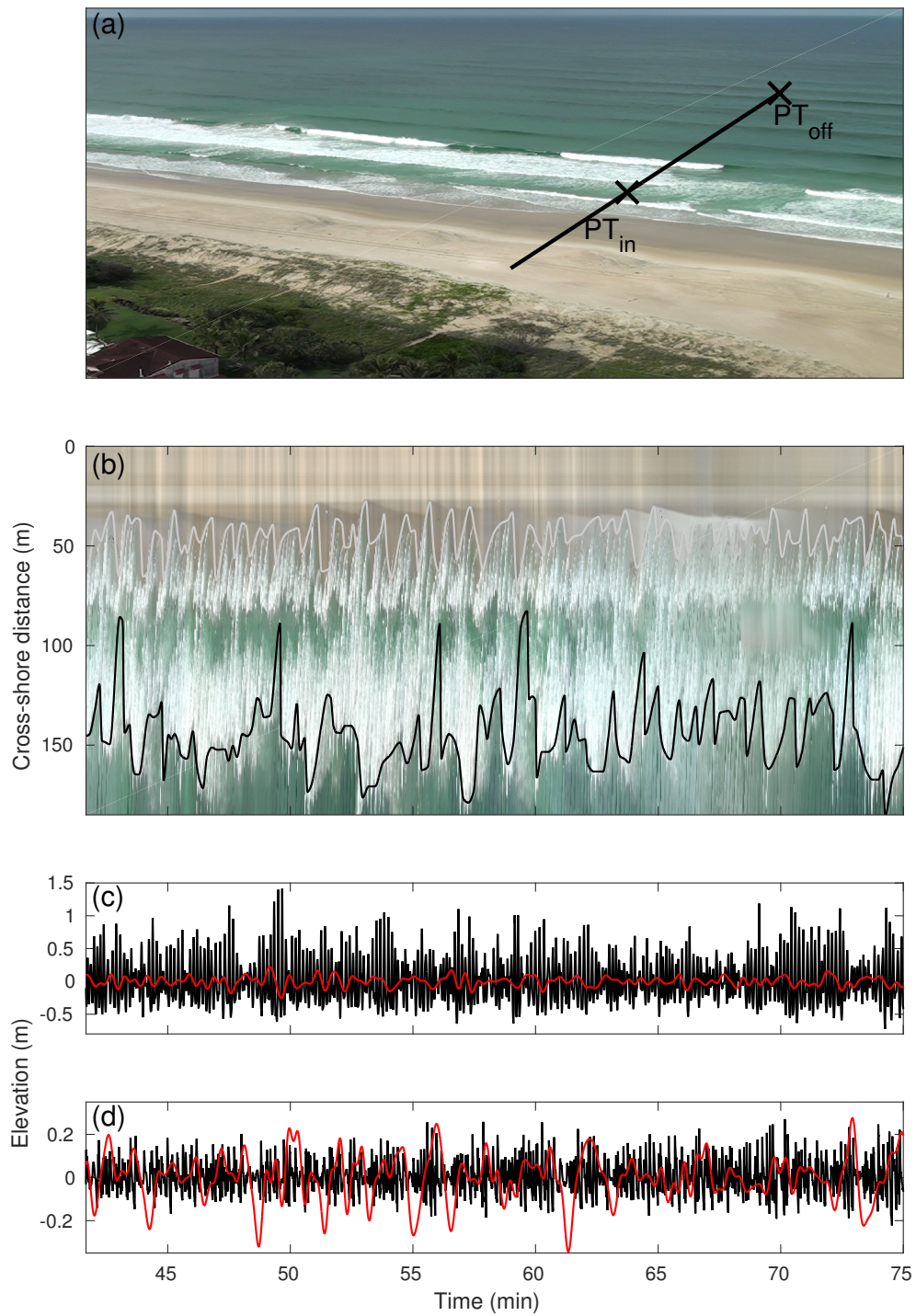


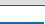


FIGURE 6.1: (a) Original image with the cross-shore transect. (b) Timestack of the swash and surf zone, Palm Beach QLD. Breakpoint (black line) and shoreline (grey line) excursion. (c) and (d) Short (black) and infragravity waves (red) at  $PT_{off}$  and  $PT_{in}$ , respectively.



TABLE 6.1: Field experiments and conditions. Location, date, peak period ( $T_p$ ) and significant wave height ( $H_s$ ) at the nearest wave buoy,  $H_s$ ,  $T_{low}$  (peak period at the infragravity frequency) and depth ( $h$ ) at  $PT_{off}$ . Normalized bed slope  $\beta_n$  and surf beat similarity  $\xi_{sb}$ . The color lines are use for differentiation in the following figures.

Beach	Date	Buoy		$PT_{off}$			$\beta_n$	$\xi_{sb}$	Plot
		$T_p(s)$	$H_s(m)$	$T_{low}(s)$	$h(m)$				
Conto01	30/09/14	13.5	3.4	1.7	128	5.4	0.58	0.063	
Conto02	01/10/14	13.1	2.8	1.4	128	5.4	0.58	0.059	
Conto03	02/10/14	15.0	2.8	1.8	128	4.9	0.60	0.054	
Conto04	03/10/14	13.8	2.0	1.2	128	4.9	0.60	0.050	
Palm01	03/02/15	9.5	2.0	1.6	102	5.4	0.34	0.04	
Palm02	04/02/15	11.5	2.0	1.6	102	5.6	0.34	0.032	
Palm03	05/02/15	9.8	1.6	1.1	102	5.6	0.34	0.034	
Palm04	19/02/15	10.7	2.8	–	–	–	–	–	–
Palm05	20/02/15	10.4	2.5	–	–	–	–	–	–
Palm06	21/02/15	10.4	2.5	–	–	–	–	–	–
Tallow01	08/02/14	11.0	1.0	1.25	57	5.7	0.44	0.036	
Tallow02	09/02/14	10.2	1.1	1.35	51	4.9	0.39	0.032	
Tallow03	09/05/14	12.6	2.62	–	–	–	–	–	–

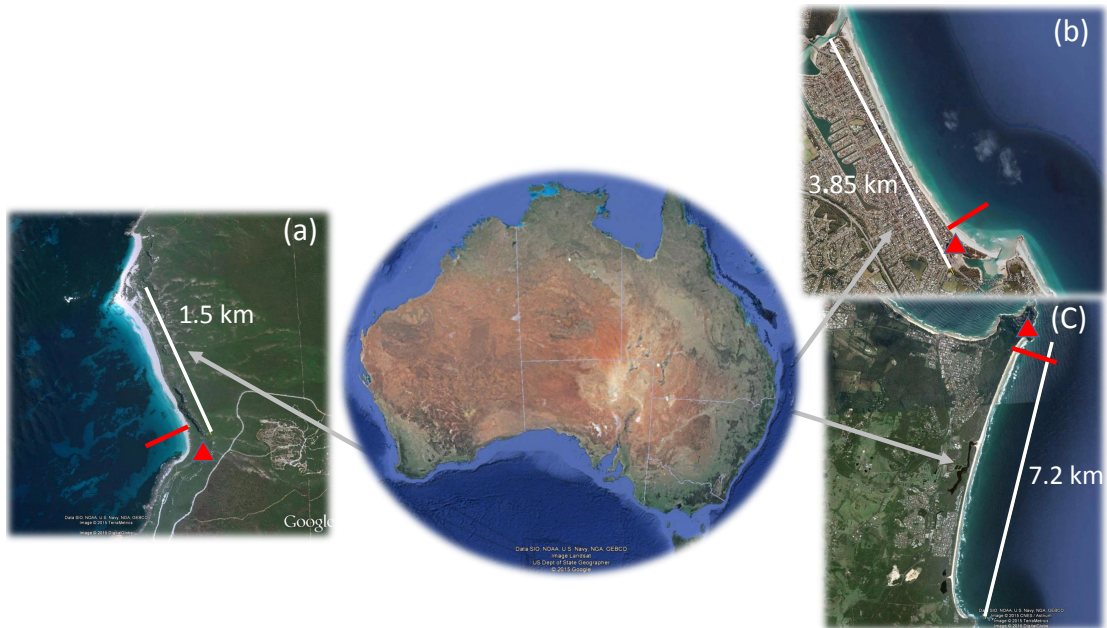


FIGURE 6.2: Geographic location of the field sites. (a) Conto Beach, WA, (b) Palm Beach, QLD and (c) Tallow Beach, NSW. The red line and the triangle indicate, respectively, the cross-shore location of the timestack and camera position for each beach. Adapted from Google Earth.

### 6.2.1 Conto Beach

Located in the south-west corner of Western Australia between Cape Naturaliste and Cape Leeuwin (Figure 6.2a), Conto Beach is a rock-sandy beach approximately 1.4km long, with a narrow and steep sub-aerial profile connected to a limestone ridge. The beach is northwest-southeast orientated, exposed to heavy southwesterly swells generated in the Indian Ocean.

Data were collected along four consecutive days with reasonably large and long period swell, for the first three days followed by smaller and windier condition during the last day of measurement. The wave conditions measured at  $PT_{off}$  and the Cape Naturalise wave buoy are presented in Figure 6.3. The wave buoy is located 60km north at a water depth of 50m.

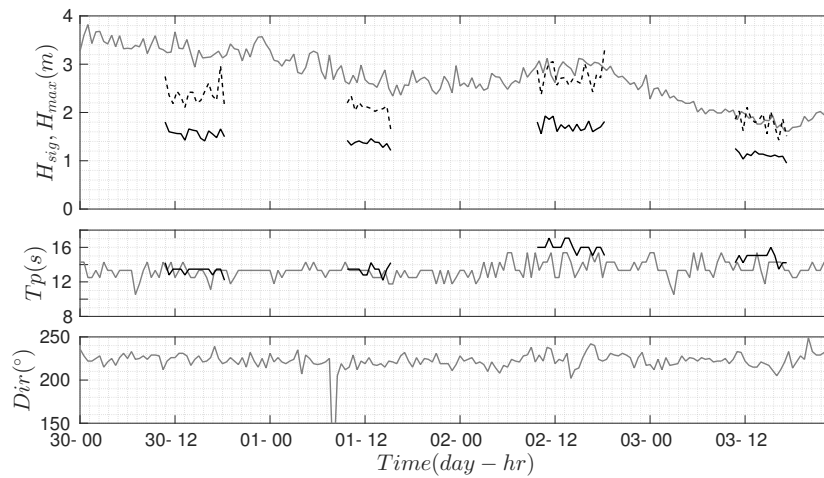


FIGURE 6.3: Wave conditions at the Cape Naturaliste wave buoy (grey line) and at  $PT_{off}$  (black line). Top panel:  $H_{sig}$  solid line and  $H_{max}$  dashed line.

During the entire fieldwork, in the center part of the beach, a strong rip-current was observed. The rip-current was continuously oscillating in both cross and long shore direction, with periods where it extend beyond the surf zone (Figure 6.4). The sequence of time average pixel intensity indicates that the intensity and shape of the rip-current was strongly affected by the infragravity waves, the interaction between those two processes has been the focus of many studies (Aagaard et al., 1997, MacMahan et al., 2004, 2006, among others).

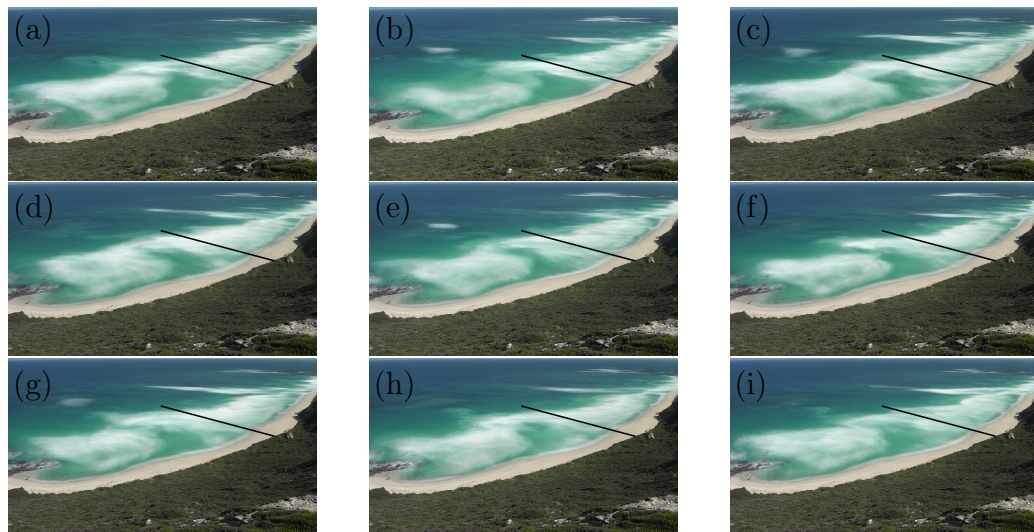


FIGURE 6.4: Sequence (a-i) of average pixel intensity images for Conto Beach. Total time of 18 minutes, each image is average over 2 minutes. Black line is the Cross-shore location of the timestacks.

### 6.2.2 Palm Beach

Palm Beach is a north-east facing beach located on the south-east coast of Queensland (Figure 6.2b). It is approximately 4km long bounded by two creeks, Talabugera Creek (to the north) and Currumbin Creek (to the south). Both creeks have training walls that extend into the surf zone. Additionally two smaller groynes (center part of the beach) and a sea wall have been built to reduce and prevent damage caused by beach erosion. According to Short (2000), the average wave height is 1.5m and the beach profile is, generally, composed of two bars approximately 200m wide, similar to most beaches in the region. Figure 6.5 shows a typical beach profile for Palm Beach; during the experiments only shallower sections of the profile were measured.

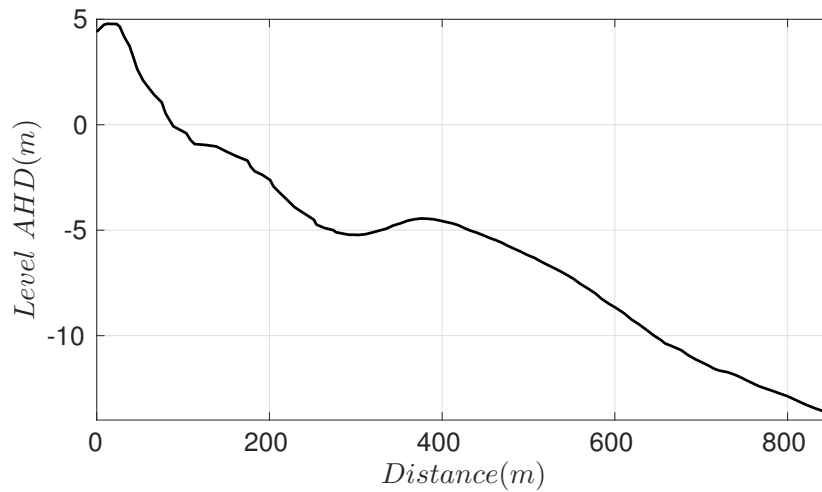


FIGURE 6.5: Palm Beach profile, measured at 30/04/10. Data from Haines (2013).

Two separate fieldwork experiments were conducted, with 3 days duration each. During the first experiment the wave conditions at  $PT_{off}$  were similar for the first two days. On the last day the waves dropped considerably, even though the offshore  $H_s$  and  $T_p$ , were relatively constant during the entire experiment. The most significant change was in the wave direction, which shifted on the last day from east to south-east (Figure 6.6). Due to the orientation of the coast, most of the Gold Coast beaches are less exposed to southerly waves, hence this probably explains the smaller nearshore conditions. The offshore wave condition was measured at the Gold Coast wave buoy, located in Southport, approximately 15km north of Palm beach, at water depths of 17m. The surf zone was relatively small ( $< 100\text{m}$ ) during the entire experiment with the waves breaking only on the inner bar (Figure 6.7).

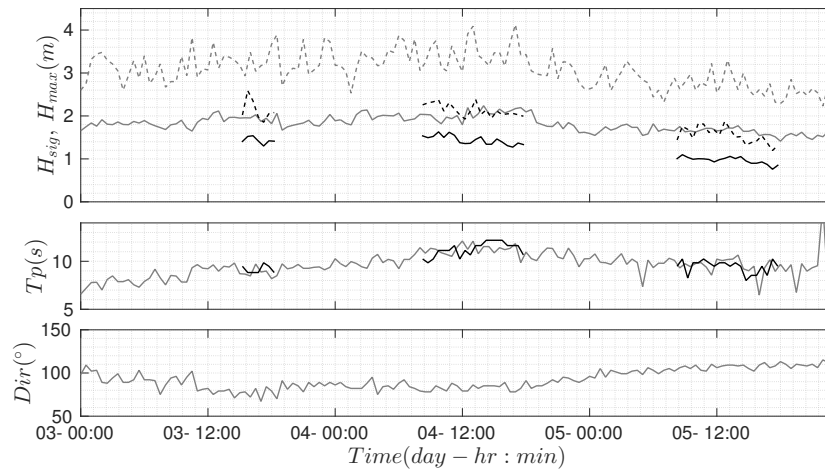


FIGURE 6.6: Wave conditions at the Gold Coast wave buoy (gray line) and at  $PT_{off}$  (black line). Top panel:  $H_{sig}$  solid line and  $H_{max}$  dashed line. Top panel:  $H_{sig}$  solid line and  $H_{max}$  dashed line.



FIGURE 6.7: Image of pixel intensity average over 5 minutes, Palm Beach.

The second fieldwork experiment was performed under more energetic wave conditions. No pressure sensor was deployed offshore as a result, only remote video sensing was used. The wave conditions were again stable throughout the three days, with slightly bigger waves on the first day. However, even though the wave conditions were similar, at the wave buoy, wave breaking and the surf zone width were quite variable between the days. The changes in the surf zone and their relationship with the surf beat are further investigated later in the Chapter. For both campaigns the camera was placed on an apartment balcony approximately 65m high, closer to southern end of the beach.

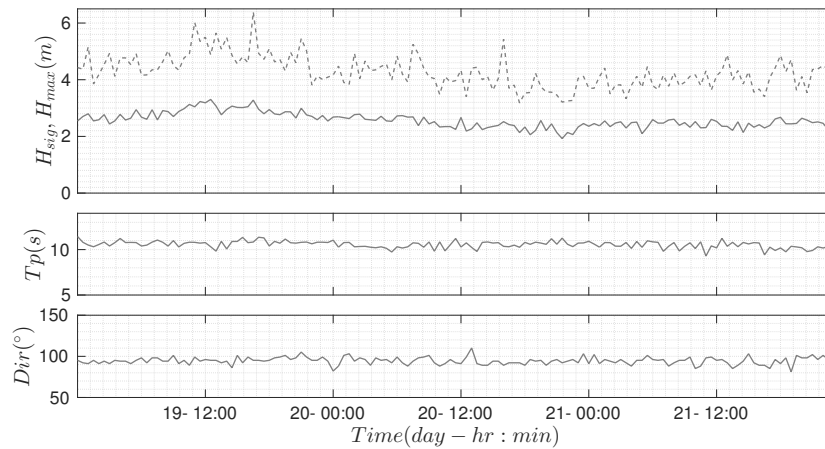


FIGURE 6.8: Wave conditions at the Gold Coast wave buoy for the second fieldwork experiment in Palm Beach. Top panel:  $H_{sig}$  solid line and  $H_{max}$  dashed line.

### 6.2.2.1 Tallow Beach

Tallow Beach is located in the north coast of New South Wales (Figure 6.2c). It is approximately 7.2km long and northwest-southeast orientated. Two separate fieldwork experiments were conducted. The first experiment was carried out during two days with mild wave conditions (Figure 6.9). Two pressure sensors were deployed in the inner surf zone and at the shoaling zone. Data from the Byron Bay wave buoy, located in front of Tallow Beach at a depth of approximately 60m, was not available for the period. The wave data from the Gold Coast wave buoy was used instead (Figure 6.9). Tallow Beach is well exposed to south and southeast swells, hence bigger waves are expected there when compared to the Gold Coast. Both video and pressure data were collected at the northern end of the beach. The camera was placed on the head land, approximately 60 meters high, capturing the entire surf zone (Figure 6.10).

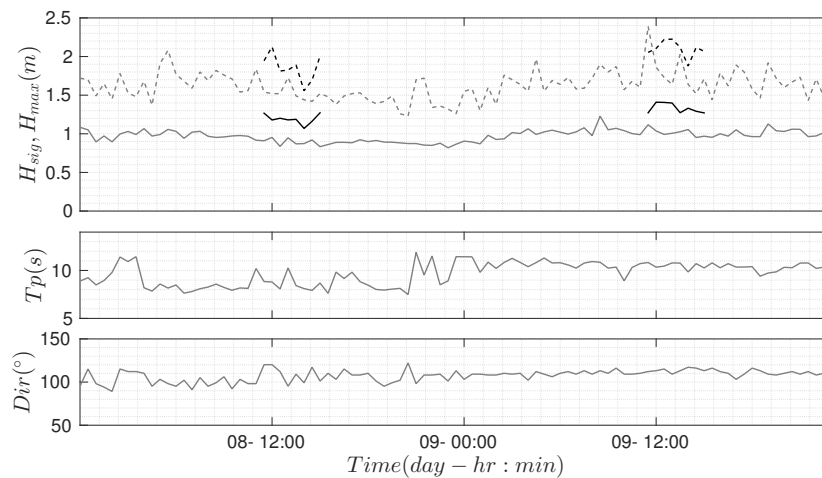


FIGURE 6.9: Wave conditions at the Gold Coast wave buoy (gray line) and at  $PT_{off}$  (black line). Top panel:  $H_{sig}$  solid line and  $H_{max}$  dashed line.



FIGURE 6.10: Image of pixel intensity averaged over 5 minutes, Tallow Beach.

The second fieldwork experiment was performed during three days under bigger wave conditions (Figure 6.11). However, due to the unfavorable rainy weather the sequence of images were compromised for the first two days, only the results of the last day are considered here. Pressure sensors were not deployed, the video data were collected at the same location of the first fieldwork.



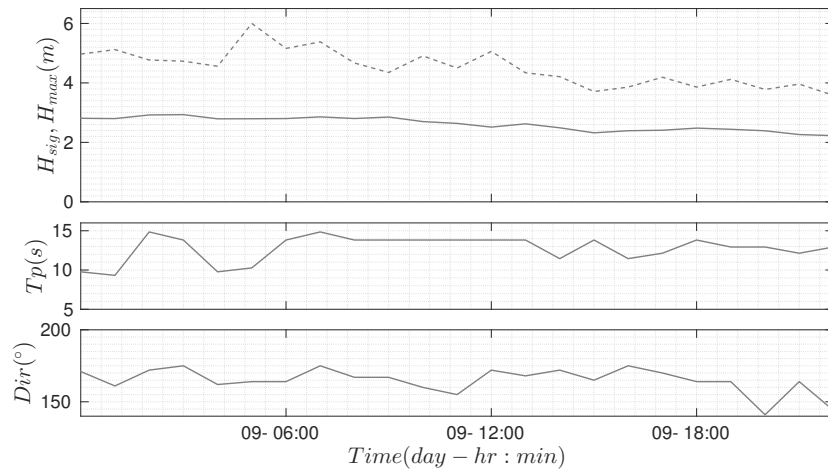


FIGURE 6.11: Wave conditions at the Byron Bay wave buoy. Top panel:  $H_{sig}$  solid line and  $H_{max}$  dashed line.

## 6.3 Results and Discussion

### 6.3.1 Power Relationship Between Short and Infragravity Wave Height

Infragravity wave dependence on short wave amplitude have been previously discussed in Section 3.6. The same methodology was applied here to estimate the power relationship between short and infragravity wave amplitude.

Similarly to the results obtained for the laboratory data, the power relationship between short and total infragravity wave amplitude outside the surf zone, for the field data, is close to quadratic ( $m = 1.84$ ), decaying to linear ( $m = 1$ ) in the inner surf zone, at  $PT_{in}$ . This initial result suggests bound wave dominance at  $PT_{off}$  and at  $PT_{in}$  strong bound wave dissipation, and/or strong influence of long waves generated by breakpoint forcing, which are linearly dependent on  $H$  (Baldock and Huntley, 2002, Nagase and Mizuguchi, 2001).

Extending the same analysis to discrete frequencies showed that, for the laboratory data,  $m$  is strongly dependent on frequency, varying from  $m \approx 2$ , in the low frequencies, to  $m \approx 0.5$ , at high frequencies (Figure 3.22, see also Baldock and

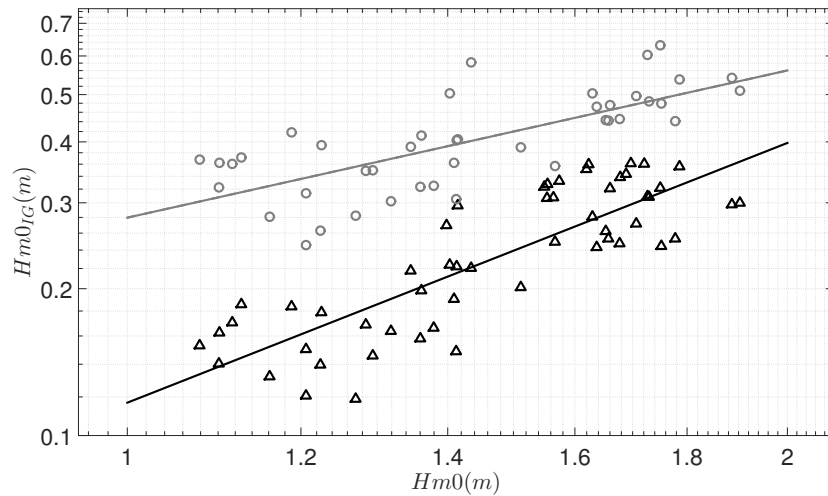


FIGURE 6.12: Power relation between  $Hm0$  and  $Hm0_{IG}$ .  $\triangle$ —  $Hm0$  and  $Hm0_{IG}$  at  $PT_{off}$ .  $\circ$ —  $Hm0$  at  $PT_{off}$  and  $Hm0_{IG}$  at  $PT_{in}$ .

Huntley (2002)). As expected from a random wave type of forcing, the energy spectrum of the surface elevation in the field has also multiple energy peaks at the infragravity band (Figure 6.13). However, differently from the laboratory cases, each spectrum has a distinct shape and frequency peaks, hence estimating  $m$  for each frequency bin of the spectrum would not be appropriate. For that reason, the frequency dependence is investigated by splitting the infragravity band ( $f_{IGi}$ ) into three sub-bands: high ( $0.02 < f_{IG1} \leq 0.04\text{Hz}$ ), mid ( $0.01 < f_{IG2} \leq 0.02\text{Hz}$ ) and low ( $0.0025 < f_{IG3} \leq 0.01\text{Hz}$ ) frequencies and comparing the  $Hm0_{IGi}$  of each sub-band with  $Hm0$ .

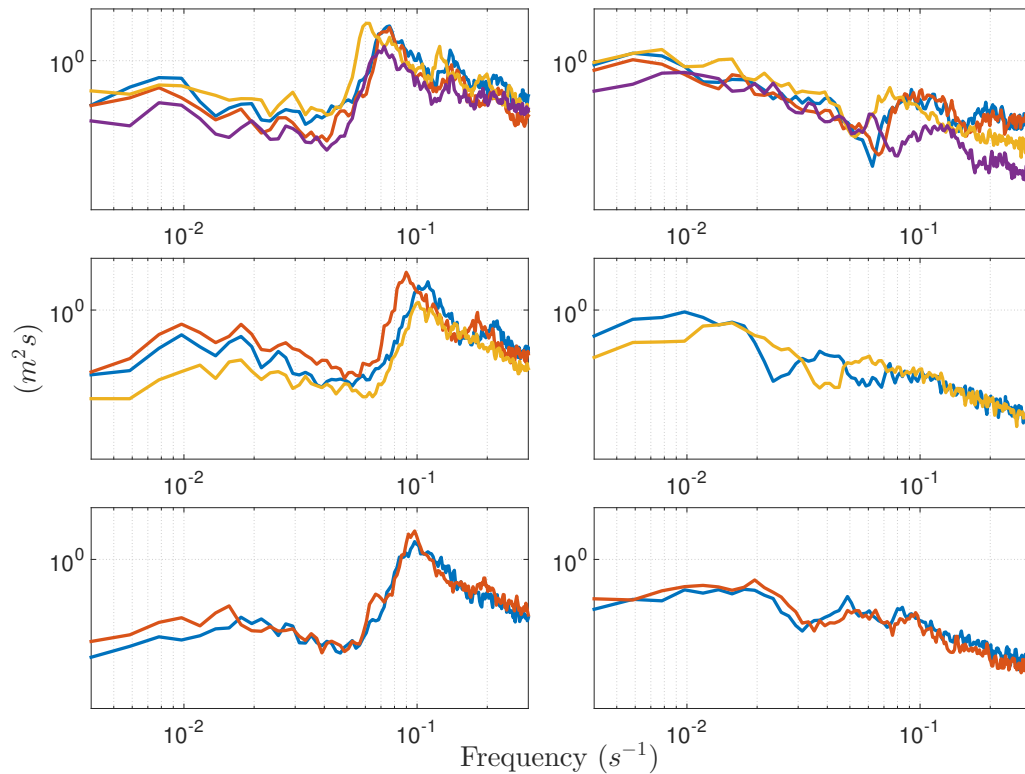


FIGURE 6.13: Surface elevation spectrum. Left:  $PT_{off}$  and right:  $PT_{in}$ . Top, center and bottom panels are, respectively, Conto, Palm and Tallow Beach. Different days of data collection are represented by different colors indicated in Table 6.1.

As shown in Figure 6.14, inside the surf zone, for the two higher frequency bands  $m < 1$ , indicating strong dissipation, while for the lowest frequency band,  $m = 2$  suggests weak or absent dissipation. A similar trend was found for the laboratory data (Figure 3.22). This pattern can be justified by two mechanisms: the decaying of the forced bound wave due to the removal of the forcing (short wave breaking) (Baldock, 2012), and the relatively stronger dissipation of higher frequency infragravity waves, in the surf zone (Battjes et al., 2004). Further details on both mechanism are found in Sections 3.5 and 5.4).

van Dongeren et al. (2007) and de Bakker et al. (2014) have shown that infragravity wave dissipation due to breaking close to the shoreline is important, mainly for relatively mild waves and mild beach face slopes. van Dongeren et al. (2007)

showed that the normalized bed slope (equation 3.11, see also Battjes et al. (2004)) controls the reflection coefficient at the shoreline according to

$$\beta_H = \frac{h_x}{2\pi f_{IG}} \sqrt{\frac{g}{H_{IG}}} \quad (6.1)$$

$$R = 0.2\pi\beta_H^2. \quad (6.2)$$

$\beta_H$  is the adapted normalized beach slope,  $f_{IG}$  and  $H_{IG}$  are respectively the infragravity frequency and infragravity wave height close to the shoreline.  $R$  is the reflection coefficient, values smaller than 1 suggest dissipation via breaking at the shoreline and values larger than 1 full reflection. For most of the data it is expected that  $R \gg 1$  (Figure 6.14, open gray circles), with the exception of the high frequency part of the infragravity waves at Tallow Beach (full gray circles,  $0.5 < R < 0.8$ ). This result suggests that the dissipation is not mainly controlled by infragravity wave breaking. Even though, in the field, it is not possible to determine the main region of dissipation, is likely that the length of the surf zone and the decay of the forcing (dissipation of the short waves) are causing the dissipation.

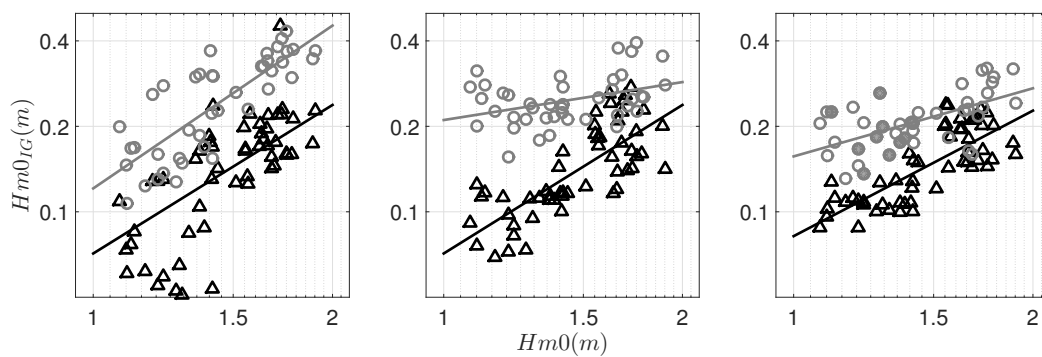


FIGURE 6.14: Power relation between  $Hm0$  and  $Hm0_{IGi}$ .  $\triangle$ —  $Hm0$  and  $Hm0_{IGi}$  at  $PT_{off}$ .  $\circ$ —  $Hm0$  at  $PT_{off}$  and  $Hm0_{IGi}$  at  $PT_{in}$ . Left:  $0.0025 < f_{IG3} \leq 0.01\text{Hz}$ , center:  $0.01 < f_{IG2} \leq 0.02\text{Hz}$  and right:  $0.02 < f_{IG1} \leq 0.04\text{Hz}$ . Full gray circles  $R < 1$ .

For the laboratory random cases, outside the surf zone,  $m$  is also frequency dependent. This was further analyzed by calculating the same power relationship, but for incident and outgoing signal, separately. It was shown that, for the incident waves, at all frequencies,  $m \approx 2$  the expected result for forced bound waves. For the outgoing waves, on the other hand,  $m$  has a well marked frequency dependence (Figure 3.23). Based on that, it is possible to infer that for the laboratory data, at higher frequencies, the infragravity wave signal is dominated by outgoing waves. On the contrary, at  $PT_{off}$ ,  $m$  is close to quadratic for all frequency bands ( $\approx 1.7$ ), with slightly larger values for the lower frequencies, suggesting bound wave dominance.

The cross-correlation between wave envelope and total infragravity wave signal at  $PT_{off}$  shows the strong presence of bound waves (Figure 6.16), even though for most cases the outgoing signal is also significant as discussed below.

### 6.3.2 Incident and Outgoing Infragravity Waves

The infragravity waves may manifest as cross-shore (leaky waves), refractively trapped (edge waves) or a combination of both. On natural systems, due to three dimensional shape and the spatial variability of the forcing mechanisms, the propagation patterns of infragravity waves can be quite complex with a superposition of leaky and edge waves. From the collected data its not possible to precisely separate cross-shore from long-shore processes. However, the interpretation of the cross-correlation results and the observation of spatial structure of the surf zone can provide important information about the cross-shore evolution of the infragravity waves.

The typical cross-correlation results between two time series containing incident and reflected signals have been discussed in Section 3.2 (see also Janssen et al. (2003)). For an idealized case, the expected result for such an analysis is 4 peaks at four different lags, representing the four possible combinations between incident and reflected waves at each location (Figures 3.2 and 3.3). These correlation peaks

were also partially observed in the field data. For instance, by cross-correlating the infragravity surface elevation at  $PT_{off}$  and at  $PT_{in}$  (Figure 6.15) it is possible to identify the correlation peaks related to the incident waves (positive lags) and the reflected waves (negative lags). Note that the lags corresponding to the correlation peak of the reflected signals are slightly smaller than the lags of the incident signal. This is to be expected as the incident waves are mainly forced waves traveling at the group velocity, while the free reflected waves propagate faster, at  $\sqrt{gh}$ .

During the shoaling process the bound wave changes significantly, both in amplitude and shape (Sections 3.3 and 3.4), while the free reflected waves reverse shoals without much change in shape. For that reason, when analyzing infragravity signals at different locations the reflected-reflected peak in the cross-correlation is usually stronger than the incident-incident peak (see also Figure 3.16). This result is to be expected only when the propagation structure is predominantly cross-shore, which is likely the case for Palm and Tallow beaches. In contrast, at Conto Beach, the incident-incident correlation peak is consistently stronger than the reflected-reflected peak, suggesting a less dominant cross-shore propagation pattern.

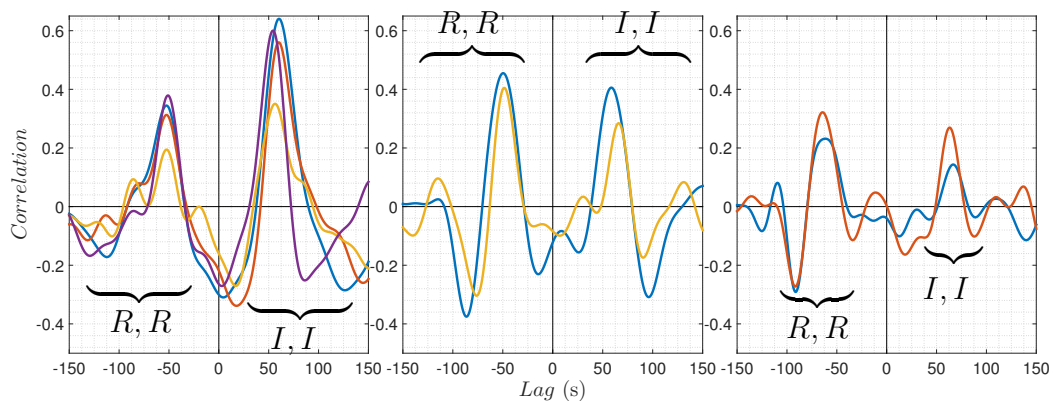


FIGURE 6.15: Cross-correlation between infragravity surface elevation at  $PT_{off}$  and  $PT_{in}$ . Left: Conto Beach, center: Palm Beach and right: Tallow Beach.  $I, I$  and  $R, R$  are the correlation peaks related to incident-incident signal and reflected-reflected signal respectively.

Furthermore, no peaks related to the correlation between incident and reflected waves were observed. These peaks are expected to be small due to the mentioned

changes in shape between bound and reflected waves. In this analysis the stronger correlation for the other two possible combinations lead to the suppression of the smaller peaks. The correlation between incident and reflected waves is better represented when, in the cross-correlation analysis, only one of the time series contains the reflected signal. For example, when applying the analysis to the wave envelope, that contains only the incident signal (the propagation of the short wave envelope), and infragravity surface elevation as in Figure 6.16. The results shows that the wave envelope is also significantly correlated with the reflected infragravity waves, mainly for Palm Beach and Tallow Beach. The negative correlation peaks at  $\tau \approx 120$ s (Palm Beach) and  $\tau \approx 145$ s (Tallow Beach) represents the travel time for the incident infragravity waves to propagate from  $PT_{off}$  to the shore plus the travel time for the reflected infragravity waves to travel from the shoreline back to  $PT_{off}$ .

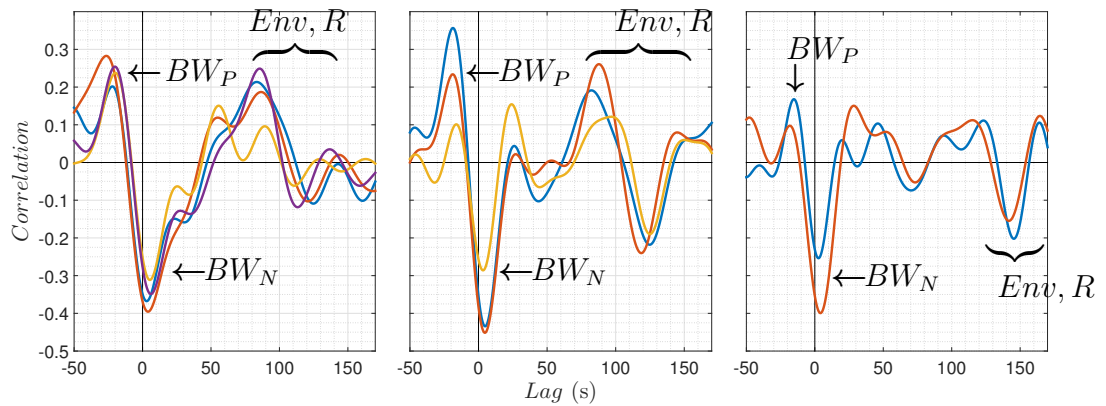


FIGURE 6.16: Cross-correlation between wave envelope and infragravity surface elevation at  $PT_{off}$ . Left: Conto Beach, center: Palm Beach and right: Tallow Beach.  $BW_N/BW_P$  are the peaks related to the cross-correlation between short wave envelope ( $Env$ ) and the negative/positive part of the bound wave.  $Env, R$  is the cross-correlation between the short wave envelope and the reflected signal.

The same observation applies to the cross-correlation between the infragravity waves at  $PT_{off}$  and the breakpoint excursion (Figure 6.17). For this data pair, the peak with positive lag represents the correlation between incident long waves and the breakpoint excursion. The lag is the travel time of the long waves from  $PT_{off}$  to the mean breakpoint. The peak with negative lag is the correlation between the reflected signal and the breakpoint excursion. The lag is the travel

time between the incident signal and the breakpoint plus the reflected travel time from the shoreline to  $PT_{off}$ . Note that differently from Figure 6.16, the peak between the incident and reflected signals has a negative lag. This is only the effect of the ordering of the data pair in the cross-correlation analysis (see Section 3.2). The horizontal axis is orientated positive shoreward, hence the offshore motion of the breakpoint is positively correlated with the bound wave.

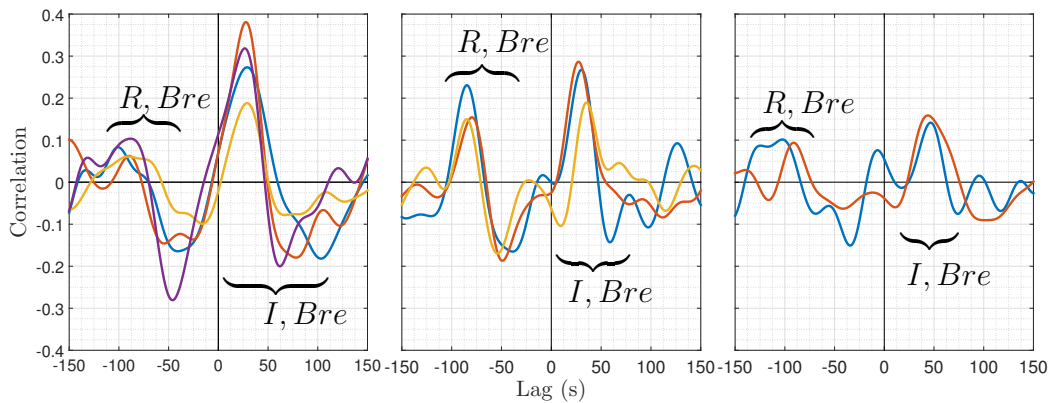


FIGURE 6.17: Cross-correlation between low-frequency motion at  $PT_{off}$  and the breakpoint excursion. Left: Conto Beach, center: Palm Beach and right: Tallow Beach. ( $I, Bre/R, Bre$ ) are the correlation peaks related to the incident/reflected infragravity wave signal and the breakpoint oscillation.

### 6.3.3 Breakpoint Forced Wave and the Positive Part of Bound Wave

In Sections 3.4 and 5.1 it was shown that the bound wave shoals with a leading positive surge, differing in shape from the horizontal bottom solution of Longuet-Higgins and Stewart (1962). When bound waves with leading surges are cross-correlated with the wave envelope, the result is a N-shaped cross-correlation, where the negative peak represents the correlation with the negative part of the bound wave, and the positive peak is the correlation with the positive leading part of the bound wave (Figure 6.16).

The N-shaped cross-correlation gets stronger towards the surf zone, this intensification can be observed in the cross-correlation peaks related to either the



reflected( $PT_{off}$ )/reflected( $PT_{in}$ ) signal in Figure 6.16 and short wave envelope/reflected signal in Figure 6.17. However, in the surf zone identifying whether the positive correlation peak has originated from the leading bound wave surge, or was forced by the breakpoint oscillation or a combination of both mechanisms is difficult. This is not the case at  $PT_{off}$  as it is located always outside the surf zone, hence the possibility of the calculated positive peaks being generated by breakpoint forcing is eliminated. Determining the main forcing of the positive surges in the surf zone is further investigated below.

### 6.3.4 Relationship Between Wave Groups, Breakpoint, Shoreline Excursion and Infragravity waves

Previously in Section 5.5 it was shown, numerically, that the breakpoint and the shoreline oscillations were good proxies for the wave group envelope (outside the surf zone) and the infragravity waves in the inner surf zone, respectively. The field data, for most of the cases, showed similar results. The shoreline is always well correlated with infragravity waves at  $PT_{in}$  (Figure 6.18).

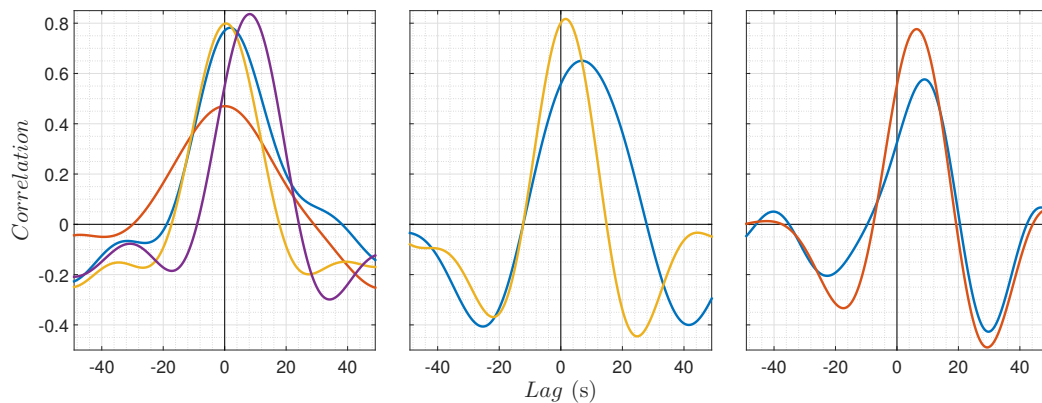


FIGURE 6.18: Cross-correlation between infragravity surface elevation at  $PT_{in}$  and Shoreline excursion. Left: Conto Beach, center: Palm Beach and right: Tallow Beach.

The breakpoint, for some days analyzed, is however poorly correlated with the wave envelope (Figure 6.19). At Conto beach a strong rip-current located in the center part of the beach (Figure 6.7) was present during the entire experiment. It

is possible that its interaction with the waves may have changed the breakpoint structure. During *Tallow01* and *Tallow02* data collection the waves were reasonably small, with a well defined breaking zone at the inner bar and a less marked, but significant, breaking zone at the outer bar (Figure 6.10). Hence, defining the breakpoint position was more subjective. The Palm beach data shows the most consistent results, during the data collection the breakpoint was well defined with small cross-shore variation in the surf zone (Figure 6.7).

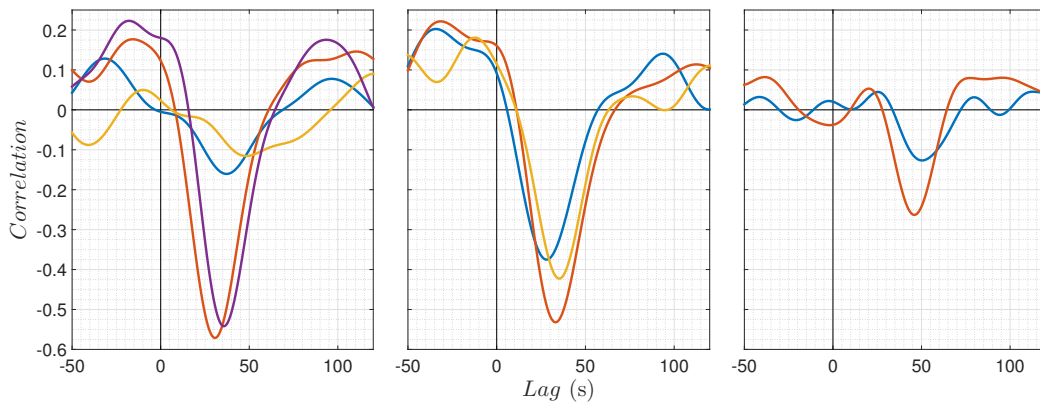


FIGURE 6.19: Cross-correlation between wave envelope at  $PT_{off}$  and breakpoint excursion. Left: Conto Beach, center: Palm Beach and right: Tallow Beach.

### 6.3.5 Determining Surf Zone Infragravity Wave Forcing

In Section 5.5.1, the cross-correlation analysis was used, in numerical simulations, to provide information about infragravity wave forcing in the surf zone. It has also been clarified in Sections 3.2.1 and 4.5 that for a random wave scenario, containing incident and reflected waves, the cross-correlation analysis displays the progressive patterns of incident and reflected signals, instead of the standing wave pattern occurring at discrete frequencies.

Based on the understanding of the expected propagation patterns generated by each forcing mechanism, and using both the cross-correlation analysis between the breakpoint and the run-up excursion, and the estimated travel time from the mean breakpoint to the shoreline, it is possible to infer the main dominant surf

beat mechanism that generated the infragravity waves observed in the inner/swash zone. For the days shown in figure 6.20 the positive peaks at lags close to the travel time of the bores suggests bound wave dominance. The negative correlation peaks at zero or negative lags are likely to be the positive leading part of the bound wave generated during the shoaling process (see Section 3.3 and 5.2). The smallest correlation peaks are observed for *Tallow01* and *Tallow02*, probably due to the fact that the breakpoint was not well defined for these days. Note that a better correlation is obtained when cross-correlating the wave envelope at  $PT_{off}$ , instead of the breakpoint excursion, and the shoreline excursion (Figure 6.21), which does not occur for the other days analyzed.

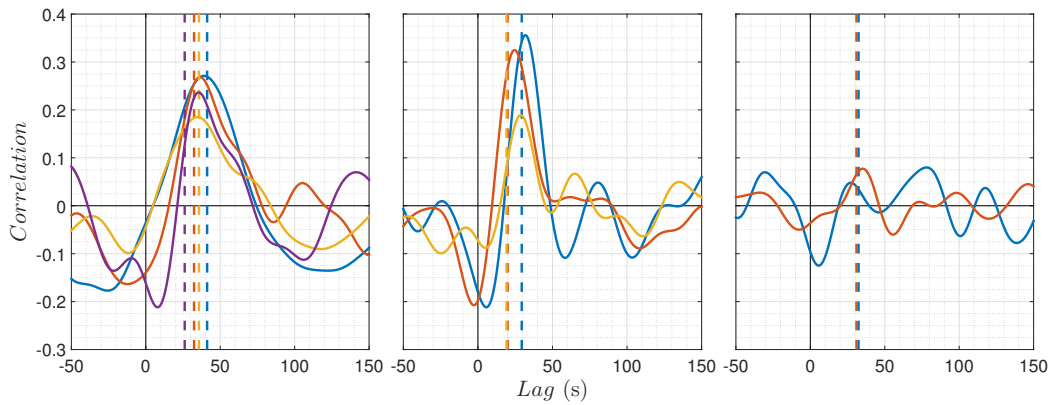


FIGURE 6.20: Cross-correlation between breakpoint and run-up excursion. Left: Conto Beach, center: Palm Beach and right: Tallow Beach. Dashed lines are the mean propagation time of the bore from the breakpoint to the shoreline.

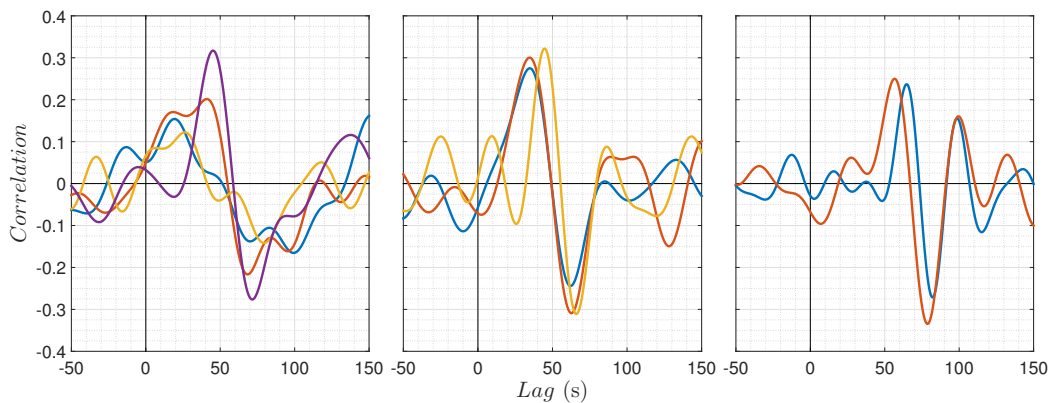


FIGURE 6.21: Cross-correlation between wave envelope at  $PT_{off}$  and run-up excursion. Left: Conto Beach, center: Palm Beach and right: Tallow Beach.

For most of the days analyzed the results suggest bound wave dominance over breakpoint forcing. However, for three days (*Palm04*, *Palm06* and *Tallow03*) the cross-correlation between breakpoint and shoreline excursions indicated breakpoint forcing. Figure 6.22 and 6.23 exemplify those differences. For *Palm01* infragravity wave depressions are propagating along with the bores generated by the breaking of the bigger waves within the wave groups, suggesting bound wave dominance. On average, the opposite is occurring for *Palm04*, even though the correlation is relatively weaker. The negative correlation peak (at lag close to the bore travel time) indicates incident breakpoint forced long wave dominance over the bound waves. During *Palm01* the waves were relatively small with a smaller surf zone and plunging breaking conditions. On the other hand, for *Palm04* the waves were bigger and the surf zone was very wide, with a visible spilling type of wave breaking (Figure 6.23).

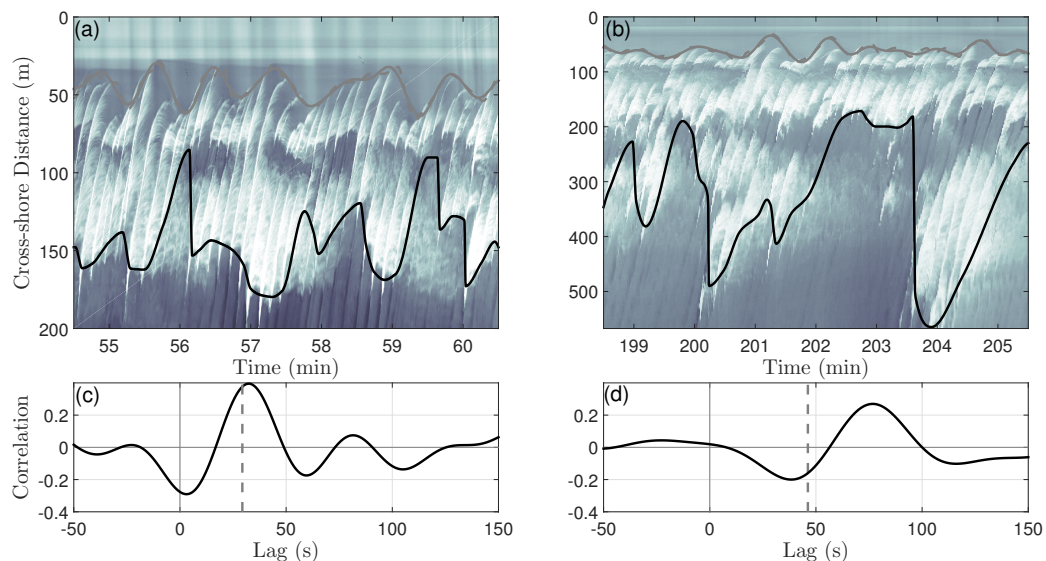


FIGURE 6.22: Timestack and cross-correlation between breakpoint and run-up excursion for *Palm01* (left) and *Palm04* (right). Dashed lines are the mean propagation time of the bores from the initial breakpoint to the maximum run-up.

Interestingly during the second fieldwork experiment performed at Palm Beach (*Palm04, 05, 06*) the offshore waves were quite stable for the entire experiment. However, in shallow water the wave conditions were visibly different for each day.

Based on visual observation the waves did not change much in size, but the shape of the waves and the width of the surf zone were clearly different for each day, as shown in the timestacks in Figure 6.23.

The cross-correlation analysis of the breakpoint and shoreline excursion showed that for *Palm04* and *Palm06*, in the inner/swash zone, the infragravity waves were mainly breakpoint forced (Figure 6.23). The opposite was found for *Palm05*, where the results indicate bound wave dominance.

As shown in Figures 5.12 and 6.19, the breakpoint is generally a proxy for the short wave envelope at the shoaling zone. However as discussed and verified in Sections 3.7 and 4.5, the breakpoint also oscillates at frequencies that are not present in the short wave envelope. It was demonstrated for bichromatic wave groups cases that particular frequencies measured in the surface elevation, both inside and outside (depending on the  $\chi$  values) the surf zone, were not present in the short wave group envelope. But they were well marked in the breakpoint excursion. Note that, based on the bound wave theory, the generated infragravity waves must have the same frequencies as the forcing (short wave envelope). The observation of infragravity waves at frequencies that are not present in the short wave envelope is a clear indication of surf beat forced by surf zone oscillations (Figures 4.23 and 4.24).

Here the same approach used in Section 4.5 is applied to the field data. By comparing the spectra of surface elevation, short wave envelope (at  $PT_{off}$ ), shoreline and breakpoint oscillation, it is possible to detect infragravity waves with frequencies that are not in the short wave envelope (no bound wave forcing at these frequencies), but only present in the breakpoint spectrum. Figure 6.24 shows the results for *Palm03*, *Conto03* and *Conto04*. Even though the previous analysis showed that for those days the bound wave release is the main forcing mechanism in the surf zone, there are still infragravity waves at frequencies that match only the breakpoint spectrum, which are indicated by the vertical dashed lines. While these waves are constantly present in the shoreline excursion, the same does not occur at  $PT_{off}$ , which may suggest an interference pattern outside the surf zone.

The analytical (Symonds et al., 1982) and numerical solution for the outgoing wave and nondimensional surf zone width ( $\chi$ ) is shown in Figure 4.20.

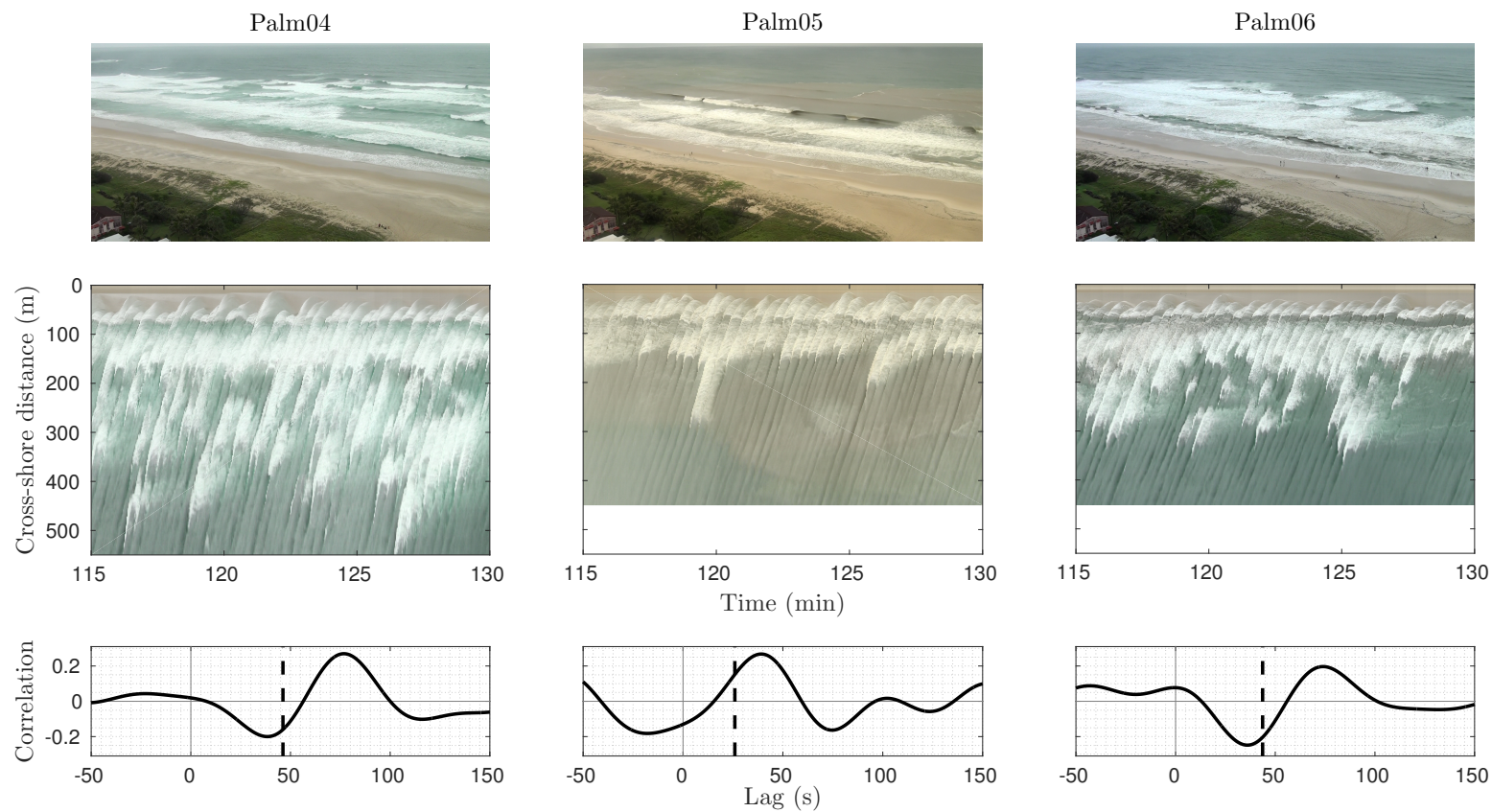


FIGURE 6.23: Top panels: original image; Mid panels: timestacks; Bottom panels: cross-correlation between breakpoint and run-up excursion for *Palm04,05,06*. Dashed lines are the mean propagation time of the bores from the initial breakpoint to the maximum run-up.

In order to evaluate a possible interference pattern,  $\chi$  was calculated (equation 2.17), for each frequency, using the mean position of the breakpoint and shoreline excursion as the surf zone width (Table 6.2). The infragravity wave identified for *Palm03* is strongly present at  $PT_{off}$ , indicating a constructive interference. For *Conto03* the signal is weak at  $PT_{off}$ , the calculated  $\chi = 7$  suggests a weak constructive interference. No peak is observed at  $PT_{off}$ , for *Conto04*, indicating a destructive interference which is expected for  $\chi = 4.6$ .

TABLE 6.2: Target frequency ( $f$ ), mean surf zone width ( $X_{mean}$ ), normalized surf zone width ( $\chi$ ) and expected outgoing wave amplitude interference.

Location	$f(Hz)$	$X_{mean}(m)$	$\chi$	Outgoing Wave Interference
<i>Palm03</i>	0.0185	100	8.4	strongly constructive
<i>Conto03</i>	0.014	184	7.0	weak constructive
<i>Conto04</i>	0.016	94	4.6	destructive

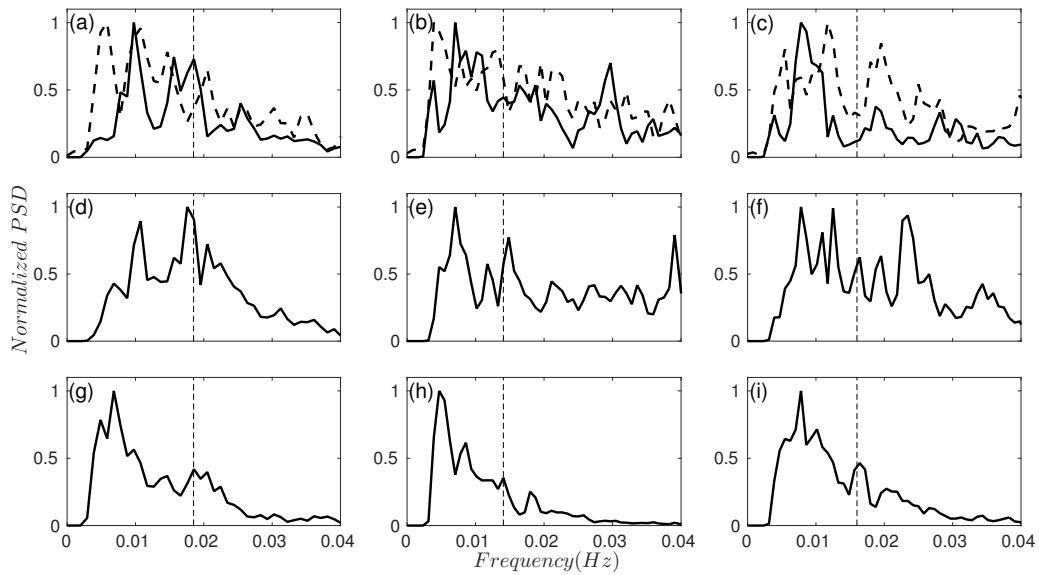


FIGURE 6.24: Normalized power spectrum of surface elevation (full line) and short wave envelope (dot-dashed line) at  $PT_{off}$  (a-b-c), run-up (d-e-f) and breakpoint excursion (g-h-i). Vertical dashed lines indicate the frequency peaks that are on the surface elevation, run-up and breakpoint excursion spectra, but are not in the short wave envelope spectrum. Panels: *Palm03* (left), *Conto03* (center) and *Conto04* (right).



## 6.4 Conclusions

A novel method to determine the dominant infragravity forcing mechanism in the inner surf and swash zone has been presented. The breakpoint oscillations and the shoreline motion are measured remotely via video and their relationship identified via cross-correlation. The identification of the dominant forcing mode, either bound wave or breakpoint, was interpreted based on the specific relationships previously determined. Thirteen field data sets, of video images and pressure sensors deployed at the shoaling zone and at the inner surf zone, were collected from three different beaches.

Similar to what was observed for the laboratory data and numerical results, the infragravity wave dissipation inside the surf zone is frequency dependent, being stronger at higher frequencies. For all beaches, outside the surf zone, the infragravity wave amplitude dependence on short wave amplitude is frequency independent and likely to be dominated by bound waves.

The cross-correlation results between the short wave envelope and infragravity waves at  $PT_{off}$  (Figure 6.16), and between the infragravity signal at  $PT_{off}$  and  $PT_{in}$  (Figure 6.15) showed that strong shape change occurs in the shoaling and surf zone. In the inner surf zone, the incident surf beat is generally  $\mathcal{V}$ -shaped, similar to what was observed by Contardo and Symonds (2013), List (1992), Masselink (1995), Pomeroy et al. (2012). After shoreline reflection, between  $PT_{in}$  and  $PT_{off}$  the outgoing wave propagates without much change in shape, as expected for a progressive long wave. Both laboratory data and numerical results presented in the previous chapters have shown that the surf zone is the region where the changes in shape of the surf beat is stronger, suggesting a contribution of breakpoint forcing. However, based on Figure 6.16 and the results of section 6.3.5, it possible to infer that the positive part of the bound wave is also important.

The relationship between the breakpoint and shoreline excursions suggested that

for most of the days analyzed bound wave release was the dominant forcing mechanism. However, for *Palm04*, *Palm06* and *Tallow03* breakpoint forcing was dominant. The results suggested that inside the surf zone the dominant forcing is strongly dependent on the surf zone width and the type of short wave breaking. Infragravity waves generation by bound wave release is stronger for conditions with relatively narrow surf zones and plunging waves. Breakpoint forcing is dominant for wider surf zones and spilling breaker conditions. This result, summed to the observed dissipation in the surf zone, suggests that the bound waves remained forced inside the surf zone, being dissipated during short wave breaking (Baldock, 2012).

Measured surf beat at frequencies that were not in the short wave envelope spectrum, but present in the breakpoint oscillation spectrum, and their reasonable agreement with the expected outgoing wave amplitude interference patterns, suggested that these waves are likely to be forced by the breakpoint mechanism.

Finally, this work shows that the breakpoint and shoreline oscillations are relevant features to interpret the surf beat mechanics. The adopted methodology is based on commonly used techniques that can be easily implemented in remote sensing systems used for regular coastal monitoring, enabling easier data collection in more extreme wave conditions.

# Chapter 7

## Thesis Summary and Future Research

### 7.1 Summary of Conclusions

In order to achieve the initial goal of determining, in the field, the main surf beat forcing mechanism in the inner surf and swash zone, a practical methodology has been proposed and tested. The technique uses the advantage of the visual manifestation of breakpoint and run-up excursion, which can be measured remotely. By comparing the observed cross-correlation between these two features with their expected cross-correlation result for each forcing mechanism, bound wave release and breakpoint forcing are differentiated. The expected relationship for each mechanism was determined after an extensive investigation of the infragravity wave dynamics that comprised a critical literature review, re-analysis of previous published laboratory data and numerical modeling. Numerical validation, implementation and testing of the infragravity wave forcing mechanisms were done before using this tool in the investigation. The main contributions of the Thesis to the key aspects explored in this work (Chapter 2.3) are summarized below.

It was confirmed here that the positive surge leading the negative part of bound wave, observed in many different studies, is forced by bound wave shoaling. However, after compiling the information from the analysis performed for the laboratory data and from the numerical simulations it is still not possible to precisely determine whether, in the presence of short amplitude modulated waves, the positive part of the bound wave is forced or free.

On the other hand, when the infragravity waves are numerically modelled uncoupled from the short waves (using only radiation stress gradients) the results are conclusive. The forced part is purely negative and changes during the forcing propagation over a sloping bottom generate positive free waves. It has been also shown that for this scenario the previously observed group frequency dependence on bound wave shoaling is actually caused by the interference between forced (negative) and positive free waves and not by different rates of energy transfer.

A general overview of infragravity wave dissipation inside the surf zone was presented. From the literature review three different hypothesis were investigated, two of these are directly related to the bound wave release and/or dissipation. The bound wave release mechanism proposed by Nielsen et al. (2008) has been numerically investigated. For a horizontal bottom it was demonstrated that by stretching the region of the forcing decay (similar to short wave dissipation in the surf zone) the amplitude of the released bound wave was reduced when compared to the same bound wave released during an abrupt removal of the forcing. This result is in qualitative agreement with the observed infragravity wave dissipation frequency dependence, where higher frequencies are strongly dissipated. Interestingly, the opposite results were obtained when the same approach was extended to infragravity waves forced over a sloping bottom. It was shown that this is likely to occur due to an interference with the positive free wave, generated during the shoaling process, and the negative released free wave, generated during the forcing cessation.

As mentioned above, the infragravity wave dissipation is strongly frequency dependent, which has been confirmed in the laboratory data, numerical simulations

and field data. This dependence is likely to be partially explained by the surf zone width, as proposed by Battjes et al. (2004) and/or the bound wave remaining forced inside the surf zone and decaying with forcing (short wave breaking), as suggested by Baldock et al. (2004) and Baldock (2012).

Clear evidence of the breakpoint forcing mechanism was observed for some of the laboratory cases. For the bichromatic cases, new evidence of breakpoint forcing surf beat at multiple frequencies, including at triad combinations, has been presented.

The breakpoint and shoreline oscillations were confirmed as proxies for the short wave envelope (at the shoaling zone) and the infragravity wave oscillation in the inner surf zone, respectively. From the numerical investigation and the large amount of laboratory data re-analyzed, clear and distinct relationships between the breakpoint and shoreline excursions have been established for each generation mechanism.

The relationship between breakpoint and shoreline oscillations suggested breakpoint forcing dominance for the laboratory data, in agreement with Baldock and Huntley (2002). On the other hand, for the field data, for most of the days analyzed, bound wave release was dominant. From the thirteen data sets, in only three the analysis indicated breakpoint forcing dominance. Inside the surf zone, the forcing dominance is strongly dependent on the surf zone width and the type of short wave breaking. Infragravity wave generation by bound wave release is stronger for conditions with relatively narrow surf zones and plunging waves. Breakpoint forcing is dominant for wider surf zones and spilling breaker conditions. For the field data, a similar analysis as that used for the bichromatic cases has shown that for some of the data sets, even where bound wave release was clearly dominant, some other frequencies measured in the surface elevation are likely to be forced by surf zone oscillations, i.e breakpoint forcing.

## **7.2 Suggestions for Future Research**

It is clear that some of the aspects investigated in this thesis have not been entirely resolved. However, following the important findings presented here, some new insights for further investigation are proposed.

The study has shown that establishing a full link between the dynamics of coupled and uncoupled treatment of infragravity waves with respect to the amplitude modulated short waves is needed. Another important task is determining whether, under natural conditions, the bound wave is purely negative or is evenly distributed around the still water line.

Introducing long-shore variability to the numerical analysis and defining the breakpoint and shoreline relationship in the presence of refractively trapped long waves may extend the applicabilities of the methodology proposed here.

Finally additional data would be useful to investigate particular conditions leading to either the bound wave release or breakpoint forcing dominance such as run-up amplitude, run-up distribution and infragravity wave dissipation in the surf zone.

# Bibliography

- Aagaard, T. and Holm, J. Digitization of wave run-up using video records. *Journal of Coastal Research*, 5(3):547–551, 1989. doi: 10.2307/4297566.
- Aagaard, T., Greenwood, B., and Nielsen, J. Mean currents and sediment transport in a rip channel. *Marine Geology*, 140(1–2):25–45, 1997. doi: 10.1016/S0025-3227(97)00025-X.
- Aarninkhof, S. G. J., Ruessink, B. G., and Roelvink, J. A. Nearshore subtidal bathymetry from time exposure video images. *Journal of Geophysical Research: Oceans*, 110(C6), 2005a. doi: 10.1029/2004JC002791.
- Aarninkhof, S. G. J., Ruessink, B. G., and Roelvink, J. A. Nearshore subtidal bathymetry from time-exposure video images. *Journal of Geophysical Research: Oceans*, 2005b.
- Baldock, T. and Holmes, P. Simulation and prediction of swash oscillations on a steep beach. *Coastal Engineering*, 36(3):219–242, 1999. doi: 10.1016/S0378-3839(99)00011-3.
- Baldock, T. and Simmonds, D. Separation of incident and reflected waves over sloping bathymetry. *Coastal Engineering*, 38(3):167–176, 1999. doi: 10.1016/S0378-3839(99)00046-0.
- Baldock, T., Huntley, D., Bird, P., O’Hare, T., and Bullock, G. Breakpoint generated surf beat induced by bichromatic wave groups. *Coastal Engineering*, 39(2–4):213–242, 2000. doi: 10.1016/S0378-3839(99)00061-7.
- Baldock, T. E. Long wave generation by the shoaling and breaking of transient wave groups on a beach. *Proceedings of the Royal Society of London A: Mathematical, Physical and Engineering Sciences*, 462(2070):1853–1876, 2006. doi: 10.1098/rspa.2005.1642.
- Baldock, T. E. Dissipation of incident forced long waves in the surf zone - implications for the concept of ”bound” wave release at short wave breaking. *Coastal Engineering*, 60:276–285, 2012. doi: 10.1016/j.coastaleng.2011.11.002.
- Baldock, T. E. and Huntley, D. A. Long-wave forcing by the breaking of random gravity waves on a beach. *Royal Society of London Proceedings Series A*, 458: 21–77, 2002. doi: 10.1098/rspa.2002.0962.

- Baldock, T. E., O'Hare, T. J., and Huntley, D. A. Long wave forcing on a barred beach. *Journal of Fluid Mechanics*, 503:321–343, 2004. doi: 10.1017/S002211200400792X.
- Battjes, J. A., Bakkenes, H. J., Janssen, T. T., and van Dongeren, A. R. Shoaling of subharmonic gravity waves. *J. Geophys. Res.*, 109(C2):n/a–n/a, 2004. doi: 10.1029/2003JC001863.
- Bowers, E. Low frequency waves in intermediate water depths. *Coastal Engineering Proceedings*, 1(23), 1992.
- Box, G. E. P., Jenkins, G. M., and Reinsel, G. C. *Time Series Analysis: Forecasting and Control. 3rd ed.* Englewood Cliffs, NJ: Prentice Hall, 1994.
- Butt, T. and Russell, P. Hydrodynamics and cross-shore sediment transport in the swash-zone of natural beaches: A review. *Journal of Coastal Research*, 16(2):255–268, 2000.
- Chen, Q. Fully nonlinear boussinesq-type equations for waves and currents over porous beds. *Journal of Engineering Mechanics*, 132(2):220–230, 2006. doi: 10.1061/(ASCE)0733-9399(2006)132:2(220).
- Choi, J., Kirby, J. T., and Yoon, S. B. Boussinesq modeling of longshore currents in the sandyduck experiment under directional random wave conditions. *Coastal Engineering*, 101:17–34, 2015. doi: 10.1016/j.coastaleng.2015.04.005.
- Contardo, S. and Symonds, G. Infragravity response to variable wave forcing in the nearshore. *Journal of Geophysical Research: Oceans*, 118(12):7095–7106, 2013. doi: 10.1002/2013JC009430.
- de Bakker, A., Tissier, M., and Ruessink, B. Shoreline dissipation of infragravity waves. *Continental Shelf Research*, 72:73–82, 2014. doi: 10.1016/j.csr.2013.11.013.
- Dong, G., Ma, X., Perlin, M., Ma, Y., Yu, B., and Wang, G. Experimental study of long wave generation on sloping bottoms. *Coastal Engineering*, 56(1):82–89, 2009. doi: 10.1016/j.coastaleng.2008.10.002.
- Elgar, S. and Guza, R. T. Shoaling gravity waves: comparisons between field observations, linear theory and a nonlinear model. *J. Fluid Mech.*, 158:47–70, 1985.
- Fengyan, S., Kirby, J., and Tehranirad, B. *Tsunami benchmark results for spherical coordinate version of FUNWAVE-TVD (version 2.0)*. Newark, DE: Center for Applied Coastal Research, Department of Civil and Environmental Engineering, University of Delaware, 2012.
- Fengyan, S., Kirby, J., Tehranirad, B., Harris, J., and Grilli, S. *Fully Nonlinear Boussinesq Wave Model with TVD Solver Documentation and User's Manual (version 2.0)*. Newark, DE: Center for Applied Coastal Research, Department of Civil and Environmental Engineering, University of Delaware, 2013.



- Freilich, M. and Guza, R. T. Nonlinear effects on shoaling surface gravity waves. *Philos. Trans. Royal Soc. London, Ser A.*, 311:1–41, 1993.
- Frigaard, P. and Brorsen, M. A time-domain method for separating incident and reflected irregular waves. *Coastal Engineering*, 24(3–4):205–215, 1995. doi: 10.1016/0378-3839(94)00035-V.
- Fuhrman, D. R. and Madsen, P. A. Tsunami generation, propagation, and run-up with a high-order boussinesq model. *Coastal Engineering*, 56(7):747–758, 2009. doi: 10.1016/j.coastaleng.2009.02.004.
- Gallagher, B. Generation of surf beat by non-linear wave interactions. *Journal of Fluid Mechanics*, 49:1–20, 1971. doi: 10.1017/S0022112071001897.
- Guedes, R. M. C., Bryan, K. R., Coco, G., and Holman, R. A. The effects of tides on swash statistics on an intermediate beach. 116(C4):n/a–n/a, 2011. doi: 10.1029/2010JC006660.
- Guedes, R. M. C., Bryan, K. R., and Coco, G. Observations of wave energy fluxes and swash motions on a low-sloping, dissipative beach. *Journal of Geophysical Research: Oceans*, 118(7):3651–3669, 2013. doi: 10.1002/jgrc.20267.
- Guza, R. and Bowen, A. Resonant interactions for waves breaking. on a beach. *Coastal Engineering Proceedings*, 1(15), 1976.
- Guza, R., Thornton, E., and Holman, R. Swash on steep and shallow beaches. *Coastal Engineering Proceedings*, 1(19), 1984. doi: 10.9753/icce.v19.%25p.
- Haines, P. Palm beach gold coast management options feasibility assessment. Technical report, BMT WBM Pty Ltd, 2013.
- Hansen, N., Sand, S., Lundgren, H., Sorensen, T., and Gravesen, H. Correct reproduction of group-induced long waves. *Coastal Engineering Proceedings*, 1(17), 1980.
- Hasselmann, K., Barnett, T. P., Bouws, E., Carlson, H., Cartwright, D. E., Enke, K., Ewing, J. A., Gienapp, H., Hasselmann, D. E., Kruseman, P., Meerburg, A., Müller, P., Olbers, D. J., Richter, K., Sell, W., and Walden, H. Measurements of wind-wave growth and swell decay during the joint north sea wave project (JONSWAP), 1973.
- Henderson, S. M., Guza, R. T., Elgar, S., Herbers, T. H. C., and Bowen, A. J. Non-linear generation and loss of infragravity wave energy. *Journal of Geophysical Research: Oceans*, 2006.
- Herbers, T. H. C., Elgar, S., and Guza, R. T. Infragravity-frequency (0.005–0.05 Hz) motions on the shelf. part i: Forced waves. *Journal of Physical Oceanography*, 24:917–927, 1994. doi: 10.1175/1520-0485(1994)024<0917:IFHMOT>2.0.CO;2.
- Holland, K. T. and Holman, R. A. The statistical distribution of swash maxima on natural beaches. *J. Geophys. Res.*, 98:10271–10278, 1993. doi: 10.1029/93JC00035.

- Holland, T., Holman, R., Lippmann, T., Stanley, J., and Plant, N. Practical use of video imagery in nearshore oceanographic field studies. *IEEE J. Oceanic Eng.*, 22(1):81–92, 1997. doi: 10.1109/48.557542.
- Holman, R., Sallenger, A. H., Lippmann, T., and Haines, J. W. The application of video image processing to the study of nearshore processes. *Oceanography*, 6: 78–84, 1993.
- Holman, R. A., Haller, M. C., Lippmann, T. C., Holland, K. T., and Jaffe, B. E. Advances in nearshore processes research: Four decades of progress. *Coastal Forum*, 83(1):39–51, 2015.
- Janssen, T. T., Battjes, J. A., and van Dongeren, A. R. Long waves induced by short-wave groups over a sloping bottom. *Journal of Geophysical Research: Oceans*, 2003.
- Johnson, D. and Pattiaratchi, C. Boussinesq modelling of transient rip currents. *Coastal Engineering*, 53(5–6):419–439, 2006. doi: 10.1016/j.coastaleng.2005.11.005.
- Kennedy, A. B., Chen, Q., Kirby, J. T., and Dalrymple, R. A. Boussinesq modeling of wave transformation, breaking, and runup 1: 1D. *J. Wtrwy., Port, Coast., and Oc. Engrg.*, 126:39–47, 2000.
- Kirby, J. T., Wei, G., Chen, Q., Kennedy, A. B., and Dalrymple, R. A. *FUNWAVE 1.0. Fully nonlinear Boussinesq wave model. Documentation and user's manual. Report CACR-98-06*. Newark, DE: Center for Applied Coastal Research, Department of Civil and Environmental Engineering, University of Delaware, 1998.
- Kobayashi, N. Numerical modeling of wave runup on coastal structures and beaches. *Marine Technology Society Journal*, 33(3):33–37, 1999.
- Kostense, J. Measurements of surf beat and set-down beneath wave groups. *Coastal Engineering Proceedings*, 1(19), 1984.
- Lara, J. L., Ruju, A., and Losada, I. J. Reynolds averaged navier-stokes modelling of long waves induced by a transient wave group on a beach. *Proceedings of the Royal Society of London A: Mathematical, Physical and Engineering Sciences*, 2010. doi: 10.1098/rspa.2010.0331.
- Lippmann, T. and Holman, R. A. Wave group modulations in cross-shore breaking patterns. In: *Proceedings of the 23rd International Conference on Coastal Engineering. ASCE. Venice, Italy*, pages 918–931, 1992.
- Lippmann, T. C., Holman, R. A., and Bowen, A. J. Generation of edge waves in shallow water. *Journal of Geophysical Research: Oceans*, 102(C4):8663–8679, 1997. doi: 10.1029/96JC03722.
- List, J. H. A model for the generation of two-dimensional surf beat. *Journal of Geophysical Research: Oceans*, 97(C4):5623–5635, 1992. doi: 10.1029/91JC03147.

- Longuet-Higgins, M. and Stewart, R. Radiation stress in water waves, a physical discussion with applications. *Deep Sea Res.*, 11:529–563, 1964.
- Longuet-Higgins, M. S. and Stewart, R. W. Changes in the form of short gravity waves on long waves and tidal currents. *Journal of Fluid Mechanics*, 8:565–583, 1960. doi: 10.1017/S0022112060000803.
- Longuet-Higgins, M. S. and Stewart, R. W. Radiation stress and mass transport in gravity waves, with applications to 'surf beats'. *J. Fluid Mech.*, 11:481–504, 1962. doi: 10.1017/S0022112062000877.
- Lynett, P. J., Melby, J. A., and Kim, D.-H. An application of boussinesq modeling to hurricane wave overtopping and inundation. *Ocean Engineering*, 37(1):135–153, 2010. doi: 10.1016/j.oceaneng.2009.08.021.
- MacMahan, J. H., Reniers, A. J. H. M., Thornton, E. B., and Stanton, T. P. Infragravity rip current pulsations. *Journal of Geophysical Research: Oceans*, 2004.
- MacMahan, J. H., Thornton, E. B., and Reniers, A. J. Rip current review. *Coastal Engineering*, 2006.
- Madsen, P., Sørensen, O., and Schäffer, H. Surf zone dynamics simulated by a boussinesq type model. part II: surf beat and swash oscillations for wave groups and irregular waves. *Coastal Engineering*, 32(4):289–319, 1997. doi: 10.1016/S0378-3839(97)00029-X.
- Madsen, P. A. and Fuhrman, D. R. Run-up of tsunamis and long waves in terms of surf-similarity. *Coastal Engineering*, 55(3):209–223, 2008. doi: 10.1016/j.coastaleng.2007.09.007.
- Masselink, G. Group bound long waves as a source of infragravity energy in the surf zone. *Continental Shelf Research*, 1995.
- McArdle, S. B. and McLachlan, A. Sand beach ecology: Swash features relevant to the macrofauna. *Journal of Coastal Research*, 8(2):398–407, 1992.
- Mei, C. C. and Benmoussa, C. Long waves induced by short-wave groups over an uneven bottom. *Journal of Fluid Mechanics*, 139:219–235, 1984. doi: 10.1017/S0022112084000331.
- Mei, C. C., Stiassnie, M., and Yue, D. K.-P. *Theory and Applications of Ocean Surface Waves: Part 1: Linear Aspects; Part 2: Nonlinear Aspects: 23 (Advanced Series on Ocean Engineering)*. World Scientific Publishing Company, expanded ed edition edition, 2005.
- Mizuguchi, M. and Toita, H. Generation of second-order long waves by a wave group in a laboratory flume and its control. *Coastal Engineering Proceedings*, 1(25), 1996.
- Molin, B. On the generation of long-period second order free waves due to changes in the bottom profile. *Ship Res. Inst. Rep.*, 68:1–22, 1982.

- Nagase, S. and Mizuguchi, M. Laboratory experiment on long wave generation by time-varying breakpoint. *Coastal Engineering Proceedings*, 1(25), 2001.
- Nielsen, P. Groundwater dynamics and salinity in coastal barriers. *Journal of Coastal Research*, 15(3):732–740, 1999.
- Nielsen, P. *Coastal and estuarine processes*. World Scientific, 2009.
- Nielsen, P. and Baldock, T. E. Shaped surf beat understood in terms of transient forced long waves. *Coastal Engineering*, 57(1):71–73, 2010. doi: 10.1016/j.coastaleng.2009.09.003.
- Nielsen, P., de Brye, S., Callaghan, D. P., and Guard, P. A. Transient dynamics of storm surges and other forced long waves. *Coastal Engineering*, 55(6):499–505, 2008. doi: 10.1016/j.coastaleng.2008.02.006.
- Orszaghova, J., Taylor, P. H., Borthwick, A. G., and Raby, A. C. Importance of second-order wave generation for focused wave group run-up and overtopping. *Coastal Engineering*, 94:63–79, 2014. doi: 10.1016/j.coastaleng.2014.08.007.
- Phillips, M. O. *The Dynamics of the Upper Ocean*. Cambridge University Press, 1977.
- Pomeroy, A., Lowe, R., Symonds, G., Van Dongeren, A., and Moore, C. The dynamics of infragravity wave transformation over a fringing reef. *Journal of Geophysical Research: Oceans*, 2012.
- Power, H. E., Holman, R. A., and Baldock, T. E. Swash zone boundary conditions derived from optical remote sensing of swash zone flow patterns. *J. Geophys. Res.*, 116(C6):n/a–n/a, 2011. doi: 10.1029/2010JC006724.
- Proudman, J. The effects on the sea of changes in atmospheric pressure. *Geophys. Suppl. Mon. Not. R. Astron. Soc.*, 2:197–209, 1929.
- Rapp, R. J. and Melville, W. K. Laboratory measurements of deep-water breaking waves. *Philosophical Transactions of the Royal Society of London A: Mathematical, Physical and Engineering Sciences*, 331(1622):735–800, 1990. doi: 10.1098/rsta.1990.0098.
- Raubenheimer, B. and Guza, R. T. Observations and predictions of run-up. *Journal of Geophysical Research: Oceans*, 101(C11):25575–25587, 1996. doi: 10.1029/96JC02432.
- Reniers, A. J. H. M., Roelvink, J. A., and Thornton, E. B. Morphodynamic modeling of an embayed beach under wave group forcing. *Journal of Geophysical Research: Oceans*, 109(C1), 2004.
- Ruessink, B. G., Kleinhans, M. G., and van den Beukel, P. G. L. Observations of swash under highly dissipative conditions. *Journal of Geophysical Research: Oceans*, 103(C2):3111–3118, 1998. doi: 10.1029/97JC02791.

- Schäffer, H. A. Infragravity waves induced by short-wave groups. *Journal of Fluid Mechanics*, 247:551–588, 1993. doi: 10.1017/S0022112093000564.
- Schäffer, H. A. Second-order wavemaker theory for irregular waves. *Ocean Engineering*, 23(1):47–88, 1996. doi: 10.1016/0029-8018(95)00013-B.
- Sheremet, A., Guza, R. T., Elgar, S., and Herbers, T. H. C. Observations of nearshore infragravity waves: Seaward and shoreward propagating components. *Journal of Geophysical Research: Oceans*, 107(C8):10–1–10–10, 2002. doi: 10.1029/2001JC000970.
- Shi, F., Kirby, J. T., Harris, J. C., Geiman, J. D., and Grilli, S. T. A high-order adaptive time-stepping {TVD} solver for boussinesq modeling of breaking waves and coastal inundation. *Ocean Modelling*, 43–44:36–51, 2012. doi: 10.1016/j.ocemod.2011.12.004.
- Short, A. D. *Beaches of the Queensland Coast, Cooktown to Coolangatta*. Sydney University Press, University of Sydney, 2000.
- Stockdon, H. F. and Holman, R. A. Estimation of wave phase speed and nearshore bathymetry from video imagery. *Journal of Geophysical Research: Oceans*, 105 (C9):22015–22033, 2000. doi: 10.1029/1999JC000124.
- Stockdon, H. F., Holman, R. A., Howd, P. A., and Jr., A. H. S. Empirical parameterization of setup, swash, and runup. *Coastal Engineering*, 53(7):573–588, 2006. doi: 10.1016/j.coastaleng.2005.12.005.
- Symonds, G. and Bowen, A. J. Interactions of nearshore bars with incoming wave groups. *J. Geophys. Res.*, 89(C2):1953–1959, 1984. doi: 10.1029/JC089iC02p01953.
- Symonds, G., Huntley, D. A., and Bowen, A. J. Two-dimensional surf beat: Long wave generation by a time-varying breakpoint. *J. Geophys. Res.*, 87(C1):492–498, 1982. doi: 10.1029/JC087iC01p00492.
- Tehrani-rad, B., Fengyan, S., Kirby, J., Harris, J., and Grilli, S. *Tsunami benchmark results for fully nonlinear Boussinesq wave model FUNWAVE-TVD, version 1.0*. Newark, DE: Center for Applied Coastal Research, Department of Civil and Environmental Engineering, University of Delaware, 2011.
- Thomson, J., Elgar, S., Raubenheimer, B., Herbers, T. H. C., and Guza, R. T. Tidal modulation of infragravity waves via nonlinear energy losses in the surf-zone. *Geophysical Research Letters*, 2006.
- Tonelli, M. and Petti, M. Hybrid finite volume – finite difference scheme for 2dh improved boussinesq equations. *Coastal Engineering*, 56(5–6):609–620, 2009. doi: 10.1016/j.coastaleng.2009.01.001.
- van Dongeren, A., Battjes, J., Janssen, T., van Noorloos, J., Steenhauer, K., Steenbergen, G., and Reniers, A. Shoaling and shoreline dissipation of low-frequency waves. *Journal of Geophysical Research: Oceans*, 2007.

- 
- Van Leeuwen, P. J. *Low frequency wave generation due to breaking wind waves*. PhD thesis, Delft Univ. of Technol., Delft, Netherlands, 1992.
- Wei, G., Kirby, J. T., and Sinha, A. Generation of waves in boussinesq models using a source function method. *Coastal Engineering*, 36(4):271–299, 1999. doi: 10.1016/S0378-3839(99)00009-5.
- Whitham, G. B. Mass, momentum and energy flux in water waves. *Journal of Fluid Mechanics*, 12:135–147, 1962. doi: 10.1017/S0022112062000099.